Alma Mater Studiorum · Università di Bologna

DOTTORATO DI RICERCA IN MATEMATICA
CICLO XXX

Settore concorsuale di afferenza: 01/A3

Settore scientifico disciplinare: MAT/05

Minimal Surfaces in Sub-Riemannian Structures and Functional Geometry of the Visual Cortex

Presentata da: Emre Baspinar

Coordinatore dottorato:
Chiar.ma Prof.ssa
Giovanna Citti

Supervisore:
Chiar.ma Prof.ssa
Giovanna Citti

Co-supervisore:
Chiar.mo Prof.
Alessandro Sarti

Esame finale 2018

To my parents Nevin, Huseyin, my brother Mert, and to A. Sapmaz

Contents

Preface

Neuromathematics and neurogeometry are disciplines which harmonize different scientific and philosophical fields. They are the formalized expressions of the effort of understanding the concept of perception and in particular visual perception. They are related to philosophy in the exact sense because they find their constructive norms in phenomenology. In fact they are the scientific disciplines which naturalize the phenomenology. In other words they put the phenomenology on a rigorous scientific basis in a formal way.

In this thesis we try to understand the relations between phenomenology and neurosciences by using the precise language of mathematics. I hope that this modest contribution here will lead to new questions and perspectives. This study has been a joyful and stimulating adventure for me. I hope that the reader will share this joy with me.

Bologna
April 2018

Emre Baspinar

Notation

- C^0: The space of continuous functions
- C^p: The space of $p-$order differentiable functions
- C^∞: The space of smooth functions
- L^p: The space of $p-$integrable functions
- L^∞: The space of bounded measurable functions
- $\mathbb{R}^n$: $n-$dimensional Euclidean space
- S^1: Real numbers in $[0, 2\pi]$
- $\mathbb{N}^+$: Positive integers
- $\mathbb{C}$: Complex numbers
- $\text{rank}(F)$: Rank of set of vectors F
- $\text{span}\{X\}$: The span of the vector fields X
- $R(f)$ Range of map f
- $\inf f$: Infimum of f
- $\max f$: Maximum of f
- $\det(f)$: Determinant of f
- $\ker f$: Kernel of operator f
- $\text{Re}\{f\}$: Real part of f
- $\text{Im}\{f\}$: Imaginary part of f
- $f\big|_q$ or $f_{|_q}$: Operator f at point q
- $\langle ., . \rangle$: Standard inner product
- $\bigcup$: Union of sets

- $\oplus$: Direct sum
- $\otimes$: Tensor product
- i: Imaginary unit if it is not an index number

Chapter 1

Introduction

The objective of this thesis is to develop geometrical models of vision consistent with the characteristics of the visual cortex and study geometric evolutions in the relevant geometry arising from the models for visual processing. The models rely on empirical data existing in phenomenology of perception and neurophysiology. The focus of the models are on the first stage visual perception tasks. The main problem is the identification of visual features for the organization of visual forms based on certain symmetry and invariance principles suggested by the empirical data. This study could be seen as a part of the effort for understanding phenomenology in terms of natural sciences, towards a more complete theory of cognition. The models are described with instruments of sub-Riemannian differential geometry and partial differential equations. These equations are governed by differential constraints in the tangent plane, and they seem totally degenerate from a Riemannian point of view. Hence classical theory of geometric evolution equations does not apply and the properties of solutions to such equations are still largely unknown.

1.1 The problem of perception in neural sense

The question of how we perceive has been an intriguing topic since the ancient times. For example we can consider the philosophical effort around the concept of *entelechy*, which started with the early attempts of the Aristotelian school to answer the question. We can think Husserl in phenomenology and its relation to natural sciences. We may consider Berlin school of experimental psychology formulating perception based on Gestalt psychology (or theory) [170], [112], [111], which is closely related to our present work here.

Gestalt psychology is a theory for understanding the principles underlying the configuration of local forms which gives rise to a meaningful global perception. It focuses on perception in a general way. The main idea of Gestalt psychology is that the mind constructs the global whole by rather grouping *similar* fragments than simply summing the fragments as if they are indifferent. In terms of visual perception, those similar fragments are the point stimuli with the same (or closely) valued features of the same type.

For example, we tend to group the same colored objects in an image and to perceive them as an ensemble rather than the differently colored ones.

There have been many psychophysical studies which attempted to provide quantitative parameters describing the tendencies of the mind in visual perception based on Gestalt psychology. A particularly important one for our study here is the pioneering work of Field et. al. [64] where they propose a representation, *association field*, which models certain Gestalt principles and shows that it is more likely that the brain perceives the fragments which are similary oriented and aligned along a curvilinear path together than that it perceives the fragments with rapidly changing orientations and without any alignment.

We have known that the neurons (simple cells) in the primary visual cortex (V1) perform boundary detection since the neurophysiological experiments of Hubel and Wiesel [87], [88], [86]. Furthermore recent imaging technologies such as optical imaging, functional MRI and diffusion tensor MRI have made it possible to make neurophysiological observations at a wide range of scales. As a result, now we know that V1 is capable of detecting and grouping different features. It confirms the aforementioned psychophysical results. Moreover those perceptual procedures are dependent on the functional architecture of V1 [20].

Several models which attempted to harmonize this empirical framework based on the association fields and the functional architecture of V1 with different mathematical instruments were proposed. Koenderink et. al. [109], [110] focused on differential geometric approaches in order to study the visual spaces. They modeled the invariance of the simple cells with respect to certain symmetries in terms of a family of Gaussian functions. Hoffman [83], [84] provided the basic framework of the models of vision and interpreted the functional architecture of V1 as a fiber bundle. Following a similar reasoning, Petitot and Tondut [132] developed further the fiber bundle structure proposed by Hoffman and provided a model which was coherent with both orientation sensitive simple cell behavior and the long-range horizontal connectivity between the simple cells within V1. They started from that the simple cell orientation selectivity induces a contact geometry (associated to the first Heisenberg group) rendered by the fibers of orientations. They showed that a specific family of curves found via a constraint minimization in the contact geometry coincides almost completely with the association fields reported by Field et. al. [64]. Zucker [174] presented a differential geometric model which employed a fiber bundle structure in order to explain the neural connectivity from a point of view based on Frenet frames.

1.2 Sub-Riemannian geometric analysis instruments

New mathematical instruments have been developed independently and they were aimed to describe anisotropic problems. Sub-Riemannian (also known as Carnot-Carathéodory) space is a space whose metric structure may be considered as a constrained geometry, where motion is possible only along a given set of directions changing from point to point. More precisely a sub-Riemannian structure can be described by a choice of vector

fields, which are the analogues of the directional derivatives.

The development of this theory began with a celebrated paper of Hörmander [85], who studied for the first time the operators represented as a sum of squares of smooth vector fields. He proved that although these operators seem totally degenerate from an elliptic point of view, the solution of associated partial differential equations can be regular in any direction. Two years later, Bony [17] proved a maximum principle for Hörmander type operators by showing that the maxima of the solutions propagate along the integral curves of the vector fields and their commutators. In 1975 Folland [68], and immediately after Rothschild and Stein [138], provided estimates of the fundamental solutions of these type of operators. One of the closely related problems is the problem of the estimates associated to the distance in these spaces. Main results in these directions are due to Chow [33], Nagel Stein and Weinger [126]. These results opened a new direction of research in sub-Riemannian geometric analysis, which is able to confront with strongly anisotropic structures such as the geometry of the visual cortex. Nowadays the theory of linear operators in sub-Riemannian structures is well-established (see for example [14]). Much less is known in the theory of non-linear differential equations, for example geometric evolution equations or minimal surfaces. We refer to Chapter 6 and Chapter 7 for a review of state of the art results related to the geometric evolutions and minimal surfaces within this context. Here we mention only the fact that the notion of surface has been given in 2001 by Franchi, Serapioni, Serra Cassano [72] in sub-Riemannian settings.

1.3 Sub-Riemannian models of the visual cortex

Citti and Sarti [35] observed that the group of roto-translations (SE(2)) with a sub-Riemannian metric was providing a precise geometrical framework for the functional architecture of V1. They introduced in [145], [35] the vector fields associated to the sub-Riemannian geometry of SE(2) in order to model the long-range horizontal connectivity characterizing the association fields. Furthermore they proposed an algorithm of surface reconstruction via a subelliptic mean curvature flow generating a minimal surface in the limit. It was performing completion of missing level sets of an image, along the SE(2) horizontal curves, which were the curves coinciding with the association fields of Field et. al. [64]. The algorithm of Citti-Sarti [35] poses interesting questions from a purely analytic point of view, since, as we mentioned before, the theory of geometric evolution equations and of minimal surfaces in this setting are not completely known.

Furthermore Sarti, Citti and Petitot [146] provided a generalized version of the model to an orientation-scale selective framework.

The interpretation of V1 based on SE(2) inspired new image processing algorithms. Duits and Franken [50], [51] proposed image enhancement and completion algorithms in the SE(2) framework arising from a specific invertible wavelet transform. We refer also to Sanguinetti et. al. [140], [141], Boscain et. al. [19], [18] and Franceschiello et. al. [34] for some examples of image reconstruction algorithms using sub-Riemannian evolution equations in the same model framework.

Apart from those, some algorithms were proposed for the construction of feature preference maps of the simple cells in the model framework based on SE(2). We refer to the works of Barbieri et. al. [4], [5], where they constructed orientation preference maps using the spectral space associated to SE(2).

Finally, perceptual grouping of spatial visual features was modeled in the SE(2) framework by Sarti and Citti in [144] and by Favali et. al. in [61], [62]. Furthermore in [37], Cocci et. al. proposed a model for the grouping of spatio-temporal visual features in a generalized framework inspired by the one proposed in [35].

Our study considers the model of Citti and Sarti [35] and its generalized version by Sarti, Citti and Petitot [146] as the point of departure. Our original contributions are both theoretical and applied:

- A novel sub-Riemannian model of the functional architecture of V1, which models the orientation-frequency selective phase shifted simple cell behavior and the associated horizontal connectivity (see Chapter 5),
- The proof of the convergence in the Euclidean setting of the cortical based completion algorithm proposed by Citti-Sarti [35], where they indeed conjectured that iterative diffusion of a function followed by a maximum selection procedure tends to a sub-Riemannian mean curvature flow (see Chapter 6 and our submitted manuscript [9]),
- Uniqueness of viscosity solution to sub-Riemannian mean curvature flow in the Heisenberg group and asymptotic behavior of the vanishing viscosity solutions to sub-Riemannian mean curvature flow in step 2 Carnot groups and SE(2) which are generated by the above mentioned neural model (submitted manuscript, see Chapter 7),
- A novel image enhancement algorithm based on sub-Riemannian diffusion and Laplace-Beltrami flow in the sub-Riemannian geometry associated to our neural model with frequency and phase (see Chapter 8),
- Multi-scale orientation map and scale preference map construction by using the Bargmann transform in the reducible representation (see Chapter 9 and our published article [8]),
- Multi-frequency orientation map and frequency preference map construction by using the Bargmann transform in the reducible representation associated to the spatial frequency space, and their statistical comparisons to the corresponding neurophysiologically observed maps (see Chapter 10).

1.4 Outline of the thesis

The thesis is organized in three parts. Part I is dedicated to the modeling of V1. Part II explains the analytical results related to a diffusion driven motion, sub-Riemannian

mean curvature flow and an image enhancement algorithm. It contains a first proof of convergence of the model provided in [35], the proof of uniqueness of viscosity solution to the sub-Riemannian mean curvature flow equation in the Heisenberg group. Then it presents a new surface evolution algorithm for image enhancement. Part III presents two geometrical models for constructing orientation, scale and frequency preference maps of the simple cells. Those models rely on our extended sub-Riemannian model framework and on the framework provided in [146].

Part I: Geometry of the visual cortex

In this part Chapter 2, Chapter 3 and Chapter 4 give the fundamentals which we use throughout the thesis while Chapter 5 presents our extended V1 model with frequency and phase.

In Chapter 2 we consider first the phenomenology of perception and start with the explanation of Gestalt psychology. We explain the Gestalt principles and how they are related to a specific visual problem: the problem of perceptual completion. We will describe the problem in terms of the studies of Kanizsa [104], [105] and the psychophysical results of Field et. al. [64]. Then we will continue with the neurophysiology of the perception and provide a description of the visual cortex. In particular we will explain the behavioral characteristics of the simple cells, the hypercolumnar architecture of V1 and the concept of pinwheels.

In Chapter 3 we will give a presentation of the main definitions and notions of sub-Riemannian geometry. We will present the notions of fiber bundles, integral curves, Lie groups and algebras, and horizontality. Finally, we will present the Gabor functions which we use as the mathematical interpretation of simple cell receptive profiles and the reasoning behind this choice based on Gabor functions.

In Chapter 4 we provide our reference models which employ different sub-Riemannian geometries. We first give the intuition behind feature selectivity and a description of the Gabor transform together with the inverse transform. Then we present the model of Petitot and Tondut [132] and the model given in [35]. Those two models are based on orientation selectivity alone. We continue with a generalization, proposed by Sarti, Citti and Petitot [146], of the model given in [35]. In this case also scale selectivity is taken into account. We present the hypercolumnar structure of the visual cortex, starting from the concepts related to simple cell receptive profiles. We explain the hypercolumnar geometry in terms of Lie group theory, sub-Riemannian geometry and fiber bundles. Then we give information about a particular mechanism: lifting of visual stimulus in combination with maximum selection. This mechanism inspires us in our feature map construction models which will be presented in Part III. Finally we explain the horizontal connectivity and how the simple cells propagate their activity along the horizontal connectivity in this setting, relating those concepts to the surface reconstruction algorithm proposed in [35].

Chapter 5 contains our first original contribution. We present our sub-Riemannian orientation-frequency selective V1 model with shifted phase simple cell behavior. We provide the simple cell receptive profile in this setting and the transformation law through

which we obtain the set of all receptive profiles in V1. This set is associated to the hypercolumnar architecture of V1 which can be considered as a Lie group or as a sub-Riemannian structure. All those concepts are equivalent, yet they provide different understandings of the hypercolumnar architecture. Each simple cell receptive profile in the set of receptive profiles renders an output resulting from the filtering of a given visual stimulus with Gabor functions. This output represents the response of the simple cell to the stimulus. This part until here is mostly about visual feature extraction and the geometric representation of the extracted features. We will continue with the horizontal connectivity which endows the sub-Riemannian setting with the horizontal integral curves modeling the simple cell connectivity in V1. Then we will show a specific case of the coherent state condition related to Gabor functions in this setting, justifying our choice of Gabor function as the mathematical representation of a simple cell receptive profile in our extended framework. Finally we will give the relation of our model to curvatured detection based on the technique proposed by Dobbins et. al. [49].

Part II: Geometric evolutions in Lie groups for visual completion and enhancement

In Part II, Chapter 6 and Chapter 7 provide the theoretical results in relation to some geometric evolutions in Lie groups associated to the models of vision and Chapter 8 contains our image enhancement algorithm which performs in the sub-Riemannian framework of our extended visual cortex model presented in Chapter 5. The results in Chapter 6 and Chapter 7 provide the proofs related to the surface reconstruction algorithm proposed in the model framework of [35] and the proof of uniqueness of the solution to sub-Riemannian mean curvature flow in the Heisenberg group.

We give in Chapter 6 first a description of the surface reconstruction algorithm proposed in [35] and its relation to our result. Then we give an overview of necessary tools from non-linear semigroup theory and evolving graphs by curvature. We prove certain properties of the iterative operator describing each evolution step of the surface reconstruction algorithm. Then we provide the main result of the chapter: Evolution of a function via Laplace-Beltrami flow induces mean curvature flow of the surface underlying the function.

In Chapter 7 we present the formulation of the problem of uniqueness of viscosity solution to sub-Riemannian mean curvature flow. Then we give an overview of the literature related to the problem and the relevant definitions. Afterwards we provide some geometric properties of the solutions to sub-Riemannian mean curvature flow. Finally we prove the uniqueness of the viscosity solution to the sub-Riemannian mean curvature flow in the Heisenberg group setting. The result is generic for any level set so equivalently applies to surfaces as well and it is closely related to the mean curvature flow of a surface in the geometries associated to the models of the primary visual cortex. Finally we give the core idea of the uniqueness proof which allows us to generalize the proof to Carnot groups of step 2.

In Chapter 8 we propose an image enhancement algorithm employing our sub-Riemannian model framework. The algorithm uses sub-Riemannian diffusion or Laplace-

Beltrami flow in a reduced version of the 5-dimensional sub-Riemannian geometry associated to our model with frequency and phase. We describe the evolution equations that we use for the enhancement. We provide the algorithmic steps and the corresponding discrete scheme employing central finite differences. Finally we present our experimental results.

Part III: Feature map construction via a Bargmann transform

In this part we focus on our geometrical models proposed for orientation map construction at both single and multi-scale levels, scale map construction, orientation map construction at multi-frequency level and frequency map construction.

The model in Chapter 9 employs the orientation-scale selective model framework [146] presented in Chapter 4. We start directly with the neurally inspired procedure constructing the orientation and scale maps using the Bargmann transforms performing on a noise stimulus. Then we provide a comparison of our model to previously proposed models for orientation map construction. In the end we give our simulation results showing the orientation maps produced through the model.

In Chapter 10 we rely on an analogous procedure to the one presented in Chapter 9. However this time the model is proposed for multi-frequency orientation map construction and it uses the geometrical framework of the extended model presented in Chapter 5. The constructed orientation and frequency maps introduce a new type of configuration based on the structures which are called pinwheels and dipoles. We first describe those two structures and their interrelations to each other. Then we summarize the neurophysiological procedure which is used for obtaining the orientation and frequency maps from the visual cortex of a cat as explained by Ribot et. al. [134], [135]. We continue with our model procedure which we use in order to construct the orientation and frequency maps. Finally we provide our model simulations and compare our results statistically to the experimental results reported by Ribot et. al. in [134] and [135] in order to show up to which level our model is consistent with the neurophysiological evidence.

Chapter 11 is dedicated to the conclusion of the thesis.

Part I

Geometry of the visual cortex

Chapter 2

Phenomenology of perception and neurophysiology of the visual cortex

Perceptual organization is an operation performed by our visual systems. It is the process of grouping visual elements in such a way to obtain a coherent interpretation of a visual scene. The principles underlying such organization have been first expressed by Gestalt psychology at the phenomenological level, that is, using only subjective experience, without any neurophysiological evidence. According to Gestalt psychology, the whole is different from the sum of its parts, and the principles which can explain the perceptual organization are often referred to as the *laws of perceptual organization* [169], [170].

The visual cortex is the main unit of the mammalian brain which is responsible for the perceptual organization of local visual features. It is known based on neurophysiological evidence that the visual cortex contains neurons (simple cells) which are locally sensitive to several visual features such as orientation, frequency, scale, color, ocular dominance and so on. Moreover those cells are organized in a particular way giving rise to the modular structure of the visual cortex, which is called *hypercolumnar* architecture.

Our goal in this chapter is to provide the fundamentals of Gestalt psychology and explain the neurophysiology of the visual cortex, in particular the primary visual cortex (V1). We will first summarize the laws of perceptual organization and explain the problem of perceptual completion within the context of the works of Kanizsa [104], [105]. This problem is particularly important because it formulates the question of how certain laws of perceptual organization should be mathematically interpreted in order that we can provide a geometrical framework for the perceptual organization of local visual features. Afterwards we will explain the neurophysiological properties of V1. Finally we will give some information about feature maps and in particular about orientation maps.

2.1 The laws of perceptual organization

Gestalt psychology is a philosophical, psychological and biological theory which attempts to provide the principles explaining the mental process which produces meaningful and structured *global* perceptions by employing the local properties of visual information acquired by the individual. Underlying idea is that the perception of global whole within a structured environment is a product of multi-feature interactions stimulated by the visual information corresponding to several local pieces in the whole. Recent neurophysiological studies confirm that Gestalt psychology plays a central role in the visual tasks that the brain performs by exploiting the local properties of visual data, namely spatial position, orientation, frequency and scale (see [167] for a review).

The perception according to Gestalt psychology is realized based on the notion of *prägnanz*, which means that full perception from ambiguous stimuli is formed in a simple, ordered, regular and symmetrical way. Prägnanz is recognized through the laws of perceptual organization [169], [170]:

- **Law of good continuity:** We group rather the aligned pieces than those with sharp abrupt directional changes when we perceive an object as a whole formed by the pieces (see Figure 2.1).
- **Law of proximity:** We tend to perceive the parts spatially or temporally close to each other in an image as they belong to the same perceptual unit (see Figure 2.2).
- **Law of similarity:** We perceive rather similar pieces as grouped together (see Figure 2.2).
- **Law of closure:** We perceive forms and figures in their complete appearance despite the absence of some of their parts (we see for example the triangle in Figure 2.2 although there are some missing parts of the edges).
- **Law of symmetry:** Spatially symmetric pieces are more likely to be perceived as together than the non-symmetric ones.
- **Law of common fate:** We tend to group the pieces which are subjected to the same spatial or temporal change instead of the pieces experiencing different spatial or temporal change.

2.2 The question of perceptual completion

The visual system is able to perceive a curve even if some parts are missing, as we see in Figure 2.1. This is a particular example of a general phenomena called *perceptual completion* which can lead to the perception of contours or figures which are not actually present in the visual stimulus. Such contours are called *subjective contours*.

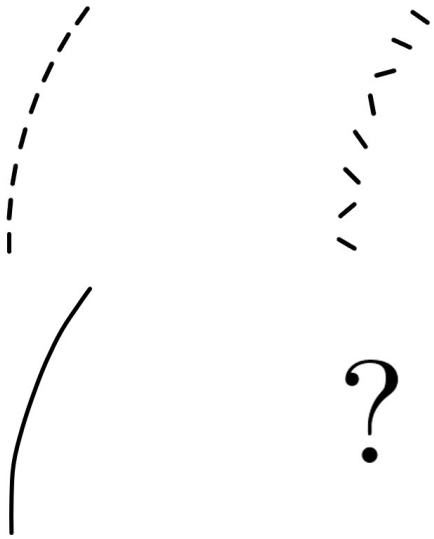

Figure 2.1: An example of the law of good continuity. We can recognize a curve on the left while we cannot on the right since the directions of the pieces change abruptly.

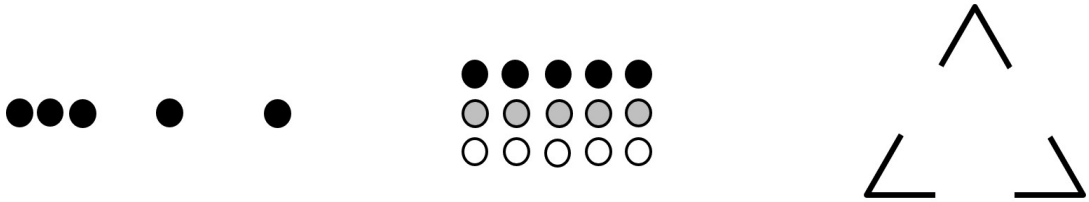

Figure 2.2: Examples of the law of proximity (left), the law of similarity (middle) and the law of closure (right).

Kanizsa [104], [105] classified two types of completion as *modal* completion and *amodal* completion. The first type is the completion with the modality of the vision. That is, we really see the completed object as a result of that the object has a different brightness with respect to the background. We recognize the occluding object in an image as a result of the modal completion. In the second type, the completion is without the modality of vision. In other words, we do not experience the completion visually but we know it. In this case the occluded object is perceived as a whole although only some specific fragments of the object evoke our sensory receptors. Kanizsa triangle and Ehrenstein's illusion (see Figure 2.3) provide clear examples of both completion types resulting in subjective contours.

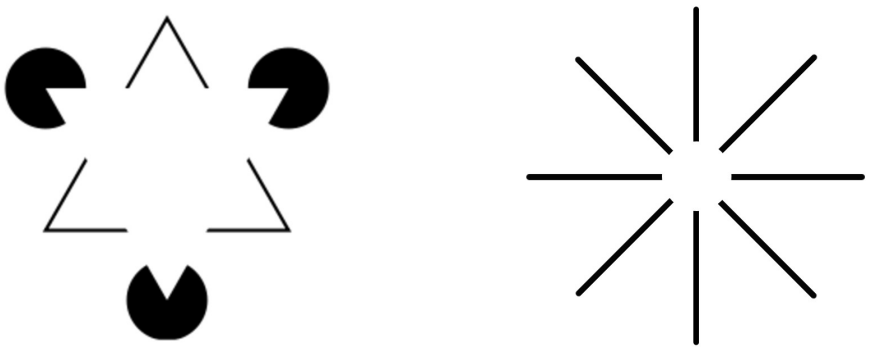

Figure 2.3: Left: Kanizsa triangle. There is no direct stimulus but we see a bright triangle on the top level (modal completion). We see also another triangular which is behind the bright one (amodal completion). Right: Ehrenstein illusion. We see a white circle at the center although there is no direct stimulus (modal completion) while we have the impression of that each vertical, horizontal or diagonal line fragment constitutes a whole line occluded by the white circle (amodal completion).

In particular Field et. al. in [64], studied the law of good continuity from a psychophysical point of view. They focused on the ability of the visual system to recognize the coherently aligned patches constituting curves or lines in a background of randomly oriented patches. In their experiments they considered many test images with coherently aligned patches with different distances and/or angles between each other (see Figure 2.4, which shows some examples of such test images). Consequently they introduced the notion of the *association fields*, as a characterization of all possible contours in good continuity with aligned fragments (see Figure 2.5). The association fields are considered as the geometrical representations of the law of good continuity.

Several mathematical models relying on Gestalt psychology can be found in the literature in relation to perceptual completion. Classical point of view of those models for the reconstruction of subjective contours is based on the minimization of the elastica functional given by

$$\int_{\gamma} (1 + k^2)\, ds,$$

with respect to a distance function of an appropriate metric, where k represents the curvature of the missing boundary (subjective contour) γ to be reconstructed (see [128], [125] for details). As mentioned in [121] and [2] the same idea can be extended to the level sets of an image $I : \mathbb{R}^2 \simeq M \to \mathbb{R}$ and in this case reconstruction of surfaces can be achieved by minimizing

$$\int_M |\nabla I| \Big(1 + \Big| \operatorname{div} \Big(\frac{\nabla I}{|\nabla I|}\Big)\Big|\Big)\, dx\, dy.$$

So each level set can be reconstructed as an elastica curve.

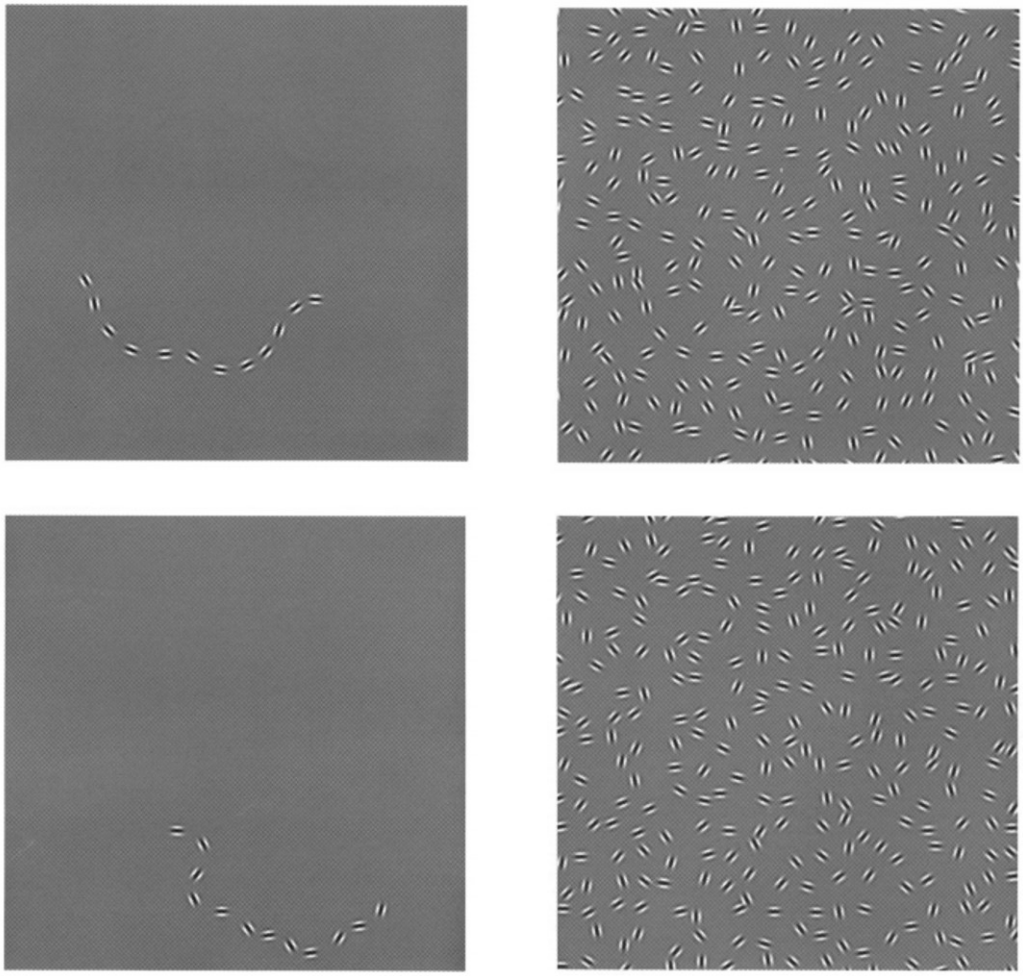

Figure 2.4: Two stimuli which were used in the experiments of Field et. al. [64]. The stimuli with aligned patches which we detect (left) and the stimuli plus the background with randomly oriented patches (right) are shown. It was reported that the stimulus at the bottom was more difficult to be detected by the subjects.

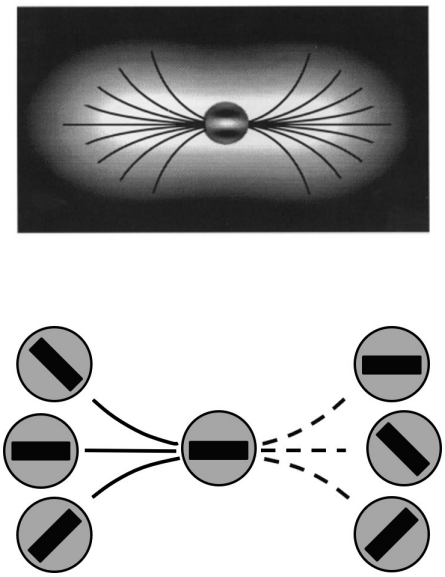

Figure 2.5: Top: All possible association fields passing through a horizontally aligned patch as shown by Fields et. al. [64]. Bottom: An illustration of the association fields. The solid curves represent the association fields between strongly associated patches while the dashed curves represent the fields between weakly associated patches.

2.3 Between phenomenology and neurophysiology of vision

Certain psychological experiments suggest that the principles underlying association fields are implemented within the mammalian primary visual cortex (see for example [20]). Those results show that the neural connectivity between the simple cells of the primary visual cortex has an anisotropic behavior which links preferentially the simple cells which are stimulated by similarly oriented contours having a colinear alignment. It is deduced from those results that perceptual grouping is closely related to the neural connectivity within the primary visual cortex [66], [20], [148]. Those connections articulate the saliency of distributed cortical responses, resulting in a perceptual grouping in accordance with the geometrical structure underlying the visual stimulus.

2.4 Neurophysiology of the visual cortex

The perceptual organization mechanisms relying on the laws of perceptual organization are neurophysiologically implemented in the visual cortex. The visual cortex is a part of the cerebral cortex and it is located in the occipital lobe which is the section of the brain towards the back of the head.

The cerebral cortex is the outermost layer of the gray matter of the brain. It is responsible for perceptual and cognitive tasks. The perceptual tasks employ the sensory

inputs such as visual inputs. The visual cortex is the particular part which processes the visual inputs received from the retina in order to provide a complete visual perception.

The light arrives at the retina and the photoreceptor cells (*rods and cones*) on the retinal layer respond to it by producing neural impulses which are called *action potentials*. These impulses are transmitted to the visual cortex V1 via the retino-geniculo-cortical paths illustrated in Figure 2.6.

In particular we will focus on the simple cells in V1, which are the first cells that process the retinal input.

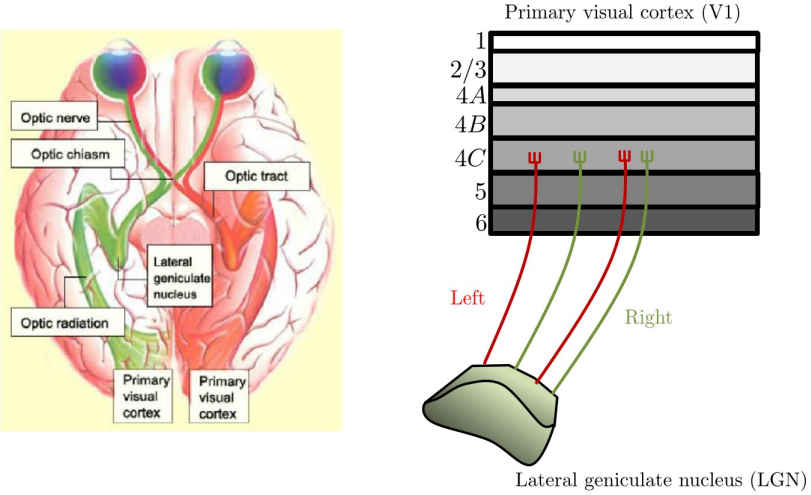

Figure 2.6: Left: An illustration of the visual pathway from the eyes to the primary visual cortex (taken from [131]). Right: An illustration of the axons from the lateral geniculate nucleus (LGN) to V1. The majority of the axons comes to the layer $4C$.

2.4.1 The simple cells in V1

The simple cells in V1 are sensitive to several visual features, in particular to orientation, spatial frequency and scale. Each simple cell receives input from a different region of the retina, called *receptive field* (RF). In classical sense a RF contains ON (excitatory) and OFF (inhibitory) regions. The decomposition of RF into those regions depends on the nature of the cell response given to light and dark luminance stimulation. More precisely the response to a stimulation is modeled by the simple cell *receptive profile* (RP).

A receptive profile can be interpreted as a function defined on the 2-dimensional retinal plane $M \simeq \mathbb{R}^2$, and vanishing outside the receptive field. The receptive profile of a cell will depend on the position q and on the selected feature(s) p, which can be orientation, frequency, scale and so on. Moreover the simple cells are coupled, in the sense that their RPs can be odd or even functions. Therefore they are represented as functions with complex values:

$$\Psi_{(q,p)} : M \to \mathbb{C}.$$

The function $\Psi_{(q,p)}$ is usually chosen as a Gabor function or a function of Gaus-

sian derivatives since those function types are capable of encoding the above mentioned features (see Figure 2.7).

The response $O_p^I(q)$ of a simple cell to a stimulus I at the point q with feature p can be written as an integral:

$$O_p^I(q) = \int_M I(x)\Psi_{(q,p)}(x)dx. \tag{2.1}$$

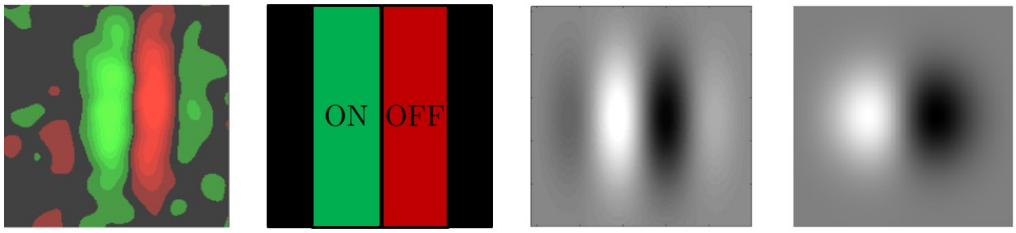

Figure 2.7: Left: Experimentally observed receptive profile of an odd cell with ON (green) and OFF (red) regions (taken from DeAngelis et. al. [45]). Middle left: An idealized illustration of the receptive profile. Middle right: Odd part of a Gabor function. Right: A first order Gaussian derivative.

The pioneering experiments of Hubel and Wiesel [87], [88], [86], which brought to them the Nobel prize, showed that the simple cells are organized in a particular way based on columnar modules, which are called *hypercolumns*, in V1. The hypercolumns are the main structures characterizing the functional geometry of V1.

2.4.2 Functional organization of V1

The functional organization of V1 is characterized by its layers, retinotopy, hypercolumns and neural connectivity.

Layered structure

The primary visual cortex (as well as the entire cerebral cortex) consists of six parallel layers to the surface of the cortex. Those layers are numbered from 1 to 6. We are interested in rather layer 4 and in particular its sublayer 4C to which major part of the neural paths from the lateral geniculate nucleus (LGN) is connected (see Figure 2.6).

Retinotopy

The visual stimulus on the retina is not represented in V1 exactly in the same way as on the retina, but it is subjected to a deformation. The *retinotopy* (or *retinotopic map*) is the map which represents this deformation and it is a diffeomorphism from the retina to a subset of the cortical space, called the *retinotopic plane*. The retinotopic map is a conformal logarithmic map, i.e., it preserves the angles (see Figure 2.8).

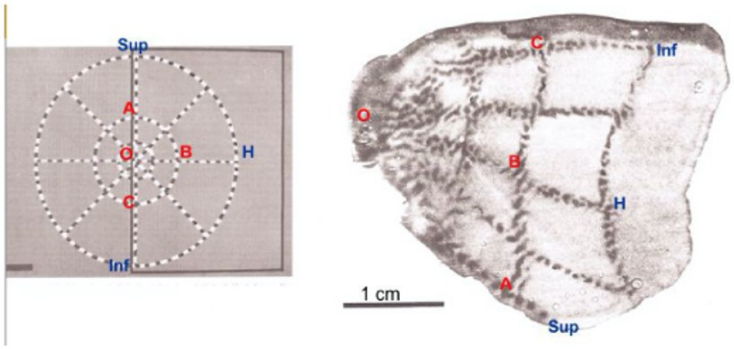

Figure 2.8: Retinotopic map of a macaque (taken from Tootell [160]). The highlighted points are mapped from the retina (left) to V1 (right).

Throughout the thesis we will systematically ignore the retinotopic map in modeling procedures and represent the stimulus detected by the simple cells with no deformation.

Hypercolumns and neural connectivity

In the early 60's, Hubel and Wiesel [86] observed that along an electrode penetration parallel to the cortical surface preferred orientation angles of the simple cells change from 0 to π, while they remain the same along the orthogonal electrode penetrations (see Figure 2.9).

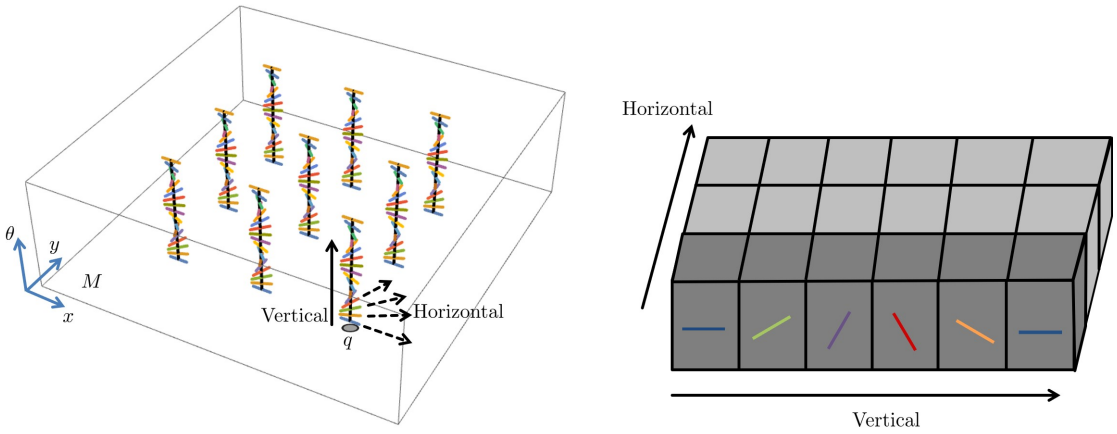

Figure 2.9: Hypercolumns contain the simple cells selective to all possible orientation angles at every point on the retina. Along vertical electrode penetrations the orientation preference angles vary smoothly while along horizontal electrode penetrations they remain the same.

In this case a parallel electrode penetration takes place along a hypercolumn which contains the simple cells sensitive to all possible values of the considered feature and responding to visual stimulus activating RFs at the specific retinal point q.

Similar experiments have been made subsequently for other visual features, in particular for scale and spatial frequency (see, e.g., [15], [46], [90], [149], [96], [154], [137], [135], which provide results related to the organization of frequency preference map of V1 and its interrelation with orientation map) and possibly with shifted phases (see for example the results of Tsao et. al. [162]).

Human psychophysical experiments provide evidence for a certain organization of spatial frequency preference maps in V1 based on the results suggesting that spatial frequencies are continuously distributed on the frequency map. In the literature (see for example [12] for spatial frequency adaptation and [168] providing results related to spatial frequency discrimination tasks) it is suggested that the visual cortex has multiple processing channels of which each one is tuned to one single spatial frequency among a variety of spatial frequencies. In the light of those results several studies using optical imaging on the cat visual cortex were conducted (see for example the analysis of Hübener et. al. [90], Issa et. al. [96], and the recent works of Ribot et. al. [134], [135]) and it was shown that each simple cell in V1 responds preferentially to visual stimuli with specific orientation and spatial frequency. Earlier studies related to the cat primary visual cortex proposed laminar [119], clustered [159], or columnar [161], [150], [16] organizations of spatial frequency maps. Those studies together with [124] and [158] suggest that across the cortical surface the cortical cells vary tangentially while they vary radially through the cortical lamenae. However although the neurophysiological organization and the functional architecture of orientation preference maps are well explained (see, e.g., [88], [157], [15]), the cortical organization of spatial frequency preference maps of the simple cells and the interrelations between the frequency maps and other maps are still not well-understood.

The preferred orientation angles, and more generally the considered feature of the simple cells change smoothly *inside* a hypercolumn, along a direction called *vertical* while they remain the same between the simple cells located along the directions transverse (which are also called *horizontal*) to hypercolumns. The vertical connections are called *intracolumnar short-range connections* while the horizontal connections are called *long-range horizontal connections* (see the works of Das and Gilbert [43], Bosking et.al. [20] for neurophysiological explanations related to those connections). The neural connectivity refers to the system of those connections.

Neural connectivity, feature selection and completion

The vertical connections play role in feature selection of the simple cells in presence of a visual stimulus.

Once a visual stimulus I activate the RFs corresponding to the simple cells in the hypercolumn at the point q, the hypercolumn fires and every simple cell inside responds

to the stimulus, giving rise (according to the formula given in (2.1)) to an output

$$O_p^I(q),$$

which depends on the position and the considered feature.

A specific one among them, the simple cell selective to the same feature p as the stimulus has, is selected via a cortical mechanism (which takes into account all the output values in the hypercolumn), and which can be for example the cell which gives the highest response magnitude:

$$O^I_{\bar{p}(q)}(q) = \max_p O_p^I(q), \quad \text{where} \quad p(q) = p. \tag{2.2}$$

However we will see that this selection mechanism can be modeled also by a different operator. In this way, a single value of the considered feature at the point q is detected.

The horizontal connections are important in the interactions and communication between the simple cells for neural activity propagation within V1, during the processing of the extracted features from the stimulus. The activity propagation is restricted to the horizontal connectivity and it is involved notably in the perceptual completion process mentioned in Section 2.2. Indeed the association fields studied by Field et. al. [64], which describes this phenomena from a purely phenomenological point of view, can be considered as the psychophysical counterpart of the neural activity propagation along the long-range horizontal connections.

2.4.3 Pinwheels

The hypercolumnar structure of V1 can be represented on a 2-dimensional plane in terms of so-called *feature preference maps* (or *feature maps*). A feature map shows the preferred value of each simple cell for the feature extracted from the visual stimulus at every point on the retina.

In particular *orientation map* has been a topic of interest and studied extensively. An orientation map shows the orientation angle preferences of the simple cells at every point on the 2-dimensional retinal plane. It was first obtained by Bosking et. al. [20] from V1 of a tree shrew. They first projected a stimulus with an object having a certain orientation angle on a screen in front of the animal. During the projection they measured the activation pattern of the tree shrew V1. Then they repeated the same procedure with the same types of stimuli but each time with a different orientation angle. At the end they obtained the preferred orientation angles at each point on the retinotopic plane of the tree shrew by combining the measurements through a vector sum. Finally they assigned a certain color to each orientation angle value and represented the orientation preference map on a 2-dimensional plane (see the left column of Figure 2.10).

Orientation maps are largely continuous, i.e., the preferred orientation angles vary smoothly across the map. However we notice certain singularities interrupting periodically the continuity. Those singularities are called *pinwheels*. They can be described as the centers of a circular region where we can find all possible orientation preference angles as we walk around the center in clockwise or counterclockwise direction (see the

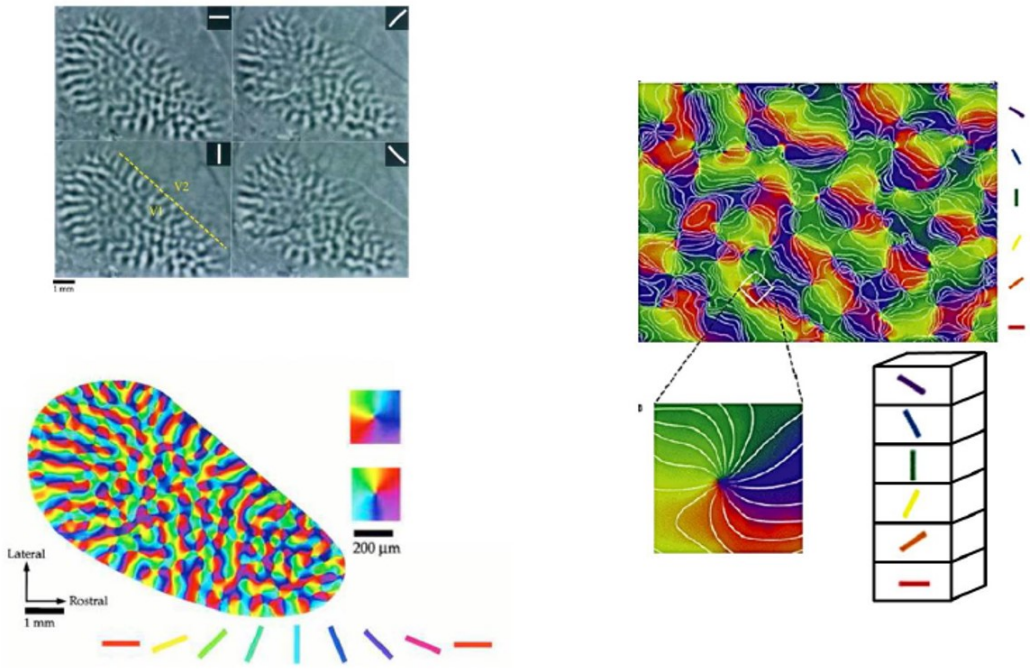

Figure 2.10: Orientation maps and pinwheels adapted from Bosking et. al. [20] and Petitot et. al. [131]. Left top: Responses of a tree shrew V1 to stimuli with four different orientations. Black and white correspond to low and high response magnitudes, respectively. Left bottom: The orientation map obtained from the responses and represented in terms of a color map. Two pinwheels are highlighted. Right: An illustration of an orientation map with iso-orientation lines (white lines) and a highlighted pinwheel as the representation of a hypercolumn on the orientation map.

right column of Figure 2.10). Note also that the pinwheels are the idealizations of the hypercolumns on an orientation map. In other words, they are the 2-dimensional representations of the hypercolumns, which are actually located in the 3-dimensional cortical space.

As one passes through V1-V2-V3 areas of the cortex, the sizes of the simple cells increase and the lattice of the orientation map extends while the pinwheels are preserved, as visualized in Figure 2.11 (see also the experimental results of Kennedy et. al. [106] and Levitt et. al. [114], which show the size differences between the simple cells in V1 and V2 of baboons).

Finally we note that feature maps have been observed also with frequency, scale and ocular dominance. In particular the functional organization and characteristics of spatial frequency preferences have been topics of interest in the neurophysiology community recently (see for example [96], [151], [164], [156], [127] and [134], which report several results related to spatial frequency maps). The interrelations between orientation and

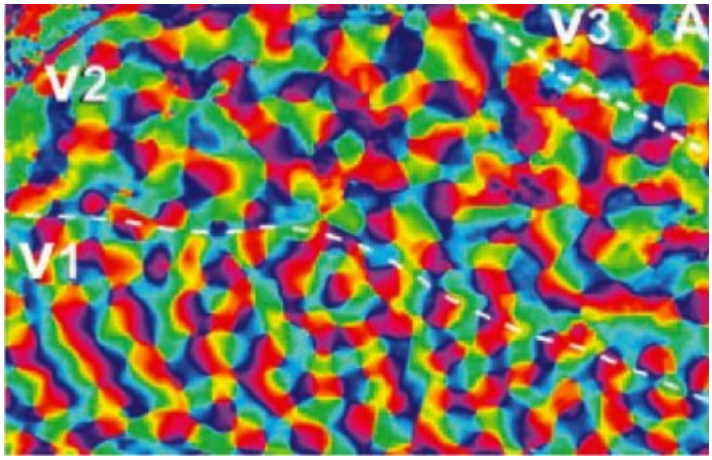

Figure 2.11: Orientation maps of V1, V2 and V3 of the cortex as shown by Petitot [131]. The sizes of the simple cells increase as one goes from V1 to V3 and the lattice structure of the map extends.

spatial frequency preference maps of the simple cells in the visual cortex have been studied in the pioneering works of Shoham et. al. [149], Issa et. al. [96], [95], and more recently by Ribot et. al. [134], [135]. We will study frequency maps extensively in Chapter 10.

Chapter 3

Sub-Riemannian geometry

In this chapter we give the necessary mathematical definitions and instruments which are required in the framework of our study. We give basic definitions related to differential geometry such as manifolds, smooth manifolds and provide the notions of tangent space, fiber bundle and vector fields in Section 3.1. Then in Section 3.2 we provide the notion of integral curves, which model the cortical long-range horizontal connections characterized by association fields. The functional architecture of the cortex induces a sub-Riemannian geometry. In Section 3.3 we provide a description of sub-Riemannian manifolds and their basic properties. Group structures underlying the model geometries are of the family of Lie groups. Therefore we give basic notions of Lie groups and algebras in Section 3.4 and introduce a specific Lie group family: Carnot groups. Finally in Section 3.5 we show some sub-Riemannian differential operators and in Section 3.6 provide an uncertainty principle with its minimizing (coherent state) condition describing the operators which minimize the uncertainty.

We refer to [14], [101], [165] and [27] for the details of definitions and explanations provided in the chapter.

3.1 Definition of fiber bundles

Definition 3.1. *(Manifold) A topological space M is a* manifold *of dimension d if every point on M has a neighborhood U homeomorphic to an open subset of $\mathbb{R}^d$. The homeomorphism*

$$\varphi : U \to \mathbb{R}^d,$$

is called coordinate system *or* chart. *If $m \in U$ and $\varphi(m) = 0$ then it is said that the coordinate system is centered at m.*

Definition 3.2. *(Smooth structure) A* smooth structure $\mathcal{F}$ *on manifold M is defined as a collection*

$$\{\varphi_\alpha : \alpha \in A\},$$

of coordinate systems

$$\varphi_\alpha : U_\alpha \to \mathbb{R}^d,$$

and it satisfies the followings:

- $\bigcup_{\alpha \in A} U_\alpha = M$.
- *Coordinate transition* $\varphi_\alpha \circ \varphi_\beta^{-1} : \varphi_\beta(U_\alpha \cap U_\beta) \to \varphi_\alpha(U_\alpha \cap U_\beta)$ *between local coordinate systems is* C^∞ *for every* $\alpha, \beta \in A$.
- *If a coordinate system* φ *satisfies that* $\varphi \circ \varphi_\alpha^{-1}$ *and* $\varphi_\alpha \circ \varphi^{-1}$ *are* C^∞ *for every* $\alpha \in A$, *then* $\varphi \in \mathcal{F}$.

Definition 3.3. *(Differentiable manifold) A manifold* M *with the smooth structure* $\mathcal{F}$ *is called* differentiable *or* smooth manifold.

Consider two differentiable manifolds M and M' with dimensions d and d', respectively. Consider also a function $f : M \to M'$. The function f is C^∞ at $m \in M$ if for every coordinate system $\varphi : M \to \mathbb{R}^d$ of M and for every coordinate system $\varphi' : M' \to \mathbb{R}^{d'}$ of M' with $m \in U$ and $f(m) \in U'$, the function $\phi' \circ f \circ \phi^{-1} : \phi(U) \subset \mathbb{R}^d \to \phi'(U') \subset \mathbb{R}^{d'}$ is C^∞ in a neighborhood of $\varphi(m)$. Such a function f is called *differential map* between M and M'. Now more specifically consider a C^∞ function $\gamma : \mathcal{I} \to M$ where $\mathcal{I}$ is a real interval. Function $\gamma(t)$ is called a *curve* passing through $m \in M$ at time t_0 if $\gamma(t_0) = m$. Furthermore a C^∞ function f which is defined in some neighborhood of m is *horizontal* at m if $\dfrac{df(\gamma(t))}{dt} = 0$ for every curve passing through m at time $t = 0$.

Definition 3.4. *(Fiber and vector bundles) A fiber bundle is a structure* (E, M, π, F) *with fiber* F, *a projection map* $\pi : E \to M$ *where topological spaces* E *and* M *denote the* total space *and the* base space, *respectively. Condition for a fiber bundle is that the projection map must satisfy that for every* $m \in M$ *an open neighborhood* $U \subset M$ *exists such that there is a homeomorphism* $\phi : \pi^{-1}(U) \to U \times F$. *Furthermore if*

$$\mathrm{proj}_U \, \phi = \pi|_{\pi^{-1}(U)},$$

where $\mathrm{proj}_U : U \times F \to U$ *denotes the natural projection onto the* U *component, the homeomorphism* ϕ *is called* local trivialization. *Note that if the fiber* F *constitutes a real vector space and the local trivialization is a bijective linear map, then the fiber bundle is called* vector bundle.

Fiber bundles are particularly important in our study since they are the basic geometric structures that we use in order to model the hypercolumnar architecture of the primary visual cortex.

A specific type of vector bundle is tangent bundle:

Definition 3.5. *(Tangent vector, space and bundle) Let* M *be a differentiable manifold with dimension* d. *A linear functional* v *at* $m \in M$ *is called* tangent vector *at* m *if it is defined on* C^∞ *real-valued functions in a neighborhood of* m *in such a way that* $v(f) = 0$ *for any* f *which is horizontal at* m.

The set T_mM denotes the set of of all tangent vectors at $m \in M$ and it is called the tangent space to M at m. The tangent bundle TM of M is defined as

$$TM := \bigcup_{m \in M} \{(m, v) : \quad m \in M, \quad v \in T_mM\}.$$

Definition 3.6. *(Differential at a point) Consider a C^∞ map $\psi : M \to M'$ where M and M' are two differentiable manifolds. Let $m \in M$ and $v \in T_mM$. Linear map $d_m\psi : T_mM \to T_{\psi(m)}M'$ is called* differential *of ψ and it is defined as*

$$(d_m\psi(v))(f) := v(f \circ \psi),$$

where f is a C^∞ function in the neighborhood $\psi(m)$ and $d_m\psi(v) \in M'_{\psi(m)}$ is the tangent vector in $T_{\psi(m)}M'$, associated to v.

The differential at a point is needed in fact for the differential between tangent bundles. In this case, differently from the case of $d_m\psi$ (which maps from T_mM to $T_{\psi(m)}M'$) the differential $d\psi$ between tangent bundles is realized as a map from the tangent bundle TM to TM' and it is defined as follows:

Definition 3.7. *(Differential as a map between tangent bundles) Consider two differentiable manifolds M, M' and their corresponding tangent bundles TM, TM'. Let $\psi : M \to M'$ be a C^∞ map. Then the differential $d\psi : TM \to TM'$ is defined with $m \in M$ and $v \in T_mM$ as*

$$d\psi(m, v) := (\psi(m), d_m\psi(v)).$$

Definition 3.8. *(Section) Consider a vector bundle (E, M, π, F). A* section *of E is defined as the differential map $\varsigma : M \to E$ with $\pi \circ \varsigma = \mathrm{id}_M$ where id_M denotes the identity map on M.*

A vector field can be considered as an assignment of a tangent vector to every point on the differentiable manifold M.

Definition 3.9. *(Vector field) A* vector field *on M is defined as a section of the tangent bundle TM.*

Additionally a smooth vector field $X : C^\infty(M) \to C^\infty(M)$ on a manifold M is defined for all $f, h \in C^\infty(M)$ as a linear map such that

$$X(fh) := fX(h) + X(f)h.$$

We define a bilinear map: Lie bracket (or the commutator).

Definition 3.10. *(Lie bracket) Let X and Y be two vector fields on a differentiable manifold M. The* Lie bracket *$[X, Y]$ is a bilinear antisymmetric map and it is defined as*

$$[X, Y](f) = X(Y(f)) - Y(X(f)),$$

for all f being a C^∞ function defined on M. Furthermore the Jacobi identity holds:

$$[[X,Y],Z]+[[Y,Z],X]+[[Z,X],Y]=0,$$

for any vector fields X, Y, Z on M.

Additionally if $[X,Y]=0$, it is said that X and Y commute with each other. In other words Lie bracket gives a measurement of non-commutativity of vector fields.

Recall that an abstract Lie algebra is defined as follows:

Definition 3.11. *(Lie algebra) A Lie algebra $\mathfrak{g}$ over $\mathbb{R}$ is a real vector space together with a bilinear operation $[.,.]:\mathfrak{g}\times\mathfrak{g}\to\mathfrak{g}$, called the Lie bracket, which satisfies anti-commutativity and Jacobi identity.*

Definition 3.12. *It is said that the Lie algebra $\mathrm{Lie}(X_1,X_2,\ldots,X_k)=\mathfrak{g}$ is generated by vector fields $X_1,X_2,\ldots,X_k$ if the smallest subalgebra of $\mathfrak{g}$ containing $X_1,X_2,\ldots,X_k$ is $\mathfrak{g}$ itself. It is equivalently defined as the closure of the given set with respect to the operations of sum, scalar product and bracket.*

3.2 Integral curves of vector fields

Let us consider a $d-$dimensional differentiable manifold M, its tangent bundle TM and a smooth section (i.e., smooth vector field) X of TM. Consider also a C^∞ function $\gamma_m:\mathcal{I}\to M$ where $\mathcal{I}$ is an open interval (real). Then the following system of differential equations can be written:

$$\begin{aligned}\frac{d\gamma_m}{dt}(t)=&X(\gamma_m(t)),\quad t\in\mathcal{I},\\ \gamma_m(0)=&m\in M.\end{aligned}$$

Thanks to the Picard-Lindelöf theorem [117] there is indeed a unique solution γ_m for each $m\in M$, defined on an open interval $\mathcal{I}=\mathcal{I}_0$ around 0 and correspond to the given initial condition $\gamma_m(0)=m$. The solution depends on the initial point $\gamma_m(0)=m$ smoothly so the following holds:

Lemma 3.1. *For each $m\in M$ there exists an open neighborhood U of m and an open interval $\mathcal{I}$ around 0 which satisfies that for every $n\in U$ the curve γ_n solving*

$$\begin{aligned}\frac{d\gamma_n}{dt}(t)=&X(\gamma_n(t)),\quad t\in\mathcal{I},\\ \gamma_n(0)=&n\in M,\end{aligned}$$

is defined on $\mathcal{I}$. The map $(t,n)\mapsto\gamma_n(t)$ is smooth.

We refer to [101, Chapter 1] for details.

Finally the integral curves can be defined.

Definition 3.13. *The smooth map $(t,n)\mapsto\gamma_n(t)$ is the* local flow *of the vector field X. The* integral curve *of X through n is the curve γ_n.*

Note that a specific family of the integral curves are interpreted as the mathematical counterparts of the long-range horizontal connections between simple cells.

3.3 Sub-Riemannian manifolds

In order to describe sub-Riemannian manifolds and their basic properties, measurement of length and angle on a manifold is required. The notion of measurement in a vector space is usually given by a scalar product.

Definition 3.14. *(Riemannian metric and manifold) A* Riemannian metric *on a differentiable manifold M with dimension d is a scalar product defined on each tangent space T_pM where $p \in M$.*

If we consider local coordinates $x = (x^1, x^2, \ldots, x^d)$, then the metric $(g_{ij})_x$ is a positive definite, symmetric matrix with components g_{ij} where $i, j \in \{1, 2, \ldots, d\}$. In terms of the metric components, the product of two vectors

$$V = \sum_i v^i \frac{\partial}{\partial x^i}, \quad W = \sum_j w^j \frac{\partial}{\partial x^j} \quad \in T_pM,$$

with coordinate representations $(v^1, v^2, \ldots, v^d)$ and $(w^1, w^2, \ldots, w^d)$ is defined as

$$\langle V, W \rangle := \sum_{i,j} g_{ij}(x(p)) v^i w^i = \sum_{i,j} \langle \frac{\partial}{\partial x^i}, \frac{\partial}{\partial x^j} \rangle v^i w^i.$$

Generalization of Riemannian manifolds leads to sub-Riemannian manifolds. An important notion related to the sub-Riemannian manifolds is *distribution*.

A differentiable distribution $\mathcal{D}$ on a d-dimensional differentiable manifold M assigns $k-$dimensional subspace $\mathcal{D}_p \subset T_pM$ to each point $p \in M$. Every point p has a neighborhood $\mathcal{B}_p$ and k differentiable linearly independent vector fields $X_1, X_2, \ldots, X_k$ defined on $\mathcal{B}_p$ which form a basis of $\mathcal{D}_q$, i.e., $\mathcal{D}_q = \text{span}\{X_1, X_2, \ldots, X_k\}(q)$ for all $q \in \mathcal{B}_p$. The collection of all $\mathcal{D}_p$ is the distribution $\mathcal{D} \subset TM$. We will consider always that $k < d$.

Definition 3.15. *The distribution D on M is called* involutive *or* integrable *if $[X, Y] \in \mathcal{D}$ for any $X, Y \in D$.*

Analogously a non-involutive distribution is equivalent to non-integrable distribution. The equivalence of those notions are due to the Frobenius theorem [75].

Note that a distribution can be defined in terms of one-forms alternatively. Consider the cotangent bundle of the $d-$dimensional differentiable manifold M. The cotangent bundle is defined analogously to the tangent bundle TM but now the vector components in T_pM at each point $p \in M$ are replaced with the dual vectors in the dual tangent space T_p^*M. A one-form on M is a section of the cotangent bundle T^*M. It is the dual analogue of a vector field. In terms of local coordinate variables $(x_1, x_2, \ldots, x_d)$ a one-form is written as

$$\Theta = \sum_{j=1}^{d} \Theta^j dx_j,$$

with smooth functions $\Theta^j(x)$ of x.

We will be interested in codimension-1 geometries. In that case a distribution can be defined alternatively to Definition 3.15 as the kernel of a proper one-form, i.e.,

$$\mathcal{D} = \ker \Theta.$$

Note that a one-form which satisfies the non-integrability condition in a codimension-1 geometry is called *contact form*.

A sub-Riemannian metric $(g_{ij})_p$ is defined as the analogue of the Riemannian metric but its application is on the vectors from the distribution, i.e., $(g_{ij})_p : \mathcal{D}_p \times \mathcal{D}_p \to \mathbb{R}$ for all $p \in M$ where M is a sub-Riemannian manifold defined as follows:

Definition 3.16. *(Sub-Riemannian manifold) A $d-$dimensional real manifold M which is endowed with a non-integrable distribution $\mathcal{D}$ of rank k (where $k < d$) and a sub-Riemannian metric is called* sub-Riemannian manifold.

Note that k is strictly smaller than d and it is essential for sub-Riemannian manifolds. If it is equal, then the distribution $D_p = T_pM$ at each point $p \in M$ (therefore the distribution $\mathcal{D}$) becomes integrable. In this case the manifold M would be a Riemannian manifold.

On the sub-Riemannian manifold M, the distribution $\mathcal{D} \subset TM$ is called *horizontal distribution* and the vectors $v \in \mathcal{D}_p$ are called *horizontal vectors*. The sub-Riemannian metric is defined on the distribution $\mathcal{D}$. Furthermore the sections of the horizontal distribution are called *horizontal vector fields*. The integral curves of horizontal vector fields are *horizontal integral curves*.

The condition for the horizontal distribution to be able to recover the ambient space is provided by the Chow's theorem [33]. First let us define the bracket generating vector fields.

Definition 3.17. *(Bracket generating horizontal vector fields) Horizontal vector fields $X_1, X_2, \ldots, X_k$ defined on a sub-Riemannian manifold M are called bracket generating at $p \in M$ if the following holds*

$$\mathrm{Lie}(X_1, X_2, \ldots, X_k)(p) = T_pM.$$

If T_pM can be generated by commutators of step $\leq r$, at every point $p \in M$ then the horizontal vector fields $X_1, X_2, \ldots, X_k$ is said to be bracket generating *vector fields of step r on M.*

The distribution $\mathcal{D}$ is bracket generating of step r at the point $p \in M$ if it admits a system of generators which are *bracket generating* vector fields of step r on M. In the literature it is alternatively said that the vector fields fulfill the Hörmander condition [85] if they are bracket generating.

Finally the condition for the global connectivity is given via the Chow's theorem [33]:

Theorem 3.1. *(Chow, 1939) Let $\mathcal{D}$ be a bracket generating distribution on a connected sub-Riemannian manifold M. Then any two points on M can be connected by a horizontal piecewise regular curve.*

We refer to [27] for the proof. The natural distance between some points p and q on M is denoted by $d_M(p,q)$. In Carnot-Carathéodory spaces it is the infimum of lengths of the horizontal curves connecting p and q and called *Carnot-Carathéodory distance*.

3.4 Lie groups and Lie algebras

In this section we introduce the notions of Lie group and Lie algebra together with related properties, since they provide examples of sub-Riemannian manifolds. We present also an example of a Lie group family: Carnot groups of step 2.

Definition 3.18. *(Lie group) A group G associated to a differentiable manifold is called* Lie group *if the multiplication map*

$$G \times G \ni (g,h) \mapsto gh \in G,$$

and the inverse map

$$G \ni g \mapsto g^{-1} \in G,$$

are differentiable.

Lie group G acts from left on a differentiable manifold M if there exists a differentiable map

$$G \times M \ni (g,m) \mapsto gm \in M,$$

with

$$g(h\,m) = (gh)m, \quad \text{for all} \quad g,h \in G, \quad m \in M.$$

An action from right is defined analogously.

Lie group G is endowed with the diffeomorphisms *left translation*

$$\begin{aligned} L_g : & G \to G \\ & h \mapsto gh \end{aligned}$$

and the *right translation*

$$\begin{aligned} R_g : & G \to G \\ & h \mapsto hg. \end{aligned}$$

A vector field X on G is *left-invariant* if it satisfies

$$L_{g^*}X(h) = X \circ L_g = X(gh), \quad \text{for all} \quad g,h \in G, \tag{3.1}$$

where L_{g^*} denotes the differential of L_g in the sense of Definition 3.7. In other words left-invariant vector field X satisfies

$$X(f \circ L_g) = (Xf) \circ L_g,$$

where f is a C^∞ function on G.

Note that there exists a left-invariant vector field

$$X(g) := L_{g^*}V, \tag{3.2}$$

on G for every $V \in T_eG$ where e denotes the identity element of G. Therefore one has an isomorphism between T_eG and the space of left-invariant vector fields on G (see [101, Theorem 1.7.1]).

Note that the set of left-invariant vector fields, with the operations of sum, scalar product and bracket is an algebra. Hence we can give the following definition:

Definition 3.19. *(Lie algebra of a Lie group G) The* Lie algebra $\mathfrak{g}$ *of a Lie group G is defined as the set of all left-invariant vector fields on G and it is identified as T_eG, equipped with the bilinear operation of Lie bracket.*

Two Lie groups are particularly important for the present study: Roto-translation group and Carnot groups of step 2.

Example: Carnot groups

We have seen, a Lie group G induces an algebra. Vice versa an algebra can be used to define a Lie group. In particular Carnot groups can be defined, starting from the properties of the associated algebra.

We say that a Lie algebra $\mathfrak{g}$ is *stratified* if it has the sub-spaces $\mathfrak{g}_1, \mathfrak{g}_2, \dots, \mathfrak{g}_\ell$ such that

$$\begin{aligned} \mathfrak{g} =& \mathfrak{g}_1 \oplus \mathfrak{g}_2 \oplus \cdots \oplus \mathfrak{g}_\ell, \\ \mathfrak{g}_k =& [\mathfrak{g}_1, \mathfrak{g}_{k-1}] \quad \text{for} \quad k = 2, \dots, \ell \quad \text{where} \quad [\mathfrak{g}_1, \mathfrak{g}_\ell] = \{0\}, \end{aligned}$$

with $[\mathfrak{g}_i, \mathfrak{g}_j] = \text{span}\{[X, Y] : X \in \mathfrak{g}_i,\, Y \in \mathfrak{g}_j\}$ for any two indices $i, j < \ell$.

Definition 3.20. *(Carnot groups) A Carnot group is a simply connected nilpotent Lie group whose Lie algebra is stratified. In particular if*

$$\mathfrak{g} = \mathfrak{g}_1 \oplus \mathfrak{g}_2 \oplus \cdots \oplus \mathfrak{g}_r,$$

G is said to be of step r.

Remark 3.1. *Using the representation of the associated Lie algebra, it can be proved that a* Carnot group *can be identified with $\mathbb{R}^d$ possessing the following properties:*

- *$\mathbb{R}^d$ can be split in such a way that $\mathbb{R}^d = \mathbb{R}^{d_1} \times \mathbb{R}^{d_2} \times \cdots \times \mathbb{R}^{d_r}$, where $d_1 = \dim(\mathfrak{g}_1), \cdots, d_r = \dim(\mathfrak{g}_r)$.*
- *If we consider a basis of $\mathfrak{g}_1$, and we call $X_1, X_2, \dots, X_{d_1}$ the associated vector fields obtained by left translation, then by definition*

$$\text{rank}(\text{Lie}(X_1, X_2, \dots, X_{d_1})(x)) = d, \quad \textit{for every } x \in G.$$

- *The dilation map* $\delta_\sigma : \mathbb{R}^d \to \mathbb{R}^d$ *defined as*

$$\delta_\sigma(x) = \delta_\sigma(x^{(1)}, x^{(2)}, \dots, x^{(r)}) = (\sigma_1 x^{(1)}, \sigma_2 x^{(2)}, \dots, \sigma_r x^{(r)}), \quad x^{(i)} \in \mathbb{R}^{d_i},$$

is an automorphism of G *for every* $\sigma_i > 0$.

A well known Carnot group of step 2 is the n^{th} Heisenberg group $\mathbb{H}^n$. It is a $2n+1$ dimensional Carnot group with the stratified algebra

$$\mathfrak{g} = \mathfrak{g}_1 \oplus \mathfrak{g}_2,$$

where $\mathfrak{g}_1$ is $2n-$dimensional and generated by the vector fields $X_1, \dots, X_n, Y_1, \dots, Y_n$ and $\mathfrak{g}_2 = \text{span}\{T\}$. The non-zero commutators of the generators are given by

$$[X_j, Y_j] = -4T, \quad j = 1, 2, \dots, n.$$

We represent the elements $h, h' \in \mathbb{H}^n$ as

$$h = (x, y, t) = (x_1, \dots, x_n, y_1, \dots, y_n, t), \quad h' = (x', y', t') = (x'_1, \dots, x'_n, y'_1, \dots, y'_n, t').$$

Then the group multiplication of $\mathbb{H}^n$ is written as

$$h\, h' = (x, y, t)\, (x', y', t') = (x + x', y + y', t + t' + 2\langle y, x' \rangle - 2\langle x, y' \rangle),$$

with the standard inner product $\langle .\,, .\rangle$ of $\mathbb{R}^n$. Observe here that the unit element $e = 0$ and homogeneous dilations are given by $\delta_\sigma h = (\sigma x, \sigma y, \sigma^2 t)$ for $\sigma > 0$.

Recall that a left-invariant vector field X must satisfy $X(g) = L_{g^*} X(e)$ due to (3.1) and (3.2). If we denote the standard basis in $\mathbb{R}^{2n+1}$ by $\partial_{x_1}, \partial_{x_2}, \dots, \partial_{x_n}, \partial_{y_1}, \dots, \partial_{y_n}, \partial_t$ then the Lie algebra is generated by the left-invariant vector fields

$$X_j = \partial_{x_j} + 2y_j \partial_t, \quad Y_j = \partial_{y_j} - 2x_j \partial_t, \quad \text{with } j = 1, 2, \dots, n \quad \text{and} \quad T = \partial_t, \quad (3.3)$$

which can be obtained from $X_j(e) = \partial_{x_j}$, $Y_j(e) = \partial_{y_j}$ and $T(e) = \partial_t$ via

$$L_{g^*}(e) = \begin{pmatrix} \mathbb{I}_n & 0 & 0 \\ 0 & \mathbb{I}_n & 0 \\ 2y & -2x & 1 \end{pmatrix},$$

where $\mathbb{I}_n$ denotes the n-by-n identity matrix.

Finally note that thanks to the commutator $[X_j, Y_j] = -4\partial_t$ we have

$$\begin{aligned} \text{rank}(\text{Lie}(X_1, \dots, X_n, Y_1, \dots, Y_n)(e)) &= \dim(\text{span}\{\partial_{x_1}, \dots, \partial_{x_n}, \partial_{y_1}, \dots, \partial_{y_n}, -4\partial_t\}) \\ &= 2n + 1, \end{aligned}$$

hence

$$\text{rank}(\text{Lie}(X_1, \dots, X_n, Y_1, \dots, Y_n)(h)) = 2n + 1 \quad \text{for all } h \in \mathbb{H}^n.$$

In this case it is said that the vector fields $X_1, \dots, X_n, Y_1, \dots, Y_n$ fulfill the bracket generating condition which is given in Definition 3.17 (see also [33]).

3.5 Differential operators in sub-Riemannian setting

Definition 3.21. *(Horizontal gradient) Let $D \subset G$ be an open set and let (X_j) with $j = 1, \cdots, n$ be a family of smooth vector fields defined on D. Consider some function $f : D \to \mathbb{R}$. If there exists $X_j f$ for every $j = 1, \cdots, n$ we define the horizontal gradient of a function f as*

$$\nabla_G f := (X_1, \cdots, X_n).$$

A function f is of class C^1_G if $\nabla_G f$ is continuous, with respect to the Carnot-Carathéodory distance d_G defined in terms of the metric generated by the vector fields X_j with $j = 1, 2, \ldots, n$ in G. A function f is of class C^2_G if $\nabla_G f$ is of class C^1_G and by induction all C^k_G classes are defined. Note that a C^1_G function is not differentiable with respect to X_j if $j > n$. It follows that a function of class C^1_G is not of class C^1 in the standard Euclidean sense. If the group G has step r, a function f of class C^r_G is of class C^1 in Euclidean sense. As a consequence a function f of class C^∞_G is smooth in a general sense, which allows us to study diffusion in these spaces.

Definition 3.22. *The vector fields X_j are self-adjoint, which means that they satisfy the condition*

$$\int X_j f g = -\int f X_j g,$$

for every smooth function f, g.

It is simple to prove that in Carnot groups and in the roto-translation group the left-invariant vector fields are self-adjoint, hence we will always assume that the left-invariant vector fields are self-adjoint for simplicity.

Definition 3.23. *If the vector fields X_j are self-adjoint and $\phi = (\phi_1, \cdots \phi_n)$ is a C^1_G section of the horizontal tangent bundle, we define divergence of ϕ as follows:*

$$\mathrm{div}_G(\phi) := \sum_{j=1}^{n} X_j \phi_j.$$

Accordingly we define sub-Laplacian operator as

$$\Delta_G := \mathrm{div}_G(\nabla_G) = \sum_{j=1}^{n} X_j^2.$$

More generally we will call operators of the type

$$\sum_{i,j=1}^{n} a_{i,j} X_i X_j, \tag{3.4}$$

uniformly subelliptic operators where $a_{i,j}$ represents the elements of an $n \times n$ positive definite matrix. An operator of this type is the subelliptic analogous of an elliptic

operator. Note that (3.4) can be written also in divergence form as

$$-\sum_{i,j=1}^{n} X_i(a_{i,j}X_j).$$

Recall that this operator is totally degenerate from an elliptic point of view, and in general operators represented as sum of squares of n vector fields in a d-dimensional space with $n < d$ do not have regular solutions, even in presence of a regular second member.

We are now ready to state the well known theorem on hypoellipticity due to Hörmander (see the article of Hörmander [85]):

Theorem 3.2. *(Hörmander theorem) If $X_1, \cdots, X_m$ satisfy the Hörmander rank condition (bracket generating condition), then the associated supelliptic operator and the heat operator are hypoelliptic operators. This means that any solution u of the equation*

$$\Delta_G u = f,$$

with $f \in C^\infty$ is of class C^∞.

This is the main reason why we will be able to study visual models with sub-Riemannian operators.

Uniformly subelliptic operators admit a fundamental solution Γ, of class C^∞ out of the poles. Existence and local estimates of the fundamental solution in terms of the Carnot-Carathéodory distance have been first proved by Rothshild-Stein [67], Folland [68] and Folland-Stein [138].

Calling $B(g, R)$ a ball of the Carnot-Carathéodory metric and $|B(g, R)|$ its measure, they proved that fundamental solution can be locally estimated as

$$|\Gamma(g, h)| \leq C \frac{d_G^2(g, h)}{|B(g, d_G(g, h))|},$$

for every $g, h \in G$ and for a suitable constant C. In this setting we can study the heat equation as well:

$$(\partial_t - \Delta_G)u = 0.$$

Gaussian estimates for this equation have been first studied by Jerison and Sánchez-Calle [99], [98]. We refer to the book [14] for a recent review.

3.6 An uncertainty principle for non-commutative vector fields

It is widely known that the uncertainty principle applies to any couple of non-commutative self-ajoint operators in L^2 spaces (see for example [69]).

The uncertainty principle in a general framework with standard measure is written as in [69]:

Proposition 3.1. *Let us denote a Hilbert space endowed with the scalar product* $\langle .\,,\,. \rangle$ *by* $\mathcal{H}$*. Consider two self-adjoint operators* P_1 *and* P_2*. Then the following inequality holds:*

$$|\langle \psi, [P_1, P_2]\psi \rangle| \leq 2\|P_1\psi\|\|P_2\psi\|, \tag{3.5}$$

for all ψ *in the domain of* $[P_1, P_2]$*.*

Proof. Since P_1 and P_2 are self-adjoint, it can be written that

$$\begin{aligned} |\langle \psi,\, [P_1,\, P_2]\psi \rangle| =& |\langle \psi,\, (P_1P_2 - P_2P_1)\psi \rangle| \\ =& |\langle P_1\psi,\, P_2 f \rangle - \langle P_2\psi,\, P_1\psi \rangle| \\ =& 2|\mathrm{Im}\{\langle P_1\psi, P_2\psi \rangle\}|. \end{aligned}$$

Then the Cauchy-Schwarz inequality gives the result:

$$2|\mathrm{Im}\{\langle P_1\psi, P_2\psi \rangle\}| \leq 2\|P_1\psi\|\|P_2 f\|.$$

□

The proof shows that in order to achieve the minimum uncertainty (i.e., to achieve the equality in (3.5)), the non-commutative operators P_1 and P_2 must be the imaginary multiples of each other. More precisely:

Proposition 3.2. *The minimizers of inequality* (3.5) *fulfill the following:*

$$P_1\psi = i\lambda P_2\psi \iff |\langle \psi, [P_1, P_2]\psi \rangle| = 2\|P_1\psi\|\|P_2\psi\|. \tag{3.6}$$

In words the condition $P_1\psi = i\lambda P_2$ *with* $\lambda \in \mathbb{R}$ *gives the minimizers of the uncertainty principle* (3.5)*, which are called* coherent states.

Proof. See the proof of Proposition 3.1. □

Chapter 4

Sub-Riemannian models of the visual cortex

Simple cells extract the local information of visual features in such a way that we can implement a representation of the extracted features in terms of differential instruments. However it is not possible to provide a coherent global unity of the locally detected features without an additional mechanism which integrates them. Neural connectivity of the simple cells endow the primary visual cortex (V1) with such an integration mechanism respecting the Gestalt principle of good continuity (see Chapter 2 for a description of the principle). These two mechanisms, the feature extraction and the connectivity, together characterize the functional geometry of V1.

Several models were proposed for the functional geometry of V1 in relation to orientation selective behavior of the simple cells. Early models date back to 80s. Koenderink and van Doorn [109], [110] pointed out the similarity between Gaussian derivative functions and simple cell receptive profiles and proposed visual models based on the functions of Gaussian derivatives as the representations of the receptive profiles. It indeed encouraged many studies relying on the choice of a family of Gaussian derivative functions and Gaussian kernels, among which we would like to mention the works of Young [171], [172] and Lindeberg [115], [116]. In addition to those studies, there are some others which employ Gabor functions as the representations of the receptive profiles. The motivation for this second choice relies on an uncertainty principle as was elaborated by Daugman [44] through a generalization of the hypothesis of Marĉelja [120] (see also [100] where Jones and Palmer compare statistically the results obtained via Gabor functions and the neurophysiological results collected from V1 of a cat). Furthermore Hoffman [83], [84] proposed to model the hypercolumnar architecture of V1 as a fiber bundle. Following the latter school, which makes the choice based on Gabor functions, and by further developing the model proposed by Petitot and Tondut [132], where hypercolumnar architecture was interpreted as a fiber bundle associated to the contact geometry realized by the Heisenberg group, Citti and Sarti [35] proposed a new model of the functional geometry of the primary visual cortex (V1).

The model interprets the hypercolumnar architecture of V1 as a fiber bundle on the

retinal plane associated to the roto-translation group (SE(2)). Simple cell connectivity is modeled based on the horizontal distribution of the sub-Riemannian manifold of SE(2). Following a similar framework, but this time including also the scale selectivity of the simple cells, this model was generalized by Sarti, Citti and Petitot [146].

The theoretical criterion underpinning the modeling parts in this thesis relies on the so-called neurogeometrical approach described by Petitot-Tondut [132], Citti-Sarti [35] and Sarti-Citti-Petiot [146]. Following this approach, processing capabilities of sensorial cortices and particularly of the visual cortex are modeled based on the geometrical structure of the neural connectivity. Global and local symmetries of a visual stimulus are inherited by the cortical structure that presents their invariances (see Sanguinetti et. al. [142]). Then the structure is defined on groups of the invariances that are also spaces, i.e., on Lie groups.

In the present study we consider the generalized model of Sarti, Citti and Petitot [146] as the point of departure of our research. Therefore after we give an intuition about orientation selectivity and brief descriptions of the frameworks proposed by Petitot-Tondut [132], and Citti-Sarti [35], we will spare large part of this chapter for the presentation of the reference model, which takes into consideration both orientation and scale, and the relations between those three models.

4.1 Feature selectivity

What do we mean exactly by selectivity and in particular by orientation selectivity? Conceptually, by selectivity we mean that the correspondence of a detector unit (simple cell) to a certain feature (orientation, frequency, scale, ocular dominance and so on) coincides with the stimulus feature of the same type. In our particular setting we consider only visual stimulus, simply image functions on a 2-dimensional plane which represents the retinal plane (or the retinotopic plane) M isomorphic to $\mathbb{R}^2$.

Consider the simple cells. If we restrict ourselves to their orientation selective behavior, we can say that the cells detect pairs $(q, p) \in M \times F$ of a retinal position $q \in M$ and an orientation p at q. Note that orientation can be represented in different ways and depending on the representation the space F is determined. We say that a simple cell at q is selective to orientation θ if the cell gives the highest response to a stimulus at q with the orientation θ, in comparison to all the other cells responding to the same stimulus. The highest response is observed when the preferred orientation angle of the cell and the orientation angle of the stimulus coincide with each other. A similar description for selectivity to some other visual feature can be made as well. In fact the concept of selectivity can be extended to multiple features and in this case we use the term *multi-feature* selectivity (such as orientation-frequency selectivity and orientation-scale selectivity).

4.2 Gabor filters as models of receptive profiles

Let us recall that the simple cells of visual areas evoke impulse responses to stimulus applied on the retinal plane $M \simeq \mathbb{R}^2$ and every simple cell is identified by its receptive

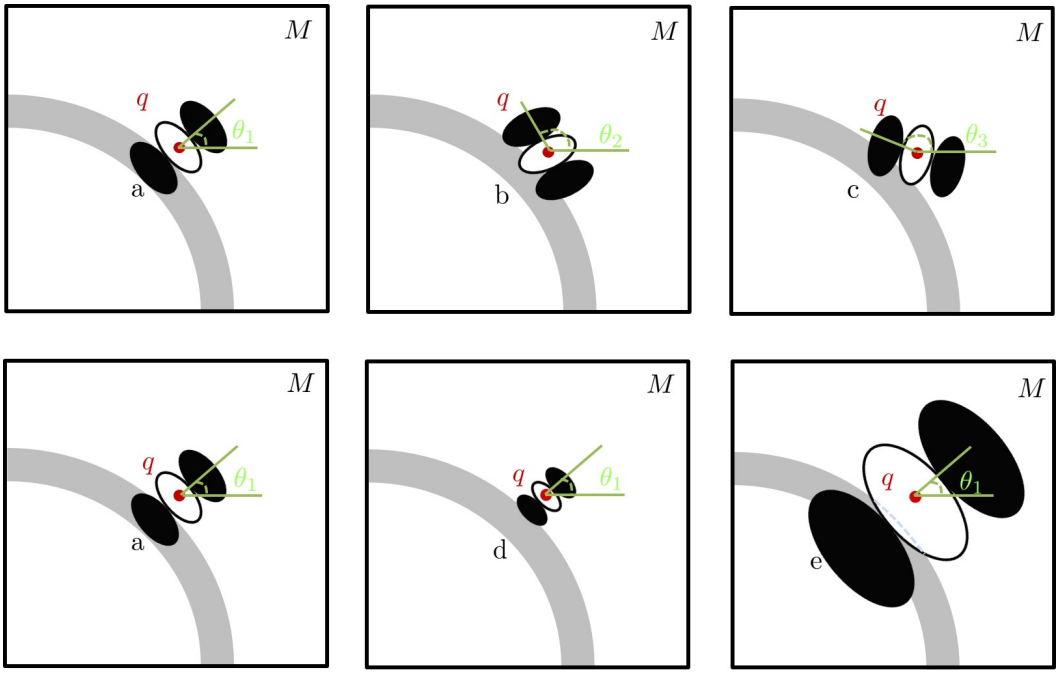

Figure 4.1: An illustration of orientation and scale selectivity. The range of intensity values vary from -1 (black) to 1 (white) and grey represents a negative intensity value. Top: Simple cells a, b and c, selective to the orientation angles θ_1, θ_2 and θ_3 (from left to right) at the point q on the retinal plane M. The maximum response to the boundary of the stimulus is given by cell a. Bottom: Cell a gives the highest response with respect to cells b and c, which are selective to the same orientation but to different scales.

field (RF) which is the domain of the retina to which the cell is sensitive/responding and connected through the retino-geniculo-cortical paths (see Figure 2.6). Once the RF of a simple cell is stimulated it elicits the impulse response, which is the simple cell receptive profile (RP). We denote the RP of the simple cell at the retinal position q and selective to the feature p by $\Psi_{(q,p)} : M \to \mathbb{C}$ (see Figure 4.2).

As we mentioned previously the first models of the simple cell receptive profiles date back to 80's. Almost in the same years it has been proved that both models in terms of derivatives or difference of Gaussian functions [109], [110] [171] and in terms of Gabor filters [44], [100] are plausible. Here we are mostly interested in Gabor filtering, which seems more flexible, and can be extended in order to consider many features.

The approach proposed by Daugmann in [44], relies on an uncertainty principle. It is motivated by the fact that the simple cell RPs are responsible for selection of positions and directions of boundaries. Hence Daugmann looks for the simple cell RP functions which are minima of the uncertainty principle both in spatial and frequency planes, in other words in the Heisenberg group. We gave in (3.3) a possible representation of the Heisenberg algebra. It is easy to verify that the operators

$$\hat{X}_j = x_j, \quad \hat{Y}_j = i\partial_{x_j}, \quad \text{for } j = 1, \cdots d,$$

satisfy the same commutation rules as the vector fields in (3.3), with

$$\hat{T} = -i.$$

Then these vector fields define a different representation of the same algebra. As a consequence minima of the associated uncertainty principle are found as the solutions of the equation (3.6), and they are the Gabor filters:

$$\Phi_{(q,p)}(x) = e^{ip\cdot x} e^{-(x-q)^2}, \quad \text{for} \quad p, q \in \mathbb{R}^d.$$

In general, given a window function $g \in L^2(\mathbb{R}^d)$, the family of the associated Gabor functions is defined as the shifted and modulated versions of $g_{(q,p)}$:

$$\Phi_{(q,p)}(x) = e^{ip\cdot x} g(x-q) = g_{(q,p)}(x).$$

The window function g restricts the analysis around specific points q, i.e., it provides the spatial localization of the Gabor function. Once we choose a suitable window function we can define the continuous Gabor transform as follows:

Definition 4.1. *Let $g \in L^2(\mathbb{R}^d)$ be a window function. Then the continuous Gabor transform of a signal $I \in L^2(R^d)$ is defined as:*

$$G_I(q,p) = \int_{R^d} I(x)\overline{g(x-q)}e^{-ip\cdot x}dx,$$

with $\overline{g(x-q)}$ denoting the complex conjugate of $g(x-q)$.

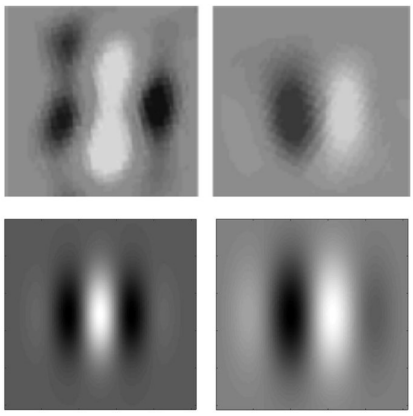

Figure 4.2: Top: Experimentally observed receptive profiles of even (left) and odd (right) simple cells with ON (white) and OFF (black) regions (taken from Sarti and Citti [143]). Bottom: Odd (left) and even (right) parts of a Gabor function.

Here $G_I(q,p)$ is called the *Gabor coefficient* corresponding to the frequency p at q.

The contribution of each coefficient to the signal I can be recognized more clearly through the Plancherel's formula [133] which is written as follows:

$$||G_I(q,p)||_{L^2(\mathbb{R}^d\times\mathbb{R}^d)} = 2\pi||I||_{L^2(\mathbb{R}^d)}||g||_{L^2(\mathbb{R}^d)}, \tag{4.1}$$

and it implies that the energy of the signal f is conserved when the Gabor transform is applied.

Gabor coefficients are complete and continuous Gabor transform is invertible. The initial signal can be recovered through the following inversion formula:

$$I(x) = \frac{1}{2\pi||g||^2_{L^2}} \int_{\mathbb{R}^d}\int_{\mathbb{R}^d} G_I(q,p) g_{(q,p)}(x)\, dq\, dp. \tag{4.2}$$

We refer to [139] for an extension of Gabor properties to more general group settings.

4.3 Model of the cortex as a fiber bundle

Extending some previous studies of Hoffmann [83], [84], Petitot and Tondut [132] proposed to model the hypercolumnar structure of the visual cortex in terms of a fiber bundle on the retinal plane $M \simeq \mathbb{R}^2$ which was not only justified by the neurophysiological evidence, but also capable of explaining boundary completion.

They idealized the hypercolumnar architecture as the fiber bundle (E, M, π, F) on the base plane M (the retinal plane) with the 3-dimensional total space $E \simeq M \times F$, the fiber $F = \mathbb{R}$ and the projection map $\pi : E \to M$. A copy of F at each point q on the retina was interpreted as the hypercolumn at the point.

In order to understand the model structure let us first consider a visual stimulus on the retinal plane M, simply a contrast image. Note that the boundaries of the surfaces

in the image can be identified via the Euclidean gradient of the image. Then we may describe the boundary coordinates of a surface in the image in terms of a smooth curve $\gamma(t) = (x(t), y(t)) \in M$ where $t \in \mathcal{I} = [0, T]$ with real time interval $\mathcal{I}$ and final time $T > 0$. Additionally the curve (which can as well be thought as a level set of an intensity value) can be written in terms of a graph such as $(x, y(x))$ with free variable x. In this case to each point $(x, y(x))$ of the curve one can assign a point

$$(x, y, p = \frac{dy}{dx}),$$

in the total space E and this point is called the *1-jet* of (x, y).

This construction of the fiber bundle is closely related to the orientation selectivity of the simple cells. Note that once a point $(x, y) \in M$ is stimulated by an image function $I : M \to \mathbb{R}$ the hypercolumn of the simple cells on (x, y) is activated. In the hypercolumn, the simple cell selective to the direction

$$p = \frac{dy}{dx}, \tag{4.3}$$

gives the highest response to the stimulus.

Formally, this orientation selective simple cells induce a 1-form

$$-p\,dx + dy,$$

which is associated to the fiber bundle (E, M, π, F). The kernel of this form is generated by the vector fields

$$X_1^{\mathbb{H}^1} = \partial_x + p\partial_y, \quad X_2^{\mathbb{H}^1} = \partial_p,$$

which describes the horizontal distribution of the 1^{st} Heisenberg group $\mathbb{H}^1$.

In the model proposed in [132], subjective boundaries and the long-range horizontal connectivity in the visual cortex have been described as minima of a length functional with a constraint term.

It is simple to verify that the Lie algebra generated by the vector fields $X_1^{\mathbb{H}^1}$ and $X_2^{\mathbb{H}^1}$ satisfies the same commutation rules as the Heisenberg algebra defined in (3.3). This remark is at the basis of another class of models.

4.4 Sub-Riemannian models of the cortex for orientation and scale selectivity

Citti and Sarti [35] improved in a unitary way the models of both Daugmann [44] and Petitot-Tondut [132], and proposed a new model of the primary visual cortex.

They recognized that the minimal constraint model of Petitot and Tondut [132] was indeed a model in a sub-Riemannian space, and introduced a model in SE(2) which better described the invariances of the visual cortex. Moreover they provided the relation between the geometrical point of view of Petitot-Tondut [132] and the action of the simple cells described as Gabor filters by Daugmann [44]. In this way their model considered

the action of the cells on the image as a whole, and it was no longer necessary to restrict the cells each time to a single boundary curve as in the previous model of Petitot and Tondut [132].

Sarti, Citti and Petitot [146] proposed a generalized version of this model. The generalized version modeled both orientation and scale selective behavior of the V1 simple cells. We remark that the generalized model boils down to the classical orientation selective model of Citti and Sarti [35] once it is adjusted to a fixed scale. For this reason they can be presented together.

4.4.1 The set of receptive profiles as a Lie group

An important neurophysiological observation is that any receptive profile in a family of simple cells is a translated, rotated and dilated version of a certain reference receptive profile which is called *mother profile*. For this reason the simple cell receptive profiles are obtained from a mother function via rotations and translations in the model of Citti, Sarti [35].

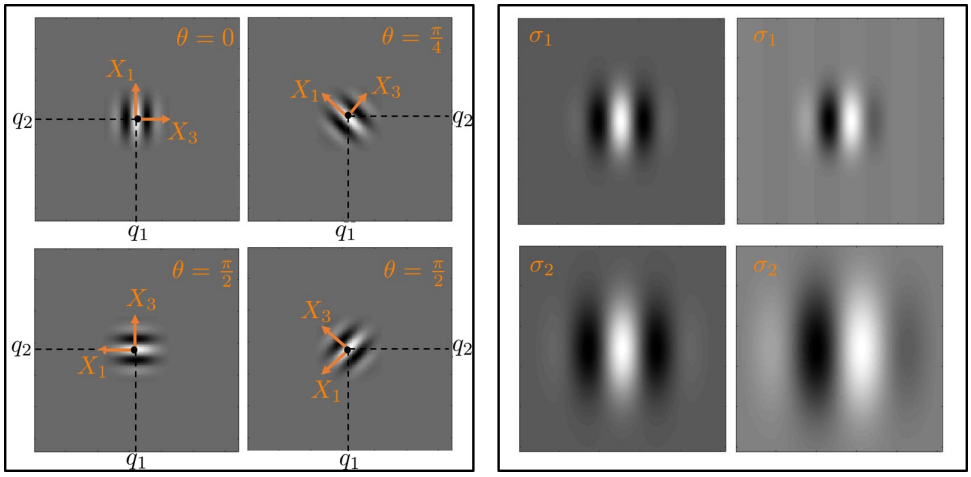

Figure 4.3: Some Gabor functions. Left block: Even parts of the rotated Gabor functions with a fixed scale. Here X_1 and X_3 shows the directions of the vector fields, which are along the two principal axes of the Gabor functions (see also (4.9)). Right block: Even (left column) and odd (right column) parts of the Gabor functions with a fixed orientation and different scales σ_1 and σ_2.

The translation to the point q, rotation by the angle θ and dilation by the parameter $\sigma \in \mathbb{R}$, is expressed as

$$A_{(q,\theta)}(\tilde{x}, \tilde{y}) = \begin{pmatrix} q_1 \\ q_2 \end{pmatrix} + R_\theta \begin{pmatrix} \tilde{x} \\ \tilde{y} \end{pmatrix}, \tag{4.4}$$

where R_θ denotes the rotation matrix

$$R_\theta = \begin{pmatrix} \cos(\theta) & -\sin(\theta) \\ \sin(\theta) & \cos(\theta) \end{pmatrix}.$$

Then any receptive profile $\Psi_{(q,\theta)}$ is obtained from the mother function through the following relation:

$$\Psi_{(q,\theta)}(x,y) = \Psi_0(A^{-1}_{(q,\theta)}(x,y)), \tag{4.5}$$

with $A^{-1}_{(q,\theta)}$ denoting the inverse transform of $A_{(q,\theta)}$.

The set of parameters

$$G^{\mathrm{SE}(2)} = \{(x,y,\theta) \in \mathbb{R}^2 \times S^1\},$$

define a group, SE(2), with the composition law induced by applying in sequence two rigid motions $A_{(q,\theta)}$ and $A_{(q_1,\theta_1)}$.

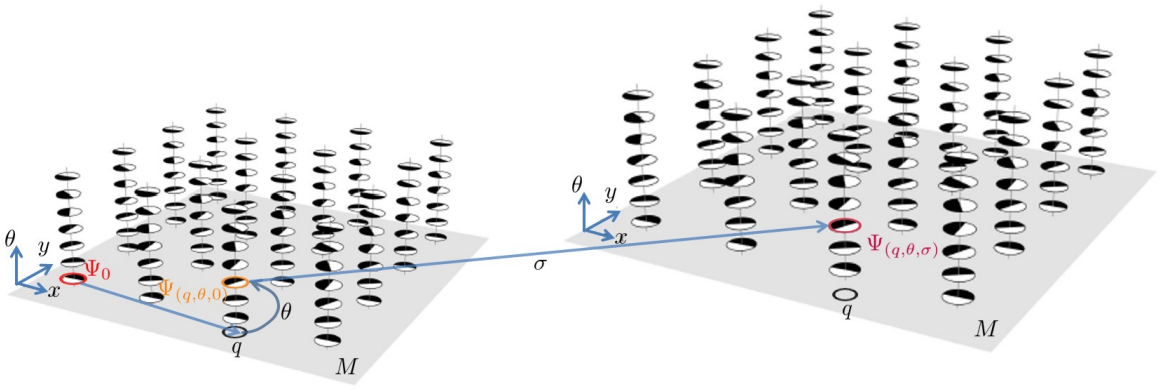

Figure 4.4: Illustration of the set of odd cell receptive profiles (modified from Sarti and Citti [143]). Any receptive profile $\Psi_{(q,\theta,\sigma)}$ can be obtained from the mother profile Ψ_0 up to a translation to q, a rotation by θ and a dilation by σ through (4.7).

In the multi-scale version of the model, which takes into account rotation, translation and dilation [146] (see Figure 4.4 for an illustration of the transform in terms of odd receptive profiles), a 4-dimensional matrix was considered and the transform was given as:

$$A_{(q,\theta,\sigma)}(\tilde{x},\tilde{y}) = \begin{pmatrix} q_1 \\ q_2 \end{pmatrix} + \mathrm{e}^{\sigma} R_\theta \begin{pmatrix} \tilde{x} \\ \tilde{y} \end{pmatrix}. \tag{4.6}$$

In this case the general receptive profile becomes:

$$\Psi_{(q,\theta,\sigma)}(x,y) = \Psi_0(A^{-1}_{(q,\theta,\sigma)}(x,y)). \tag{4.7}$$

The original model can be recovered from this one by fixing $\sigma = 0$.

The set of all parameters $(x,y,\theta,\sigma) \in \mathbb{R}^2 \times S^1 \times \mathbb{R}$ establishes the Lie group

$$G \simeq \{A_{(x,y,\theta,\sigma)} : (x,y,\theta,\sigma) \in \mathbb{R}^2 \times S^1 \times \mathbb{R}\},$$

with the left-translation

$$\begin{aligned} L_g : G &\to G \\ h &\mapsto gh \end{aligned}$$

realized by the group multiplication law which is written for two elements

$$g = (x_1, y_1, \theta_1, \sigma_1), \quad h = (x_2, y_2, \theta_2, \sigma_2), \quad g, h \in G,$$

as

$$gh = \Big(\begin{pmatrix} x_1 \\ x_2 \end{pmatrix} + \mathrm{e}^{\sigma_1+\sigma_2} R_{\theta_1+\theta_2} \begin{pmatrix} x_2 \\ y_2 \end{pmatrix}, \, \theta_1 + \theta_2, \, \sigma_1 + \sigma_2 \Big) \in G.$$

Parameters $(x, y, \theta) \in \mathbb{R}^2 \times S^1$ of the original model with $\sigma = 0$ define a subgroup of G.

4.4.2 Associated left-invariant vector fields

Let us compute the set of left-invariant vector fields, defined by (3.1), in the two Lie groups given in Section 4.4.1. Let us start with SE(2).

The differential of L_g is given by

$$L_{g^*} = \begin{pmatrix} \cos(\theta) & 0 & -\sin(\theta) \\ \sin(\theta) & 0 & \cos(\theta) \\ 0 & 1 & 0 \end{pmatrix}.$$

The left-invariant vector fields are written as

$$\begin{aligned} X_1^{\mathrm{SE}(2)} &= \cos(\theta)\partial_x + \sin(\theta)\partial_y, \\ X_2^{\mathrm{SE}(2)} &= \partial_\theta, \\ X_3^{\mathrm{SE}(2)} &= -\sin(\theta)\partial_x + \cos(\theta)\partial_y. \end{aligned} \tag{4.8}$$

Let us explicitly note that $X_1^{\mathrm{SE}(2)}$ and $X_2^{\mathrm{SE}(2)}$ do not commute and

$$[X_1^{\mathrm{SE}(2)}, X_2^{\mathrm{SE}(2)}] = -X_3^{\mathrm{SE}(2)},$$

similarly $X_3^{\mathrm{SE}(2)}$ and $X_2^{\mathrm{SE}(2)}$ do not commute and

$$[X_3^{\mathrm{SE}(2)}, X_2^{\mathrm{SE}(2)}] = X_1^{\mathrm{SE}(2)}.$$

The analogous procedure for the generalized group G provides the left-invariant vector fields

$$\begin{aligned} X_1 &= \mathrm{e}^{\sigma}\big(\cos(\theta)\partial_x + \sin(\theta)\partial_y\big), \\ X_2 &= \partial_\theta, \\ X_3 &= \mathrm{e}^{\sigma}\big(-\sin(\theta)\partial_x + \cos(\theta)\partial_y\big), \\ X_4 &= \partial_\sigma. \end{aligned} \tag{4.9}$$

4.4.3 Receptive profiles and group uncertainty principle

We have already mentioned that Gabor filters could be obtained as minima of the uncertainty principle in the Heisenberg group. In the model of Citti and Sarti [35], (as well as in the one of Sarti, Citti and Petitot [146]) different non-commutative vector fields have been introduced. Furthermore due to Proposition 3.1 any non-commutative vector field couple satisfies an ad hoc uncertainty principle. Using this fact Barbieri, Citti, Sarti and Sanguinetti noted in [5] that Gabor filters are minima of the uncertainty principle also in SE(2).

Similarly in the case of the model with position, orientation and scale, we may apply the principle to the vector fields X_1 and X_2 and we obtain the Gabor filters as the minimizers. Analogously if we consider the couple of X_3 and X_4, we find a different parametrization of the same set of minimizers. Therefore it is possible to impose the uncertainty principle at every scale and obtain the set of the Gabor filters at any scale. Hence a suitable choice of the mother function compatible with the model and the experimental data is

$$\Psi_0(x, y) = e^{ipx} e^{-(x^2+y^2)}. \tag{4.10}$$

In general, on a Lie group we could define different invariant structures, in terms of either Riemannian or sub-Riemannan metric. In our case the natural metric of the visual cortex is induced by the hypercolumnar structure and the action of the simple cells.

4.4.4 Output of the simple cells and maximum selection

We recall from Section 2.4.2 that, once a visual stimulus is present at the retinal point $q \in M$ it activates the hypercolumn on $q \in M$.

If p denotes either the value θ of the fiber variable in the orientation model, or (θ, σ) in the orientation-scale one, the response output $O_p^I(q)$ of the simple cell with RP $\Psi_{(q,p)}$ to the stimulus $L^2(M) \ni I : M \to \mathbb{R}$ is found by the linear filtering of the stimulus with the RP:

$$O_p^I(q) = \int_M I(x, y)\Psi_{(q,p)}(x, y)\, dx\, dy.$$

The output is complex valued with real and imaginary parts corresponding to even and odd simple cell responses, respectively. The odd part has been studied in the classical framework of the model of Citti and Sarti [35], the even one in [147].

We call the map

$$I(q) \mapsto O_p^I(q),$$

lifting of the image I at the point $q \in M$.

As we mentioned in Section 2.4.2 an additional mechanism which is called *maximum selection* is applied on the lifted image. It is basically choosing the response of the simple

cell giving the highest response to $I(q)$ among all the cells in the hypercolumn located on q and it is defined as

$$\big(\bar{\theta}(q), \bar{\sigma}(q)\big) = \arg\max_{(\theta,\sigma)} \big(\tilde{O}^I_{(\theta,\sigma)}(q)\big), \tag{4.11}$$

at every point $q \in M$, where $\tilde{O}^I_{(\theta,\sigma)}$ denotes either even or odd cell response.

This additional mechanism is needed for a sharp tuning of the simple cell feature selectivity to the stimulus.

The main distinction between odd and even cells is that the odd cells give the higher response on boundaries, while the even cells give the higher response in the interior regions of the objects in the visual stimulus.

This two-fold procedure assigns a point $(q, \bar{\theta}, \bar{\sigma})$ in the cortical space to each point q on the retinal plane. In other words the lifting and the maximum selection on the stimulus induce lifting of the curves underlying the stimulus (or rather the level sets as the domain of the stimulus) as well (see Figure 4.5 as an example of the two-fold procedure in the case with a fixed scale). We use the term lifting interchangeably for both lifting of the stimulus and the lifting of its domain depending on the context.

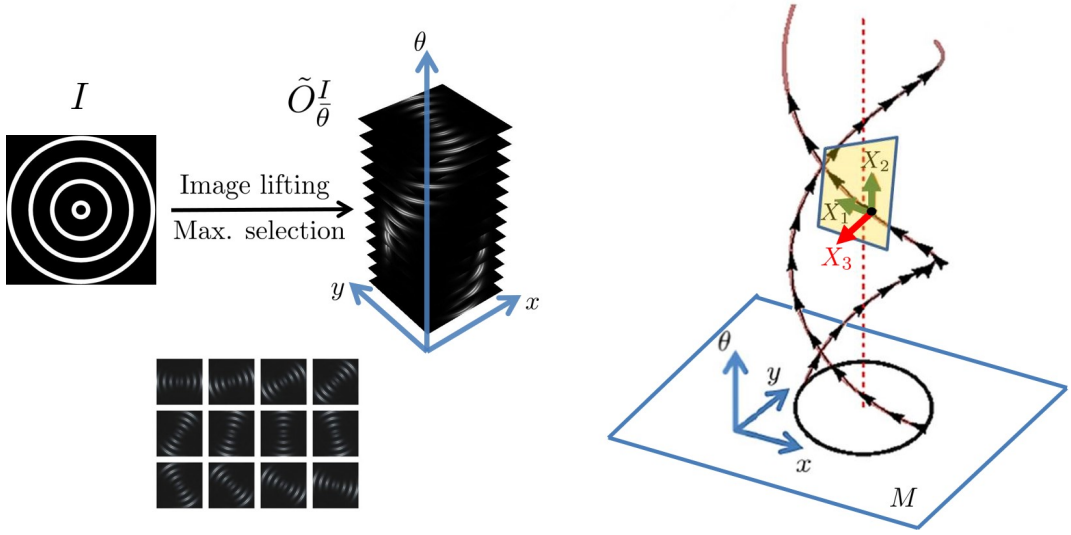

Figure 4.5: Left: The stimulus I is lifted to the set of output responses $\tilde{O}^I_{\bar{\theta}}$, where the maximum responses on each $\bar{\theta}$ layer is on the bottom. Right: The lifting and the maximum selection on the stimulus induce a lifting of the level sets underlying the image. Here the lifted level set of the outermost circle in I is shown. Note that at each point along the lifted level set the horizontal tangent directions are restricted to X_1 and X_2.

4.4.5 The sub-Riemannian structure of the cortex

In the work of Citti and Sarti [35] it has been proved that the value $\bar{\theta}(q)$ selected by the odd simple cells via (4.11) in presence of a visual stimulus at a point q is the orientation

of the boundary passing through the point q:

$$\bar{\theta}(q) = \arctan(\frac{dy}{dx}). \tag{4.12}$$

This property, analogous to (4.3), which was only formally postulated by Petitot and Tondut [132], is now deduced from the neurophysiological behavior of the simple cells. The same property has been confirmed in the work of Sarti, Citti and Petitot [147] for the even simple cells.

We formally deduce from (4.12) that $\tan(\theta) = dy/dx$. Therefore a natural contact form $\Theta^{\mathrm{SE}(2)}$ is defined:

$$\Theta^{\mathrm{SE}(2)} : T\,\mathrm{SE}(2) \to \mathbb{R}, \quad \Theta^{\mathrm{SE}(2)} = -\sin(\theta)dx + \cos(\theta)dy.$$

Using the contact form, Citti and Sarti [35] induced a sub-Riemannian geometry on the cortical space SE(2).

Precisely the space can be induced with the structure $(\mathrm{SE}(2), \mathcal{D}^{\mathrm{SE}(2)}, (g_{ij})_q)$ where

$$\begin{aligned}\mathcal{D}^{\mathrm{SE}(2)} =& \mathrm{span}\{X_1^{\mathrm{SE}(2)}, X_2^{\mathrm{SE}(2)}\},\\ (g_{ij})_q =& \big((\cos(\theta)dx + \sin(\theta)dy) \otimes (\cos(\theta)dx + \sin(\theta)dy) + d\theta \otimes d\theta\big)\big|_q,\end{aligned}$$

at every $q \in \mathrm{SE}(2)$.

Remark 4.1. *In the generalized model of Sarti, Citti and Petitot [146] with the scale, the orientation selective one-form is given by*

$$\Theta = e^{-\sigma}(-\sin(\theta)dx + \cos(\theta)dy),$$

the horizontal distribution is defined as

$$\mathcal{D} = \ker\Theta = \mathrm{span}\{X_1, X_2, X_4\},$$

and the space is characterized by a symplectic structure defined as the 2-form which is obtained by differentiating Θ as

$$\begin{aligned}\omega_q :& T_qG \times T_qG \to \mathbb{R}\\ \omega_q =& e^{-\sigma}\big((\cos(\theta)dx + \sin(\theta)dy) \wedge d\theta + (-\sin(\theta)dx + \cos(\theta)dy) \wedge d\sigma\big)\big|_q,\end{aligned}$$

and defined at every $q \in G$.

4.4.6 Connectivity and activity propagation

Recall that the hypercolumns are connected to each other through the strongly anisotropic long-range horizontal connections [43], [20]. If we consider only orientations, the horizontal connections link preferentially the simple cells at different spatial locations but selective to the same orientation.

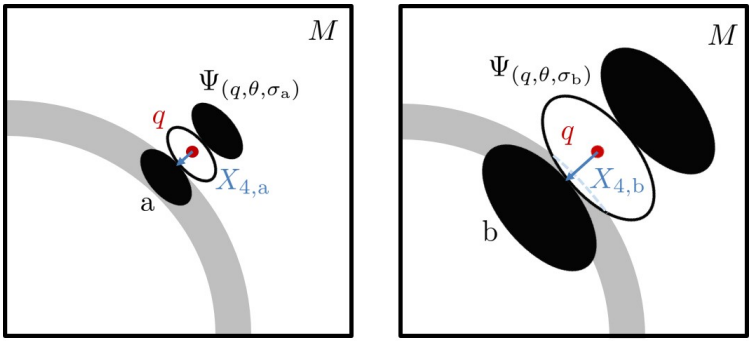

$X_{3,a} = e^{\sigma_a}(\cos(\theta), \sin(\theta))$ $X_{4,b} = e^{\sigma_b}(\cos(\theta), \sin(\theta))$

Figure 4.6: Illustration of the orientation and scale selectivity of the even simple cells a and b. The associated one-form Θ to the receptive profile selects both the orientation and scale by using the receptive profile gradient direction X_4 weighted by the scale. The profile with the weighted gradient vector coinciding with the stimulus orientation and scale (i.e., the profile $\Psi_{(q,\theta,\sigma_a)}$ with scale σ_a and weighted gradient direction $X_{4,a}$) gives the maximum response (see also Figure 4.1).

This is compatible with the metric having non-vanishing eigenvalues in the directions of $X_1^{\mathrm{SE}(2)}$ and $X_2^{\mathrm{SE}(2)}$, and vanishing eigenvalue in the direction of $X_3^{\mathrm{SE}(2)}$.

Once a simple cell is stimulated, its activation propagates between the simple cells along those horizontal connections. This machinery is closely related to the specific connectivity patterns within V1: the association fields [64]. The association fields coincide with the anisotropic behavior of the long-range horizontal connections in the psychophysical level. In the classical framework of Citti and Sarti [35] those association fields were modeled as the horizontal integral curves associated to $\mathcal{D}^{\mathrm{SE}(2)} = \mathrm{span}\{X_1^{\mathrm{SE}(2)}, X_2^{\mathrm{SE}(2)}\}$.

As a result the propagation along the connectivity pattern can be modeled as a diffusion along the horizontal curves. In other words, the propagation takes place through the differential operators associated to the sub-Riemannian structure (see Section 4.4.5). Hence if

$$u_0(q, \theta) = O_\theta^I(q),$$

is the output of the simple cells, it is as well the initial condition of the diffusion process. This means that a good model for the cortical activity propagation is the evolution equation given by

$$\partial_t u = \Delta_{\mathrm{SE}(2)} u, \quad u_{|t=0} = u_0.$$

As mentioned in Section 3.5, this is a sub-Riemannian differential equation which has been studied starting from the classical results of Rothshild and Stein [138], Jerison and Sánchez-Calle [99], [98].

4.4.7 Joint action of activity propagation and maximum selection

One of the main contributions of the article of Citti-Sarti [35] was to propose a relation between the neural activity propagation, maximum selection and perceptual completion.

We will see in Chapter 6 that the diffusion process, together with the previously described maximum selection gives rise to a diffusion driven process. The set of activated cells under the maximum selection will become a surface. The diffusion restricted to this surface will lead to a tangential diffusion, and result in a mean curvature flow. In the limit the whole process will define a minimal surface, which will be considered as the models of perceptual completion of surfaces. Therefore the model proposed in [35] is able to complete not only boundaries but also surfaces.

Chapter 5

A sub-Riemannian model of the cortex with frequency and phase

In this chapter we propose a novel generalized model of the primary visual cortex (V1) extended from the model of Citti-Sarti [35]. In the model of Citti-Sarti the cortex was interpreted as a fiber bundle over a 2-dimensional retinal plane with only orientation introduced as intrinsic variable. Now we generalize the model to a fiber bundle over the retinal plane where, in addition to orientation, spatial frequency and phase are present as intrinsic variables. The variables orientation and phase constitute a fiber on each point of the retinal plane, which is the base space at each frequency, resulting in a 5-dimensional sub-Riemannian manifold. The receptive profiles of the simple cells selective to orientation, spatial frequency and with possible phase shifts are interpreted as Gabor functions on a high dimensional feature space and they are coherent states (minimizers) of an uncertainty principle in the non-commutative setting of the sub-Riemannian geometry. The versatility of the Gabor functions makes it possible to encode the multi-feature selectivity of the simple cells via the introduction of additional feature variables associated to frequency and phase into the classical Gabor function given by (4.7) and (4.10). We convolve the given visual stimulus with rotated, modulated and phase shifted Gabor filter banks and obtain output responses of the simple cells in the sub-Riemannian geometry as the lifting of given visual stimulus. In the case of the previous visual cortex models (see Chapter 4) exact inverse of the lifting was not possible due to the lack of frequency and phase components of the lifting. However now it is possible since we have all the frequency and phase components of the lifting. We study the extended sub-Riemannian framework, corresponding geometrical instruments endowing it with a spatio-spectral connectivity which provides a novel geometric model of the association fields, the horizontal integral curves in the 5-dimensional sub-Riemannian structure. We explain the uncertainty principle in this sub-Riemannian framework, which is the motivation behind the choice of the Gabor function as the receptive profile (RP).

5.1 Neurophysiological motivation

We have seen in Chapter 2 that the simple cells encode visual features, namely, orientation, frequency and scale. However the relevant models of V1 [132], [35], [146], which were presented in Chapter 4, considered only orientation or orientation-scale selectivity.

In order to fill this gap we study orientation-frequency selectivity of the simple cells with shifted phases and propose our extended geometric model. We start from the geometric structure of a 5-dimensional manifold $\mathcal{M}$ which is defined by the set of features which we consider in the model. We denote the position coordinates on the retinal plane $M \simeq \mathbb{R}^2$ by $q = (q_1, q_2) \in M$, frequency $\omega \in \mathbb{R}^+$ and orientation $\theta \in S^1$ tacitly by $r = |r|(\cos(\theta), \sin(\theta)) = \omega(\cos(\theta), \sin(\theta))$, and the phase by $\phi \in S^1$.

We will endow this set with a sub-Riemannian structure which generalizes the one presented in Section 4.4.5 and which will be able to describe more sophisticated families of the simple cells. In particular we will introduce a suitable lifting map:

$$I(q) \mapsto O^I_{(r,\phi)}(q),$$

at every point $q = (q_1, q_2) \in M$, which describes the action of a suitable family of the simple cells.

5.2 Extended model geometry

5.2.1 Receptive profiles, symplectic structure and contact form

Orientation-frequency selectivity with shifted phases of a simple cell is represented in RP of the cell via a straightforward generalization of the classical Gabor function given by (4.7) and (4.10). Being inspired by the RP model which was suggested by Barbieri et. al. [3] for the complex cells in V1, we propose to represent RP of a simple cell in our setting with the Gabor functions of the type

$$\Psi_z(x, y, s) := \mathrm{e}^{-i\left(r\cdot(x-q_1,\, y-q_2)-v(s-\phi)\right)}\mathrm{e}^{-|x-q_1|^2-|y-q_2|^2}, \tag{5.1}$$

with the spatial frequency[1] $\omega > 0$ and $r = (r_1, r_2) = (-\omega\sin(\theta),\, \omega\cos(\theta))$, where we represent the coordinates associated to a 6-dimensional space $\mathcal{N}$ with $z = (q_1, q_2, \phi, r_1, r_2, v) \in \mathbb{R}^6$. Note that $v \in \mathbb{R}$ is included in the receptive profile expression (5.1) for the sake of completeness and it will be fixed to a suitable value in the sequel.

We may express z as a complex variable $z = (q_1, q_2, \phi) + i(r_1, r_2, v) \in \mathbb{C}^3$ and write the symplectic structure, naturally defined on the complex structure $\mathbb{C}^3$ of z, as follows:

$$\Omega = d\tilde{\Theta} = \omega\big(\cos(\theta)dx + \sin(\theta)dy\big) \wedge d\theta + \big(\sin(\theta)dx - \cos(\theta)dy\big) \wedge d\omega - dv \wedge ds,$$

where $\tilde{\Theta}$ denotes the Liouville form

$$\tilde{\Theta} = r_1 dx + r_2 dy - v ds.$$

[1] Spatial frequency refers to $\omega = \frac{2\pi}{\lambda}$ with a wavelength $\lambda > 0$ in our terminology.

This structure is defined on the 5-dimensional space $\mathcal{M}$ which is the reduced version of the 6-dimensional space $\mathcal{N}$ when $v = 1$. We can express each point z on $\mathcal{M}$ as:

$$\mathcal{M} = \mathbb{R}^2 \times S^1 \times \mathbb{R}^+ \times S^1 \ni z = \{q_1, q_2, \theta, \omega, \phi\} = (q, p),$$

where p denotes the feature variables (θ, ω, ϕ). Then we may write the associated Gabor function given by (5.1) as follows:

$$\Psi_{(q,p)}(x, y, s) := \mathrm{e}^{-i\left(\omega(-\sin(\theta), \cos(\theta))\cdot(x-q_1, y-q_2)-(s-\phi)\right)}\mathrm{e}^{-|x-q_1|^2-|y-q_2|^2}. \tag{5.2}$$

In the case of the V1 complex cells with spatio-temporal dynamics, the variable v represents the velocity of a two-dimensional plane wave propagation (see the study of Barbieri et. al [3] for details). However in our case we are not interested in the complex cells and the simple cells do not encode any temporal features. Within this context we interpret $s - \phi$ as the phases centered at ϕ, which is a different case than the case considering also temporal dynamics [3] and interprets $s - \phi$ as time centered at the instant ϕ. Therefore we are not concerned with different velocities changing in time. This is the motivation for us to fix v.

Note that the manifold $\mathcal{M}$ is endowed with the following 1-form:

$$\Theta_{(\theta,\omega)} = r_1 dx + r_2 dy - ds = -\omega \sin(\theta) dx + \omega \cos(\theta) dy - ds.$$

Indeed Θ is a contact form since

$$\Theta \wedge d\Theta \wedge d\Theta = \omega \; dx \wedge dy \wedge d\theta \wedge d\omega \wedge ds,$$

is a volume form hence it is maximally non-degenerate, i.e., non-vanishing for all points on the manifold $\mathcal{M}$.

5.2.2 Horizontal vector fields

Horizontal vector fields are defined as the elements of

$$\ker \Theta = \{X \in T\mathcal{M} : \; \Theta(X) = 0\},$$

where $T\mathcal{M}$ denotes the tangent bundle of the 5-dimensional manifold $\mathcal{M}$. The horizontal vector fields are found explicitly as:

$$\begin{aligned} X_1 &= \cos(\theta)\partial_x + \sin(\theta)\partial_y, \quad X_2 = \partial_\theta, \\ X_3 &= -\sin(\theta)\partial_x + \cos(\theta)\partial_y + \omega\partial_s, \quad X_4 = \partial_\omega. \end{aligned} \tag{5.3}$$

The corresponding horizontal distribution is given as follows:

$$\mathcal{D}^{\mathcal{M}} = \mathrm{span}(X_1, X_2, X_3, X_4).$$

All non-zero commutators related to the horizontal vector fields given in (5.3) follow as:

$$\begin{aligned}[X_1, X_2] &= \sin(\theta)\partial_x - \cos(\theta)\partial_y,\\ [X_2, X_3] &= -\cos(\theta)\partial_x - \sin(\theta)\partial_y,\\ [X_3, X_4] &= -\partial_s.\end{aligned}$$

Note that the horizontal vector fields are bracket generating since

$$T_z\mathcal{M} = \operatorname{span}(X_1, X_2, X_3, X_4, [X_1, X_2])(z),$$

for all $z \in \mathcal{M}$, where $T_z\mathcal{M}$ denotes the tangent space of $\mathcal{M}$ at z. As a result they provide the connectivity of any two points on $\mathcal{M}$ through the horizontal integral curves defined on $\mathcal{M}$ due to the Chow's theorem [33] (see Theorem 3.1).

Remark 5.1. *The horizontal distribution $\mathcal{D}_z^{\mathcal{M}}$ at a point $z \in \mathcal{M}$ can be thought as the sub-Riemannian analogue of the Euclidean tangent space. However differently from the Euclidean case, $\mathcal{D}_z^{\mathcal{M}}$ is spanned by four vector fields X_1, X_2, X_3 and X_4 while the tangent space $T_z\mathcal{M}$ is spanned by five. This situation results in degeneracy of the sub-Riemannian geometry. Moreover non-commutativity of the horizontal vector fields makes it challenging to study within the sub-Riemannian geometry, yet we are able to fulfill the bracket generating condition thanks to the non-commutativity.*

5.3 Set of receptive profiles

Recall that an important property of Gabor functions is that any Gabor function can be obtained from a mother function, up to a certain transformation law. Consider the point $0 = (0, 0, 0, 0) \in M \times S^1 \times \mathbb{R}^+ \times S^1$. Then a suitable choice of the mother function with a frequency ω is:

$$\Psi_0(x, y, s) = \mathrm{e}^{-i(\omega y - s)}\mathrm{e}^{-x^2-y^2}. \tag{5.4}$$

Then we set

$$A_{(q,\theta,\phi)}(\tilde{x}, \tilde{y}, \tilde{s}) = \begin{pmatrix} q_1 \\ q_2 \\ \phi \end{pmatrix} + \begin{pmatrix} \cos(\theta) & -\sin(\theta) & 0 \\ \sin(\theta) & \cos(\theta) & 0 \\ 0 & 0 & 1 \end{pmatrix} \begin{pmatrix} \tilde{x} \\ \tilde{y} \\ \tilde{s} \end{pmatrix} = (x, y, s). \tag{5.5}$$

As a result at each frequency any receptive profile can be written as

$$\Psi_{(q,p)}(x, y, s) = \Psi_0\big(A^{-1}_{(q,\theta,\phi)}(x, y, s)\big). \tag{5.6}$$

5.4 Functional architecture as a Lie group

Receptive profiles evoke a group structure at each frequency ω. We can describe the group structure underlying the set of receptive profiles by using (5.5).

First we notice that the elements (q, θ, ϕ) induce the group:

$$G_\omega \simeq \{A_{(q,\theta,\phi)} : \ (q, \theta, \phi) \in M \times S^1 \times S^1\},$$

which is indeed a Lie group associated to a fixed frequency ω.

Then we write the group multiplication law for two elements

$$g = (q^g, \theta_1, \phi_1), \quad h = (q^h, \theta_2, \phi_2), \quad g, h \in G_\omega,$$

as

$$gh = \Big(\begin{pmatrix} q_1^g \\ q_2^g \end{pmatrix} + R_{\theta_1+\theta_2} \begin{pmatrix} q_1^h \\ q_2^h \end{pmatrix}, \ \theta_1 + \theta_2, \ \phi_1 + \phi_2 \Big),$$

by using the transformation given in (5.5).

The differential L_{g^*} of the left-translation

$$\begin{aligned} L_g : \ G_\omega &\to G_\omega \\ h &\mapsto gh, \end{aligned}$$

is given by

$$L_{g^*} = \begin{pmatrix} \cos(\theta) & 0 & -\sin(\theta) & 0 \\ \sin(\theta) & 0 & \cos(\theta) & 0 \\ 0 & 1 & 0 & 0 \\ 0 & 0 & \omega & 0 \end{pmatrix}.$$

The vector fields X_1, X_2 and X_3 are bracket generating due to that

$$\operatorname{span}(X_1, X_2, X_3, [X_1, X_2])(g) = T_g G_\omega,$$

for every $g \in G_\omega$. Hence X_1, X_2 and X_3 generate the Lie algebra.

5.5 Functional architecture as a sub-Riemannian structure

The functional geometry is associated to a sub-Riemannian structure at each frequency ω. Let us denote the submanifold G_ω of G with points $h = (q, \theta, \phi, \omega) = (q, p)$ restricted to a fixed ω. In this case the horizontal distribution is found by

$$\mathcal{D}^{G_\omega} = \operatorname{span}(X_1, X_2, X_3).$$

Furthermore the induced metric $(g_{ij})_h^{G_\omega} : T_h G_\omega \times T_h G_\omega \to \mathbb{R}$ is defined on $\mathcal{D}^{G_\omega}$ as the 2-form

$$\begin{aligned} (g_{ij})_h^{G_\omega} := \big(&(\cos(\theta)dx + \sin(\theta)dy) \otimes (\cos(\theta)dx + \sin(\theta)dy) + d\theta \otimes d\theta \\ &+ (-\sin(\theta)dx + \cos(\theta)dy + \omega\, ds) \otimes (-\sin(\theta)dx + \cos(\theta)dy + \omega\, ds) \big)\big|_h, \end{aligned}$$

at every $h \in G_\omega$.

Finally the associated sub-Riemannian structure to the frequency ω is written as the following triple:

$$(G_\omega, \mathcal{D}^{G_\omega}, (g_{ij})_h^{G_\omega}).$$

5.6 Output of the simple cells

We obtain a simple cell output response to a general visual stimulus $I(q)$ at the point $q = (q_1, q_2) \in M \simeq \mathbb{R}^2$ as a convolution with rotated and phase shifted Gabor filter banks at each frequency:

$$O_p^I(q) = \int_M I(x,y)\Psi_{(q,p)}(x,y,s)\,dx\,dy = \mathrm{e}^{is}\int_M I(x,y)\Psi_{(q,p)}(x,y,0)\,dx\,dy. \tag{5.7}$$

Remark 5.2. *Note that we consider the whole complex structure of the convolution* (5.7) *as the output response of a simple cell. It is different from the cases of the previous visual cortex models which were choosing either real (even) or imaginary (odd) part of the output response. In other words they were not taking into account the half of the information which they obtained from a visual stimulus.*

5.7 Horizontal connectivity in the extended geometry

Our extended model lifts the points in the given visual stimuli to the 5-dimensional manifold $\mathcal{M}$. Lifting mechanism leaves each lifted point isolated from each other if there is no connection between the lifted points. Therefore we would like to endow the model with an integration mechanism which provides to us an integrated form of the local feature vectors obtained from the lifted image at each point on $\mathcal{M}$.

We propose to model the association fields in the case of multi-feature selectivity with frequency and phase as the horizontal integral curves associated to the 5-dimensional sub-Riemannian geometry of $\mathcal{M}$.

Consider a horizontal integral curve $(q_1, q_2, \theta, \omega, \phi) = \gamma : \mathcal{I} \to \mathcal{M}$, which is described by the horizontal vector fields given in (5.3) and which starts from an initial point $\hat{z} = (\hat{q}_1, \hat{q}_2, \hat{\theta}, \hat{\omega}, \hat{\phi})$. Let us denote the velocity of γ by γ'. At each time $t \in \mathcal{I}$ the velocity is a vector $\gamma'(t) \in \mathrm{span}(X_1, X_2, X_3, X_4)\big(\gamma(t)\big)$ at $\gamma(t) = (q_1(t), q_2(t), \theta(t), \omega(t), \phi(t)) \in \mathcal{M}$. In order to compute the horizontal integral curves we first consider the vector field γ', with coefficients $c_{i\in\{1,2,3,4\}}$ (which are not necessarily constants), defined as

$$\gamma'(t) = X(\gamma(t)) = (c_1X_1 + c_2X_2 + c_3X_3 + c_4X_4)(\gamma(t)),$$

for all $t \in \mathcal{I}$. Then we have

$$\begin{aligned}
q_1'(t) &= c_1\cos(\theta(t)) - c_3\sin(\theta(t)),\\
q_2'(t) &= c_1\sin(\theta(t)) + c_3\cos(\theta(t)),\\
\theta'(t) &= c_2,\\
\omega'(t) &= c_4,\\
\phi'(t) &= c_3\,\omega(t).
\end{aligned} \tag{5.8}$$

In the case of that the coefficients c_i are real constants where $c_2 \neq 0$, we solve the system of ordinary differential equations (5.8) of t with initial condition $\hat{z}$ and find the solution

as follows:

$$\begin{aligned}
q_1(t) &= \hat{q}_1 + \frac{1}{c_2}\big(- c_3\cos(\hat{\theta}) + c_3\cos(c_2 t + \hat{\theta}) - c_1\sin(\hat{\theta}) + c_1\sin(c_2 t + \hat{\theta})\big),\\
q_2(t) &= \hat{q}_2 + \frac{1}{c_2}\big(c_1\cos(\hat{\theta}) - c_1\cos(c_2 t + \hat{\theta}) - c_3\sin(\hat{\theta}) + c_3\sin(c_2 t + \hat{\theta})\big),\\
\theta(t) &= c_2 t + \hat{\theta},\\
\omega(t) &= c_4 t + \hat{\omega},\\
\phi(t) &= \frac{1}{2}\big(c_3 c_4 t^2 + 2t c_3\hat{\omega} + 2\hat{\phi}\big).
\end{aligned} \tag{5.9}$$

If $c_2 = 0$ then the solution becomes

$$\begin{aligned}
q_1(t) &= \hat{q}_1 + t\big(c_1\cos(\hat{\theta}) - c_3\sin(\hat{\theta})\big),\\
q_2(t) &= \hat{q}_2 + t\big(c_3\cos(\hat{\theta}) + c_1\sin(\hat{\theta})\big),\\
\theta(t) &= \hat{\theta},\\
\omega(t) &= c_4 t + \hat{\omega},\\
\phi(t) &= \frac{1}{2}(c_3 c_4 t^2 + 2t\, c_3\,\hat{\omega} + 2\hat{\phi}).
\end{aligned} \tag{5.10}$$

Note that (5.9) and (5.10) describe the whole family of the horizontal integral curves described by the horizontal distribution

$$\mathcal{D}^{\mathcal{M}} = \bigcup_{\omega\in\mathbb{R}^+} \mathcal{D}^{G_\omega} = \operatorname{span}(X_1, X_2, X_3, X_4).$$

However we are mainly interested in two specific subfamilies corresponding to the horizontal vector fields which reside in either one of the two orthogonal $\mathcal{D}_z^{\mathcal{M}}$ subspaces which are defined for every point $z = (q, \theta, \omega, \phi) \in \mathcal{M}$ as:

$$S_1\mathcal{D}_z^{\mathcal{M}} = \operatorname{span}(X_1, X_2)(z), \quad S_2\mathcal{D}_z^{\mathcal{M}} = \operatorname{span}(X_3, X_4)(z),$$

satisfying $\mathcal{D}_z^{\mathcal{M}} = S_1\mathcal{D}_z^{\mathcal{M}} \oplus S_2\mathcal{D}_z^{\mathcal{M}}$ (see Figure 5.1 for an illustration of the orthogonal layout of $S_1\mathcal{D}_z^{\mathcal{M}}$ and $S_1\mathcal{D}_z^{\mathcal{M}}$ at points z on an orientation fiber corresponding to some fixed ω and ϕ, i.e., an horizontal integral curve along $X_1 + X_2$).

We remark here that $S_1\mathcal{D}_z^{\mathcal{M}}$ is the horizontal tangent space $T_{(q,\theta)}\mathrm{SE}(2)$ of SE(2) at the point z (which is the classical sub-Riemannian geometry corresponding to the model of Citti-Sarti [35]) once frequency ω and phase ϕ are fixed. In other words at each point $z = (q, \theta, \omega, \phi)$ with ω and ϕ fixed on $\mathcal{M}$, one finds the submanifold SE(2).

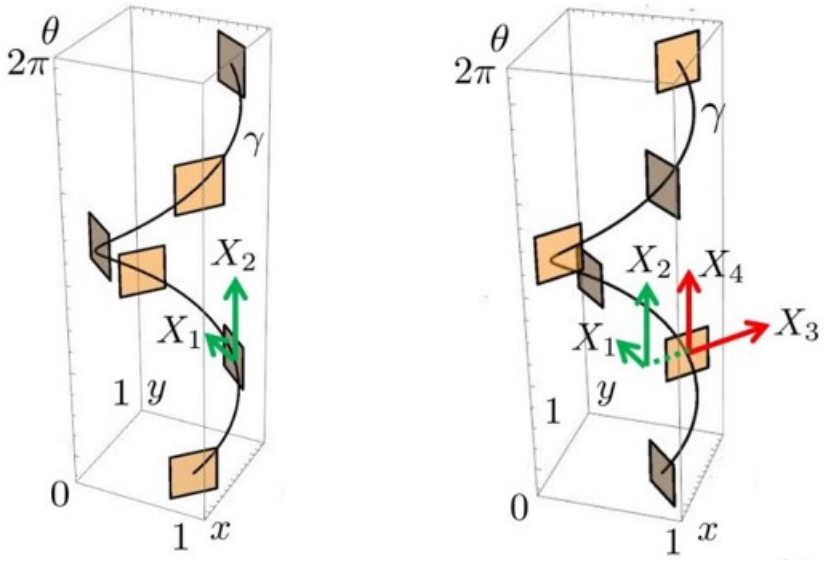

Figure 5.1: An integral curve along the vector field $X_1 + X_2$. It represents an orientation fiber once ω and ϕ are fixed. At six points on the curve the tangent planes spanned by X_1, X_2 (left) and X_3, X_4 (right) are shown.

5.8 Coherent states in the extended geometry

We have already noted that Gabor filters are the minimizers of the uncertainty principle in the Heisenberg group (see Section 4.4.3). However here we are working in a different structure which contains SE(2). Hence in order to show the internal coherence of the model, we prove that the Gabor filters given by (5.2) can be considered as the minimizers of the uncertainty principle in the structure considered here.

Recall that the coordinate transform $A_{(q,\theta,\phi)}$ given by (5.5) acts on the Gabor mother function Ψ_0 through (5.6). We consider the inverse transform $A^{-1}_{(q,\theta,\phi)}$ at every fixed point $q = (q_1, q_2) \in M$ as a map from each frequency layer of the 5-dimensional manifold to the cortical plane. Then its differential sends the vector fields X_1 and X_2 on the 5-dimensional manifold to the vector fields $\mathcal{X}_1$ and $\mathcal{X}_2$ on the retinal plane which are found as:

$$\begin{aligned} \mathcal{X}_1 &= (dA^{-1}_{(q,\theta,\phi)})(X_1) = X_1 A^{-1}_{(q,\theta,\phi)} = \partial_{\tilde{x}}, \\ \mathcal{X}_2 &= (dA^{-1}_{(q,\theta,\phi)})(X_2) = X_2 A^{-1}_{(q,\theta,\phi)} = \tilde{y}\partial_{\tilde{x}} - \tilde{x}\partial_{\tilde{y}}, \end{aligned} \tag{5.11}$$

where $\tilde{x}$ and $\tilde{y}$ are described via (5.5).

At this point we recall that SE(2) is a submanifold of $\mathcal{M}$. Additionally X_1 and X_2 are the horizontal vector fields on $\mathrm{SE}(2)_{(\omega,\phi)}$ where by subindices we denote the point at which the submanifold SE(2) is located on $\mathcal{M}$. So to each frequency-phase pair (ω, ϕ)

the submanifold $\mathrm{SE}(2)_{(\omega,\phi)}$ can be associated. We observe more specifically that dA^{-1} sends the vector fields X_1 and X_2 from the submanifold $\mathrm{SE}(2)_{(\omega,\phi)}$ to the 2-dimensional retinal plane M. Analogous case is valid also for X_3 and X_4. That is at each pair (q,θ), the differential dA^{-1} maps X_3 and X_4 to the retinal plane and on this plane the mapped vector fields are written as:

$$\begin{aligned}\mathcal{X}_3 = (dA^{-1}_{(q,\theta,\phi)})(X_3) =& X_3 A^{-1}_{(q,\theta,\phi)} = \partial_{\tilde{y}} + \omega\partial_{\tilde{s}},\\ \mathcal{X}_4 = (dA^{-1}_{(q,\theta,\phi)})(X_4) =& X_4 A^{-1}_{(q,\theta,\phi)} = \partial_{\omega},\end{aligned}$$

where $\mathcal{X}_4 = X_4$ since $A_{(q,\theta,\phi)}$ has no action on frequency component.

For the non-commutative vector field pairs $\{\mathcal{X}_1, \mathcal{X}_2\}$ and $\{\mathcal{X}_3, \mathcal{X}_4\}$ the conditions for the coherent states ψ of the uncertainty principle on the 2-dimensional real plane are written as:

$$\mathcal{X}_1\psi = i\lambda_1\mathcal{X}_2\psi, \quad \mathcal{X}_3\psi = i\lambda_2\mathcal{X}_4\psi. \tag{5.12}$$

Indeed the Gabor functions of the type $\Psi_{(q,p)}$ given by (5.2) are coherent states since

$$\begin{aligned}\mathcal{X}_1\Psi_{(q,p)}(x,y,s) &= -2\tilde{x}\Psi_{(q,p)}(x,y,s), \quad \mathcal{X}_2\Psi_{(q,p)}(x,y,s) = i\tilde{x}\omega\Psi_{(q,p)}(x,y,s),\\ \mathcal{X}_3\Psi_{(q,p)}(x,y,s) &= -2\tilde{y}\Psi_{(q,p)}(x,y,s), \quad \mathcal{X}_4\Psi_{(q,p)}(x,y,s) = -i\tilde{y}\Psi_{(q,p)}(x,y,s),\end{aligned}$$

satisfy (5.12) for $\lambda_1 = \frac{2}{\omega}$ and $\lambda_2 = -2$. Therefore the Gabors are the functions which provide the optimal compromise between orientation and spatial position detections (thanks to the first condition in (5.12)) and between frequency and phase detections (thanks to the second condition in (5.12)).

5.9 Relation to curvature detection

Some cells in the visual cortex are selective to length information of elongated objects in a given visual stimulus. Such cells were discovered by Hubel and Wiesel [89] and now they are called *endstopped cells*. Hubel and Wiesel noted in [89] that the endstopped cells might have a role in curvature detection. However the relation between those cells and the process of curvature detection has not been clearly understood. In [49] Dobbins et. al. propose a mathematical model which relate endstopping behavior to curvature. They consider the curvature as the local deviation of an elongated object from the straight line passing through the point on the elongated object where the local deviation is examined. The basic idea is that the difference of the responses of two simple cells (among which one is large and the other one is small sized) at the point on the elongated structure models the endstopping behavior and changes proportionally to the curvature at the point.

Our model is closely related to curvature detection in a similar sense. Let us disregard phase and consider in our model two receptive profiles $\Psi_{(q,\theta,\omega_H)}$ and $\Psi_{(q,\theta,\omega_L)}$ with a high frequency ω_H and a low frequency ω_L, respectively. The high frequency cell detects fine structures while the low frequency cell detects coarse structures. We denote the given responses of those two cells to a stimulus $I(q)$ corresponding to a particular contrast

pattern with the orientation θ and a frequency ω by $\tilde{O}^I_{(\theta,\omega_H)}$ and $\tilde{O}^I_{(\theta,\omega_L)}$ where tilde represents the real part of the corresponding output (alternative choices are also possible, see Section 4.4.4). Then we may apply exactly the same idea which Dobbins et. al. [49] propose. In this case we write the curvature measurement at q as

$$K(q) = C\big(C(\tilde{O}^I_{\omega_H}(q)) - C(\tilde{O}^I_{\omega_L}(q))\big),$$

where C is a clipping function

$$C(r) = \begin{cases} 1 & \text{if } r > 0 \\ 0 & \text{if } r \leq 0, \end{cases}$$

which is needed in order to avoid the positive contribution of negative response values to the curvature measurement. In this way the excitation of the endstopped cell comes from the high frequency simple cell and the inhibition comes from the low frequency simple cell. Note that if q is a point on a straight line then $K(q)$ is zero while it is a positive value if q is on a curve, and the value increases as the deviation of the curve from the straightness becomes larger.

Part II

Geometric evolutions in Lie groups for visual completion and enhancement

Chapter 6

A diffusion driven motion by curvature

In this chapter we introduce an algorithm of diffusion driven motion by curvature of a surface and study its convergence. One of the first algorithms of this type was first introduced by Bence-Merriman-Osher in [122] and its convergence was provided by Evans [56]. More recently a new version of the algorithm was proposed in [35]. The latter one was a model of perceptual completion which was inspired by the functionality of the visual cortex based on simple cell orientation selectivity. We consider the algorithm proposed in [35] as the starting point. Here we slightly modify the algorithm proposed in [35] and provide a proof of convergence in the Euclidean setting, following the approach introduced by Evans [56].

In Section 6.1 we provide the background inspiring our algorithm and we present the algorithm of the diffusion driven motion by curvature provided in [35]. Afterwards we give the algorithm of the diffusion driven motion by curvature in a general Euclidean setting, an idea of the proof of the convergence of this algorithm and give our main result: convergence result (Theorem 6.1). In Section 6.2 we overview the main instruments of the non-linear semigroup theory necessary for the proof of Theorem 6.1, and the weak definition of the viscosity solution of the Euclidean mean curvature flow equation. In Section 6.3 and Section 6.4 we give a formal definition of operator H, which indexes the concentration, and show that H is contractive. Proofs in Section 6.3 and Section 6.4 are more delicate than the previous ones of Evans [56] since the initial datum is given only on a surface. Then in Section 6.5 we conclude the proof of Theorem 6.1 by applying a general theorem of Brezis and Pazy [26]. Finally in Section 6.6 we present the numerical scheme and some simulation results of our algorithm in two dimensional case.

6.1 Previous results and modeling motivation

6.1.1 Motion by curvature

Geometric flow is the evolution of a surface $\Sigma_0 \subset \mathbb{R}^n$ whose points move with speed equal to a function of the mean curvature and direction normal to the evolving surface $\Sigma_t \subset \mathbb{R}^n$. In particular mean curvature flow has been studied by several authors such as Huisken [92], Gage-Hamilton [77], Grayson [82] and Altschuler-Grayson [55], [1], who exploited parametric methods of differential geometry. For an overview of other geometric flows we refer to [79], [118], [80]. We also note that geometric flows and in particular mean curvature flow have been widely studied based on a level set approach in combination with the theory of viscosity solutions (see the explanations of Crandall-Ishii-Lions in [39] for more details about the theory of viscosity solution) since the works of Osher-Sethian [129], Evans-Spruck [60] and Chen-Giga-Goto [32].

Here we will be interested in the motion by curvature of surfaces which are expressed as a graph of a smooth function $\gamma : \mathbb{R}^{n-1} \to \mathbb{R}$. In this case the motion by curvature equation is written as

$$\partial_t \gamma = \sqrt{1 + |\nabla \gamma|^2}\, K, \qquad \text{where } K = \operatorname{div}\left(\frac{\nabla \gamma}{\sqrt{1 + |\nabla \gamma|^2}} \right). \tag{6.1}$$

Motion by mean curvature can be obtained through an algorithm introduced by Bence-Merriman-Osher [122] which provides a relation between the mean curvature flow and the heat flow. The algorithm is organized in two steps: An initial surface Σ_0 is first diffused during an interval of time t/n, then a concentration step recovers a new surface $\Sigma_{1,t/n}$, at time t/n. After n iterations, a surface $\Sigma_{n,t}$ is obtained.

The convergence, as n tends to $+\infty$, to the solution Σ_t of the mean curvature flow with initial datum Σ_0 was proved by Evans [56] and Barles-Georglin [7]. Variants of the algorithm were proposed by Ishii [93], Ishii-Pires-Souganidis [94], Vivier [166], Leoni [113] and Goto-Ishii-Ogawa [81]. A generalization of the diffusion driven mean curvature flow algorithm inspired by the behavior of the neurons of the primary visual cortex was proposed in [35]. In this last problem, the surface corresponds to a density of neural activity and it is represented as density measure concentrated in the set where the density takes its maximum, while in the problem of Bence-Merriman-Osher [122] the surface is the boundary of a set, identified by its indicator function. In the neurophysiological problem this surface of activity is diffused along neural connectivity, giving rise to a diffusion driven mean curvature flow. In this perspective, a two step technique was used where the first step was applying a diffusion to a function on an initial surface, and the second step was choosing the point corresponding to the maximum value along the direction normal to the surface. Those two steps were generating a new surface. Formally this problem can be considered as the derivative of the previous one of Bence-Merriman-Osher, and the existing proof of convergence provided by Evans [56] cannot be directly applied. A local approximation result was provided in [35] but a complete proof was still missing, even in the Euclidean case.

6.1.2 A diffusion driven model of perceptual completion

A cortically based algorithm of diffusion driven curvature inspired by the behavior of the neurons of the primary visual cortex was proposed in [35].

We have described the selectivity process which assigns to every point q of the retinal plane an orientation $\bar{\theta}$ and a scale $\bar{\sigma}$ (see (4.11)). In [35] a similar process but only for orientation was proposed through the map

$$(x, y) \mapsto (q(x, y), \bar{\theta}(x, y)), \tag{6.2}$$

for every point (x, y) of the retinal plane $M \simeq \mathbb{R}^2$. Using the fact that $q(x, y) = (x, y)$ we can interpret this surface as the zero level set of a function u such that

$$u(q, \theta) = \theta - \bar{\theta}(q), \tag{6.3}$$

and the zero level set can be identified as a regular surface in the sub-Riemannian structure of the model framework provided in [35].

Note that (6.2) evokes also a lifting of the level lines of the image $I : M \to \mathbb{R}$ to the function F defined on a lifted surface S as

$$F(x_1(x, y), x_2(x, y), \bar{\theta}(x, y)) = I(x, y),$$

where $\bar{\theta}$ was given in (6.2). The surface S and the function F defined on S are processed through some differential operators defined on $SE(2)$, which model the activity propagation of the simple cells in the visual cortex. More precisely two mechanisms operate on the lifted surface S:

(a) A sub-Riemmanian diffusion along the vector fields $X_1^{\mathrm{SE}(2)}$ and $X_2^{\mathrm{SE}(2)}$ (see (4.8)) which model the propagation of information through the cortical lateral connectivity. This operator can be expressed as

$$\partial_t u - (X_1^{\mathrm{SE}(2)})^2 u - (X_2^{\mathrm{SE}(2)})^2 u,$$

where $(X_1^{\mathrm{SE}(2)})^2$ and $(X_2^{\mathrm{SE}(2)})^2$ are the second derivatives in the directions of $X_1^{\mathrm{SE}(2)}$ and $X_2^{\mathrm{SE}(2)}$, respectively, with u defined in (6.3). The operator is formally degenerate, in the sense that its second fundamental form has zero determinant at every point. The same type of operators has been deeply studied by Hörmander in [85], Rothshild-Stein in [138], Jerison in [99], Jerison and Sánchez-Calle in [98], [99], and it is known that the operator is hypoelliptic. There is a large literature which has been produced on these type of operators after the aforementioned classical studies. We refer to [14] for a recent presentation of the state of the art results (see also Chapter 3).

(b) A concentration on the surface of maxima in order to model the maximum selection mechanism and the orientation tuning.

In the work of Citti and Sarti [35] the authors studied a two step algorithm of a diffusion driven motion where (a) and (b) were applied iteratively and proved that at each step the surface was performing an increment in the normal direction with speed equal to the sub-Riemannian mean curvature. However a complete proof was still missing, even in the Euclidean setting. Hence we start here with Euclidean geometry and provide the proof in this geometry.

6.1.3 Convergence result

Here we modify the algorithm of [35]: We apply it to graphs, and propose to take the maximum in a fixed direction, which is simpler and well adapted to the setting of graphs. The motivation of using a fixed direction in the maximum selection step comes from that the feature tuning (or selection) given by (2.2) takes place neurophysiologically along the vertical connection in each hypercolumn. Note that the feature p in (2.2) can be thought as a function γ of the spatial variables x'. In this case we can reformulate (2.2) as follows:

$$O^I_{\tilde{\gamma}(x')} = \max_{\gamma} O^I_{\gamma}(x') \quad \text{where} \quad \gamma(x') = \gamma.$$

Therefore we assume that the surface can be represented as a graph and propose to choose the fixed direction as the direction of the graph function, which is the last component of the standard Euclidean basis in our case. Then we model the concentration step following the diffusion as the selection of the maximum value along this fixed direction. We provide a proof of the convergence of the algorithm by using the approach introduced by Evans in [56].

More precisely we consider a continuous and periodic function γ_0 whose graph defines a surface

$$\Sigma_0 = (x', \gamma_0(x')) \subset \mathbb{R}^n.$$

Here and in the sequel we will always denote the points in $\mathbb{R}^n$ by x and the first $(n-1)$ component by x'. We denote a unit normal by ν; since we are dealing with graphs $(x', \gamma_0(x'))$ in $\mathbb{R}^n$, we will also consider a unit vector e_n in the direction of the last coordinate. We denote a Dirac delta on the surface Σ_0 by δ_{Σ_0}, and we introduce a new two step algorithm:

- We first apply heat diffusion during an interval $[0, T]$ (with $T > 0$) of time

$$\begin{cases} \partial_t u = \Delta u & \text{in } \mathbb{R}^n \times (0, \infty) \\ u = < \nu, e_n > \delta_{\Sigma_0} & \text{on } \Sigma_0 \times \{t = 0\}. \end{cases} \tag{6.4}$$

- Then we define the new surface at time t as the zero level set of the derivative along e_n via

$$\Sigma_t := \{x \in \mathbb{R}^n : \ \partial_{x_n} u(x, t) = 0\}. \tag{6.5}$$

  We will prove that Σ_t is the graph of a new function

$$\gamma_1 = H(t)\gamma_0. \tag{6.6}$$

Finally, we apply the iterative procedure, which is expressed by $\gamma_j = H\left(\frac{t}{j}\right)^j \gamma_0$, and show that γ_j converges to the solution of motion by curvature. Precisely our main result is stated as follows:

Theorem 6.1. *If γ_0 is a continuous and periodic function, and γ is the unique solution to (6.1) with initial datum γ_0, then*

$$\gamma(x', t) = \lim_{j\to\infty} H\left(\frac{t}{j}\right)^j \gamma_0, \quad \textit{uniformly for } x \in \Sigma_t \textit{ and } t \geq 0 \textit{ in compact sets.}$$

The proof of convergence of our algorithm is partially inspired by the proof of Evans [56], but we deeply simplify it, since we study in a graph setting.

6.2 Non-linear semigroups and curvature flow of graphs

Definition 6.1. *Let B be a Banach space, and A be a $B-$valued non-linear operator with domain $D(A) \subset B$. We say that $-A$ is $m-$dissipative if*

- *$R(I + \lambda A) = B$ for every $\lambda > 0$,*
- *its resolvent $J_\lambda = (I + \lambda A)^{-1}$ is a single-valued contraction.*

For $m-$dissipative operators $-A$ it is possible to apply the fundamental generation theorem of Crandall and Liggett [40, Theorem I, p.266] which gives a weak definition of the solution to an evolution equation in the setting of a non-linear semigroup:

Theorem 6.2. *If $-A$ is $m-$dissipative operator on a Banach space B, then for all $\gamma_0 \in B$ the limit*

$$M(t)(\gamma_0) := \lim_{j\to\infty, \lambda j\to t} (I + \lambda A)^{-j} \gamma_0,$$

exists locally uniformly in t. This limit is called non-linear semigroup solution generated by A.

From now on B will denote the space of periodic α-Hölder continuous functions and $(B, ||\cdot||)$ will be the Banach space obtained by endowing B with the sup norm $||\cdot||$.

Definition 6.2. *A continuous function $\gamma : \mathbb{R}^{n-1} \to \mathbb{R}$ is a weak subsolution (resp. a supersolution) of*

$$\gamma(x') - \lambda \sum_{i,j=1}^{n-1} \left(\delta_{ij} - \frac{\gamma_{x_i}(x')\gamma_{x_j}(x')}{1 + |\nabla\gamma(x')|^2}\right)\gamma_{x_i x_j}(x') = f(x'),$$

in $\mathbb{R}^{n-1}$ *if for every* $x' \in \mathbb{R}^{n-1}$ *and smooth* $\phi : \mathbb{R}^{n-1} \to \mathbb{R}$ *such that* $\gamma - \phi$ *has a maximum (resp. a minimum) at* x' *one has*

$$\gamma(x') - \lambda \sum_{i,j=1}^{n-1} \left(\delta_{ij} - \frac{\phi_{x_i}(x')\phi_{x_j}(x')}{1 + |\nabla\phi(x')|^2} \right) \phi_{x_i x_j}(x') \leq (resp.\ \geq)\ f(x'),$$

where the first and second order spatial derivatives are shown by the subindices. Viscosity solutions are the functions which are simultaneously supersolutions and subsolutions.

Definition 6.3. *We say that* $\gamma \in B$ *belongs to* $D(A)$ *if there exist* $f \in B$ *and* $\lambda > 0$ *such that* γ *is a weak solution (in the sense of Theorem 6.2) of*

$$\gamma - \lambda \sum_{i,j=1}^{n-1} a_{ij}(\nabla\gamma)\gamma_{x_i x_j} = f, \text{ where } a_{ij}(\nabla\gamma) := \left(\delta_{ij} - \frac{\gamma_{x_i}\gamma_{x_j}}{1 + |\nabla\gamma|^2} \right),$$

in $\mathbb{R}^{n-1}$. *In this case we will write*

$$(I + \lambda A)\gamma = f. \tag{6.7}$$

The operator A is defined in a dense set of B, and arguing as in [56, Theorem 2.3, Theorem 2.5], it is possible to show that

Proposition 6.1. *The operator* $-A$ *introduced in Definition 6.3 is* $m-$*dissipative and its generated weak semigroup solution coincides with the viscosity solution defined in Definition 6.2.*

6.3 Definition of operator H

In this section we formally define the operator H mentioned in (6.6) and in Theorem 6.2.

We assume that the initial surface Σ_0 is the graph of some smooth function $\gamma : \mathbb{R}^{n-1} \to \mathbb{R}$, and evolve the measure $< \nu, r > \delta_{\Sigma_0}$ during an interval of time $[0, T]$. Then the solution of (6.4), restricted to the surface which is embedded to the ambient space $\mathbb{R}^n$ (see [91]), can be written for all $t \in [0, T]$ as

$$u(s,t) = \frac{1}{(4\pi t)^{n/2}} \int_{\Sigma_t} \sqrt{4\pi t}\, \mathrm{e}^{-|x-s|^2/4t} < \nu, r > d\sigma_t, \tag{6.8}$$

where $d\sigma_t$ denotes the surface measure element on Σ_t.

We will define the operator H in terms of the maximum of u in the direction of the last component of the canonical basis, i.e., $r = e_n$. Hence we will start with studying the restriction of u in this direction.

Theorem 6.3. *Let u be the function defined as in* (6.8) *and $\gamma \in B$. If $s' \in \mathbb{R}^{n-1}$ and there exists a value $\gamma^t(s')$ such that*

$$\partial_{x_n} u(s', \gamma^t(s'), t) = 0,$$

then

$$\gamma^t(s') = t v_{s_0} + \gamma(s'), \quad v_{s_0} = \sqrt{1 + |\nabla\gamma(s_0)|^2}\, K + O(t^{1/2}) \quad \text{as } t \to 0,$$

where K is the mean curvature at $s_0 \in \Sigma_0$.

Proof. We may assume $s_0 = 0 = (0, \dots, 0) \in \Sigma_0 \subset \mathbb{R}^n$ without losing the generality. Then we impose that there is a point $t > 0$ such that

$$\partial_{x_n} u(t v_{s_0} e_n, t) = 0.$$

More precisely,

$$0 = \partial_{x_n} u(t v_{s_0} e_n, t) = \frac{1}{(4\pi t)^{(n-1)/2}} \int\limits_{\Sigma_t} < x - t v_{s_0} e_n, e_n > \mathrm{e}^{-|x - t v_{s_0} e_n|^2/4t} \frac{1}{\sqrt{1 + |\nabla\gamma|^2}} d\sigma_t.$$

Consider Σ_0 as the graph $(x', \gamma(x'))$ of the smooth function $\gamma : \mathbb{R}^{n-1} \to \mathbb{R}$ and write

$$0 = \int\limits_{\Sigma_t'} \Big(\gamma(x') - t v_{s_0}\Big) \mathrm{e}^{-\frac{|(x', \gamma(x')) - t v_{s_0} e_n|^2}{4t}}\, dx'.$$

Now substitute $y' = t^{-1/2} x'$ and obtain

$$0 = \int\limits_{t^{-1/2}\Sigma_t'} \Big(\gamma(x') - t v_{s_0}\Big) \mathrm{e}^{-\frac{|(t^{1/2} y', \gamma(t^{1/2} y')) - t v_{s_0} e_n|^2}{4t}} dy' + O(\mathrm{e}^{-\alpha/2t}). \tag{6.9}$$

Taylor development gives

$$\gamma(t^{1/2} y') = \sum_{i=1}^{n-1} \gamma_{x_i}(0) t^{1/2} y_i + O(t^{1/2} |y'|^3),$$

hence the argument of the exponential in (6.9) becomes

$$\frac{|(t^{1/2} y', \gamma(t^{1/2} y')) - t v_{s_0} e_n|^2}{4t} = \frac{|(t^{1/2} y', \gamma(t^{1/2} y'))|^2}{4t} + O(t)$$

$$= \frac{|t^{1/2} y'|^2 + |\gamma(t^{1/2} y'))|^2}{t} + O(t) = (\delta_{ij} + \gamma_{x_i}(0)\gamma_{x_j}(0)) y_i y_j + O(t).$$

The matrix of elements

$$g_{ij} = \delta_{ij} + \gamma_{x_i}(0)\gamma_{x_j}(0),$$

is positive definite and there exists a matrix U such that $g_{ij} = (U^T)_{ih}U_{hj}$, where the left and right subindices denote the row and column positions, respectively. Then with the change of variable $z = Uy$ we can write (6.9) as

$$0 = \int\limits_{\mathbb{R}^{n-1}} \big(\gamma(t^{1/2}(U^{-1}z)') - tv_{s_0}\big)\mathrm{e}^{-|z|^2/4}|U^{-1}|\,dz' + O(\mathrm{e}^{-\alpha/2t}),$$

as $t \to 0$. Further expanding the function γ, we obtain

$$0 = \int\limits_{\mathbb{R}^{n-1}} \Big(\sum_{i=1}^{n-1}\gamma_{x_i}(0)t^{1/2}U_{ih}^{-1}z_h + \frac{1}{2}\sum_{i,j=1}^{n-1}\gamma_{x_ix_j}(0)tU_{ih}^{-1}z_hU_{jk}^{-1}z_k - tv_{s_0}\Big) \tag{6.10}$$
$$\mathrm{e}^{-|z|^2/4}|U^{-1}|\,dz' + O(t^{3/2}).$$

The first order term in (6.10) vanishes due to the Euclidean symmetry. The second order term with $h \neq k$ vanishes as well. Hence we are left with

$$\begin{aligned} 0 &= \int\limits_{\mathbb{R}^{n-1}} \Big(\frac{1}{2}\sum_{i,j=1}^{n-1}\gamma_{x_ix_j}(0)tU_{ih}^{-1}U_{jh}^{-1}|z_h|^2 - tv_{s_0}\Big)\mathrm{e}^{-|z|^2/4}|U^{-1}|\,dz' + O(t^{3/2}) \\ &= \int\limits_{\mathbb{R}^{n-1}} \Big(\sum_{i,j=1}^{n-1}\gamma_{x_ix_j}(0)tU_{ih}^{-1}U_{jh}^{-1} - tv_{s_0}\Big)\mathrm{e}^{-|z|^2/4}|U^{-1}|\,dz' + O(t^{3/2}). \end{aligned}$$

Since

$$\sum_{i,j=1}^{n-1}\gamma_{x_ix_j}(0)U_{ih}^{-1}U_{jh}^{-1} = \sum_{i,j=1}^{n-1}\Big(\delta_{ij} - \frac{\gamma_{x_i}(0)\gamma_{x_j}(0)}{1+|\nabla\gamma(0)|^2}\Big)\gamma_{x_ix_j},$$

the integral in (6.10) boils down to

$$0 = \Delta\gamma(0) - \frac{\sum\limits_{i,j=1}^{n-1}\gamma_{x_i}(0)\gamma_{x_j}(0)\gamma_{x_ix_j}(0)}{1+|\nabla\gamma(0)|^2} - v_{s_0} + O(t^{1/2}),$$

which implies

$$v_{s_0} = (1+|\nabla\gamma(0)|^2)^{1/2}\,\mathrm{div}\left(\frac{\nabla\gamma(0)}{\sqrt{1+|\nabla\gamma(0)|^2}}\right) + O(t^{1/2}),$$

as $t \to 0$. □

Lemma 6.1. *Let u be the function defined as in (6.8) and $\gamma \in B$. Let $s' \in \mathbb{R}^{n-1}$ and $t > 0$. If $\inf u_0 > 0$ and there exists a value $\gamma^t(s')$ such that $u_{x_n}(s', \gamma^t(s'), t) = 0$ then*

$$u_{x_nx_n}(s', \gamma^t(s'), t) < 0.$$

Proof. We assume as in Theorem 6.3 that, $s = 0$. Furthermore we know that if γ^t exists, then it necessarily has the expression

$$\gamma^t(s') = tv_{s_0}, \quad v_{s_0} = \sqrt{1 + |\nabla\gamma(s_0)|^2}K + O(t^{1/2}) \quad \text{as } t \to 0,$$

where K is the mean curvature at $s_0 \in \Sigma_0$. Then arguing as before we find:

$$\begin{aligned}
\partial_{x_n x_n} u(s,t) &= -\frac{1}{(4\pi t)^{(n-1)/2}} \int_{\Sigma_t} \Big(1 - \frac{(\gamma(x') - tv_{s_0})^2}{2t}\Big) \mathrm{e}^{-|x - tv_{s_0} e_n|^2/4t} \frac{1}{\sqrt{1 + |\nabla\gamma|^2}} d\sigma_x \\
&= -\int_{\mathbb{R}^{n-1}} \Big(1 - \frac{\big(\gamma(t^{1/2}(U^{-1}z)')\big)^2}{2t}\Big) \mathrm{e}^{-|z|^2/4} |U^{-1}|\, dz' + O(\mathrm{e}^{t^{3/2}}) \\
&= -\int_{\mathbb{R}^{n-1}} \Big(1 - \frac{\sum_{i,j=1}^{n-1} \gamma_{x_i}(0') U^{-1}_{ih} z_h \gamma_{x_j}(0') U^{-1}_{jk} z_k}{2}\Big) \mathrm{e}^{-|z|^2/4} |U^{-1}|\, dz' + O(\mathrm{e}^{t^{3/2}}).
\end{aligned}$$

As in the previous case we consider $h = k$. Then we obtain:

$$\begin{aligned}
&\partial_{x_n x_n} u(s,t) = \\
&= -\int_{\mathbb{R}^{n-1}} \mathrm{e}^{-|z|^2/4} |U^{-1}|\, dz' + \frac{\sum_{i,j=1}^{n-1} \gamma_{x_i}(0') U^{-1}_{ih} \gamma_{x_j}(0') U^{-1}_{jh}}{2} \int_{\mathbb{R}^{n-1}} z_h^2 \mathrm{e}^{-|z|^2/4} |U^{-1}|\, dz' \\
&\quad + O(\mathrm{e}^{t^{3/2}}).
\end{aligned}$$

Note that

$$\frac{1}{2} \int_{\mathbb{R}^{n-1}} z_h^2 \mathrm{e}^{-|z|^2/4} dz' = \int_{\mathbb{R}^{n-1}} \mathrm{e}^{-|z|^2/4} dz',$$

and also $\sum_{h=1}^{n-1} U^{-1}_{ih} U^{-1}_{jh} = g^{ij}$, resulting in

$$\sum_{i,j=1}^{n-1} \gamma_{x_i}(0') U^{-1}_{ih} \gamma_{x_i}(0') U^{-1}_{jh} = \sum_{i,j=1}^{n-1} \Big(\delta_{ij} - \frac{\gamma_{x_i}(0')\gamma_{x_j}(0')}{1 + |\nabla\gamma(0')|^2}\Big) \gamma_{x_i}(0')\gamma_{x_j}(0') = \frac{|\nabla\gamma(0')|^2}{1 + |\nabla\gamma(0')|^2}.$$

We conclude that

$$\partial_{x_n x_n} u(s,t) = -\int_{\mathbb{R}^{n-1}} \frac{1}{1 + |\nabla\gamma(0')|^2} \mathrm{e}^{-|z|^2/4} |U^{-1}|\, dz' < 0.$$

□

Remark 6.1. *For every s' and sufficiently small $t > 0$ Lemma 6.1 ensures the uniqueness of the value $\gamma^t(s')$ such that $u_{x_n}(s', \gamma^t(s'), t) = 0$. Assume by contradiction that there exist more than one point with this property. Since $u_{x_n x_n} < 0$ at these points, zeros of the function $u_{x_n}(s', t) = 0$ are isolated. Let us call σ_1, σ_2, two consecutive zeros, with $\sigma_1 < \sigma_2$. Since $u_{x_n}(s', t)$ never vanishes on the interval $]\sigma_1, \sigma_2[$, it has a constant sign. However this is a contradiction, since $u_{x_n x_n} < 0$ at both points.*

We can now give a formal definition of the operator H.

Definition 6.4. *For any $t > 0$ a function $\gamma^t \in B$ is well-defined such that $u_{x_n}(s', \gamma^t(s'), t) = 0$. We will call*

$$H(t)(\gamma) = \gamma^t.$$

6.4 Properties of operator H

In this section we prove that the operator H defined in Definition 6.4 has values in B, and it is contractive:

Theorem 6.4. *For each $t \geq 0$ the flow $H(t) : B \to B$ has the following properties*

(1) If C is a real constant, then $H(t)(\gamma + C) = H(t)\gamma + C$,

(2) If $\gamma \leq \mu$ then $\gamma^t = H(t)\gamma \leq H(t)\mu = \mu^t$,

(3) $H(t)$ is a contraction on B, i.e.,

$$||H(t)\gamma - H(t)\mu|| \leq ||\gamma - \mu||.$$

Proof. Assertion (1) follows from the definition of H. For assertions (2) and (3), consider the evolution problem given by

$$\begin{cases} \partial_t = \Delta u & \text{in } \mathbb{R}^n \times (0, \infty) \\ u =< \nu, r > \delta_{\Sigma_0} & \text{at time } t = 0. \end{cases}$$

Let us call u_γ and u_μ the solutions with initial datum defined by the graphs of γ and μ, respectively. Hence

$$u_\gamma(s, t) = \frac{1}{(4\pi t)^{(n-1)/2}} \int\limits_{\Sigma'_t} (x' - s', \gamma(x') - s_n) \mathrm{e}^{-\frac{|x'-s', \gamma(x')-s_n|^2}{4t}} dx',$$

and $u_\mu(s)$ has a similar expression in terms of μ. Note that the function

$$(\gamma - s_n) \mathrm{e}^{-\frac{|\gamma - s_n|^2}{t}},$$

decreases as a function of γ for $t > 0$ small. It follows that if $\gamma \leq \mu$ and $\gamma^t(s')$ is the function defined in Lemma 6.1, then

$$0 = u_\gamma(s', \gamma^t(s')) \geq u_\mu(s', \gamma^t(s')).$$

This implies that $\gamma^t = H(t)\gamma \leq H(t)\mu = \mu^t$ from which assertion (2) follows. We remark that a comparison principle for intrinsic functions μ and γ becomes valid as a direct consequence of assertion (2).

Assertion (3) follows from assertions (1) and (2). Let us choose s' such that

$$H(t)\gamma(s') - H(t)\mu(s') > ||H(t)\gamma(s') - H(t)\mu(s')|| - \epsilon,$$

for each $\epsilon > 0$ and call

$$H(t)\gamma(s') = \alpha, \quad H(t)\mu(s') = \beta.$$

By assertion (2) we have

$$H(t)\gamma(s') - H(t)(\mu - \beta + \alpha - \epsilon)(s') > 0,$$

and it implies by assertion (1) that there exists a point y such that

$$\gamma(y') - (\mu(y') - \beta + \alpha - \epsilon) > 0. \tag{6.11}$$

Finally (6.11) results in, by definitions of α and β, that

$$||H(t)\gamma - H(t)\mu|| < H(t)\gamma(s') - H(t)\mu(s') + \epsilon < \gamma(y') - \mu(y') + 2\epsilon \leq ||\gamma - \mu|| + 2\epsilon,$$

from which assertion (3) follows. □

6.5 Main result

We provide here the proof of Theorem 6.1. As in the proof of [30, Theorem 2] we will deduce it from the following theorem of Brezis and Pazy [26]:

Theorem 6.5. *Let B be a Banach space and $\bar{D}(A)$ be the closure of the domain of A. Suppose that there exists a family of contractive operators $\{H(t)\}_{t\geq 0}$ satisfying*

$$(I + \lambda A)^{-1}\gamma = \lim_{t\to 0^+} \left(I + \lambda t^{-1}(I - H(t))\right)^{-1} \gamma, \tag{6.12}$$

for every $\gamma \in B$ and $\lambda > 0$. Then for every $\gamma \in \bar{D}(A)$ and $t \geq 0$, one has:

$$M(t)\gamma = \lim_{j\to\infty} H\left(\frac{t}{j}\right)^j \gamma, \text{ uniformly for } t \text{ in compact sets,}$$

where $M(t)\gamma$ is the semigroup generated by A (see the definition in Theorem 6.2 above).

Let us start with the following property of the flow:

Proposition 6.2. *Let $\gamma \in B$ be a smooth function and for $t > 0$ denote by $H(t)\gamma$ its flow defined in Definition 6.4. For every $x \in \mathbb{R}^n$ one has*

$$(H(t)\gamma)(s') - \gamma(s') = -tK(s', \gamma(s'))\sqrt{1 + |\nabla\gamma(s')|^2} + o(t),$$

where the convergence $o(t)/t \to 0$ is uniform as $t \to 0$.

Proof. It is a direct consequence of Theorem 6.3. □

Proof of Theorem 6.1. We only have to show that (6.12) holds for $\lambda = 1$. For this purpose, by following [56, Theorem 5.1] and [30, Theorem 2], we define for $t > 0$ and $f \in B$ that

$$\gamma_t := \big(I + t^{-1}(I - H(t))\big)^{-1}\gamma \quad \text{and} \quad A_t\gamma := \frac{\gamma - H(t)\gamma}{t}.$$

Due to Proposition 6.1 $-A$ is $m-$dissipative and thus so is $-A_t$ ($-A$ at time t), implying for all s', x' and $t > 0$ that

$$\sup_{x'} \big|\gamma_t(x' - s') - \gamma_t(s')\big| \le \sup_{x'} \big|f(x' - s') - \gamma(s')\big|. \tag{6.13}$$

Note that (6.13) results in a bounded and equicontinuous family $\{\gamma_t\}_{t\in(0,1]}$. Therefore the Arzelà-Ascoli theorem applies.

Let $\phi \in C^\infty$ such that $\gamma_t - \phi$ has a positive maximum at x_0'. We can always assume that the maximum is strict by adding a suitable power of the distance (Euclidean) if it is needed. Since $\gamma_{t_k} \to \gamma$ uniformly on compact sets then one can find a sequence of points $x_k' \to x_0'$ as $k \to \infty$ such that $\gamma_{t_k} - \phi$ has a positive maximum at x_k' and

$$(H(t_k)\gamma_{t_k})(x_k') - (H(t_k)\phi)(x_k') \le \gamma_{t_k}(x_k') - \phi(x_k'), \quad \text{i.e.,} \quad A_{t_k}\phi(x_k') \le A_{t_k}\gamma_{t_k}(x_k').$$

Since $\gamma_t + A_t\gamma_t = f$ we have

$$\gamma_{t_k}(x_k') + \frac{\phi(x_k') - (H(t_k)\phi)(x_k')}{t_k} \le f(x_k'). \tag{6.14}$$

We find from (6.14) via Proposition 6.2 that

$$\gamma_{t_k}(x_k') - \sum_{i,j=1}^{n-1} \Big(\delta_{ij} - \frac{\phi_{x_i}(x_k')\phi_{x_j}(x_k')}{1 + |\nabla\phi(x_k')|^2}\Big)\phi_{x_ix_j}(x_k') + o(1) \le f(x_k').$$

Letting $k \to \infty$ we see that γ is a weak subsolution of (6.7) with $\lambda = 1$. Through the same reasoning one can prove that γ is also a supersolution and it completes the proof. □

6.6 Numerical scheme and simulation results

We approximate our two step algorithm given by (6.4) and (6.5) in terms of finite differences. Let us consider the general $n-$dimensional scheme. We use a uniform grid in space-time $(x_1, x_2, \ldots, x_n, t)$ with t denoting the time variable and the rest denoting the spatial variables. Then we express each point on the grid as

$$(\, x_{1,m_1},\, x_{2,m_2},\, \ldots,\, x_{n,m_n}, t_k) = (m_1 s_{x_1},\, m_2 s_{x_2},\, \ldots,\, m_n s_n,\, k\, s_t),$$

where $s_t > 0$ represents the time step and $s_{x_i} > 0$ terms $(i = 1, 2, \ldots, n)$ represent the spatial step corresponding to each spatial variable x_i. Note that we set

$$s = s_{x_1} = \cdots = s_{x_n},$$

and we choose s_t regarding the upper bound computed from Courant-Friedrichs-Lewy stability condition [38].

We follow the notation used in (6.4) and (6.5) and denote the value of the function u at the grid point $(x_{1,m_1},\, x_{2,m_2},\, \ldots,\, x_{n,m_n},\, t_k)$ by

$$u(x_{1,m_1},\, x_{2,m_2},\, \ldots,\, x_{n,m_n},\, t_k).$$

Then we approximate the first order time derivative by using a first order forward finite difference and the spatial derivatives by employing second order centered finite differences. We denote the finite difference of time by D_t and the finite difference corresponding to the second order derivative in the direction of x_i by D_{ii}. Then we write the spatial finite differences as

$$D_{ii}u(x_{1,m_1},\, x_{2,m_2},\, \ldots,\, x_{n,m_n},\, t_k) = \\ \frac{u(\ldots, x_{i,m_i+1}, \ldots, x_n,\, t_k) - 2u(\ldots, x_{i,m_i}, \ldots, x_n,\, t_k) + u(\ldots, x_{i,m_i-1}, \ldots, x_n,\, t_k)}{4s^2},$$

and the one of time as

$$D_t u(x_{1,m_1}, \ldots,\, x_{n,m_n},\, t_k) = \\ \frac{u(x_{1,m_1}, \ldots,\, x_{n,m_n}\, t_{k+1}) - u(x_{1,m_1}, \ldots,\, x_{n,m_n},\, t_k)}{s_t} = \sum_{i=1}^{n} D_{ii}u(x_{1,m_1}, \ldots,\, x_{n,m_n},\, t_k).$$

Then we iterate the algorithm by employing the explicit forward Euler method:

$$u(x_{1,m_1}, \ldots,\, x_{n,m_n},\, t_{k+1}) = u(x_{1,m_1}, \ldots,\, x_{n,m_n},\, t_k) + s_t D_t u(x_{1,m_1}, \ldots,\, x_{n,m_n},\, t_k).$$

In the numerical experiments we consider some curve evolutions (i.e., $n = 2$) where the curves are represented as the graphs of the spatial variable x_1 (see the initial curves in Figure 6.1). Here the grid points are denoted by $(x_{1,m_1},\, x_{2,m_2},\, t_k)$. In both experiments we use a 256×256 image matrix, i.e., $m_1, m_2 = 1, 2, \ldots, 256$. We fix $s_t = 0.1$. We impose Dirichlet boundary conditions and then perform the procedure with diffusion and concentration given by (6.4) and (6.5) through 5, 30 and 200 iterations. The evolutions of the curves are presented in Figure 6.1.

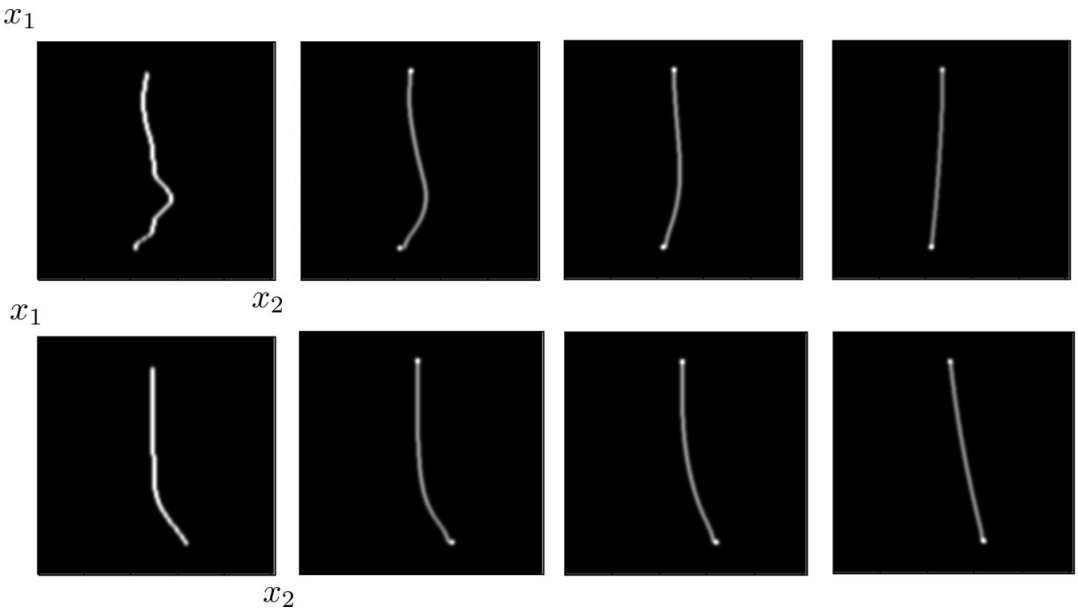

Figure 6.1: Left: Initial curves. Middle left: The resultant curves of the evolution through 5 iterations. Middle right: The results of 30 iterations. Right: The results of 200 iterations.

Chapter 7

Uniqueness of viscosity mean curvature flow solution in the Heisenberg group

In this chapter we provide a proof of the uniqueness of the viscosity solution to the mean curvature flow equation in the Heisenberg group geometry, we give the key point which generalizes the proof to the setting of step 2 Carnot groups and some asymptotic properties of the vanishing viscosity solutions, which were known in the Carnot groups but not in the group of roto-translations (SE(2)). In sub-Riemannian setting the uniqueness could not be deduced by a comparison principle, which was known only for graphs [29] and radially symmetric surfaces [63], due to presence of characteristic points. Here we prove that any viscosity solution is a limit of a sequence of solutions to a Riemannian mean curvature flow, and consequently we obtain the uniqueness and the comparison principle in the sub-Riemannian setting of the Heisenberg group. The Heisenberg group and more generally Carnot groups are particularly important due to their relation to the models of the primary visual cortex. Due to the close relation between the Heisenberg group and SE(2), our uniqueness result becomes important for the surface completion problem of the model of the visual cortex proposed by Citti and Sarti [35]. Furthermore thanks to the flexibility of the technique which we use in order to prove the uniqueness, it is possible to show the uniqueness also in the general setting of step 2 Carnot groups which are closely related to multi-feature selective visual cortex models (see for example Chapter 5).

The chapter is organized as follows: We first provide a literature review and a presentation of the problem together with our original contribution in Section 7.1. Then in Section 7.2 we provide the notions of vanishing viscosity solution and viscosity solution, and describe the generalized flow in SE(2) and Carnot group settings. In Section 7.3 we give some geometric properties of vanishing viscosity solutions. Then in Section 7.4 we prove our main theorem. From the theorem we deduce the uniqueness and the comparison principle for the viscosity solution. Finally we give the key point in our proof which generalizes the proof of uniqueness to the setting of step 2 Carnot groups.

7.1 Presentation of the problem and our contribution

Mean curvature flow describes the evolution of a surface whose points move in the normal direction, with speed equal to the curvature. The first results in the Euclidean setting have been provided by Gage [76, 78], Huisken [92], Gage-Hamilton [77], Grayson [82] and Altschuler-Grayson [1], with the methods based on differential geometry. Since mean curvature flow can develop singularities even for initially smooth surfaces, (see for example [60]), different notions of weak solution were proposed in order to study the flow after singularities: Brakke introduced in [21] an approach based on the notion of varifold and geometric measure theory, Evans-Spruck [60], [57], [58], [59] and Chen-Giga-Goto [32] independently studied existence and uniqueness of viscosity solutions via level set methods.

The level set method identifies the evolving surface at time t as a level set $M_t = \{x \in \mathbb{R}^n : \ u(x,t) = 0\}$ of a function u, which is a solution to a differential equation. In $n-$dimensional Euclidean setting the curvature can be expressed as $K = \operatorname{div}\Big(\dfrac{\nabla u}{|\nabla u|}\Big)$ and the mean curvature flow equation reads:

$$\partial_t u(x,t) = |\nabla u| K = \sum_{i,j=1}^{n} \Big(\delta_{ij} - \frac{\partial_{x_i} u \, \partial_{x_j} u}{|\nabla u|^2}\Big)\partial_{x_i x_j} u,$$

where ∂_t represents the derivative with respect to time variable and ∂_{x_i} the derivative with respect to i^{th} spatial variable.

This chapter focuses on the sub-Riemannian analogue of the mean curvature flow in a group G, which can be either a Carnot group of step 2 or the group SE(2) of rigid motions. A sub-Riemannian structure on one of these groups is defined by a triple $(G, \mathcal{D}, (g_{ij}))$, where G is the group, $\mathcal{D}$ is a horizontal distribution and (g_{ij}) is a metric on $\mathcal{D}$. The space has the bracket generating properties at step 2. That is, if we denote a basis of $\mathcal{D}$ by $\{X_1, X_2, \ldots, X_m\}$ then $\{[X_i, X_j]\}_{i,j=1,2\ldots,m}$ together with $\{X_1, X_2, \ldots, X_m\}$ spans the tangent space TG to G at every point where $[.\,,\,.]$ is the Lie bracket. Eventually we will choose a metric (g_{ij}) on $\mathcal{D}$, which will make $X_1, X_2, \ldots, X_m$ orthonormal. In the particular case where we consider SE(2), the underlying manifold will be $G = \mathbb{R}^2 \times S^1$, its elements will be expressed by $\xi = (x, y, \theta) \in \mathrm{SE}(2)$ so that x, y denote the spatial components and θ the angular (orientation) component. We will make the choice of the vector fields

$$X_1 = \cos(\theta)\partial_x + \sin(\theta)\partial_y, \quad X_2 = \partial_\theta,$$

at every $\xi \in G$, which satisfy the bracket generating condition, as it is easy to verify. We will denote the commutator by

$$X_3 = -\sin(\theta)\partial_x + \cos(\theta)\partial_y.$$

While studying a Carnot group $G = \mathbb{R}^n$ of step 2 we will denote the corresponding elements by $\xi = (x, \theta)$, with $x = (x_1, x_2, \ldots, x_m)$ representing the horizontal variables

and $\theta = (\theta_1, \theta_2, \ldots, \theta_{n-m})$ representing the variables of the second layer. It is known (see for example [138]) that a basis of bracket generating vector fields can be represented in this setting as:

$$X_i = \partial_{x_i} + \sum_{k=1}^{n-m} \sum_{l=1}^{m} f_{il}^{(k)} x_l \partial_{\theta_k}, \quad i = 1, \ldots, m, \tag{7.1}$$

with $f_{il}^{(k)} = -f_{il}^{(k)} \in \mathbb{R}$ (see [14], [29]). Furthermore the vertical vector fields in the second layer can be expressed as

$$X_i = \partial_{\theta_{i-m}}, \quad i = m+1, \ldots, n, . \tag{7.2}$$

We will use also the general notation which includes the approximating vertical vector fields as well:

$$X_{i\delta} = \delta^{\deg(X_i)-1} X_i, \quad i = 1, \ldots, n,$$

where $\delta > 0$ and $\deg(\cdot)$ gives the degree of its argument (i.e., 1 for the vector fields in the first layer and 2 for the vector fields in the second layer).

We explicitly note that the Heisenberg group can be considered as the limit structure obtained from SE(2) via a blow up procedure (see [32], [56] and [71]), hence those two structures, which have completely different group laws, share the same local structure. This is why they can be studied together, and used as models of the same types of problems. The interest in studying motion by curvature in these two groups comes from applications of image inpainting through models of the visual cortex. Recall that the first layer (V1) of the mammal visual cortex was modeled as a smooth sub-Riemannian surface with the local structure of the Heisenberg group in [132], and with the SE(2) geometry in [35]. As a consequence, some models of image completion inspired by the functionality of the cortex were proposed in [122] and [35]. Convincing completion results have been presented using mean curvature flow in these groups (see [141] and [34]). We also note that numerous image processing applications can be performed in similar sub-Riemannian geometries (see for example the algorithms proposed in [73], [50], [51], [52], [53], [11]).

The obstacle to the development of a strong numerical theory for sub-Riemannian mean curvature flow is the lack of uniqueness results in those settings. Indeed the existence of sub-Riemannian mean curvature flow solutions is known in Carnot groups (see [29]), and in general Hörmander structures (see [48]), but the uniqueness problem is still largely open. Furthermore the geometry in Carnot groups of step 2 is different from the geometry in Carnot groups of a higher order step, since it was shown in [29] that the planes are not minimal surfaces in Carnot groups of a step strictly bigger than two, resulting in the lack of a family of functions which can be used as barrier functions. Hence it is natural to focus only on step 2 groups. Up to now Capogna and Citti [29] proved the uniqueness of evolving graphs in a Carnot group by using the fact that graphs do not suffer from singularities during mean curvature flow. In the special case of the 3-dimensional Heisenberg group Ferrari, Liu and Manfredi [63] provided uniqueness under

the assumption of axisymmetricity of solutions to the sub-Riemannian mean curvature flow equation given by (7.3) in the sequel.

Here we will present a complete proof of the uniqueness of the sub-Riemannian mean curvature flow solution in the Heisenberg group by discarding the previous restrictions on the solution. Furthermore our proof can be extended to the general setting of step 2 Carnot groups.

Differential calculus in sub-Riemannian spaces is well-established (see for example [123]). Recall from Section 3.5 the horizontal gradient of a function is defined as

$$\nabla_0 = (X_1, X_2, \dots, X_m).$$

The notion of regular surface in sub-Riemannian setting has been introduced by Franchi, Serapioni and Serra Cassano [71] as the zero level set $M = \{\xi \in G : u(\xi) = 0\}$ of a smooth function u, whose horizontal gradient does not vanish. However even surfaces which are regular in the Euclidean sense have points at which the horizontal gradient vanishes. We call such points *characteristic points* and we denote the set of those points by $\Sigma(M) = \{\xi \in M : \ \left|\nabla_0 u(\xi, t)\right| = 0\}$. As a result of the presence of characteristic points we lack a definition of mean curvature in sub-Riemannian settings.

Let us recall that at non-characteristic points the horizontal normal is defined as

$$\nu_0 = \frac{\nabla_0 u}{|\nabla_0 u|},$$

and the horizontal mean curvature of the manifold M is given by

$$K_0 = \sum_{i=1}^{m} X_i \nu_{0,i}.$$

This notion has been introduced in a general setting in [42]. Results on the mean curvature equation in the special setting of the Heisenberg group were provided in [31], [29], [30], [63] and in SE(2) by [34]. We refer to [29] for more detailed references.

Analogously to the Euclidean setting, horizontal mean curvature flow is the evolution of a surface $M_0 \subset G$ with normal speed equal to the horizontal mean curvature. If M_0 is the level set of a function u_0, the flow at time t will be identified as the level set $M_t = \{\xi \in G : \ u(\xi, t) = 0\}$ of the solution of the following degenerate problem:

$$\begin{cases} \partial_t u = \sum\limits_{i,j=1}^{m} \left(\delta_{ij} - \frac{X_i u X_j u}{|\nabla_0 u|^2}\right)(X_i X_j)u & \text{in } G \times (0, \infty) \\ u(., 0) = u_0(.) \quad \text{on } G \times \{0\}. \end{cases} \tag{7.3}$$

In order to find the uniqueness we prove the following comparison principle for the viscosity solutions of the problem (7.3):

Corollary 7.1. *Assume that u and v are continuous viscosity solutions of problem* (7.3) *(as defined in Definition 7.2) such that*

- *there exists* $R > 0$ *with* $u = 0$, $v = 0$ *for* $|\xi| > R$,
- $u \leq v$ *at time* $t = 0$.

Then $u \leq v$ *for every* $t > 0$.

The proof relies on a regularization procedure together with a Riemannian approximation. More precisely we define the gradient

$$\nabla_\delta = (X_1, X_2, \dots, X_m, X_{(m+1)\delta}, \dots, X_{n\delta}),$$

with $0 < \delta < \epsilon < 1$, then for an open ball $B(0, R)$ with radius R centered at the origin we introduce the regularized problem with the Riemannian approximation

$$\begin{cases} \partial_t u_\delta^\epsilon = \sum\limits_{i,j=1}^{n} \Big(\delta_{ij} - \dfrac{X_{i\delta} u_\delta^\epsilon X_{j\delta} u_\delta^\epsilon}{|\nabla_\delta u_\delta^\epsilon|^2 + \epsilon^2}\Big) X_{i\delta} X_{j\delta} u_\delta^\epsilon \quad \text{in } B(0,R) \times (0, \infty) \\ u_\delta^\epsilon(., 0) = u_0(.) \quad \text{on } B(0,R) \times \{0\} \\ u_\delta^\epsilon(., t) = 0 \quad \text{on } \partial B(0,R) \times [0, T], \end{cases} \tag{7.4}$$

and the same problem on the whole space

$$\begin{cases} \partial_t u_\delta^\epsilon = \sum\limits_{i,j=1}^{n} \Big(\delta_{ij} - \dfrac{X_{i\delta} u_\delta^\epsilon X_{j\delta} u_\delta^\epsilon}{|\nabla_\delta u_\delta^\epsilon|^2 + \epsilon^2}\Big) X_{i\delta} X_{j\delta} u_\delta^\epsilon \quad \text{in } G \times (0, \infty) \\ u_\delta^\epsilon(., 0) = u_0(.) \quad \text{on } G \times \{0\}. \end{cases} \tag{7.5}$$

Then we use the following *vanishing viscosity* solution definition:

Definition 7.1. *A function* u *is called bounded, continuous vanishing viscosity solution of* (7.3) *if there exist a constant* $\mathcal{C}$*, for any compact set* Z *a constant* $C(Z)$*, and for any* δ, ϵ, $R > 0$ *a solution* $u_\delta^{\epsilon,R}$ *of the problem* (7.4) *such that*

- $||u_\delta^{\epsilon,R}||_\infty \leq \mathcal{C}, \quad |\nabla_E u_\delta^{\epsilon,R}(\xi, t)| \leq C(Z)$ *where* ∇_E *denotes the Euclidean gradient,*
- *there exists a function* u_δ^ϵ *which is a solution of the problem* (7.5) *such that* $u_\delta^\epsilon = \lim\limits_{R \to +\infty} u_\delta^{\epsilon,R}$ *uniformly,*
- $u = \lim\limits_{\epsilon,\delta \to 0} u_\delta^\epsilon$ *uniformly.*

This definition immediately implies that comparison principle and uniqueness are valid for vanishing viscosity solutions (see also Theorem 7.3 below). The same result will be extended to viscosity solutions, proving that those two notions, viscosity and vanishing viscosity solutions, coincide. This assertion has been already known in the Euclidean setting but not in a sub-Riemannian setting. Indeed the crucial idea of the paper is to establish the following approximation result:

Theorem 7.1. *Let v be a bounded, continuous viscosity solution of problem* (7.3) *in the sense of Definition 7.2 below, constantly equal to* 0 *outside of a compact set, and let u_δ^ϵ be a solution of problem* (7.5)*, limit of problem* (7.4)*. Then for every $0 < T < \infty$ there exist constants α and $M = M(u_0, T, \alpha)$ such that*

$$\sup_{\xi \in G, 0 \leq t \leq T} |(v - u_\delta^\epsilon)(\xi, t)| \leq M\epsilon^\alpha,$$

for all $0 < \epsilon < 1$ and $\delta = \delta(\epsilon)$.

An immediate consequence of Theorem 7.1 is the following:

Corollary 7.2. *Any continuous viscosity solution v is a vanishing viscosity solution.*

The proof of Theorem 7.1 generalizes the proof of Deckelnick [47] to the sub-Riemannian geometry of the Heisenberg group. The comparison principle of viscosity solutions is based on the maximization of

$$w(\xi, \eta, t) = u(\xi, t) - v(\eta, t) - \phi(\xi, \eta, t),$$

for a suitable function ϕ where $\xi, \eta \in G$. This function must satisfy that:

i) the sum of the second order derivatives vanish when the first order ones do,

ii) $|\nabla_0^\xi \phi(\xi, \eta, t)|^2 = |\nabla_0^\eta \phi(\xi, \eta, t)|^2$, where X_i^ξ and X_i^η denote the i^{th} horizontal vector fields at $\xi, \eta \in G$.

As noted by Ferrari, Liu and Manfredi [63] the main difficulty in extending the classical approach to the sub-Riemannian setting of the Heisenberg group is to find a function ϕ satisfying, in addition to the first condition, a stricter version of the second condition: $X_i^\xi \phi(\xi, \eta, t) = -X_i^\eta \phi(\xi, \eta, t)$. We handle this difficulty and eliminate the need of this stricter condition by using the operator ∇_δ.

Note that, with the approximated equation (7.5) we give a formal meaning to the regularized operator $|\nabla_\delta u| K_0$ at characteristic points. Indeed, formally if ξ is characteristic for every $\epsilon > 0$ then

$$\sum_{i,j=1}^{n} \Big(\delta_{ij} - \frac{X_{i\delta} u(\xi) X_{j\delta} u(\xi)}{|\nabla_\delta u(\xi)|^2 + \epsilon^2} \Big) X_{i\delta} X_{j\delta}(u(\xi)) = \sum_{i=1}^{m} X_i X_i u(\xi), \tag{7.6}$$

which is the Laplace operator of the function u in the sub-Riemannian setting of G as $\delta \to 0$.

7.2 Definitions and preliminary results

7.2.1 Definition of viscosity and vanishing viscosity solutions

Let us consider a vector field X, a point ξ in G. If $\gamma_{\xi,X}$ is a solution to the following Cauchy problem:

$$\begin{cases} \dot{\gamma}_{\xi,X}(t) = X(\gamma_{\xi,X}(t)) \\ \gamma_{\xi,X}(0) = \xi, \end{cases}$$

then we will define $\exp(X)(\xi) := \gamma_{\xi,X}(1)$. For every fixed ξ and $e = (e_1, e_2, \dots, e_n) \in \mathbb{R}^n$ the exponential map

$$e \mapsto \exp(\sum_{i=1}^{n} e_i X_i)(\xi), \tag{7.7}$$

is a local diffeomorphism from a neighborhood of 0 in $\mathbb{R}^n$ to a neighborhood of ξ. We define the superjets $\mathcal{P}^{2,+}u(\xi,t)$ and $\mathcal{P}^{2,-}u(\xi,t)$, as follows:

$$\mathcal{P}^{2,+}u(\xi,t) := \{(a,p,H) \in \mathbb{R} \times \mathbb{R}^n \times \mathcal{S}(m) \mid u\Big(\exp\big(\sum_{i}^{n} e_i X_i\big), s\Big)(\xi) \leq u(\xi,t)$$

$$+a(s-t) + \sum_{i}^{n} p_i e_i + \frac{1}{2}\sum_{i}^{m} H_{ij} e_i e_j + o(|s-t| + |e|^2) \quad \text{as} \quad (e, s-t) \to 0\},$$

and $\mathcal{P}^{2,-}u(\xi,t) = -\mathcal{P}^{2,+}(-u)(\xi,t)$ with $\mathcal{S}(n)$ representing the group of $n \times n$ symmetric matrices. Note that $(p_1, p_2, \dots, p_m)$ plays the role analogous to a horizontal gradient in this formula. However in a Carnot group of step 2, the right hand side contains the analogue of the complete gradient $(p_1, p_2, \dots, p_n)$. Furthermore $(H_{ij})_{i,j=1,2,\dots,m}$ plays the role of a horizontal Hessian. Finally we denote the closure of the superjets by $\tilde{\mathcal{P}}^{2,+}$ and $\tilde{\mathcal{P}}^{2,-}$.

Then the viscosity solution in this case is defined as follows:

Definition 7.2. *A function $u \in C^0(G \times [0,\infty))$ is called a viscosity subsolution of* (7.3) *if for every $(\xi_0, t_0) \in G \times (0,\infty)$ and every $(a,p,H) \in \tilde{\mathcal{P}}^{2,+}u(\xi_0,t_0)$ it is provided that*

$$a \leq \sum_{i,j=1}^{m} \Big(\delta_{ij} - \frac{p_i p_j}{|p|^2}\Big) H_{ij} \quad \text{if} \quad p \neq 0,$$

$$a \leq \sum_{i,j=1}^{m} \delta_{ij} H_{ij} \quad \text{if} \quad p = 0.$$

Viscosity supersolution is defined analogously where $\leq$ is replaced by $\geq$ and $\tilde{\mathcal{P}}^{2,+}u(\xi_0,t_0)$ by $\tilde{\mathcal{P}}^{2,-}u(\xi_0,t_0)$. A viscosity solution to (7.3) *is a function $u \in C^0(G \times [0,\infty))$ which is both a subsolution and supersolution.*

The condition at the characteristic points is motivated by (7.6).

We explicitly remark that the set of viscosity solutions is a larger set than the set of vanishing viscosity solutions. In other words, a vanishing viscosity solution to (7.3) is the viscosity solution which is the limit of a solution to (7.5) as $\epsilon, \delta \to 0$. Consequently vanishing viscosity solutions are also viscosity solutions (see [34]) while the fact that viscosity solutions are also vanishing viscosity solutions will be proved here in this chapter.

7.2.2 Existence and comparison results

In [60] the existence of a vanishing viscosity solution of Euclidean mean curvature flow was established under the assumption that the initial condition is identically 1 at infinity. The same theorem is already known in the two types of groups considered here: Carnot groups and SE(2) (see [29] for Carnot groups and [34] for SE(2)).

Theorem 7.2. *Assume that G is either a Carnot group or SE(2) and the initial datum u_0 is of class $C^1_E(G)$ (i.e., in the Euclidean sense). Then there is a sphere of radius R such that u_0 is identically constant out of this sphere, and there is a constant $\tilde{C}$ such that*

$$\max(\|u_0\|_{L^\infty(G)}, \|\nabla_E u_0\|_{L^\infty(G)}) \leq \tilde{C},$$

where ∇_E denotes the standard Euclidean gradient. Then for every compact set Z there is a constant $\tilde{C}(Z)$, such that for every δ and ϵ the solution of problem (7.5) satisfies

$$\|u^\epsilon_\delta(.,t)\|_{L^\infty(G)} \leq \tilde{C},$$
$$\|\nabla_E u^\epsilon_\delta(.,t)\|_{L^\infty(G)} \leq \tilde{C}(Z).$$

As a consequence, there exists a continuous vanishing viscosity solution u of problem (7.3) which satisfies

$$\|u(.,t)\|_{L^\infty(G)} \leq \tilde{C},$$
$$\|\nabla_E u(.,t)\|_{L^\infty(G)} \leq \tilde{C}(Z).$$

Recall that the regularized equation (7.5) has no critical points, hence the comparison principle established by Capogna and Citti [29] for viscosity solutions of the equation in the Carnot group settings is valid for (7.5) as well.

The proof of Theorem 7.2 in [34] is obtained via an approximation, starting with vanishing viscosity solutions, in the sense of Definition 1. Using this explicit construction, the following weak version of the comparison principle follows:

Theorem 7.3. *Let G be a Carnot group or SE(2). Assume that u and v are vanishing viscosity solutions of (7.3) in accordance with Definition 7.1, identically constant out of a compact set. Suppose further*

(i) For all $\xi \in G$, $u(\xi, 0) \leq v(\xi, 0)$,

(ii) u and v are uniformly continuous when restricted to $G \times \{t = 0\}$.

Then $u(\xi, t) \leq v(\xi, t)$ for all $\xi \in G$ and $t \geq 0$.

Proof. The solution $u^{\epsilon,R}_\delta$, which is defined on the bounded cylinder, satisfies the maximum and comparison principles. As a consequence these properties are inherited by $u^\epsilon_\delta = \lim_{R\to+\infty} u^{\epsilon,R}_\delta$ and $u = \lim_{\delta,\,\epsilon\to 0} u^\epsilon_\delta$.

□

7.3 Asymptotic behavior of solutions

In this section we establish the asymptotic behavior of solutions of equations (7.3) and (7.5) whose Euclidean analogue has been proved by Evans [60], and extended to Carnot groups in [29]. The proof is based on a comparison with an ad hoc auxiliary function. Since at this stage we have a comparison principle only for the vanishing viscosity solutions, the geometrical results hold only for that type of solutions.

7.3.1 Asymptotic behavior of the vanishing viscosity solution

Recall that in a Carnot group of step 2 we use the notation $\xi = (x, \theta)$, where $x = (x_1, \cdots, x_m)$ are the variables of the first layer, $\theta = (\theta_1, \cdots, \theta_{n-m})$ are the variables of the second layer and in SE(2) we use $\xi = (x, y, \theta)$ with spatial variables $x, y \in \mathbb{R}$ and angular variable $\theta \in S^1$. We will write $|\xi|$ in order to denote a pseudo-distance of ξ from the origin which can describe a neighborhood of infinity. In particular we will denote

$$|\xi| = \left(x^2 + y^2\right)^{1/2} \quad \text{in SE(2)}, \quad |\xi| = \left(|x|^4 + |\theta|^2\right)^{1/4} \quad \text{in a Carnot group.} \tag{7.8}$$

In the Euclidean and Carnot settings it is known that if the level sets of the initial datum are confined in some bounded region, then the corresponding level set of the solution remains in the same region during the whole mean curvature flow. This result in Carnot groups can be stated by following [29, Theorem 5.6] as:

Theorem 7.4. *Assume that G is a Carnot group of step 2, u_0 is continuous and there exists a constant $\hat{R} > 0$ such that*

$$u_0(\xi) \text{ is constant for all } \xi \in G \text{ satisfying } |\xi| \geq K \ .$$

Then there exists $R > 0$ dependent only on $\hat{R}$ such that any vanishing viscosity solution of (7.3) satisfies

$$u(\xi, t) \text{ is constant for all } \xi \in G \text{ satisfying } |\xi| \geq R \text{ and for all } t > 0.$$

Here we prove the same asymptotic behavior in SE(2). Clearly, if $\xi = (x, y, \theta) \in$ SE(2) it is sufficient to check the (x, y) variables in a neighborhood of infinity. Precisely we prove

Theorem 7.5. *Assume that $u_0 \in C^\infty(SE(2))$ and it is constant at the exterior of a cylinder. More precisely there exists a constant $\hat{R} > 0$ such that*

$$u_0(\xi) \text{ is constant for all } \xi \in SE(2) \text{ satisfying } |\xi| \geq \hat{R} \ .$$

Then there is $R > 0$ dependent only on $\hat{R}$ such that the vanishing viscosity solution u satisfies

$$u(\xi, t) \text{ is constant for all } \xi \in SE(2) \text{ satisfying } |\xi| \geq R \text{ and for all } t > 0.$$

Lemma 7.1. *Assume that $G = SE(2)$. Let us choose $0 < \delta, \epsilon < 1$ and let $h(\xi) = \frac{x^2+y^2}{2}$. For all $\xi \in G$, $t > 0$ let us call*

$$V_\delta^\epsilon(\xi, t) = \Upsilon\Big(h(\xi) + t\epsilon\Big) - Ct\epsilon^{1/2} \quad \textit{with} \quad \Upsilon(s) \equiv \begin{cases} 0 & (s \geq 2), \\ (s-2)^3 & (0 \leq s \leq 2). \end{cases}$$

Then there exists a choice of the constant C such that the function V_δ^ϵ satisfies

$$\partial_t V_\delta^\epsilon - \sum_{i,j=1}^{3} \left(\delta_{ij} - \frac{X_{i\delta} V_\delta^\epsilon X_{j\delta} V_\delta^\epsilon}{\epsilon^2 + |\nabla_\delta V_\delta^\epsilon|^2} \right) (X_{i\delta} X_{j\delta}) V_\delta^\epsilon \leq 0,$$

and at the initial time $t = 0$

$$\begin{aligned} &V_\delta^\epsilon(\xi, 0) = 0 \ \ \textit{if} \ \ h(\xi) \geq 2, \quad -1 \leq V_\delta^\epsilon(\xi, 0) \leq 0 \ \ \textit{if} \ \ 1 \leq h(\xi) \leq 2, \\ &V_\delta^\epsilon(\xi, 0) \leq -1 \ \ \textit{if} \ \ 0 \leq h(\xi) \leq 1. \end{aligned} \tag{7.9}$$

Proof. Let us first note that $\Upsilon \in C^2\big([0, \infty)\big)$, and it satisfies

$$\Upsilon'(s) = \begin{cases} 0 & (s \geq 2), \\ 3(s-2)^2 & (0 \leq s \leq 2), \end{cases} \quad \text{and} \quad \Upsilon''(s) = \begin{cases} 0 & (s \geq 2), \\ 6(s-2) & (0 \leq s \leq 2). \end{cases}$$

From this explicit expression it immediately follows that $\Upsilon' \geq 0$, $\Upsilon'' \leq 0$ and $\Upsilon \leq 0$, $|\Upsilon''| \leq 2\sqrt{3}\left(\Upsilon'\right)^{1/2}$, $|\Upsilon'|, |\Upsilon''| \leq 12$, for all $s > 0$. Besides if we call

$$v_\delta^\epsilon(\xi, t) = \Upsilon\Big(h(\xi) + t\epsilon\Big),$$

then

$$\begin{aligned} X_{i\delta} v_\delta^\epsilon(\xi, t) =& \Upsilon'(h(\xi) + \epsilon t) X_{i\delta} h, \\ (X_{i\delta} X_{j\delta}) v_\delta^\epsilon(\xi, t) =& \Upsilon'(h(\xi) + \epsilon t) X_{i\delta} X_{j\delta} h + \Upsilon''(h(\xi) + \epsilon t) X_{i\delta} h X_{j\delta} h. \end{aligned} \tag{7.10}$$

If so we see

$$\begin{aligned} \partial_t v_\delta^\epsilon - \sum_{i,j=1}^{3} &\left(\delta_{ij} - \frac{X_{i\delta} v_\delta^\epsilon X_{j\delta} v_\delta^\epsilon}{\epsilon^2 + |\nabla_\delta v_\delta^\epsilon|^2} \right) (X_{i\delta} X_{j\delta}) v_\delta^\epsilon = \\ &= \epsilon \Upsilon' - \sum_{i,j=1}^{3} \left(\delta_{ij} - \frac{(\Upsilon')^2 X_{i\delta} h X_{j\delta} h}{\epsilon^2 + (\Upsilon')^2 |\nabla_\delta h|^2} \right) (\Upsilon' X_{i\delta} X_{j\delta} h + \Upsilon'' X_{i\delta} h X_{j\delta} h) \\ &= \epsilon \Upsilon' - \left(1 - \frac{(\Upsilon')^2 X_1 h X_1 h}{\epsilon^2 + (\Upsilon')^2 |\nabla_\delta h|^2} \right) (\Upsilon' X_1 X_1 h + \Upsilon'' X_1 h X_1 h) \\ &\quad - \left(1 - \frac{(\Upsilon')^2 X_{3\delta} h X_{3\delta} h}{\epsilon^2 + (\Upsilon')^2 |\nabla_\delta h|^2} \right) (\Upsilon' X_{3\delta} X_{3\delta} h + \Upsilon'' X_{3\delta} h X_{3\delta} h) \\ &\quad + \frac{2(\Upsilon')^2 (X_1 h)^2 (X_{3\delta} h)^2 \Upsilon''}{\epsilon^2 + (\Upsilon')^2 |\nabla_\delta h|^2}, \end{aligned}$$

since $X_2 h = X_2 X_2 h = 0$ and $X_1 X_{3\delta} h = X_{3\delta} X_1 h = 0$. Using the fact that $\Upsilon'' \leq 0$, $\Upsilon' X_1 X_1 h \geq 0$, $\Upsilon' X_{3\delta} X_{3\delta} h \geq 0$ we obtain

$$\partial_t v_\delta^\epsilon - \sum_{i,j=1}^{3} \left(\delta_{ij} - \frac{X_{i\delta} v_\delta^\epsilon X_{j\delta} v_\delta^\epsilon}{\epsilon^2 + |\nabla_\delta v^\epsilon|^2} \right) (X_{i\delta} X_{j\delta}) v_\delta^\epsilon \leq \epsilon \Upsilon' - \frac{\epsilon^2 \Upsilon''(|X_1 h|^2 + |X_{3\delta} h|^2)}{\epsilon^2 + (\Upsilon')^2 |\nabla_\delta h|^2} \leq$$
$$\epsilon \Upsilon' + \frac{\epsilon^2 |\Upsilon''| \, |\nabla_\delta h|^2}{\epsilon^2 + (\Upsilon')^2 |\nabla_\delta h|^2} \leq \epsilon \Upsilon' + \frac{2\sqrt{3}\epsilon^2 |\Upsilon'|^{1/2} |\nabla_\delta h|^2}{\epsilon^2 + (\Upsilon')^2 |\nabla_\delta h|^2},$$

where we have used also the fact that $|\Upsilon''| \leq 2\sqrt{3} \left(\Upsilon'\right)^{1/2}$. We can assume here that $h(\xi) < 2$ (since otherwise the thesis is trivially true) and in this set $|\nabla_\delta h|^2 \leq 16$.

We have two cases. The first one is $\epsilon > \Upsilon'$ resulting in

$$\epsilon \Upsilon' + \frac{2\sqrt{3}\epsilon^2 |\Upsilon'|^{1/2} |\nabla_\delta h|^2}{\epsilon^2 + (\Upsilon')^2 |\nabla_\delta h|^2} \leq \epsilon \Upsilon' + \frac{2\sqrt{3}\, \epsilon^{5/2} |\nabla_\delta h|^2}{\epsilon^2} \leq \epsilon^{1/2} \Upsilon' + 32\sqrt{3}\epsilon^{1/2} \leq C\epsilon^{1/2},$$

where $C > 0$ is a fixed finite number.

In the second case where now $\epsilon < \Upsilon'$ we find the same estimate as

$$\epsilon \Upsilon' + \frac{2\sqrt{3}\epsilon^2 |\Upsilon'|^{1/2} |\nabla_\delta h|^2}{\epsilon^2 + (\Upsilon')^2 |\nabla_\delta h|^2} \leq \epsilon \Upsilon' + \frac{2\sqrt{3}\epsilon^2 (\Upsilon')^{1/2}}{(\Upsilon')^2} \leq \epsilon \Upsilon' + \frac{2\sqrt{3}\epsilon^2}{(\Upsilon')^{3/2}}$$
$$\leq \epsilon \Upsilon' + \frac{2\sqrt{3}\epsilon^2}{\epsilon^{3/2}} \leq \epsilon^{1/2} \Upsilon' + 2\sqrt{3}\epsilon^{1/2} \leq C\epsilon^{1/2}.$$

Choosing C in this way in the definition of v_δ^ϵ, we immediately deduce that V_δ^ϵ satisfies

$$\partial_t V_\delta^\epsilon - \sum_{i,j=1}^{3} \left(\delta_{ij} - \frac{X_{i\delta} V_\delta^\epsilon X_{j\delta} V_\delta^\epsilon}{\epsilon^2 + |\nabla_\delta V_\delta^\epsilon|^2} \right) (X_{i\delta} X_{j\delta}) V_\delta^\epsilon \leq 0,$$

and at the initial time $t = 0$

$$\begin{aligned} &V_\delta^\epsilon(\xi, 0) = 0 && \text{if} \quad h(\xi) \geq 2, \\ &-1 \leq V_\delta^\epsilon(\xi, 0) \leq 0 && \text{if} \quad 1 \leq h(\xi) \leq 2, \\ &V_\delta^\epsilon(\xi, 0) \leq -1 && \text{if} \quad 0 \leq h(\xi) \leq 1. \end{aligned}$$

□

Now we can provide the proof of Theorem 7.5.

Proof. By Lemma 7.1 we know that there exists a function V_δ^ϵ which satisfies

$$\partial_t V_\delta^\epsilon - \sum_{i,j=1}^{3} \left(\delta_{ij} - \frac{X_{i\delta} V_\delta^\epsilon X_{j\delta} V_\delta^\epsilon}{\epsilon^2 + |\nabla_\delta V_\delta^\epsilon|^2} \right) (X_{i\delta} X_{j\delta}) V_\delta^\epsilon \leq 0,$$

and the conditions given in (7.9) at the initial time $t = 0$. Up to a rescaling we can assume that $|u_0| \leq 1$, and $u_0 = 0$ where $x^2 + y^2 \geq 1$. Hence the conditions in (7.9) imply that $V_\delta^\epsilon(\xi, 0) \leq u_0(\xi)$ for all $\xi \in \mathrm{SE}(2)$. Applying the comparison principle to vanishing viscosity solutions obtained from regularized mean curvature equation we deduce that $V_\delta^\epsilon \leq u_\delta^\epsilon$ in $\mathrm{SE}(2) \times [0, \infty)$ for each $0 < \delta, \epsilon < 1$. This result implies

$$\lim_{\epsilon \to 0} V^\epsilon = \Upsilon\Big(\frac{|x|^2 + |y|^2}{2}\Big) = 0 \leq u(\xi, t), \tag{7.11}$$

for all $t \geq 0$ and $\xi = (x, y, \theta) \in \mathrm{SE}(2)$ satisfying $(|x|^2 + |y|^2)/2 \geq 2$. Hence $u \geq 0$ if $(|x|^2 + |y|^2)/2 \geq 2$. Arguing in the same way with the function $\tilde{V}_\delta^\epsilon = -V_\delta^\epsilon$, we deduce

$$u \leq 0 \quad \text{if} \quad (|x|^2 + |y|^2)/2 \geq 2. \tag{7.12}$$

Hence (7.11) and (7.12) give $u(\xi, t) = 0$ for all $t \in [0, T]$ and $\xi = (x, y, \theta)$ such that $(|x|^2 + |y|^2)/2 \geq 2$. □

7.3.2 Asymptotic behavior of the approximating solutions

Here we prove that the solutions of problem (7.5), which are obtained as limits of the solutions of problem (7.4), exponentially tend to a constant value.

Theorem 7.6. *Let G be either a Carnot group of step 2 or SE(2), and let u_δ^ϵ be the solution of problem (7.5), obtained as the limit of the solution of problem (7.4). For each $0 < \delta, \epsilon < 1$ there exist some finite numbers $B, b > 0$ independent of ϵ and δ such that*

$$\big|1 - u_\delta^\epsilon(\xi, t)\big| \leq B e^{-b|\xi|} \quad \textit{for all } \xi \in G \times [0, T],$$

where T is a positive finite number denoting the final time and $|\xi|$ is defined in (7.8).

Proof. The proof is based on comparing the function $1 - u_\delta^\epsilon$ with the auxiliary function

$$v_\delta^\epsilon(\xi, t) = \Upsilon(h(\xi)) \quad \text{where} \quad \Upsilon(s) = \hat{c}\mathrm{e}^{-\sigma(2T - \alpha t)s},$$

with $0 < \alpha < 1$, $0 < \sigma < \infty$ and constant $\hat{c} = 2\mathrm{e}^{4\sigma T}$. The function h will be a polynomial, and we will need to perform different choices of this function for the first and the second layer of the Carnot group and for the SE(2) group. As before we assume that

$$|u_0| \leq 1 \text{ on } G, \quad u_0 = 0 \quad \text{for all} \quad |\xi| \geq 1. \tag{7.13}$$

Now we proceed by using a procedure similar to the one in the proof of [13, Theorem 5.1], and we show that both in Carnot groups of step 2 and in SE(2) we have

$$\partial_t v_\delta^\epsilon - \sum_{i,j=1}^{n} \left(\delta_{ij} - \frac{X_{i\delta} v_\delta^\epsilon X_{j\delta} v_\delta^\epsilon}{\epsilon^2 + |\nabla_\delta v_\delta^\epsilon|^2} \right) (X_{i\delta} X_{j\delta}) v_\delta^\epsilon \geq 0. \tag{7.14}$$

In a Carnot group of step 2 we will consider a function $h(\xi) = |x|^2 + \sum_{s=1}^{n-m} \sqrt{1+\theta_s^2}$ where x denotes the horizontal and θ the vertical variables. Furthermore we will express the horizontal vector fields X_i by using (7.1) and the approximating vertical vector fields $X_{i\delta}$ by using (7.2). In this case we write all the vector fields as:

$$X_j h = 2x_j + \sum_{k,s} f_{jk}^{(s)} x_k \frac{\theta_s}{\sqrt{1+\theta_s^2}}, \quad j = 1, \dots, m,$$

$$X_i X_j h = 2\delta_{ij} + \sum_s f_{ji}^{(s)} \frac{\theta_s}{\sqrt{1+\theta_s^2}} + \sum_{p,k,s} f_{ip}^{(s)} f_{jk}^{(s)} \frac{x_k x_p}{(1+\theta_s^2)^{3/2}}, \quad i,j = 1, \dots, m,$$

$$X_{j\delta} h = \frac{\delta \theta_{j-m}}{\sqrt{1+\theta_{j-m}^2}}, \quad j = m+1, \dots, n,$$

$$X_{i\delta} X_{j\delta} h = \frac{\delta_{ij}\delta^2}{(1+\theta_{j-m}^2)^{3/2}}, \quad i,j = m+1, \dots, n,$$

$$X_{i\delta} X_j h = \frac{\delta}{(1+\theta_{i-m}^2)^{3/2}} \sum_k f_{jk}^{(i)} x_k = X_j X_{i\delta} h, \quad i = m+1, \dots, n, \quad j = 1, \dots, m.$$

We use the derivatives of v_δ^ϵ computed in (7.10) and the fact that $X_i X_{j\delta} h = X_{j\delta} X_i h$, then we write the curvature operator on the function v_δ^ϵ as:

$$\begin{aligned}
&\partial_t v_\delta^\epsilon - \sum_{i,j=1}^{n} \left(\delta_{ij} - \frac{X_{i\delta} v_\delta^\epsilon X_{j\delta} v_\delta^\epsilon}{\epsilon^2 + |\nabla_\delta v_\delta^\epsilon|^2} \right) (X_{i\delta} X_{j\delta}) v_\delta^\epsilon \\
&= \partial_t v_\delta^\epsilon - \sum_{i,j=1}^{m} \left(\delta_{ij} - \frac{(\Upsilon')^2 X_i h X_j h}{\epsilon^2 + (\Upsilon')^2 |\nabla_\delta h|^2} \right) (\Upsilon' X_i X_j h + \Upsilon'' X_i h X_j h) \\
&\quad - 2 \sum_{i=1}^{m} \sum_{j=m+1}^{n} \left(- \frac{(\Upsilon')^2 X_i h X_{j\delta} h}{\epsilon^2 + (\Upsilon')^2 |\nabla_\delta h|^2} \right) (\Upsilon' X_i X_{j\delta} h + \Upsilon'' X_i h X_{j\delta} h) \\
&\quad - \sum_{i,j=m+1}^{n} \left(\delta_{ij} - \frac{(\Upsilon')^2 X_{i\delta} h X_{j\delta} h}{\epsilon^2 + (\Upsilon')^2 |\nabla_\delta h|^2} \right) (\Upsilon' X_{i\delta} X_{j\delta} h + \Upsilon'' X_{i\delta} h X_{j\delta} h) \\
&= \partial_t v_\delta^\epsilon - Q_1 - Q_2 - Q_3.
\end{aligned}$$

Let us first consider Q_1. Due to the symmetry of $\delta_{ij} - \frac{(\Upsilon')^2 X_i h X_j h}{\epsilon^2 + (\Upsilon')^2 |\nabla_\delta h|^2}$ and the anti-symmetry of $f_{ji}^{(s)}$ we deduce that

$$\sum_{i,j=1}^{m} \left(\delta_{ij} - \frac{(\Upsilon')^2 X_i h X_j h}{\epsilon^2 + (\Upsilon')^2 |\nabla_\delta h|^2} \right) \Upsilon' \Big(2\delta_{ij} + \sum_s f_{ji}^{(s)} \frac{\theta_s}{\sqrt{1+\theta_s^2}} + \sum_{p,k,s} f_{ip}^{(s)} f_{jk}^{(s)} \frac{x_k x_p}{(1+\theta_s^2)^{3/2}} \Big) =$$

$$= \Upsilon' \sum_{i,j=1}^{m} \left(\delta_{ij} - \frac{(\Upsilon')^2 X_i h X_j h}{\epsilon^2 + (\Upsilon')^2 |\nabla_\delta h|^2} \right) \left(2\delta_{ij} + \sum_{p,k,s} f_{ip}^{(s)} f_{jk}^{(s)} \frac{x_k x_p}{(1+\theta_s^2)^{3/2}} \right) \leq 0,$$

since $\Upsilon' < 0$ and the matrix of coefficients of the equation is positive semidefinite. On the other hand we see by using $\Upsilon'' > 0$ that

$$\sum_{i=1}^{m} \left(\delta_{ij} - \frac{(\Upsilon')^2 (X_i h)^2}{\epsilon^2 + (\Upsilon')^2 |\nabla_\delta h|^2} \right) \Upsilon'' X_i h X_j h = \sum_{\substack{i,j=1 \\ i \neq j}}^{m} \left(- \frac{(\Upsilon')^2 X_i h X_j h}{\epsilon^2 + (\Upsilon')^2 |\nabla_\delta h|^2} \right) \Upsilon'' X_i h X_j h$$

$$+ \sum_{i=1}^{m} \left(1 - \frac{(\Upsilon')^2 (X_i h)^2}{\epsilon^2 + (\Upsilon')^2 |\nabla_\delta h|^2} \right) \Upsilon'' (X_i h)^2$$

$$\leq \sum_{i=1}^{m} \left| 1 - \frac{(\Upsilon')^2 (X_i h)^2}{\epsilon^2 + (\Upsilon')^2 |\nabla_\delta h|^2} \right| \Upsilon'' (X_i h)^2 \leq \Upsilon'' \sum_{i=1}^{m} |X_i h|^2 \leq Z_1 \Upsilon'' |x|^2.$$

Therefore

$$Q_1 \leq Z_1 \Upsilon'' |x|^2 \leq Z_1 \sigma^2 (2T - \alpha t)^2 \Upsilon |x|^2,$$

where $Z_1 > 0$ is a fixed finite number.

We continue with Q_2 and thanks to the antisymmetry of $f_{ik}^{(j)}$ we find that

$$Q_2 \leq 2 \sum_{i=1}^{m} \sum_{j=m+1}^{m} \left| \frac{(\Upsilon')^2 X_i h X_{j\delta} h}{\epsilon^2 + (\Upsilon')^2 |\nabla_\delta h|^2} \right| |\Upsilon' X_i X_{j\delta} h| \leq \sum_{j=m+1}^{n} \sum_{i=1}^{m} |\Upsilon' X_i X_{j\delta} h|$$

$$\leq 2 \sum_{i=1}^{m} \sum_{j=m+1}^{n} |\Upsilon'| \, | \frac{\delta}{(1+\theta_{j-m}^2)^{3/2}} \sum_k f_{ik}^{(j)} x_k | \leq 2\delta |x| |\Upsilon'| \leq \delta (|x|^2 + 1) \sigma \alpha \Upsilon.$$

Finally we consider Q_3. Note that

$$Q_3 \leq \left| \sum_{i=m+1}^{n} \left(\delta_{ii} - \frac{(\Upsilon')^2 (X_{i\delta} h)^2}{\epsilon^2 + (\Upsilon')^2 |\nabla_\delta h|^2} \right) \Upsilon'' (X_{i\delta} h)^2 - \sum_{\substack{i,j=m+1 \\ i \neq j}}^{n} \left(\frac{(\Upsilon')^2 (X_{i\delta} h)^2 (X_{j\delta} h)^2}{\epsilon^2 + (\Upsilon')^2 |\nabla_\delta h|^2} \right) \Upsilon'' \right|$$

$$\leq \left| \sum_{i=m+1}^{n} \left(\delta_{ii} - \frac{(\Upsilon')^2 (X_{i\delta} h)^2}{\epsilon^2 + (\Upsilon')^2 |\nabla_\delta h|^2} \right) \Upsilon'' (X_{i\delta} h)^2 \right| \leq \sum_{i=m+1}^{n} \Upsilon'' \frac{\delta^2 \theta_{i-m}^2}{1 + \theta_{i-m}^2} \leq Z_3 \sigma^2 (2T - \alpha t)^2 \Upsilon,$$

where $Z_3 > 0$ is a fixed finite number.

As a consequence

$$\partial_t v^\epsilon - Q_1 - Q_2 - Q_3 \geq$$

$$\geq \sigma \alpha \Upsilon (|x|^2 + 1) - Z_1 \sigma^2 (2T - \alpha t)^2 \Upsilon |x|^2 - \delta (|x|^2 + 1) \sigma \alpha \Upsilon - Z_3 \sigma^2 (2T - \alpha t)^2 \Upsilon \geq 0,$$

if σ and δ are small.

We choose for the SE(2) setting $h(\xi) = \frac{x^2+y^2}{2}$. Then by using $X_2 h = 0$, $\Upsilon' X_1 X_1 h < 0$, $\Upsilon' X_{3\delta} X_{3\delta} h < 0$ and $\Upsilon'' > 0$ we obtain

$$\begin{aligned}\partial_t v_\delta^\epsilon - \sum_{i,j=1}^{3} \left(\delta_{ij} - \frac{X_{i\delta} v_\delta^\epsilon X_{j\delta} v_\delta^\epsilon}{\epsilon^2 + |\nabla_\delta v_\delta^\epsilon|^2} \right) (X_{i\delta} X_{j\delta}) v_\delta^\epsilon \geq & \partial_t v_\delta^\epsilon - \sum_{i=1}^{3} \frac{\epsilon^2}{\epsilon^2 + (\Upsilon')^2 |\nabla_\delta h|^2} \Upsilon''(X_{i\delta} h)^2 \\ \geq & \sigma\alpha\Upsilon|x|^2,\end{aligned}$$

and we conclude as before that (7.14) is satisfied. Note that

$$\partial_t (1 - u_\delta^\epsilon) - \sum_{i,j=1}^{3} \left(\delta_{ij} - \frac{X_{i\delta}(1-u_\delta^\epsilon) X_{j\delta}(1-u_\delta^\epsilon)}{\epsilon^2 + |\nabla_\delta (1-u_\delta^\epsilon)|^2} \right) (X_{i\delta} X_{j\delta})(1 - u_\delta^\epsilon) = 0.$$

Recall that $0 \leq |1 - u_0| \leq 2$ due to (7.13). Hence, applying the comparison principle for vanishing viscosity solutions to the functions $1 - u_\delta^\epsilon$ (as well as $u_\delta^\epsilon - 1$) and v_δ^ϵ we find

$$|1 - u_\delta^\epsilon| \leq v_\delta^\epsilon \quad \text{in } G \times [0, T].$$

The proof is complete. □

7.4 Viscosity and vanishing viscosity solutions

In this section we prove Theorem 7.1 which says that any viscosity solution is a limit of a family of special vanishing viscosity solutions obtained with the procedure of [47]. We provide the proof in the Heisenberg group explicitly and give some explanations related to the generalization of the proof to the Carnot groups of step 2. We will denote the corresponding group by G. Note that in the case of the Heisenberg group, $m = 2$ and $n = 3$ while they can be higher in a general Carnot group setting.

We choose a parameter γ such that

$$\gamma > 2, \tag{7.15}$$

which is to be fixed later.

We use the approximating Riemannian setting with the vector fields

$$X_1 = \partial_x + y\partial_\theta, \quad X_2 = \partial_y - x\partial_\theta, \quad X_{3\delta} = \delta\partial_\theta,$$

with $0 < \delta < \epsilon < 1$.

For any two points $\xi = (x_\xi, y_\xi, \theta_\xi)$, $\eta = (x_\eta, y_\eta, \theta_\eta) \in \mathbb{R}^3$ in the Heisenberg group G we will denote

$$e_1 = x_\xi - x_\eta, \quad e_2 = y_\xi - y_\eta, \quad e_3 = \theta_\xi - \theta_\eta - (x_\xi y_\eta - y_\xi x_\eta).$$

Furthermore we denote the vector fields which take the derivatives with respect to ξ and η by

$$\begin{aligned} X_1^\xi &= \partial_{x_\xi} + y_\xi \partial_{\theta_\xi}, \quad X_2^\xi = \partial_{y_\xi} - x_\xi \partial_{\theta_\xi}, \quad X_{3\delta}^\xi = \delta\partial_{\theta_\xi}, \\ X_1^\eta &= \partial_{x_\eta} + y_\eta \partial_{\theta_\eta}, \quad X_2^\eta = \partial_{y_\eta} - x_\eta \partial_{\theta_\eta}, \quad X_{3\delta}^\eta = \delta\partial_{\theta_\eta}. \end{aligned}$$

Then we define

$$d_0(\xi,\eta)=\left(e_1^2+e_2^2\right)^{1/2},\quad d_\beta(\xi,\eta)=\left(e_1^2+e_2^2+\beta^2e_3^2\right)^{1/2},\quad d_3(\xi,\eta)=|\beta e_3|, \tag{7.16}$$

where $\beta>0$ will be chosen in such a way that $\beta=\delta$.

Besides we introduce the function

$$\phi(\xi,\eta,t)=\frac{\mu}{\gamma}\epsilon^{1-\frac{\gamma}{2}}d_\beta^\gamma(\xi,\eta)+\frac{Mt}{2T}\epsilon^\alpha,$$

where $\alpha>0$ is a parameter to be fixed in the sequel.

If u and u_δ^ϵ are the solutions of (7.3) and (7.5), respectively (note that u is continuous while u_δ^ϵ is smooth), with the same initial condition $u(\xi,0)=u_\delta^\epsilon(\xi,0)$, we write our test function as follows:

$$\omega(\xi,\eta,t)=u(\xi,t)-u_\delta^\epsilon(\eta,t)-\phi(\xi,\eta,t), \tag{7.17}$$

with suitable constants $M\geq 0$ and $0<\delta<\epsilon<1$ where δ to be fixed later. Furthermore

$$\mu=\frac{\gamma 4^\gamma \mathrm{Lip}(u_0)^\gamma}{M^{\gamma-1}}, \tag{7.18}$$

where $\mathrm{Lip}(u_0)$ denotes the Lipschitz constant of u_0 with respect to d_β.

Lemma 7.2. *Let u and u_δ^ϵ be continuous functions such that $u(\xi,0)=u_\delta^\epsilon(\xi,0)$, for every $\xi\in G$. Let d_β be the distance defined in* (7.16) *and ω be the test function defined in* (7.17)*. Assume that*

- *There exist constants B_ϵ, b_ϵ $R_\epsilon>0$ such that for every $|\xi|>R_\epsilon$*

$$|1-u(\xi,t)|\leq B_\epsilon e^{-b_\epsilon|\xi|^2},\quad |1-u_\delta^\epsilon(\xi,t)|\leq B_\epsilon e^{-b_\epsilon|\xi|^2},$$

- *There exists a constant $\tilde{C}>0$, such that for every $\xi\in G$, $t>0$*

$$|u(\xi,t)|\leq\tilde{C},\qquad |u_\delta^\epsilon(\xi,t)|\leq\tilde{C}.$$

- $$\sup_{\xi\in G,0\leq t\leq T}(u-u_\delta^\epsilon)(\xi,t)>M\epsilon^\alpha. \tag{7.19}$$

Then

$$\sup_{\substack{\xi,\eta\in G,\\ 0\leq t\leq T}}\omega(\xi,\eta,t)=\sup_{\substack{d_\beta(\xi,\eta)\leq r,\ |\xi|,|\eta|\leq R_\epsilon\\ 0\leq t\leq T}}\omega(\xi,\eta,t)$$

where $r:=\left(\frac{2\gamma\tilde{C}}{\mu}\epsilon^{\frac{\gamma}{2}-1}-\frac{M\gamma}{4\mu}\epsilon^{\alpha+\frac{\gamma}{2}-1}\right)^{\frac{1}{\gamma}}$ *and* $\tilde{R}_\epsilon:=r+\sqrt{\frac{4B_\epsilon}{Mb_\epsilon}\epsilon^{-\alpha}}$.

Proof. We first show that the supremum on the whole space is equal to the supremum under the condition that $d_\beta(\xi,\eta) \le r$. Indeed using (7.17) and (7.19) we observe

$$\sup_{\substack{\xi,\eta\in G,\\ 0\le t\le T}} \omega(\xi,\eta,t) \ge M\epsilon^\alpha - \frac{M}{2T}\epsilon^\alpha T = \frac{M}{2}\epsilon^\alpha. \tag{7.20}$$

Note that when $d_\beta(\xi,\eta) \ge r$ we have

$$\begin{aligned}\omega(\xi,\eta,t) \le& \sup_{\xi\in G,\,0\le t\le T} u(\xi,t) + \sup_{\eta\in G,\,0\le t\le T}\Big(-u_\delta^\epsilon(\eta,t)\Big) - \frac{\mu}{\gamma}\epsilon^{1-\frac{\gamma}{2}} d_\beta(\xi,\eta)^\gamma\\ \le& 2\tilde{C} - \frac{\mu}{\gamma}\epsilon^{1-\frac{\gamma}{2}} d_\beta(\xi,\eta)^\gamma \le \frac{M}{4}\epsilon^\alpha,\end{aligned}$$

due to the choice of r. Consequently we deduce that

$$\sup_{\substack{\xi,\eta,\in G,\\ 0\le t\le T}} \omega(\xi,\eta,t) = \sup_{\substack{\xi,\,\eta\,\in\, G,\ d_\beta(\xi,\eta)\,\le\, r,\\ 0\le t\le T}} \omega(\xi,\eta,t).$$

Now we show that the supremum is not achieved in a neighborhood of infinity. Indeed for $|\eta| \ge \tilde{R}_\epsilon$, we see by the first assumption that

$$|1 - u_\delta^\epsilon(\eta,t)| \le B_\epsilon \mathrm{e}^{-b_\epsilon|\eta|^2} \le \frac{B_\epsilon}{b_\epsilon|\eta|^2} \le \frac{M}{8}\epsilon^\alpha.$$

Analogously

$$|1 - u(\xi,t)| \le \frac{M}{8}\epsilon^\alpha,$$

for $|\xi| \ge \tilde{R}_\epsilon$. If $|\eta|$, $|\xi| \ge \tilde{R}_\epsilon$, then it follows that

$$\omega(\xi,\eta,t) \le \big|1 - u(\xi,t)\big| + \big|1 - u_\delta^\epsilon(\eta,t)\big| \le \frac{M}{4}\epsilon^\alpha.$$

Therefore we deduce

$$\sup_{\substack{\xi,\eta\in G,\\ 0\le t\le T}} \omega(\xi,\eta,t) = \sup_{\substack{\xi,\,\eta\,\in\, G,\\ |\xi|\le\tilde{R}_\epsilon,\,0\le t\le T}} \omega(\xi,\eta,t),$$

We will denote the point where ω is maximum by $(\hat{\xi},\hat{\eta},\hat{t})$.

Finally we see that $\hat{t} > 0$ must hold. Observe for $t = 0$ that

$$\begin{aligned}\omega(\xi,\eta,0) &= u_0(\xi) - u_0(\eta) - \frac{\mu}{\gamma}\epsilon^{1-\frac{\gamma}{2}} d_\beta(\xi,\eta)^\gamma\\ &\le d_\beta(\xi,\eta)\Big(\mathrm{Lip}(u_0) - \frac{\mu}{\gamma}\epsilon^{1-\frac{\gamma}{2}} d_\beta(\xi,\eta)^{\gamma-1}\Big).\end{aligned} \tag{7.21}$$

Consider the first case with $d_\beta(\xi,\eta) \leq \frac{1}{4\,\mathrm{Lip}(u_0)} M\epsilon^\alpha$. Then from (7.21) we deduce

$$\omega(\xi,\eta,0) \leq \frac{M}{4}\epsilon^\alpha,$$

which together with (7.19) ensures that the maximum is not achieved at $t = 0$.

Now consider the second case where $d_\beta(\xi,\eta) > \frac{1}{4\mathrm{Lip}(u_0)} M\epsilon^\alpha$. Then we observe that (7.18) and (7.21) give

$$\omega(\xi,\eta,0) \leq d_\beta(\xi,\eta)\Big(\mathrm{Lip}(u_0) - \frac{\mu}{\gamma}\epsilon^{1-\frac{\gamma}{2}} d_\beta(\xi,\eta)^{\gamma-1}\Big) \leq 0,$$

which contradicts (7.20) and ensures that $\hat{t} > 0$. □

We will need the following remarks for the proof of Theorem 7.1.

Remark 7.1.

$$\begin{aligned} X_1^\xi e_1 = 1, \quad X_1^\xi e_2 = 0, \quad X_1^\xi e_3 = e_2,\\ X_2^\xi e_1 = 0, \quad X_2^\xi e_2 = 1, \quad X_2^\xi e_3 = -e_1,\\ X_{3\delta}^\xi e_1 = 0, \quad X_{3\delta}^\xi e_2 = 0, \quad X_{3\delta}^\xi e_3 = \delta, \end{aligned}$$

$$\begin{aligned} X_1^\eta e_1 = -1, \quad X_1^\eta e_2 = 0, \quad X_1^\eta e_3 = e_2,\\ X_2^\eta e_1 = 0, \quad X_2^\eta e_2 = -1, \quad X_2^\eta e_3 = -e_1,\\ X_{3\delta}^\eta e_1 = 0, \quad X_{3\delta}^\eta e_2 = 0, \quad X_{3\delta}^\eta e_3 = -\delta. \end{aligned}$$

Remark 7.2.

$$X_1^\xi \phi(\xi,\eta) = \mu\epsilon^{1-\frac{\gamma}{2}} d_\beta^{\gamma-2}(\xi,\eta)\Big(e_1 + \beta^2 e_3 e_2\Big),$$

$$X_2^\xi \phi(\xi,\eta) = \mu\epsilon^{1-\frac{\gamma}{2}} d_\beta^{\gamma-2}(\xi,\eta)\Big(e_2 - \beta^2 e_3 e_1\Big),$$

$$X_{3\delta}^\xi \phi(\xi,\eta) = \mu\epsilon^{1-\frac{\gamma}{2}} d_\beta^{\gamma-2}(\xi,\eta)\delta\beta^2 e_3,$$

$$X_1^\eta \phi(\xi,\eta) = \mu\epsilon^{1-\frac{\gamma}{2}} d_\beta^{\gamma-2}(\xi,\eta)\Big(-e_1 + \beta^2 e_3 e_2\Big),$$

$$X_2^\eta \phi(\xi,\eta) = \mu\epsilon^{1-\frac{\gamma}{2}} d_\beta^{\gamma-2}(\xi,\eta)\Big(-e_2 - \beta^2 e_3 e_1\Big),$$

$$X_{3\delta}^\eta \phi(\xi,\eta) = -\mu\epsilon^{1-\frac{\gamma}{2}} d_\beta^{\gamma-2}(\xi,\eta)\delta\beta^2 e_3.$$

Remark 7.3.

$$X_1^\xi X_1^\xi \phi(\xi,\eta) = (\gamma-2)\mu\epsilon^{1-\frac{\gamma}{2}} d_\beta^{\gamma-4}(\xi,\eta)\Big(e_1+\beta^2 e_3 e_2\Big)^2 + \mu\epsilon^{1-\frac{\gamma}{2}} d_\beta^{\gamma-2}(\xi,\eta)\Big(1+\beta^2 e_2^2\Big),$$

$$\begin{aligned} X_1^\xi X_2^\xi \phi(\xi,\eta) = {} & (\gamma-2)\mu\epsilon^{1-\frac{\gamma}{2}} d_\beta^{\gamma-4}(\xi,\eta)\Big(e_2-\beta^2 e_3 e_1\Big)\Big(e_1+\beta^2 e_3 e_2\Big) \\ & -\mu\epsilon^{1-\frac{\gamma}{2}} d_\beta^{\gamma-2}(\xi,\eta)\beta^2\Big(e_2 e_1+e_3\Big), \end{aligned}$$

$$X_1^\xi X_{3\delta}^\xi \phi(\xi,\eta) = (\gamma-2)\mu\epsilon^{1-\frac{\gamma}{2}} d_\beta^{\gamma-4}(\xi,\eta)\Big(\delta\beta^2 e_3\Big)\Big(e_1+\beta^2 e_3 e_2\Big) + \mu\epsilon^{1-\frac{\gamma}{2}} d_\beta^{\gamma-2}(\xi,\eta)\delta\beta^2 e_2,$$

$$\begin{aligned} X_2^\xi X_1^\xi \phi(\xi,\eta) = {} & (\gamma-2)\mu\epsilon^{1-\frac{\gamma}{2}} d_\beta^{\gamma-4}(\xi,\eta)\Big(e_1+\beta^2 e_3 e_2\Big)\Big(e_2-\beta^2 e_3 e_1\Big) \\ & +\mu\epsilon^{1-\frac{\gamma}{2}} d_\beta^{\gamma-2}(\xi,\eta)\Big(-\beta^2 e_1 e_2+\beta^2 e_3\Big), \end{aligned}$$

$$X_2^\xi X_2^\xi \phi(\xi,\eta) = (\gamma-2)\mu\epsilon^{1-\frac{\gamma}{2}} d_\beta^{\gamma-4}(\xi,\eta)\Big(e_2-\beta^2 e_3 e_1\Big)^2 + \mu\epsilon^{1-\frac{\gamma}{2}} d_\beta^{\gamma-2}(\xi,\eta)\Big(1+\beta^2 e_1^2\Big),$$

$$X_2^\xi X_{3\delta}^\xi \phi(\xi,\eta) = (\gamma-2)\mu\epsilon^{1-\frac{\gamma}{2}} d_\beta^{\gamma-4}(\xi,\eta)\delta\beta^2 e_3\Big(e_2-\beta^2 e_3 e_1\Big) - \mu\epsilon^{1-\frac{\gamma}{2}} d_\beta^{\gamma-2}(\xi,\eta)\delta\beta^2 e_1,$$

$$X_{3\delta}^\xi X_1^\xi \phi(\xi,\eta) = (\gamma-2)\mu\epsilon^{1-\frac{\gamma}{2}} d_\beta^{\gamma-4}(\xi,\eta)\delta\beta^2 e_3\Big(e_1+\beta^2 e_3 e_2\Big) + \mu\epsilon^{1-\frac{\gamma}{2}} d_\beta^{\gamma-2}(\xi,\eta)\beta^2\delta e_2,$$

$$X_{3\delta}^\xi X_2^\xi \phi(\xi,\eta) = (\gamma-2)\mu\epsilon^{1-\frac{\gamma}{2}} d_\beta^{\gamma-4}(\xi,\eta)\delta\beta^2 e_3\Big(e_2-\beta^2 e_3 e_1\Big) - \mu\epsilon^{1-\frac{\gamma}{2}} d_\beta^{\gamma-2}(\xi,\eta)\beta^2\delta e_1,$$

$$X_{3\delta}^\xi X_{3\delta}^\xi \phi(\xi,\eta) = (\gamma-2)\mu\epsilon^{1-\frac{\gamma}{2}} d_\beta^{\gamma-4}(\xi,\eta)(\delta\beta^2 e_3)^2 + \mu\epsilon^{1-\frac{\gamma}{2}} d_\beta^{\gamma-2}(\xi,\eta)(\delta\beta)^2.$$

Remark 7.4.

$$X_1^\eta X_1^\eta \phi(\xi,\eta) = (\gamma-2)\mu\epsilon^{1-\frac{\gamma}{2}} d_\beta^{\gamma-4}(\xi,\eta)\Big(-e_1+\beta^2 e_3 e_2\Big)^2 + \mu\epsilon^{1-\frac{\gamma}{2}} d_\beta^{\gamma-2}(\xi,\eta)\Big(1+\beta^2 e_2^2\Big),$$

$$\begin{aligned} X_1^\eta X_2^\eta \phi(\xi,\eta) = {} & (\gamma-2)\mu\epsilon^{1-\frac{\gamma}{2}} d_\beta^{\gamma-4}(\xi,\eta)\Big(-e_2-\beta^2 e_3 e_1\Big)\Big(-e_1+\beta^2 e_3 e_2\Big) \\ & -\mu\epsilon^{1-\frac{\gamma}{2}} d_\beta^{\gamma-2}(\xi,\eta)\beta^2\Big(e_2 e_1-e_3\Big), \end{aligned}$$

$$X_1^\eta X_{3\delta}^\eta \phi(\xi,\eta) = -(\gamma-2)\mu\epsilon^{1-\frac{\gamma}{2}} d_\beta^{\gamma-4}(\xi,\eta)\Big(\delta\beta^2 e_3\Big)\Big(-e_1+\beta^2 e_3 e_2\Big) - \mu\epsilon^{1-\frac{\gamma}{2}} d_\beta^{\gamma-2}(\xi,\eta)\delta\beta^2 e_2,$$

$$X_2^\eta X_1^\eta \phi(\xi,\eta) = (\gamma-2)\mu\epsilon^{1-\frac{\gamma}{2}} d_\beta^{\gamma-4}(\xi,\eta)\Big(-e_1+\beta^2 e_3 e_2\Big)\Big(-e_2-\beta^2 e_3 e_1\Big) + \mu\epsilon^{1-\frac{\gamma}{2}} d_\beta^{\gamma-2}(\xi,\eta)\Big(-\beta^2 e_1 e_2 - \beta^2 e_3\Big),$$

$$X_2^\eta X_2^\eta \phi(\xi,\eta) = (\gamma-2)\mu\epsilon^{1-\frac{\gamma}{2}} d_\beta^{\gamma-4}(\xi,\eta)\Big(-e_2-\beta^2 e_3 e_1\Big)^2 + \mu\epsilon^{1-\frac{\gamma}{2}} d_\beta^{\gamma-2}(\xi,\eta)\Big(1+\beta^2 e_1^2\Big),$$

$$X_2^\eta X_{3\delta}^\eta \phi(\xi,\eta) = -(\gamma-2)\mu\epsilon^{1-\frac{\gamma}{2}} d_\beta^{\gamma-4}(\xi,\eta)\delta\beta^2 e_3\Big(-e_2-\beta^2 e_3 e_1\Big) + \mu\epsilon^{1-\frac{\gamma}{2}} d_\beta^{\gamma-2}(\xi,\eta)\delta\beta^2 e_1,$$

$$X_{3\delta}^\eta X_1^\eta \phi(\xi,\eta) = -(\gamma-2)\mu\epsilon^{1-\frac{\gamma}{2}} d_\beta^{\gamma-4}(\xi,\eta)\delta\beta^2 e_3\Big(-e_1+\beta^2 e_3 e_2\Big) - \mu\epsilon^{1-\frac{\gamma}{2}} d_\beta^{\gamma-2}(\xi,\eta)\beta^2\delta e_2,$$

$$X_{3\delta}^\eta X_2^\eta \phi(\xi,\eta) = -(\gamma-2)\mu\epsilon^{1-\frac{\gamma}{2}} d_\beta^{\gamma-4}(\xi,\eta)\delta\beta^2 e_3\Big(-e_2-\beta^2 e_3 e_1\Big) + \mu\epsilon^{1-\frac{\gamma}{2}} d_\beta^{\gamma-2}(\xi,\eta)\beta^2\delta e_1,$$

$$X_{3\delta}^\eta X_{3\delta}^\eta \phi(\xi,\eta) = (\gamma-2)\mu\epsilon^{1-\frac{\gamma}{2}} d_\beta^{\gamma-4}(\xi,\eta)(\delta\beta^2 e_3)^2 + \mu\epsilon^{1-\frac{\gamma}{2}} d_\beta^{\gamma-2}(\xi,\eta)(\delta\beta)^2.$$

Remark 7.5.

$$X_1^\xi X_1^\eta \phi(\xi,\eta) = (\gamma-2)\mu\epsilon^{1-\frac{\gamma}{2}} d_\beta^{\gamma-4}(\xi,\eta)\Big(-e_1+\beta^2 e_3 e_2\Big)\Big(e_1+\beta^2 e_3 e_2\Big) + \mu\epsilon^{1-\frac{\gamma}{2}} d_\beta^{\gamma-2}(\xi,\eta)\Big(-1+\beta^2 e_2^2\Big),$$

$$X_1^\xi X_2^\eta \phi(\xi,\eta) = (\gamma-2)\mu\epsilon^{1-\frac{\gamma}{2}} d_\beta^{\gamma-4}(\xi,\eta)\Big(e_1+\beta^2 e_3 e_2\Big)\Big(-e_2-\beta^2 e_3 e_1\Big) + \mu\epsilon^{1-\frac{\gamma}{2}} d_\beta^{\gamma-2}(\xi,\eta)\beta^2\Big(-e_2 e_1 - e_3\Big),$$

$$X_2^\xi X_1^\eta \phi(\xi,\eta) = (\gamma-2)\mu\epsilon^{1-\frac{\gamma}{2}} d_\beta^{\gamma-4}(\xi,\eta)\Big(e_2-\beta^2 e_3 e_1\Big)\Big(-e_1+\beta^2 e_3 e_2\Big) + \mu\epsilon^{1-\frac{\gamma}{2}} d_\beta^{\gamma-2}(\xi,\eta)\beta^2\Big(-e_1 e_2 + e_3\Big),$$

$$X_2^\xi X_2^\eta \phi(\xi,\eta) = (\gamma-2)\mu\epsilon^{1-\frac{\gamma}{2}} d_\beta^{\gamma-4}(\xi,\eta)\Big(e_2-\beta^2 e_3 e_1\Big)\Big(-e_2-\beta^2 e_3 e_1\Big) + \mu\epsilon^{1-\frac{\gamma}{2}} d_\beta^{\gamma-2}(\xi,\eta)\Big(-1+\beta^2 e_1^2\Big).$$

Remark 7.6.

$$X_1^\eta X_1^\xi \phi(\xi,\eta) = (\gamma-2)\mu\epsilon^{1-\frac{\gamma}{2}} d_\beta^{\gamma-4}(\xi,\eta)\Big(-e_1+\beta^2 e_3 e_2\Big)\Big(e_1+\beta^2 e_3 e_2\Big)$$
$$+\mu\epsilon^{1-\frac{\gamma}{2}} d_\beta^{\gamma-2}(\xi,\eta)\Big(-1+\beta^2 e_2^2\Big),$$

$$X_1^\eta X_2^\xi \phi(\xi,\eta) = (\gamma-2)\mu\epsilon^{1-\frac{\gamma}{2}} d_\beta^{\gamma-4}(\xi,\eta)\Big(-e_1+\beta^2 e_3 e_2\Big)\Big(e_2-\beta^2 e_3 e_1\Big)$$
$$+\mu\epsilon^{1-\frac{\gamma}{2}} d_\beta^{\gamma-2}(\xi,\eta)\beta^2\Big(-e_2 e_1+e_3\Big),$$

$$X_2^\eta X_1^\xi \phi(\xi,\eta) = (\gamma-2)\mu\epsilon^{1-\frac{\gamma}{2}} d_\beta^{\gamma-4}(\xi,\eta)\Big(-e_2-\beta^2 e_3 e_1\Big)\Big(e_1+\beta^2 e_3 e_2\Big)$$
$$+\mu\epsilon^{1-\frac{\gamma}{2}} d_\beta^{\gamma-2}(\xi,\eta)\beta^2\Big(-e_3-e_1 e_2\Big),$$

$$X_2^\eta X_2^\xi \phi(\xi,\eta) = (\gamma-2)\mu\epsilon^{1-\frac{\gamma}{2}} d_\beta^{\gamma-4}(\xi,\eta)\Big(-e_2-\beta^2 e_3 e_1\Big)\Big(e_2-\beta^2 e_3 e_1\Big)$$
$$+\mu\epsilon^{1-\frac{\gamma}{2}} d_\beta^{\gamma-2}(\xi,\eta)\Big(-1+\beta^2 e_1^2\Big).$$

We use Remarks 7.2-7.4 and find the estimates given in the remarks below.

Remark 7.7.

$$|X_1^\xi\phi(\xi,\eta)+X_1^\eta\phi(\xi,\eta)| \le 2\mu\epsilon^{1-\frac{\gamma}{2}} d_\beta^{\gamma-2}(\xi,\eta)\beta^2|e_3e_2| \le 2\beta\mu\epsilon^{1-\frac{\gamma}{2}} d_\beta^{\gamma-1}(\xi,\eta)d_0(\xi,\eta),$$

$$|X_2^\xi\phi(\xi,\eta)+X_2^\eta\phi(\xi,\eta)| \le 2\beta\mu\epsilon^{1-\frac{\gamma}{2}} d_\beta^{\gamma-1}(\xi,\eta)d_0(\xi,\eta),$$

$$|X_{3,\delta}^\xi\phi(\xi,\eta)+X_{3,\delta}^\eta\phi(\xi,\eta)| = 0.$$

Remark 7.8.

$$|\nabla_\delta^\xi\phi(\xi,\eta)|^2 = |\nabla_\delta^\eta\phi(\xi,\eta)|^2 = \mu^2\epsilon^{2-\gamma} d_\beta^{2\gamma-4}(\xi,\eta)\Big((e_1^2+e_2^2)(1+\beta^4 e_3^2)+\delta^2\beta^4 e_3^2\Big) \ge$$
$$\ge \mu^2\epsilon^{2-\gamma} d_\beta^{2\gamma-4}(\xi,\eta)\Big(d_0^2(\xi,\eta)+\beta^2\delta^2 d_3^2(\xi,\eta)\Big).$$

Remark 7.9. *From now on we denote by $\tilde{K}$ a fixed positive number which is not necessarily the same each time it appears. We have*

$$|X_i^\xi X_j^\xi\phi(\xi,\eta)| \le \tilde{K}\mu\epsilon^{1-\frac{\gamma}{2}}\gamma d_\beta(\xi,\eta)^{\gamma-2} \quad \text{if } i,j\le m,$$

$$|X_i^\xi X_j^\xi\phi(\xi,\eta)| \le \tilde{K}\delta\beta\mu\epsilon^{1-\frac{\gamma}{2}}\gamma d_\beta(\xi,\eta)^{\gamma-3} d_0(\xi,\eta) \quad \text{if } i\ge m+1 \text{ or } j\ge m+1,$$

$$|X_i^\xi X_j^\xi\phi(\xi,\eta) - X_i^\eta X_j^\eta\phi(\xi,\eta)| \le \tilde{K}\beta(\gamma-2)\mu\epsilon^{1-\frac{\gamma}{2}} d_\beta^{\gamma-3}(\xi,\eta)d_0^2(\xi,\eta),$$
$$X_{3\delta}^\xi X_{3\delta}^\xi\phi(\xi,\eta) - X_{3\delta}^\eta X_{3\delta}^\eta\phi(\xi,\eta) = 0.$$

Remark 7.10. *We use Remarks 7.5 and 7.6. Then for $\beta \leq 1$ we find the following estimates:*

$$(X_1^\xi X_1^\xi + X_1^\eta X_1^\eta + X_1^\xi X_1^\eta + X_1^\eta X_1^\xi)\phi(\xi,\eta) \leq 2\mu\epsilon^{1-\frac{\gamma}{2}}\beta^2 d_\beta^\gamma(\xi,\eta)\gamma,$$

$$(X_1^\xi X_2^\xi + X_1^\eta X_2^\eta + X_1^\xi X_2^\eta + X_1^\eta X_2^\xi)\phi(\xi,\eta) \leq 2\mu\epsilon^{1-\frac{\gamma}{2}}\beta^2 d_\beta^\gamma(\xi,\eta)\gamma,$$

$$(X_2^\xi X_1^\xi + X_2^\eta X_1^\eta + X_2^\xi X_1^\eta + X_2^\eta X_1^\xi)\phi(\xi,\eta) \leq 2\mu\epsilon^{1-\frac{\gamma}{2}}\beta^2 d_\beta^\gamma(\xi,\eta)\gamma,$$

$$(X_2^\xi X_2^\xi + X_2^\eta X_2^\eta + X_2^\xi X_2^\eta + X_2^\eta X_2^\xi)\phi(\xi,\eta) \leq 2\mu\epsilon^{1-\frac{\gamma}{2}}\beta^2 d_\beta^\gamma(\xi,\eta)\gamma.$$

Let us now provide the proof of our main theorem, Theorem 7.1.

Proof. We argue by contradiction and assume that for each $M \geq 0$ there exists an ϵ such that $0 < \delta < \epsilon < 1$ and

$$\sup_{\xi\in G, 0\leq t\leq T} |(u - u_\delta^\epsilon)(\xi,t)| > \frac{M\epsilon^\alpha}{\beta\delta}.$$

Due to Theorem 7.2 and Theorem 7.6 we can apply Lemma 7.2 and deduce that the function ω defined in (7.17) attains its maximum at an interior point $(\hat{\xi},\hat{\eta},\hat{t})$ satisfying

$$d_\beta(\hat{\xi},\hat{\eta}) \leq \Big(\frac{2\gamma\tilde{C}}{\mu}\epsilon^{\frac{\gamma}{2}-1} - \frac{M\gamma}{4\mu}\epsilon^{\alpha+\frac{\gamma}{2}-1}\Big)^{\frac{1}{\gamma}}. \tag{7.22}$$

Since the function u is only continuous, we replace the derivatives of u with the superjet $\mathcal{P}^{2,+}u(\xi,t)$ (see Subsection 7.2.1 for the superjet definition). Note that u_δ^ϵ is smooth so we have $-X_i^\eta u_\delta^\epsilon(\hat{\eta},\hat{t}) = X_i^\eta\phi(\hat{\xi},\hat{\eta},\hat{t})$ and $-X_i^\eta X_j^\eta u_\delta^\epsilon(\hat{\eta},\hat{t}) \leq X_i^\eta X_j^\eta\phi(\hat{\xi},\hat{\eta},\hat{t})$. We know by [39, Theorem 8.3] that for every $\rho > 0$ there exist symmetric matrices $H = (H_{ij})_{i,j,=1,\cdots,m}$ and $Y = (Y_{ij})_{i,j,=1,\cdots,m}$ such that

(i) $(a, \nabla_0^\xi\phi(\hat{\xi},\hat{\eta},\hat{t}), H) \in \tilde{\mathcal{P}}^{2,+}u(\hat{\xi},\hat{t})$
$(b, \nabla_\delta^\eta\phi(\hat{\xi},\hat{\eta},\hat{t}), Y) \in -\tilde{\mathcal{P}}^{2,-}u_\delta^\epsilon(\hat{\eta},\hat{t})$,

(ii) $a + b = \frac{M}{2T}\epsilon^\alpha$,

(iii) $-\Big(\frac{1}{\rho} + ||A||\Big)I \leq \begin{pmatrix} H & 0 \\ 0 & Y \end{pmatrix} \leq A + \rho A^2$,

where A is defined in our Heisenberg group case:

$$A = \begin{pmatrix} B_{\xi\xi} & B_{\xi\eta} \\ B_{\eta\xi} & B_{\eta\eta} \end{pmatrix}, \quad B_{\zeta_1\zeta_2} = \begin{pmatrix} X_1^{\zeta_1}X_1^{\zeta_2}\phi & \frac{1}{2}(X_1^{\zeta_1}X_2^{\zeta_1}\phi + X_2^{\zeta_1}X_1^{\zeta_2}\phi) \\ \frac{1}{2}(X_1^{\zeta_1}X_2^{\zeta_2}\phi + X_2^{\zeta_1}X_1^{\zeta_2}\phi) & X_2^{\zeta_1}X_2^{\zeta_2}\phi \end{pmatrix},$$

where $\zeta_1, \zeta_2 \in \{\xi,\eta\}$.

We employ Remark 7.10 and (iii) to see that for all $z \in \mathbb{R}^m$

$$z^T(H+Y)z = \begin{pmatrix} z^T, & z^T \end{pmatrix} \begin{pmatrix} H & 0 \\ 0 & Y \end{pmatrix} \begin{pmatrix} z \\ z \end{pmatrix} \leq \begin{pmatrix} z^T, & z^T \end{pmatrix} (A + \rho A^2) \begin{pmatrix} z \\ z \end{pmatrix}.$$

As ρ goes to zero this implies for $\beta \leq 1$ that

$$z^T(H+Y)z \leq \tilde{K}(\gamma-1)\mu\epsilon^{1-\frac{\gamma}{2}}\beta^2 d_\beta^\gamma(\xi,\eta)|z|^2. \tag{7.23}$$

Since $(a, \nabla_0^\xi \phi(\hat{\xi},\hat{\eta},\hat{t}), H) \in \tilde{\mathcal{P}}^{2,+}u(\hat{\xi},\hat{t})$ and u is a viscosity subsolution of (7.3) we have

$$\begin{aligned} &a - \sum_{i,j=1}^m \Big(\delta_{ij} - \frac{X_i^\xi \phi(\hat{\xi},\hat{\eta},\hat{t}) X_j^\xi \phi(\hat{\xi},\hat{\eta},\hat{t})}{|\nabla_0^\xi \phi(\hat{\xi},\hat{\eta},\hat{t})|^2}\Big) H_{ij} \leq 0, \quad \text{if} \quad \nabla_0^\xi \phi(\hat{\xi},\hat{\eta},\hat{t}) \neq 0, \quad (7.24) \\ &a - \sum_{i,j=1}^m \delta_{ij} H_{ij} \leq 0, \quad \text{if} \quad \nabla_0^\xi \phi(\hat{\xi},\hat{\eta},\hat{t}) = 0. \end{aligned}$$

Moreover since u_δ^ϵ is smooth we have $\partial_t u_\delta^\epsilon(\hat{\eta},\hat{t}) = -b$. It is a solution and it satisfies:

$$\begin{aligned} b = -\partial_t u_\delta^\epsilon(\hat{\eta},\hat{t}) &= -\sum_{i,j=1}^n \Big(\delta_{ij} - \frac{X_{i\delta}^\eta u_\delta^\epsilon(\hat{\xi},\hat{\eta},\hat{t}) X_{j\delta}^\eta u_\delta^\epsilon(\hat{\xi},\hat{\eta},\hat{t})}{\epsilon^2 + |\nabla_\delta^\eta u_\delta^\epsilon(\hat{\xi},\hat{\eta},\hat{t})|^2}\Big) X_{i\delta}^\eta X_{j\delta}^\eta u_\delta^\epsilon(\hat{\eta},\hat{t}) \quad (7.25) \\ &\leq \sum_{i,j=1}^n \Big(\delta_{ij} - \frac{X_{i\delta}^\xi \phi(\hat{\xi},\hat{\eta},\hat{t}) X_{j\delta}^\xi \phi(\hat{\xi},\hat{\eta},\hat{t})}{\epsilon^2 + |\nabla_\delta^\xi \phi(\hat{\xi},\hat{\eta},\hat{t})|^2}\Big) X_{i\delta}^\eta X_{j\delta}^\eta \phi(\hat{\eta},\hat{t}), \end{aligned}$$

due to the fact that at the maximum point $\nabla_\delta^\eta u_\delta^\epsilon(\hat{\eta},\hat{t}) = -\nabla_\delta^\eta \phi(\hat{\xi},\hat{\eta},\hat{t})$, and

$$-X_i^\eta X_j^\eta u^\epsilon(\hat{\eta},\hat{t}) \leq X_i^\eta X_j^\eta \phi(\hat{\eta},\hat{t}), \quad -X_i^\eta X_j^\eta u^\epsilon(\hat{\eta},\hat{t}) \leq Y_{ij}.$$

Now we distinguish two cases: $\nabla_0^\xi \phi(\hat{\xi},\hat{\eta},\hat{t}) \neq 0$ and $\nabla_0^\xi \phi(\hat{\xi},\hat{\eta},\hat{t}) = 0$. Let us first consider the case with $\nabla_0^\xi \phi(\hat{\xi},\hat{\eta},\hat{t}) \neq 0$. For the sake of simplicity we write ϕ instead of explicitly writing $\phi(\hat{\xi},\hat{\eta},\hat{t})$ and d_β, d_0, d_3 instead of $d_\beta(\hat{\xi},\hat{\eta})$, $d_0(\hat{\xi},\hat{\eta})$, $d_3(\hat{\xi},\hat{\eta})$ from now on. We sum (7.24) and (7.25). Then we obtain

$$\begin{aligned} &\frac{M\epsilon^\alpha}{2T} = a + b \quad (7.26) \\ &\leq \sum_{i,j=1}^m \Big(\delta_{ij} - \frac{X_i^\xi \phi X_j^\xi \phi}{|\nabla_0^\xi \phi|^2}\Big) H_{ij} + \sum_{i,j=1}^n \Big(\delta_{ij} - \frac{X_{i\delta}^\eta \phi X_{j\delta}^\eta \phi}{(\epsilon^2 + |\nabla_\delta^\eta \phi|^2)}\Big) X_{i\delta}^\eta X_{j\delta}^\eta \phi \\ &\leq \sum_{i,j=1}^m \Big(\delta_{ij} - \frac{X_i^\xi \phi X_j^\xi \phi}{|\nabla_0^\xi \phi|^2}\Big)(H_{ij} + Y_{ij}) + 2\sum_{i=1}^n \sum_{j=m+1}^n \Big|\delta_{ij} - \frac{X_{i\delta}^\eta \phi X_{j\delta}^\eta \phi}{(\epsilon^2 + |\nabla_\delta^\eta \phi|^2)}\Big| X_{i\delta}^\eta X_{j\delta}^\eta \phi \\ &+ \sum_{i,j=1}^m \Big(\frac{X_i^\xi \phi X_j^\xi \phi}{|\nabla_0^\xi \phi|^2} - \frac{X_i^\eta \phi X_j^\eta \phi}{(\epsilon^2 + |\nabla_\delta^\eta \phi|^2)}\Big) X_i^\eta X_j^\eta \phi. \end{aligned}$$

Let us denote by I_1, I_2, I_3 three terms appearing on the right hand side of the last inequality in (7.26), and let us consider one term at a time. We set $\beta = \epsilon^\sigma$ where $\sigma > 0$ is to be fixed in the sequel. Recall from (7.22) that

$$d_\beta^\gamma \leq \frac{2\tilde{C}\gamma}{\mu}\epsilon^{\frac{\gamma}{2}-1}. \tag{7.27}$$

We use (7.23) and observe that

$$I_1 = \sum_{i,j=1}^{m}\Big(\delta_{ij} - \frac{X_i^\xi\phi X_j^\xi\phi}{|\nabla_0^\xi\phi|^2}\Big)(H_{ij}+Y_{ij}) \leq \tilde{K}(\gamma-1)\mu\epsilon^{1-\frac{\gamma}{2}}\beta^2 d_\beta^\gamma.$$

We plug the definition of μ given by (7.18) in this expression and by using (7.27) find that

$$I_1 \leq C_1\epsilon^{\frac{\gamma-2}{2(\gamma-1)}\left(1-2\frac{\sigma}{(\gamma-1)}\right)}M^{-1}, \tag{7.28}$$

with $C_1 > 0$ denoting a fixed number (which is not necessarily the same each time it appears from now on) and where we impose on $\sigma > 0$ the following conditions:

$$1-2\frac{\sigma}{(\gamma-1)} > 0, \quad 2\sigma - 1 + \frac{2}{\gamma} > \frac{\gamma-2}{2(\gamma-1)}\Big(1-2\frac{\sigma}{(\gamma-1)}\Big), \quad \text{with } \gamma > 2. \tag{7.29}$$

We continue with the second term

$$I_2 = 2\sum_{i=1}^{n}\sum_{j=m+1}^{n}\Big(\delta_{ij} - \frac{X_{i\delta}^\eta\phi X_{j\delta}^\eta\phi}{(\epsilon^2+|\nabla_\delta^\eta\phi|^2)}\Big)X_{i\delta}^\eta X_{j\delta}^\eta\phi.$$

Note that by Remarks 7.8 and 7.9 we have

$$|X_{i\delta}^\xi X_{j\delta}^\xi\phi| \leq \delta\beta\mu\epsilon^{1-\frac{\gamma}{2}}\gamma d_\beta^{\gamma-3}d_0 \quad \text{if } i \geq m+1 \text{ or } \ j \geq m+1, \tag{7.30}$$

which gives

$$I_2 \leq \tilde{K}\delta\beta\mu\epsilon^{1-\frac{\gamma}{2}}\gamma d_\beta^{\gamma-2}.$$

Furthermore if we set $\beta = \delta = \epsilon^\sigma$ and use the definition of μ given in (7.18), also the inequality (7.27) on d_β, then we find

$$I_2 \leq \tilde{K}\delta\beta\gamma^{\frac{2\gamma-2}{\gamma}}\mu^{\frac{2}{\gamma}}\epsilon^{-1+\frac{2}{\gamma}} \leq C_1\epsilon^{\frac{\gamma-2}{2(\gamma-1)}\left(1-2\frac{\sigma}{(\gamma-1)}\right)}M^{-1},$$

for the σ values satisfying the conditions given in (7.29).

We consider the last term which we can write, thanks to

$$|\nabla_\delta^\eta\phi|^2 = |\nabla_0^\xi\phi|^2 + |X_{3\delta}^\xi\phi|^2 = |\nabla_\delta^\xi\phi|^2,$$

as follows:

$$
\begin{aligned}
I_3 = &\sum_{i,j=1}^{m} \Big(\epsilon^2 \frac{X_i^\xi \phi X_j^\xi \phi \, X_i^\eta X_j^\eta \phi}{(\epsilon^2 + |\nabla_\delta^\eta \phi|^2)|\nabla_0^\xi \phi|^2}\Big) \\
&+ \sum_{i,j=1}^{m} \Big(\frac{(|X_1^\eta \phi|^2 + |X_2^\eta \phi|^2)(X_i^\xi \phi X_j^\xi \phi - X_i^\eta \phi X_j^\eta \phi) X_i^\eta X_j^\eta \phi}{(\epsilon^2 + |\nabla_\delta^\eta \phi|^2)|\nabla_0^\xi \phi|^2}\Big) \\
&+ \sum_{i,j=1}^{m} \Big(\frac{|X_{3\delta}^\eta \phi|^2 X_i^\xi \phi X_j^\xi \phi \, X_i^\eta X_j^\eta \phi}{(\epsilon^2 + |\nabla_\delta^\eta \phi|^2)|\nabla_0^\xi \phi|^2}\Big) = L_1 + L_2 + L_3.
\end{aligned}
$$

Let us consider first L_1. We employ Remarks 7.8 and 7.9 to find

$$
\begin{aligned}
|\nabla_\delta^\xi \phi| = &|\nabla_\delta^\eta \phi| \geq \delta\beta\mu\epsilon^{1-\frac{\gamma}{2}} d_\beta^{\gamma-1}, \\
|X_i^\xi X_j^\xi \phi| \leq &\mu\epsilon^{1-\frac{\gamma}{2}} \gamma d_\beta^{\gamma-2} \quad \text{ if } i,j \leq m,
\end{aligned}
$$

which provide to us

$$
\begin{aligned}
\frac{\epsilon^2 \, X_i^\eta X_j^\eta \phi}{(\epsilon^2 + |\nabla_\delta^\eta \phi|^2)} \leq &\frac{\mu\epsilon^{3-\frac{\gamma}{2}} \gamma d_\beta^{\gamma-2}}{\epsilon^2 + \mu^2\epsilon^{2-\gamma} d_\beta^{2\gamma-4}(d_0^2 + \beta^2\delta^2 d_3^2)} \\
&\leq \frac{\mu\epsilon^{3-\frac{\gamma}{2}} \gamma d_0^{\gamma-2} + \mu\epsilon^{3-\frac{\gamma}{2}} \gamma d_3^{\gamma-2}}{\epsilon^2 + \mu^2\epsilon^{2-\gamma} d_0^{2\gamma-2} + \mu^2\epsilon^{2-\gamma}\beta^2\delta^2 d_3^{2\gamma-2}} \, .
\end{aligned}
$$

We write the first term in the numerator as follows:

$$
\mu\epsilon^{3-\frac{\gamma}{2}} \gamma d_0^{\gamma-2} = \gamma \mu^{\frac{1}{\gamma-1}} \epsilon^{\frac{\gamma-2}{2(\gamma-1)}} \epsilon^{\frac{\gamma}{\gamma-1}} \mu^{\frac{\gamma-2}{\gamma-1}} \epsilon^{-\frac{(\gamma-2)^2}{2(\gamma-1)}} d_0^{\gamma-2}.
$$

Then we employ Young's inequality $mn \leq \frac{1}{p} m^p + \frac{1}{q} n^q$ with $p = \frac{2(\gamma-1)}{\gamma}$ and $q = \frac{2(\gamma-1)}{\gamma-2}$ in order to find

$$
\begin{aligned}
\mu\epsilon^{3-\frac{\gamma}{2}} \gamma d_0^{\gamma-2} &\leq \gamma \mu^{\frac{1}{\gamma-1}} \epsilon^{\frac{\gamma-2}{2(\gamma-1)}} \Big(\frac{\gamma}{2(\gamma-1)} \epsilon^2 + \frac{\gamma-2}{2(\gamma-1)} \mu^2 \epsilon^{2-\gamma} d_0^{2\gamma-2}\Big) \\
&\leq \tilde{K} \gamma \mu^{\frac{1}{\gamma-1}} \epsilon^{\frac{\gamma-2}{2(\gamma-1)}} \Big(\frac{1}{2}\epsilon^2 + \mu^2 \epsilon^{2-\gamma} d_0^{2\gamma-2}\Big). \qquad (7.31)
\end{aligned}
$$

The second term in the numerator can be handled in the same way. If we set $\beta = \delta = \epsilon^\sigma$ as before, we can write

$$
\begin{aligned}
\mu\epsilon^{3-\frac{\gamma}{2}} \gamma d_3^{\gamma-2} &= \gamma \mu^{\frac{1}{\gamma-1}} \epsilon^{\frac{\gamma-2}{2(\gamma-1)}\left(1-2\frac{\sigma}{(\gamma-1)}\right)} \epsilon^{\frac{\gamma}{\gamma-1}} \mu^{\frac{\gamma-2}{\gamma-1}} \epsilon^{-\frac{(\gamma-2)(\gamma-2-4\sigma)}{2(\gamma-1)}} d_3^{\gamma-2} \\
&\leq \tilde{K} \gamma \mu^{\frac{1}{\gamma-1}} \epsilon^{\frac{\gamma-2}{2(\gamma-1)}\left(1-2\frac{\sigma}{(\gamma-1)}\right)} \Big(\frac{1}{2}\epsilon^2 + \mu^2\beta^2\delta^2\epsilon^{2-\gamma} d_3^{2\gamma-2}\Big). \qquad (7.32)
\end{aligned}
$$

Finally we sum up (7.31) and (7.32) and we obtain

$$\begin{aligned}\frac{\epsilon^2 X_i^\xi X_j^\xi \phi}{\epsilon^2+|\nabla_\delta^\xi \phi|^2} \leq \tilde{K}\gamma\mu^{\frac{1}{\gamma-1}}\epsilon^{\frac{\gamma-2}{2(\gamma-1)}\left(1-2\frac{\sigma}{(\gamma-1)}\right)}\\ \leq C_1\Big(\frac{\gamma 4^\gamma \mathrm{Lip}(u_0)^\gamma}{M^{\gamma-1}}\Big)^{\frac{1}{\gamma-1}}\epsilon^{\frac{\gamma-2}{2(\gamma-1)}\left(1-2\frac{\sigma}{(\gamma-1)}\right)} = C_1\epsilon^{\frac{\gamma-2}{2(\gamma-1)}\left(1-2\frac{\sigma}{(\gamma-1)}\right)}M^{-1},\end{aligned}$$

which implies

$$L_1 \leq C_1\epsilon^{\frac{\gamma-2}{2(\gamma-1)}\left(1-2\frac{\sigma}{(\gamma-1)}\right)}M^{-1},$$

where we use γ and μ definitions given by (7.15) and (7.18), respectively.

Now let us tackle L_3. We use the expression of $X_{3\delta}^\eta\phi$ given in Remark 7.2, the first and the second inequalities given in (7.30) and then we observe

$$\frac{|X_{3\delta}^\eta\phi|^2 X_i^\xi X_j^\xi\phi}{(\epsilon^2+|\nabla_\delta^\eta\phi|^2)} \leq \frac{\mu^3\epsilon^{3-\frac{3\gamma}{2}}d_\beta^{3\gamma-4}\delta^2\beta^4\gamma}{\delta^2\beta^2\mu^2\epsilon^{2-\gamma}d_\beta^{2\gamma-2}} = \tilde{K}\mu\epsilon^{1-\frac{\gamma}{2}}d_\beta^{\gamma-2}\beta^2\gamma.$$

We employ (7.27) and plug $\beta=\epsilon^\sigma$ in this expression. Then we find

$$\frac{|X_{3\delta}^\eta\phi|^2 X_i^\xi X_j^\xi\phi}{(\epsilon^2+|\nabla_\delta^\eta\phi|^2)} \leq \tilde{K}\mu^{\frac{2}{\gamma}}\epsilon^{-1+\frac{2}{\gamma}+2\sigma}.$$

This result implies for the σ values satisfying (7.29) the following

$$L_3 \leq C_1\epsilon^{\frac{\gamma-2}{2(\gamma-1)}\left(1-2\frac{\sigma}{(\gamma-1)}\right)}M^{-1}.$$

Now we continue with L_2. At this point we note that

$$\begin{aligned}|X_1^\xi\phi|^2-|X_1^\eta\phi|^2 \leq 2\mu^2\epsilon^{2-\gamma}d_\beta^{2\gamma-4}\beta^2|e_1e_2e_3|,\\ |X_2^\xi\phi|^2-|X_2^\eta\phi|^2 \leq 2\mu^2\epsilon^{2-\gamma}d_\beta^{2\gamma-4}\beta^2|e_1e_2e_3|,\\ |X_1^\xi\phi X_2^\xi\phi|-|X_1^\eta\phi X_2^\eta\phi| \leq 2\mu^2\epsilon^{2-\gamma}d_\beta^{2\gamma-4}\beta^2|e_3||e_2^2-e_1^2|,\end{aligned} \tag{7.33}$$

and together with Remark 7.8 these inequalities imply that

$$|X_i^\xi\phi X_j^\xi\phi|-|X_i^\eta\phi X_2^\eta\phi| \leq 2\beta|\nabla_\delta\phi|^2 d_\beta \leq 2\beta|\nabla_\delta\phi|^2.$$

The second inequality from (7.30) and the inequalities given in (7.33) result in

$$\begin{aligned}\frac{(X_i^\xi\phi X_j^\xi\phi - X_i^\eta\phi X_j^\eta\phi)X_i^\eta X_j^\eta\phi}{(\epsilon^2+|\nabla_\delta^\eta\phi|^2)} \leq \mu\beta\epsilon^{1-\frac{\gamma}{2}}d_\beta^{\gamma-2}\\ \leq \gamma^{\frac{\gamma-2}{\gamma}}\mu^{\frac{2}{\gamma}}\epsilon^{\sigma-1+\frac{2}{\gamma}} \leq \frac{C\epsilon^{\sigma-1+\frac{2}{\gamma}}}{M^{\frac{2}{\gamma}(\gamma-1)}} \leq \frac{C}{M}\epsilon^{\frac{\gamma-2}{2(\gamma-1)}(1-\frac{2\sigma}{\gamma-1})},\end{aligned}$$

for the σ values satisfying (7.29) and

$$\sigma - 1 + \frac{2}{\gamma} > \frac{\gamma - 2}{2(\gamma - 1)}\Big(1 - 2\frac{\sigma}{(\gamma - 1)}\Big). \tag{7.34}$$

Also note that for $\gamma > 2$ the following holds

$$\frac{2}{\gamma}(\gamma - 1) > 1.$$

Finally we choose

$$\alpha = \frac{\gamma - 2}{2(\gamma - 1)}\Big(1 - 2\frac{\sigma}{(\gamma - 1)}\Big),$$

and with this choice we find that

$$\frac{M\epsilon^\alpha}{2T} \leq I_1 + I_2 + I_3 \leq C_1 M^{-1}\epsilon^\alpha.$$

This result is a contradiction for large M values, proving the assertion of the theorem if the gradient of ϕ does not vanish at the maximum point.

Now we look at the case with $|\nabla_0^\xi \phi(\hat{\xi}, \hat{\eta}, \hat{t})| = 0$. Note that zero gradient implies

$$e_1^2 + e_2^2 = 0,$$

and

$$\nabla_0^\xi \phi = \nabla_0^\eta \phi = 0.$$

In this case we can write (7.26) by using (7.24) as

$$\begin{aligned}\frac{M}{2T}\epsilon^\alpha =& a + b \leq \sum_{i,j=1}^{m} \delta_{ij} H_{ij} - \sum_{i,j=1}^{m} \delta_{ij} X_i^\eta X_j^\eta u_\delta^\epsilon(\hat{\xi}, \hat{\eta}, \hat{t}) \\ &\leq \sum_{i,j=1}^{m} \delta_{ij}(H_{ij} + Y_{ij}) + \sum_{i=1}^{n}\sum_{j=m+1}^{n} \Big(\delta_{ij} - \frac{X_{i\delta}^\eta \phi X_{j\delta}^\eta \phi}{(\epsilon^2 + |X_{3\delta}^\eta \phi|^2)}\Big) X_{i\delta}^\eta X_{j\delta}^\eta \phi.\end{aligned}$$

Note that the last term on the right hand side of the final inequality can be handled exactly in the same way as I_2 was in the previous case of non-vanishing gradient. Furthermore the first term can be tackled in exactly the same way as I_1 was. Therefore it has the same estimate as I_1 has (see (7.28)). So we can write that

$$\frac{M}{2T}\epsilon^\alpha \leq C_1 M^{-1}\epsilon^{\frac{\gamma-2}{2(\gamma-1)}\left(1-2\frac{\sigma}{(\gamma-1)}\right)},$$

and it implies for a $\sigma > 0$ satisfying (7.29), (7.34) and

$$\sigma - 1 + \frac{2}{\gamma} > \frac{\gamma - 2}{2(\gamma - 1)}\Big(1 - 2\frac{\sigma}{(\gamma - 1)}\Big) = \alpha,$$

that

$$\frac{M}{2T}\epsilon^{\alpha} \leq C_1 M^{-1}\epsilon^{\alpha}.$$

It is a contradiction for large M values.

We have obtained the contradiction for both cases with vanishing and non-vanishing horizontal gradients. The proof is complete. □

Remark 7.11. *Comparison principle was valid only for the vanishing viscosity solutions as given in Theorem 7.3. Now we have also the comparison principle for the viscosity solutions in the Heisenberg group setting, which is Corollary 7.1. It follows directly from Theorem 7.1.*

Remark 7.12. *The proof in the Heisenberg setting can be extended to the setting of step 2 Carnot groups. Let $\xi = (x_\xi, \theta_\xi), \eta = (x_\eta, \theta_\eta) \in G = \mathbb{R}^m \times \mathbb{R}^{n-m}$ denote the points in the Carnot group G.*

We write the distance function analogously to the case of the Heisenberg setting as

$$d_\beta(\xi,\eta) = (e_1^2 + e_2^2 + \cdots + e_m^2 + \beta^2 e_{m+1}^2 + \cdots + \beta^2 e_{m+1}^2)^{1/2},$$

where $\beta > 0$ and for β fixed it is equivalent to the one given in (7.16). If $e_1, e_2, \ldots, e_n$ are the displacements defined in (7.7), then there are $m \times m$ real matrices $W^{(i)}$ such that

$$\begin{aligned} e_i =& x_{\xi,i} - x_{\eta,i} \quad \text{if} \quad i = 1, 2, \ldots, m \\ e_i =& \theta_{\xi,i} - \theta_{\eta,i} - \langle W^{(i)} x_\xi, x_\eta \rangle \quad \text{if} \quad i = m+1, \ldots, n. \end{aligned}$$

Let us denote the elements of each $m \times m$ matrix $W^{(k)}$ by

$$W^{(k)} = (w_{ij}^{(k)})_{i,j \leq m} \quad \text{with} \quad k = 1, 2, \ldots, n-m.$$

Note that the basis of the bracket generating vector fields in this setting can be represented as

$$X_i = \partial_{x_i} + \sum_{k=1}^{n-m} \sum_{l=1}^{m} w_{il}^{(k)} x_l \partial_{\theta_k},$$

with $w_{il}^{(k)} = -w_{li}^{(k)}$. Let us also write the basis of the vector fields of the second layer as

$$Y_k = \partial_{\theta_k} \quad \text{with} \quad k = 1, 2, \ldots, n-m.$$

We denote the vector fields at the point ξ by X_i^ξ and Y_k^ξ. At this point we note that

$$\begin{aligned} X_i^\xi e_j =& \delta_{ij} \quad \text{if} \quad i, j = 1, \ldots, m, \\ X_i^\xi e_j =& \sum_{k=1}^{n} \sum_{l=1}^{m} w_{il}^{(k)} e_{m/2+i} \quad \text{if} \quad i = 1, \ldots, m/2,\ j = m+1, \ldots n, \\ X_i^\xi e_j =& \sum_{k=1}^{n} \sum_{l=1}^{m} w_{il}^{(k)} e_{i-m/2} \quad \text{if} \quad i = \frac{m}{2}+1, \ldots, m,\ j = m+1, \ldots n, \\ Y_{i\delta}^\xi e_j =& 0, \quad \text{if} \quad i = 1, \ldots, n,\ j = 1, \ldots m, \\ Y_{i\delta}^\xi e_j =& \delta, \quad \text{if} \quad i = 1, \ldots, n,\ j = m+1, \ldots n, \end{aligned} \tag{7.35}$$

by using an analogous notation to the one that we used in the case of the Heisenberg setting, where δ_{ij} denotes the Dirac delta, which is completely different from δ. The same computations hold also for the vector fields at η up to a sign change. It is said that the vector fields X_i^{ξ}, X_i^{η} are of degree 1 and the vector fields Y_i^{ξ}, Y_i^{η} are of degree 2. Furthermore e_i is of homogeneity 1 if $i = 1, \dots, m$ while it is of homogeneity 2 if $i = m+1, \dots, n$. The key point in the computations given in (7.35) *is that if the vector field X is of degree k, then Xe_i has homogeneity* $\hom(e_i) - k$*, where* hom *gives the homogeneity of its argument. It is exactly the same case which was observed in the case of the Heisenberg setting (see Remark 7.1).*

This result is the core of the estimations related to the first and second order derivatives of the test function $\phi(\xi, \eta, t)$, where now ξ and η are two points in a step 2 Carnot group G. Following the same technique based on the approximating vector fields $Y_{i\delta}^{\xi}$, $Y_{i\delta}^{\eta}$ in the second layer, and finding the estimates on the first and second order derivatives via the results given in (7.35)*, one can follow the same method as we did in the case of the Heisenberg group setting in order to show the uniqueness of the viscosity solution to mean curvature equations in step 2 Carnot groups.*

Chapter 8

Image enhancement in the spatial frequency geometry

In this chapter we focus on a problem related to image processing inspired by visual perception. It is the problem of coherent image enhancement with geometrical structure of a given visual stimulus (2-dimensional image). Enhancement refers to noise reduction and coherent enhancement means noise reduction in such a way that the underlying geometric structures (boundaries/contours, surfaces, textures and so on) are preserved. A large class of algorithms of image processing in Lie groups were developed by Duits et. al. in [54], [50], [51], [52], [53]. The main instrument they developed is an invertible map from the 2-dimensional retinal image to the feature space expressed in terms of Fourier instruments. They confronted with the problems of both contour completion and enhancement in presence of crossing and bifurcating curves. In particular they studied enhancement in the Heisenberg group in [53]. Another approach for image enhancement was provided in [34], which was based on Laplace-Beltrami and mean curvature flow in the sub-Riemannian setting of the model geometry proposed by Citti-Sarti [35]. We would like to quote also Kimmel et. al [108], [107], who performed an enhancement process in various lifted spaces, and in particular in the space of position, orientation and scale.

We propose our enhancement algorithm in the cortical model framework introduced in Chapter 5 and by following a similar approach to the one provided by Duits in [53]. We lift 2-dimensional initial image to the space of features (orientation, frequency and phase) via (5.7). We process the output of the lifting by using the sub-Riemannian operators defined on this space (see Section 3.5). Then we project back, using the invertibility of the Gabor transform, through the exact inversion formula given by (4.2). Even though the family of Gabor filters we consider here is the same as the one introduced by Duits in [53], our algorithm is new since we use a different metric in the feature space introduced in Chapter 5.

8.1 Processing the image in the extended geometry

The response of the simple cell located at $q = (q_1, q_2) \in M \simeq \mathbb{R}^2$, sensitive to orientation $\theta \in S^1$, frequency $\omega \in \mathbb{R}^+$ and with phase $\phi \in S^1$, to any visual stimulus $I(q)$ at the point q on the retina M is represented by $O_p^I(q)$ with $p = (\theta, \omega, \phi) \in S^1 \times \mathbb{R}^+ \times S^1$ and it is found via the output formula given in (5.7). Let us recall that the mechanism which produces the set of all responses to a given visual stimulus is called *lifting*. The lifting induces the 5-dimensional sub-Riemannian manifold $\mathcal{M}$ which was explained in Chapter 5. We refer to Chapter 5 for the details of the sub-Riemannian geometry and the notation. We also noted in Chapter 4 that this mechanism is analogous to a Gabor transform

$$G_I(q,p) = \langle I, g_{(q,p)} \rangle = \int_M I(x)\overline{g(x-q)}\mathrm{e}^{-i\,r\cdot(x-q)}dx.$$

Indeed, starting from the Gabor transform we employ the change of feature variables by using $r = |r|(-\sin(\theta), \cos(\theta)) = \omega(-\sin(\theta), \cos(\theta))$. We denote the spatial and phase variables by x and s, respectively. Then the Gabor transform of a 2-dimensional image I can be written as:

$$G_I(q,p) = \int_M I(x)\overline{\Psi_{(q,p)}(x,s)}\,dx = \mathrm{e}^{-i(s-\phi)}\int_M I(x)\overline{\Psi_{(q,\theta,\omega,0)}(x,0)}\,dx = O_p^I(q),$$

where $O_p^I(q)$ is given by (5.7) and

$$\overline{\Psi_{(q,p)}(x,s)} = \mathrm{e}^{-i(s-\phi)}\overline{\Psi_{(q,p)}(x)} = \mathrm{e}^{-i(s-\phi))}\mathrm{e}^{ir\cdot(x-q)}\overline{g(x-q)} = \overline{g_{q,r}(x)},$$

with $\Psi_{(q,p)}(x)$ implying $\Psi_{(q,\theta,\omega,0)}(x,0)$ and overline denoting the complex conjugate.

The main reason for that we can process the image in the lifted space and then project it back to the retinal plane M is that the Gabor transform is invertible. The initial signal can be recovered through the following inversion formula:

$$I(x) = \frac{1}{2\pi||g||_{L^2}^2}\int_{\mathcal{M}} G_I(q,p)g_{(q,r)}(x)\omega\,dq\,dr. \tag{8.1}$$

At this point we note that the phase term $\mathrm{e}^{-i(s-\phi)}$ is not dependent on p or q. Similarly to the case of Heisenberg group (see for example the setting of Duits et. al. [53] with Heisenberg group within the context of image analysis and [103] in relation to wavelet analysis), its effect in the case of transform and inverse transform without any processing in the phase dimension of the lifted space is merely a rotation with a constant phase value. Hence it can be avoided as long as no change in the phase component of the lifted image occurs.

Here we discard the maximum selection mechanism (see Section 4.4.7), and we consider the whole output function O_p^I. This choice is not in contradiction with the previously proposed model of Citti-Sarti [35] (which employs the maximum selection mechanism), since we can assign a probability meaning to the output O_p^I: It is maximum at

the selected feature, and it exponentially decays from the selected feature value. If we interpret the output O_p^I as a probability density, then the maximum selection mechanism associates a function, which is the deterministic counterpart of the output O_p^I.

8.2 Enhancement

Coherent enhancement on the output O_p^I (Gabor coefficient) reduces the noise, smooths the given image while it preserves the geometric structures in the image. We will perform such type of enhancement via sub-Riemannian diffusion or Laplace-Beltrami flow. We will show the results of our enhancement process in comparison with some results in the literature.

Anisotropic metric on the space of Gabor coefficients defines the sub-Riemannian Laplacian in the sub-Riemannian space generated by the simple cells as in Section 3.5:

$$\Delta_0 u = \sum_{i=1}^{4} c_i X_{ii}^2 u, \tag{8.2}$$

where coefficients c_i are non-negative constants representing the weights of the second order horizontal vector fields which are given in (5.3). However the space is not isotropic due to the metric induced by the output. The weights are used also in order to give an anisotropic characteristic to the diffusion. In particular they are used to adjust the homogeneity of the sub-Riemannian geometry. They are particularly important in the discrete case, where different dimensions of the space need not necessarily be sampled in the same way. We will use the diffusion with a simplified version of the sub-Riemannian Laplacian given in (8.2) only for comparison purposes.

It has been proved by Franceschiello et. al. in [70] that the output induces a metric on the space of the model geometry proposed in [35] and the metric elicits certain visual illusions. In the article of Franceschiello et. al. [70] a simplified diagonal metric was used. On the other hand, following the approach of Kimmel et. al. [108], [107], we choose the metric induced by the output O_p^I on the space of $\mathcal{M}$.

The metric (g_{ij}) induced by the output is defined as follows:

Definition 8.1. *(The metric induced by a graph)*

$$(g_{ij}) = \begin{pmatrix} 1 + c_1(X_1 u)^2 & \sqrt{c_1 c_2} X_1 u X_2 u & \sqrt{c_1 c_3} X_1 u X_3 u & \sqrt{c_1 c_4} X_1 u X_4 u \\ \sqrt{c_1 c_2} X_2 u X_1 u & 1 + c_2(X_2 u)^2 & \sqrt{c_2 c_3} X_2 u X_3 u & \sqrt{c_2 c_4} X_2 u X_4 u \\ \sqrt{c_1 c_3} X_3 u X_1 u & \sqrt{c_2 c_3} X_3 u X_2 u & 1 + c_3(X_3 u)^2 & \sqrt{c_3 c_4} X_3 u X_4 u \\ \sqrt{c_1 c_4} X_4 u X_1 u & \sqrt{c_2 c_4} X_4 u X_2 u & \sqrt{c_3 c_4} X_4 u X_3 u & 1 + c_4(X_4 u)^2 \end{pmatrix},$$

with constants $c_1, c_2, c_3, c_4 > 0$.

We denote the inverse metric by (g^{ij}) and its elements by g^{ij}.

Laplace-Beltrami flow provides a well-adapted enhancement to the surface underlying the image function I since the flow is restricted to the evolving level sets of the image.

Laplace-Beltrami operator is written as:

$$\Delta_{(g_{ij})}u = \sum_{i,j=1}^{4} \frac{1}{\sqrt{\det(g_{ij})}} X_i\big(\sqrt{\det(g_{ij})}g^{ij}X_j u\big), \tag{8.3}$$

where $\det(g_{ij})$ is the determinant of the induced metric. Laplace-Beltrami operator can be considered as the linearization of the motion by curvature explained in Chapter 6 and Chapter 7. We will use the Laplace-Beltrami process with the operator given in (8.3) and characterized by a reduced version of the metric provided in Definition 8.1.

The sub-Riemannian evolution equation for the enhancement is written as:

$$\begin{cases} \partial_t u = L\, u \\ u_{|t=0} = O_p^I(q), \end{cases} \tag{8.4}$$

for all $(q,p) \in \mathcal{M}$ and $0 < t \leq T$, where the operator L is chosen as

$$L = \Delta_{(g_{ij})} \quad \text{or} \quad L = \Delta_0. \tag{8.5}$$

8.3 Implementation of the algorithm

We present the steps of our algorithm based on (8.4) by starting from the initial image function $I : \mathbb{R}^2 \simeq M \to \mathbb{R}$ at $q \in M$.

1. Lift the image I to $O_p^I(q)$ by using (5.7). Choose this output as the initial value $u_{|t=0}$ of the solution to (8.4) at time $t = 0$.

2. Denote the discrete step in time by Δt. At the k^{th} iteration (i.e., $t = k\Delta t$) compute the result of the discretized version $\bar{L}$ (of the operator L) applied on the current value as $\bar{L}u$ and update the solution and the value of u by using (8.4) as follows:

$$u(t + \Delta t) = u(t) + \Delta t \bar{L}u(t).$$

3. Repeat step 2 until the final time $T =$ (number of iterations) $\times\, \Delta t$ is achieved.

4. Apply the inverse Gabor transform given by (8.1) on $u(T)$.

8.3.1 Discrete Gabor coefficients

We discretize the image function I on a uniform spatial grid as

$$I[i,j] = I(i\Delta x, j\Delta y),$$

with $i, j \in \{1, 2, \ldots, N\}$ (N is the number of samples in spatial dimensions) and $\Delta x, \Delta y \in \mathbb{R}^+$ denoting the pixel width (In general we use square images as input visual stimulus and we fix $\Delta x = \Delta y = 1$ in terms of pixel unit). Furthermore the discretized

Gabor coefficient (simple cell response) $O^I_{(\theta_k,\omega_l,\phi_m)}(q_{1,i},q_{2,j})$ of $I[i,j]$ on uniform orientation, frequency and phase grids with points $\theta_k = k\Delta\theta$, $\omega_l = l\Delta\omega$ and $\phi_m = m\Delta s$ ($k \in \{1,2,\dots,K\}$, $l \in \{1,2,\dots,L\}$, $m \in \{1,2,\dots,M\}$ where we denote the number of samples in orientation dimensions by K, in frequency dimension by L and in phase dimension by M and the distances between adjacent samples in the orientation dimension by $\Delta\theta$, in the frequency dimensions by $\Delta\omega$ and in the phase dimension by Δs) is denoted by

$$O^I_{[k,l,m]}[i,j] = O^I_{(\theta_k,\omega_l,\phi_m)}(q_{1,i},q_{2,j}),$$

where $q_{1,i} = i\Delta x$ and $q_{2,j} = j\Delta y$.

In this case the discrete version of the Gabor function given by (5.6) is written as:

$$\Psi_{[i,j,k,l,m]}[\tilde{i},\tilde{j},\tilde{n}] = \Psi_{(q_{1,i},\,q_{2,j},\,\theta_k,\,\omega_l,\,\phi_m)}(\tilde{x}_{\tilde{i}},\tilde{y}_{\tilde{j}},\tilde{s}_{\tilde{n}}),$$

where $\tilde{i},\tilde{j} \in \{1,2,\dots,\tilde{N}\}$, $\tilde{k} \in \{1,2,\dots,\tilde{K}\}$, $\tilde{n} \in \{1,2,\dots,\tilde{M}\}$ and

$$\begin{aligned}
\tilde{x}_{\tilde{i}} &= (x_{\tilde{i}} - q_{1,i})\cos(\theta_k) + (y_{\tilde{i}} - q_{2,i})\sin(\theta_k),\\
\tilde{y}_{\tilde{j}} &= -(x_{\tilde{j}} - q_{1,j})\sin(\theta_k) + (x_{\tilde{j}} - q_{2,j})\cos(\theta_k),\\
\tilde{s}_{\tilde{n}} &= s_{\tilde{n}} - \phi_m.
\end{aligned}$$

Then we fix $\tilde{s}_{\tilde{n}} = 0$ (i.e., $\tilde{n} = 0$) in the reduced framework explained in the sequel and write the discrete Gabor coefficient obtained from the image $I[i,j]$ via the discrete Gabor transform as:

$$O^I_{[k,l,m]}[i,j] = \sum_{\tilde{i},\tilde{j}} \Psi^l_{[i,j,k,m]}[\tilde{i},\tilde{j},0]\, I[\tilde{i},\tilde{j}].$$

The time correspondence in the discrete case is represented by the time index h_p where the time interval is discretized by $P \in \mathbb{N}^+$ samples and h_p represents the time instant $h_p = p\Delta t$ with Δt satisfying $T = P\Delta t$ and $p \in \{1,2,\dots,P\}$. In this case the discretized Gabor coefficient is written as

$$O^{I,p}_{[k,l,m]}[i,j] = O^{I,h_p}_{(\theta_k,\omega_l,\phi_m)}(q_{1,i},q_{2,j}) = u(t + p\Delta t).$$

8.3.2 Reduced equation

We may perform sub-Riemannian diffusion and Laplace-Beltrami procedures in each frequency and phase subspace separately. In that case we choose $c_1, c_2 > 0$ and $c_3 = c_4 = 0$. Hence the evolution equation is applied on surfaces in each frequency and phase subspace, i.e., on each $\mathrm{SE}(2)_{(\omega,\phi)}$ manifold, which is the submanifold with elements (q,θ) representing the points $(q,\theta,\omega,\phi) \in \mathcal{M}$ with fixed ω and ϕ. In this case the metric (g_{ij}) boils down to

$$(g_{ij}) = \begin{pmatrix} 1 + c_1(X_1u)^2 & \sqrt{c_1c_2}X_1uX_2u \\ \sqrt{c_1c_2}X_2uX_1u & 1 + c_2(X_2u)^2 \end{pmatrix}. \tag{8.6}$$

We choose c_1 and c_2 accordingly, regarding the fixed ω values.

8.3.3 Explicit scheme with finite differences

In this section we provide the discrete scheme related to the numerically approximated version of the algorithm. We propose an explicit finite difference scheme in order to iterate the evolution equation (8.4). The reason for choosing explicit scheme is due to the fact that implicit scheme requires large memory in our 4-dimensional (and if not reduced 5-dimensional) anisotropic framework.

We obtain the explicit scheme first by writing (8.4) in terms of the horizontal vector fields X_1, X_2, X_3 and X_4 given in (5.3). Then we follow the suggestions made by Unser [163] and Franken [74], and implement the horizontal vector fields by using central finite differences which are interpolated by B-splines on a uniform spatial sample grid. Note that B-spline interpolation is required since not all horizontal vectors are aligned with the spatial sample grid.

The interpolation is achieved by determining the coefficients $b(i,j)$

$$s(x,y) = \sum_{z,w \in Z} b(k,l)\rho(x-z, y-w),$$

in such a way that the spline polynomial $s(x,y)$ with the B-spline basis functions $\rho(x-i, y-j)$ coincides with the horizontal derivatives of the output O_p^I at the grid points. For example, in the case of the first horizontal derivative $X_1 O_p^I$, the condition $s(i\Delta x, j\Delta y) = X_1 O^I_{[k,l,m]}[i,j]$ must hold if we consider a discrete output as explained in Section 8.3.1. We refer to the explanations of Unser [163] for details. Note that finite difference schemes are preferable over Gaussian derivatives since they do not suffer from excessive blurring caused by repetitive use of the derivatives throughout the evolution in our case. Moreover Gaussian derivatives result in side lobes due to the zero-crossings in the higher order derivatives.

We fix $\Delta x = \Delta y = 1$ and define

$$\begin{aligned} e_\xi^k &:= (\Delta x \cos(\theta_k), \Delta y \sin(\theta_k)), \\ e_\eta^k &:= (-\Delta x \sin(\theta_k), \Delta y \cos(\theta_k)). \end{aligned}$$

See Figure 8.1 for an illustration of those vectors. We write the central finite differences of the first order horizontal derivatives as

$$\begin{aligned}
X_1 O^{I,p}_{[k,l,m]}[i,j] = X_1 O^{I,h_p}_{(\theta_k,\omega_l,\phi_m)}(q) &\approx \frac{1}{2\Delta x}(O^{I,h_p}_{(\theta_k,\omega_l,\phi_m)}(q+e_\xi^k) - O^{I,h_p}_{(\theta_k,\omega_l,\phi_m)}(q-e_\xi^k)), \\
X_2 O^{I,p}_{[k,l,m]}[i,j] = X_2 O^{I,h_p}_{(\theta_k,\omega_l,\phi_m)}(q) &\approx \frac{1}{2\Delta\theta}(O^{I,h_p}_{(\theta_{k+1},\omega_l,\phi_m)}(q) - O^{I,h_p}_{(\theta_{k-1},\omega_l,\phi_m)}(q)), \\
X_3 O^{I,p}_{[k,l,m]}[i,j] = X_3 O^{I,h_p}_{(\theta_k,\omega_l,\phi_m)}(q) &\approx \frac{1}{2\Delta x}(O^{I,h_p}_{(\theta_k,\omega_l,\phi_m)}(q+e_\eta^k) - O^{I,h_p}_{(\theta_k,\omega_l,\phi_m)}(q-e_\eta^k)) \\
&\quad + \frac{\omega_l}{2\Delta s}(O^{I,h_p}_{(\theta_k,\omega_l,\phi_{m+1})}(q) - O^{I,h_p}_{(\theta_k,\omega_l,\phi_{m-1})}(q)), \\
X_4 O^{I,p}_{[k,l,m]}[i,j] = X_4 O^{I,h_p}_{(\theta_k,\omega_l,\phi_m)}(q) &\approx \frac{1}{2\Delta\omega}(O^{I,h_p}_{(\theta_k,\omega_{l+1},\phi_m)}(q) - O^{I,h_p}_{(\theta_k,\omega_{l-1},\phi_m)}(q)),
\end{aligned}$$

and of the second order horizontal derivatives which we use as

$$
\begin{aligned}
X_1^2 O^{I,p}_{[k,l,m]}[i,j] = X_1^2 O^{I,h_p}_{(\theta_k,\omega_l,\phi_m)}(q) &\approx \frac{1}{(\Delta x)^2}(O^{I,h_p}_{(\theta_k,\omega_l,\phi_m)}(q+e^k_\xi) - 2O^{I,h_p}_{(\theta_k,\omega_l,\phi_m)}(q) \\
&\quad + O^{I,h_p}_{(\theta_k,\omega_l,\phi_m)}(q-e^k_\xi)), \\
X_2^2 O^{I,p}_{[k,l,m]}[i,j] = X_2^2 O^{I,h_p}_{(\theta_k,\omega_l,\phi_m)}(q) &\approx \frac{1}{(\Delta\theta)^2}(O^{I,h_p}_{(\theta_{k+1},\omega_l,\phi_m)}(q) - 2O^{I,h_p}_{(\theta_k,\omega_l,\phi_m)}(q) \\
&\quad + O^{I,h_p}_{(\theta_{k-1},\omega_l,\phi_m)}(q)), \\
X_3^2 O^{I,p}_{[k,l,m]}[i,j] = X_3^2 O^{I,h_p}_{(\theta_k,\omega_l,\phi_m)}(q) &\approx \frac{1}{(\Delta x)^2}(O^{I,h_p}_{(\theta_k,\omega_l,\phi_m)}(q+e^k_\eta) - 2O^{I,h_p}_{(\theta_k,\omega_l,\phi_m)}(q) \\
&\quad + O^{I,h_p}_{(\theta_k,\omega_l,\phi_m)}(q-e^k_\eta)) + \frac{\omega_l^2}{(\Delta s)^2}(O^{I,h_p}_{(\theta_k,\omega_l,\phi_{m+1})}(q) - 2O^{I,h_p}_{(\theta_k,\omega_l,\phi_m)}(q) \\
&\quad + O^{I,h_p}_{(\theta_k,\omega_l,\phi_{m-1})}(q)) + \frac{2}{4\Delta s\Delta_x}(O^{I,h_p}_{(\theta_k,\omega_l,\phi_{m+1})}(q+e^k_\eta) \\
&\quad - O^{I,h_p}_{(\theta_k,\omega_l,\phi_{m+1})}(q-e^k_\eta) - O^{I,h_p}_{(\theta_k,\omega_l,\phi_{m-1})}(q+e^k_\eta) \\
&\quad + O^{I,h_p}_{(\theta_k,\omega_l,\phi_{m-1})}(q-e^k_\eta)), \\
X_4^2 O^{I,p}_{[k,l,m]}[i,j] = X_4^2 O^{I,h_p}_{(\theta_k,\omega_l,\phi_m)}(q) &\approx \frac{1}{(\Delta\omega)^2}(O^{I,h_p}_{(\theta_k,\omega_{l+1},\phi_m)}(q) - 2O^{I,h_p}_{(\theta_k,\omega_l,\phi_m)}(q) \\
&\quad + O^{I,h_p}_{(\theta_k,\omega_{l-1},\phi_m)}(q)).
\end{aligned}
$$

Then the numerical iteration (discretized from step 2 of the algorithm provided in Section 8.3) with time step $\Delta t > 0$ is written as:

$$
O^{I,p+1}_{[k,l,m]}[i,j] = O^{I,h_{p+1}}_{(\theta_k,\omega_l,\phi_m)}(q_{i,1},q_{j,2}) = O^{I,h_p}_{(\theta_k,\omega_l,\phi_m)}(q_{i,1},q_{j,2}) + \Delta t \bar{L} O^{I,h_p}_{(\theta_k,\omega_l,\phi_m)}(q_{i,1},q_{j,2}), \tag{8.7}
$$

where $\bar{L}$ represents the discretized version of either Δ_0 or $\Delta_{(g_{ij})}$, with coefficients $c = \{c_1 > 0, c_2 > 0, c_3 = 0, c_4 = 0\}$, in terms of the central finite differences.

8.4 Stability analysis

The finite difference scheme which we use in our experiments is implemented by using the recipe provided by Unser et al. [163] and explained by Franken [74]. The implementation is based on sampling the horizontal left-invariant vector fields $\{X_1, X_2\}$ with discrete $\theta_k \in S^1$, $\omega_l \in \mathbb{R}^+$, $\phi_m \in S^1$ values and then interpolating via B-spline interpolation of some order (we use 3^{rd} order in our experiments). Finite difference scheme in the reduced framework is associated to the geometric setting of SE(2) at each frequency and phase subspace of the space of $\mathcal{M}$.

In this case there are two important points related to the finite difference scheme stability:

1. Suitable choice of the time step size Δt for stable evolution processes,

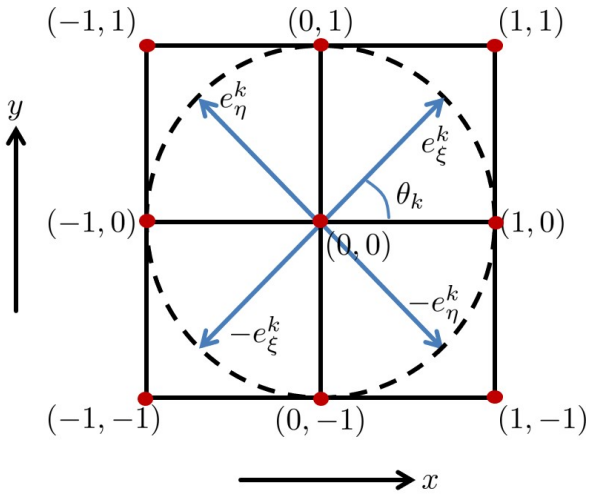

Figure 8.1: Illustration of the vectors e^k_ξ and e^k_η at $(0,0)$ with $\Delta x = \Delta_y = 1$.

2. Preserving the space homogeneity during the evolution processes.

The stability analysis for the SE(2) case is explained by Franken [74] based on Gershgorin theory. We adapt the technique used by Franken in [74] to our reduced framework and find the upper limit for the time step Δt as:

$$\Delta t \leq \frac{2\left(\frac{s_\theta}{\beta}\right)^2}{4 + 4(1+\sqrt{2})\left(\frac{s_\theta}{\beta}\right)^2},$$

where $s_\theta = \frac{2\pi}{K}$ is the sampling distance between adjacent orientation samples with $K \in \mathbb{N}^+$ denoting the number of the orientation samples and β is the ratio between orientation and spatial samples. It is either $1/8$ or $1/4$ in our experiments, yielding $\Delta t \leq 0.17$ for stable processes in both cases. We refer to [74, Chapter 6] and [41] for details.

The second point is due to that we sample each dimension by using a different number of samples. In order to perform sub-Riemannian diffusion by regarding the sample unit coherency one must choose the parameters c_1 c_2 (and also c_3 and c_4 in the non-reduced case) of the operator Δ_0 in such a way that the space homogeneity of $\mathcal{M}$ is preserved.

8.5 Experiments

In this section we present our experimental results related to the enhancement via sub-Riemannian diffusion or Laplace-Beltrami procedure.

8.5.1 Gabor transform

The delicate point related to the lifting and inversion process is that Gabor functions $\Psi_{(q,\theta,\omega,\phi)}(x, y, s)$ must be sampled (in orientation θ, frequency ω and phase ϕ dimensions) in such a way that they cover all the spectral domain (that is, they fulfill the Plancherel's formula [133] given by (4.1)).

We present some results of the Gabor transform-inverse transform procedure associated to our setting and the effects of number of samples in the orientation dimension in Figure 8.2. We use the Gabor filter banks obtained from (5.4) and (5.6) with scale value of 2 pixels (total filter size is 24 pixels) in order to lift the test images (see Figure 8.3 for some examples of those Gabor functions). On the top row the artificial 64×64 test image (left), the transformed and then inverse transformed image with frequency samples $\omega \in \{0.5, 1, \ldots, 2.5, 2.75, \ldots, 4.5, 4.625, \ldots, 6.5\}$, orientation samples $\theta \in \{\frac{2\pi}{32}, \frac{4\pi}{32}, \ldots, \frac{62\pi}{32}\}$ and phase samples $\phi \in \{0, \frac{\pi}{8}, \ldots, \frac{15\pi}{8}\}$ (middle left), similarly the lifted and inverse transformed image but with less number of phase samples $\phi \in \{0\}$ (middle right) or with less number orientation samples $\theta \in \{0, \frac{2\pi}{8}, \ldots, \frac{14\pi}{8}\}$ (right) are given. On the bottom row, the results of the same procedures with the same samples but with a real test image are given. We observe that the decrease in the number of orientation samples reduce the quality of the tansformation procedure noticeably.

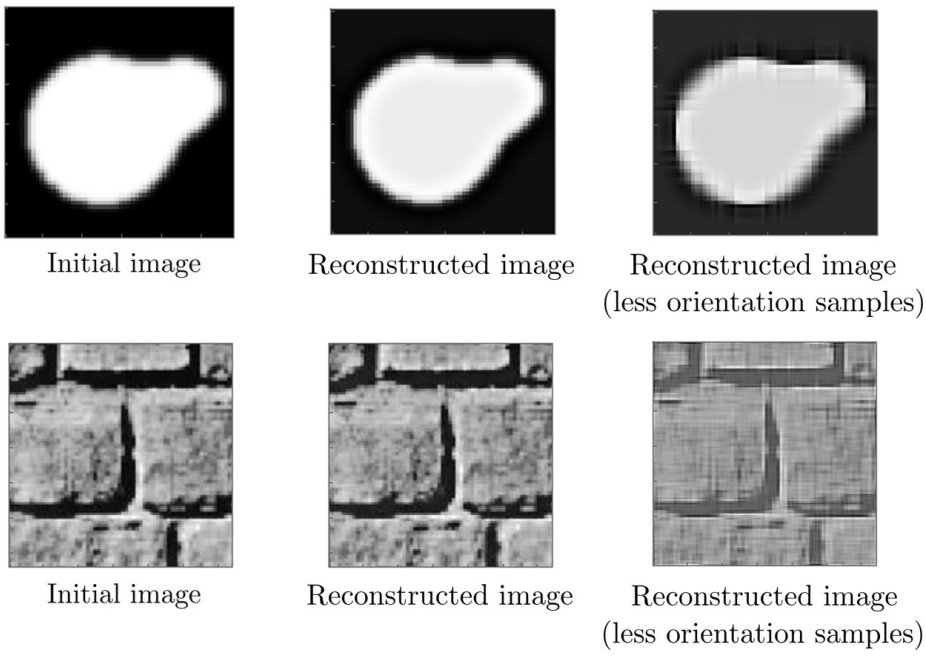

Figure 8.2: Examples of reconstructed images via transform and inverse transform procedure with Gabor functions, and the effect of number of orientation samples.

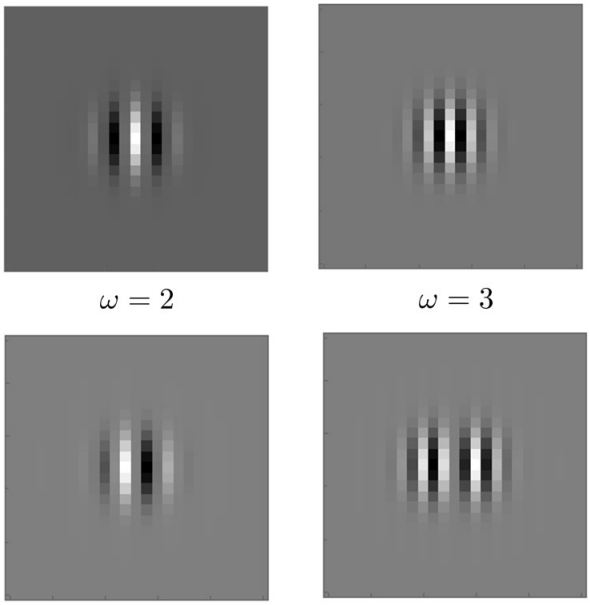

Figure 8.3: Examples of the Gabor filters used in the lifting procedure of Figure 8.2. Top: Even parts of Gabor functions with frequencies $\omega = 2, 3$. Bottom: Odd parts of the same Gabor functions.

8.5.2 Enhancement

The results presented here are obtained via the sub-Riemannian diffusion and Laplace-Beltrami procedure which are explained in Section 8.3 in terms of (8.2), (8.3) and (8.4). We use the reduced versions of those algorithms for practical considerations since the procedures are heavily memory loaded. In the reduced case the procedures will be applied in each frequency and phase sample separately. More precisely the reduced version corresponds to the operator $\bar{L}$ (see (8.7)), which is the discrete version of the operator L (see also (8.2), (8.3) and (8.5)), where $c_1, c_2 > 0$ and $c_3 = c_4 = 0$. In the case of Laplace-Beltrami operator, the corresponding metric to the reduced case is the reduced metric given by (8.6). Note that the lifting procedure is performed by the Gabor filters of the type given by (5.4) and (5.6) with scale = 2 pixels (the filter size is $12 \times$ scale = 24 pixels) and time step $\Delta t = 0.1$ in the experiments.

In Figure 8.4 we obtain the results by using the enhancement algorithm via both sub-Riemannian diffusion and Laplace-Beltrami procedures. The procedures are applied on a 64×64 artificially produced gray scale image with white noise. The lifting is achieved with frequency samples $\omega \in \{0.5, 1, \ldots, 2, 2.25, \ldots, 4.5\}$, phase samples $\phi = \{0, \frac{\pi}{8}, \ldots, \frac{\pi}{2}\}$ and orientation samples $\theta \in \{0, \frac{2\pi}{16}, \frac{4\pi}{16}, \ldots, \frac{30\pi}{16}\}$. We have image size = 64, number of orientations = 16. Then $\beta = \frac{\text{number of orientations}}{\text{image size}} = 0.25$. In order to fulfill physical unit coherency we choose $c_1 = 1$ and $c_2 = \beta^2$ in the sub-Riemnnian Laplacian Δ_0 (see (8.2)). The simulations are done with 15 and 30 iterations. We observe that

the Laplace-Beltrami procedure preserves the boundaries better in comparison to the sub-Riemannian diffusion due to the fact the metric is updated at every iteration in accordance with the evolved image.

We continue with Figure 8.5 where we apply our procedures on a real 128×128 image taken from Kimmel et. al. [107]. We use the same phase and orientation samples as in the case of Figure 8.4 while we employ the frequency samples $\omega \in \{0.5, 1, \ldots, 2, 2.25, \ldots, 4.5, 4.625, \ldots, 6\}$ for the lifting. The coefficients c_1, c_2 of the sub-Riemannian Laplacian are chosen as in the case of Figure 8.4. Then we perform the enhancement procedures with 30 and 50 iterations. In this case the Laplace-Beltrami procedure reduces the noise in the interior regions of the objects in the image while it preserves the boundaries noticeably better than the sub-Riemannian diffusion.

In Figure 8.6 we present the same results of our Laplace-Beltrami procedure shown in Figure 8.5 and the results obtained by Kimmel et. al.[107] for a comparison. In [107] they use a multi-scale Laplace-Beltrami procedure with a fixed frequency.

We show in Figure 8.7 the results related to our Laplace-Beltrami procedure applied on another real image, with dimensions 64×64, taken from Kimmel et. al. [107]. We use the same sampling parameters as in the previous case of Figure 8.5 for the lifting. We perform our Laplace-Beltrami procedure with 6 and 15 iterations. The results are presented together with the multi-scale Laplace-Beltrami results obtained by Kimmel et. al [107] for a comparison.

Original image

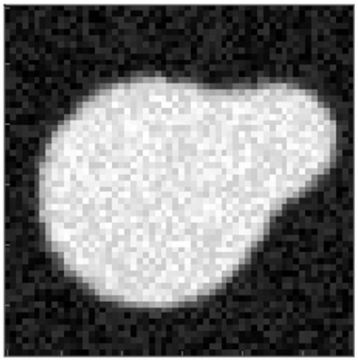

Noisy image

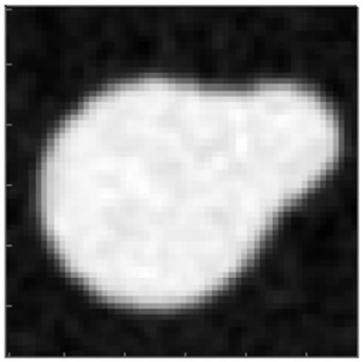

Sub-Riemannian diff.
(15 iterations)

Sub-Riemannian diff.
(30 iterations)

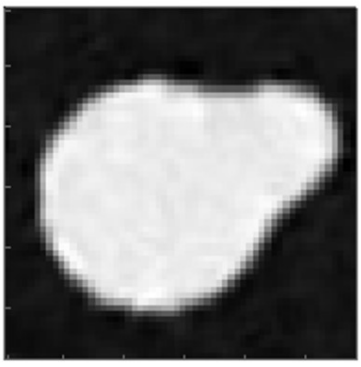

Laplace-Beltrami
(15 iterations)

Laplace-Beltrami
(30 iterations)

Figure 8.4: Top: The original 64×64 image (left) and the noisy version (right). Middle: The results of the sub-Riemannian diffusion. Bottom: The results of the Laplace-Beltrami procedure.

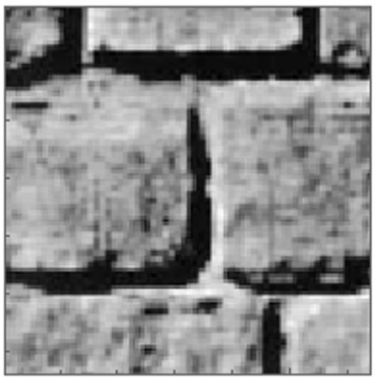

Initial image

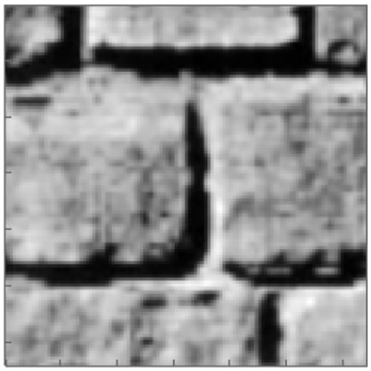

Sub-Riemannian diff.
(30 iterations)

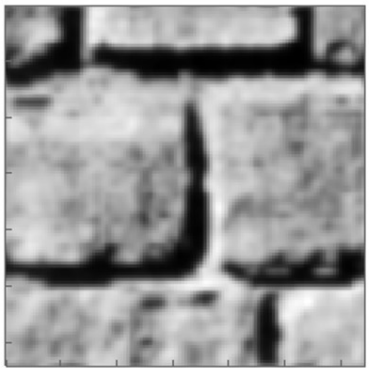

Sub-Riemannian diff.
(80 iterations)

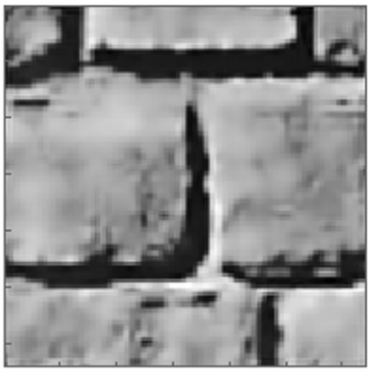

Laplace-Beltrami
(30 iterations)

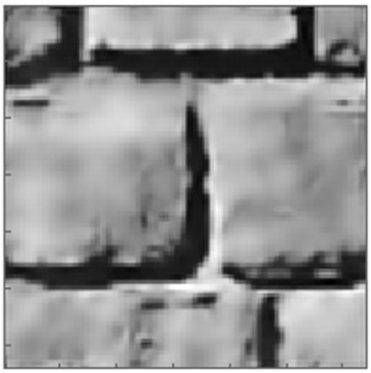

Laplace-Beltrami
(80 iterations)

Figure 8.5: Top: The initial image taken from [107]. Middle: The results of the sub-Riemannian diffusion. Bottom: The results of the Laplace-Beltrami procedure.

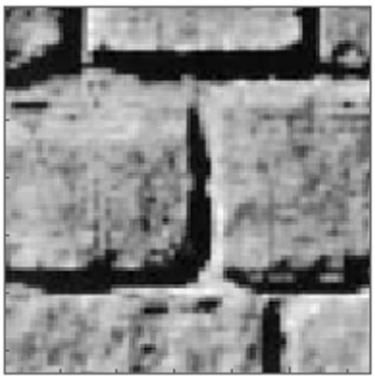

Initial image

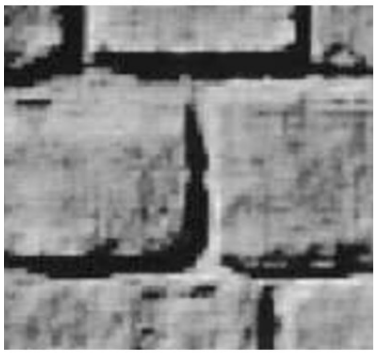

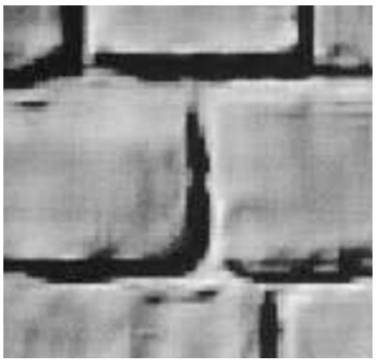

Multi-scale Laplace-Beltrami of Kimmel et. al.

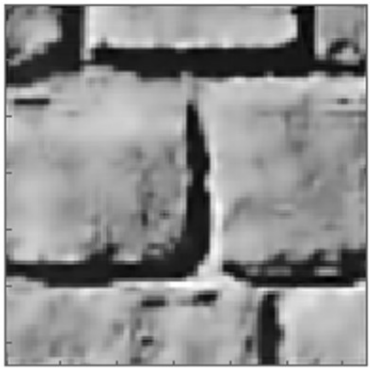

Our Laplace-Beltrami
(30 iterations)

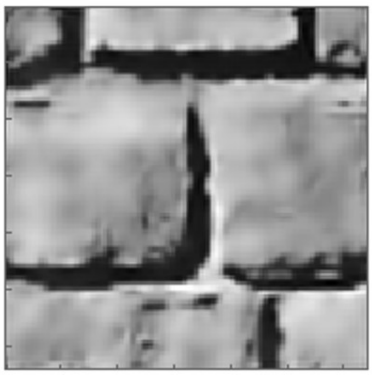

Our Laplace-Beltrami
(80 iterations)

Figure 8.6: Top: The initial image taken from [107]. Middle: The results of our Laplace-Beltrami. Bottom: The results obtained by Kimmel et. al. [107].

Initial image

Multi-scale Laplace-Beltrami of Kimmel et. al.

Our Laplace-Beltrami
(6 iterations)

Our Laplace-Beltrami
(15 iterations)

Figure 8.7: Top: The initial image taken from [108]. Middle: The results of our Laplace-Beltrami. Bottom: The results obtained by Kimmel et. al. [108].

Part III

Feature map construction via a Bargmann transform

Chapter 9

Multi-scale orientation map construction via a Bargmann transform in the cortical space

In this chapter we present a new model for the generation of orientation preference maps in the primary visual cortex (V1), considering both orientation and scale features. We use the model geometry proposed by Sarti, Citti and Petitot [146] and explained in Section 4.4. Orientation preference maps are obtained by mapping the orientation values, found from the lifting of a noise stimulus, onto the 2-dimensional retinal plane. This corresponds to a Bargmann transform in the reducible representation of the roto-translation group $\mathrm{SE}(2) = \mathbb{R}^2 \times S^1$.

As it is well known the simple cells in the primary visual cortex are organized in structures called orientation preference maps (see Figure 9.1 for an example of such maps). This special organization has been studied with geometric instruments starting by the work of Petitot and Tondut [132]. In that study the orientation maps were obtained as a superposition of randomly weighted orientation fields corresponding to all possible orientation angles around the pinwheels (see the geometric explanations of Petitot [130] related to the pinwheels). A different model, always based only on orientation was introduced by Barbieri et al. [4], [5]. In that article the orientation preference structure was recovered starting from the observation of that its Fourier transform was concentrated on an annulus. This model as the previously mentioned one, was based on properties apparently independent of the other aspects of the cortical models. Additionally to those studies, the models, in terms of cortical orientation and orientation-frequency selectivity, which were provided by Bressloff and Cowan [25], [24], and the model proposed for the cortical spatio-temporal selective behavior by Barbieri et. al. [3] are to be mentioned as useful references for the reader.

Let us recall that in the case with orientation and scale the base variables are the spatial components $(x, y) \in M \simeq \mathbb{R}^2$ on the retinal plane M and the intrinsic variables are orientation and scale parameters $(\theta, \sigma) \in S^1 \times \mathbb{R}^+$. Having two intrinsic variables in hand, we can either fix scale and obtain the orientation map of the simple cells or we

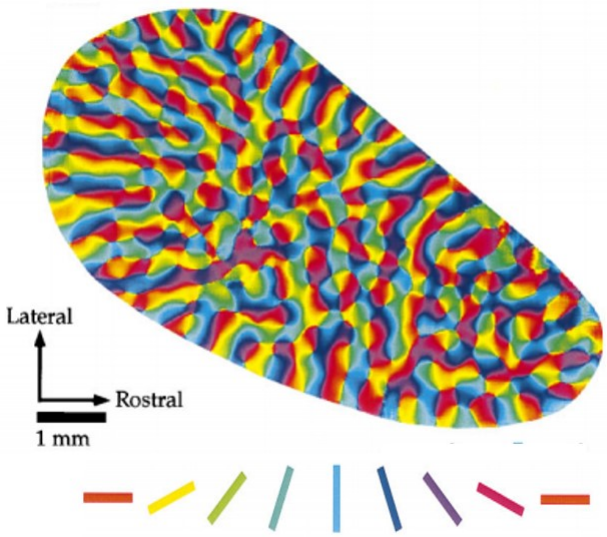

Figure 9.1: The orientation preference map of a tree shrew V1 (taken from Bosking et. al. [20, Figure 1]). It was obtained via a vector summation of the data recorded for each angle by using optical imaging.

can employ a range of scale values and obtain a multi-scale orientation map (and also a scale preference map). In this way the model integrates several visual features observed in neurophysiology, psychophysics and neuroimaging experiments and provides a more precise orientation map.

The main novelty of our approach is that the orientation map description is strongly related to the functionality of the cortex and simple cell responses in presence of a visual stimulus. Indeed we start with a random stimulus I on the retinal plane, and obtain the responses of the cells through a linear filtering of I with translated, rotated and dilated Gabor functions. Finally, we employ an integration of the output over fiber and a maximum selection in order to select the prevalent orientation and scale. This amounts to a lifting. Consequently we propose to obtain orientation maps by employing the lifting of noise stimulus through the functional structure of the cortex. We will outline that this corresponds to a Bargmann transform [6] in the reducible representation of the SE(2) group, which is different than the case in [4] where Barbieri et. al. considered the irreducible representation. As a result of the use of reducible representation all the principal morphologies present in the visual cortex are modeled in a compact way in the neurogeometrical framework. Hence our model is more plausible in neurophysiological sense.

In the specific model which we propose in this chapter, we have used only the Gabor filters without any shift in phase. In this case the Gabors can be easily replaced with derivatives of Gaussians, without loss of generality. However the choice we made based on Gabors allows us to extend the model to the true distribution of the receptive pro-

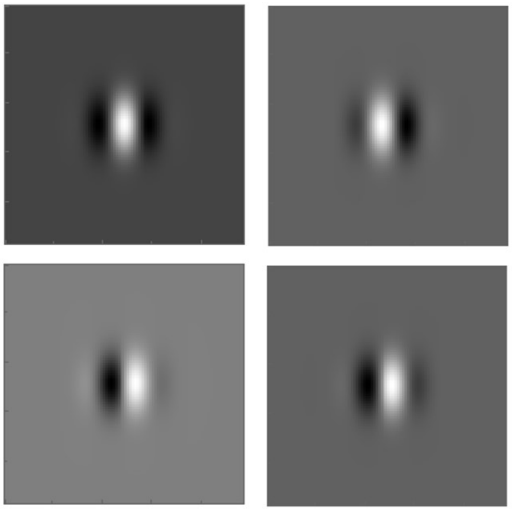

Figure 9.2: Real (or even, top row) and imaginary (or odd, bottom row) parts of the Gabor filters. The figures on the left hand side correspond to the Gabor filters with no phase shift while the ones on the right hand side correspond to the phase shifted Gabor filters with $\frac{\pi}{4}$.

files in V1 (including the asymmetric receptive profiles with shifts in phase), i.e., to a neurophysiologically coherent generic model of the visual cortex (see Chapter 5 where we present such a novel generic model which considers the additional features frequency and phase, as well as orientation). Furthermore above mentioned families of Gaussian functions account just for symmetric receptive profiles, where the shift in the phase changing the shape of the profile is not considered. In other words the Gabor functions are able to model both asymmetric simple cells and even/odd symmetric simple cells while the functions of the Gaussian derivatives model only the symmetric simple cells (see Figure 9.2 for some examples of the even/odd Gabor functions with no phase shift and their phase shifted versions). The reader can find more information about the models employing alternative choices of receptive profiles in terms of Gaussian derivatives in the works of Koenderink [109], [110] and Lindeberg [116].

We refer to Section 4.4 for the notation and explanations related to the receptive profiles, the group structure with its geometrical properties and the functional connectivity in the group geometry. We start here directly by giving the explicit procedure of the construction of the cortical preference map in Section 9.1. Afterwards, in Section 9.2, we show that the Gabor functions are minimizers of an uncertainty principle associated to orientation and also scale selectivity. Then we show that the filtering of visual stimulus with the Gabors can be interpreted as a Bargmann transform in the reducible representations. Then we provide the relation of the Bargmann transform to the orientation map construction procedure and we compare it to the above mentioned method of Barbieri et. al. [4], which uses the Bargmann transform with the Gabor functions in the irreducible representations on the Fourier domain. Finally in Section 9.4, we test the model

at different scales in order to represent the properties of orientation maps in different cortical areas where the scales of receptive profiles change. Additionally we compare our simulation results to the relevant neurophysiological findings in the literature.

9.1 The model of multi-scale orientation maps

In this section we present our model of orientation cortical maps. We propose that the cortical maps are obtained via a two step procedure: First the simple cells act on a random stimulus at a point on the retinal plane, and consequently preferred orientation and scale of the maximally activated simple cell gives the selected orientation and scale. The selected orientation and scale values at every point produce the cortical map.

Recall that the response given to a stimulus by a simple cell located at $(q_1, q_2) \in M$ and with orientation preference θ, scale preference σ is expressed by

$$O^I_{(\theta,\sigma)}(q_1, q_2) = \int_M I(x, y)\Psi_{(q_1,q_2,\theta,\sigma)}(x, y)\, dx\, dy. \tag{9.1}$$

See Figure 4.5 for an approximate visualization of such response outputs. For every retinal point (q_1, q_2) a particular value of orientation is selected via the integration on the fiber:

$$\bar{\theta}(q_1, q_2) = \frac{1}{2} \arg\Big(\int_0^{\pi} \mathrm{Re}\left\{ O^I_{(\theta,\sigma)}(q_1, q_2) \right\} \mathrm{e}^{i\theta} d\theta \Big). \tag{9.2}$$

We considered here only the real part of the output but alternative choices are possible, for example the energy or the imaginary part of the output (see Section 4.4.4 for more details). Furthermore the coefficient $1/2$ is due to the fact that a walk along an arc of angle θ around the pinwheel center corresponds to a change of orientation angle preferences of the simple cells by $\theta/2$ (we refer to the explanations of Petitot [131, Chapter 2, p.88] for details). Finally (9.2) describes a vector summation where each vector of a single orientation is weighted by the corresponding response of the simple cell. It coincides with the method which Bosking et. al. [20] used where they obtain the orientation map of the tree shrew by performing a vector summation of the activity pattern measurements from the tree shrew V1.

Lindeberg, in [115], describes a scale selection technique in terms of the Gaussian derivatives normalized by scale. It finds extrema over the scales corresponding to normalized receptive field responses by scale. A similar approach in our particular framework associated to the Gabor functions is considered and the scale selectivity is provided by the maximum of the output at the point (q_1, q_2) over the scale on the fiber at the selected value of $\bar{\theta}$:

$$\bar{\sigma}(q_1, q_2) = \underset{\sigma \in \mathbb{R}^+}{\mathrm{argmax}} \Big(\mathrm{Re}\left\{ O^I_{(\bar{\theta},\sigma)}(q_1, q_2) \right\} \Big). \tag{9.3}$$

Let us note that the maximum selectivity (9.3) for selecting the scale value is similar to the method which Sarti et. al. used in [146] (see (4.11) for a description of the

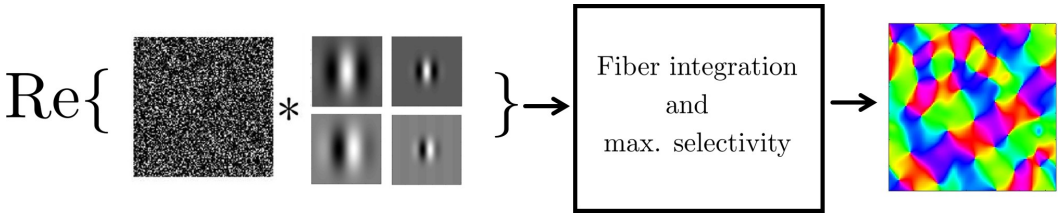

Figure 9.3: A white noise image is filtered by the Gabor filters with different scales. The Integration over fiber and the maximum selectivity among the integrated fiber values are applied on the real part of the filtering result. The orientation preference map is obtained by assigning a certain color to each orientation value.

method). However here we use the integration over fiber (9.2) in order to find the orientation preference at the point $(q_1, q_2) \in M$ and it allows us to achieve a more robust orientation selectivity. We assume that generically there is a unique maximum, so the orders in which we select $\bar{\theta}$ and $\bar{\sigma}$ are equivalent. Note that the procedure described by (9.2) and (9.3) is done for every fixed point (q_1, q_2) on the retinal plane and the selected orientations $\bar{\theta}(q_1, q_2)$ and scales $\bar{\sigma}(q_1, q_2)$ are represented at the corresponding fiber locations $(q_1, q_2) \in M$ in terms of certain color maps. In this way we obtain the multi-scale orientation map $\bar{\theta}(x, y)$ which is represented in Figure 9.8 with the same type of color map as in the classical case of Bosking et. al. [20] shown in Figure 9.1. The overall procedure for obtaining the cortical maps is schematized in Figure 9.3.

This procedure corresponds to the lifting of a general stimulus $I(x, y)$ provided by the simple cell circuitry. We explicitly note here that cortical orientation maps will be obtained by using the lifting of a random stimulus. This choice is motivated by the experimental observation of that the cortical maps arise in the early post natal period in the absence of any visual experience, only in the presence of an intrinsic random basal activation (see the studies of Tanaka et. al. [155], Bednar and Miikkulainen [10], Jegelka et. al. [97]). A refinement of the orientation maps is performed subsequently by the activation patterns based on random waves (see the results provided by Stellwagen and Shatz [152], Cang et. al. [28]).

We note that convolution with a Gabor filter will provide a smooth function. Indeed the Gabor is simply a Gaussian function multiplied by a complex exponential. The resulting function will then be a smooth function depending on the variance of the Gaussian, which is the scale. Finally the orientation selection will provide smooth functions, with values in S^1. It is well known that even harmonic functions with values in S^1 develop vortices, which will be the models for the pinwheels.

It is natural to build the feature cortical maps by means of the Gabor functions, since they are strictly related to the whole functional geometry of the cortex. In fact we will see that they arise as minimizers of the uncertainty principle in the geometrical setting here.

9.2 Orientation map as a cortical Bargmann transform

9.2.1 Gabors as minimizers of the uncertainty principle

Let us recall from Section 5.8 that the Gabor functions were the minimizers (coherent states) of an uncertainty principle in non-commutative framework.

Analogously, in the present setting here as well, the Gabors are the coherent states of the associated uncertainty principle. Consider $A_{(q_1,q_2,\theta,\sigma)}$, which is defined in (4.6). Accordingly the differential of $A^{-1}_{(q_1,q_2,\theta,\sigma)}$ sends the vector fields

$$\begin{aligned} X_1 =& \mathrm{e}^{\sigma}(\cos(\theta)\partial_x + \sin(\theta)\partial_y), \\ X_2 =& \partial_\theta, \end{aligned}$$

acting in the 4-dimensional manifold of variables (x, y, θ, σ) to new vector fields Y_1 and Y_2 defined on the retinal plane as:

$$\begin{aligned} (dA^{-1})(X_1) =& \partial_{\tilde{x}} = Y_1, \\ (dA^{-1})(X_2) =& \tilde{y}\partial_{\tilde{x}} - \tilde{x}\partial_{\tilde{y}} = Y_2, \end{aligned} \tag{9.4}$$

where $\tilde{x}$ and $\tilde{y}$ are the local coordinate variables on M as described in (4.6).

Precisely the Gabor functions of the type $\Psi_{(q_1,q_2,\theta,\sigma)}$ given by (4.7) satisfy

$$\begin{aligned} Y_1\Psi_{(q_1,q_2,\theta,\sigma)}(x,y) &= -2\tilde{x}\Psi_0(\tilde{x},\tilde{y}), \\ Y_2\Psi_{(q_1,q_2,\theta,\sigma)}(x,y) &= -i2\tilde{x}\Psi_0(\tilde{x},\tilde{y}), \end{aligned}$$

which fulfill the coherent state (minimizer) condition

$$Y_1\Psi_{(q_1,q_2,\theta,\sigma)}(x,y) = i\lambda Y_2\Psi_{(q_1,q_2,\theta,\sigma)}(x,y), \tag{9.5}$$

with $\lambda = -1$.

9.2.2 Interpretation of the cortical maps as a Bargmann transform of a random stimulus

Let us recall that the operator associated to coherent states is called the Bargmann transform:

$$\begin{aligned} (B^{SE(2)}I)(q_1,q_2,\theta,\sigma) :=& \langle \Psi_{(q_1,q_2,\theta,\sigma)},\ I\rangle_{L^2(\mathbb{R}^2)} \\ =& \int_{\mathbb{R}^2} \Psi_{(q_1,q_2,\theta,\sigma)}(\tilde{x},\tilde{y})I(\tilde{x},\tilde{y})d\tilde{x}\,d\tilde{y}. \end{aligned}$$

In particular, the response of the simple cells, being defined by (9.1) as the convolution with a Gabor coherent state, can be interpreted as the Bargmann transform in the functional architecture:

$$O^I_{(\theta,\sigma)}(q_1,q_2) = (B^{\mathrm{SE(2)}}I)(q_1,q_2,\theta,\sigma).$$

As a consequence, the orientation maps are associated to the Bargmann transform of a random stimulus.

9.3 Comparison with previous models of the cortical maps

9.3.1 Superposition of random waves

One of the first models for the construction of the orientation preference maps was proposed by Petitot in [130] where the map was obtained through the superposition of randomly weighted complex sinusoids

$$\sum_{k=1}^{N} c_k \mathrm{e}^{i2\pi\left(x\cos(2\pi k/N)+y\sin(2\pi k/N)\right)},$$

with N denoting the number of frequency samples and where the coefficients $c_k \in [0,1]$ are the white noise.

In this way the functional role of a receptive profile is disregarded since the orientation map is constructed via direct superimposition of the waves with randomly generated magnitudes, avoiding that the receptive profile naturally processes the stimulus by lifting it to the cortical space of corresponding intrinsic variables. Moreover in this procedure the complex sinusoid functions are not localized while it is known from several neurophysiological experiments that the orientation selectivity is performed locally by the simple cells (see for example the work of Field and Tolhurst [65]).

9.3.2 The Bargmann transform of the irreducible representations

In the model proposed by Barbieri et. al. in [5], the orientation map was built by starting from the coherent states in the irreducible representation.

Definition 9.1. *The representation of a group G is a map $\Phi : G \to \mathcal{A}(V)$, from the group G to the space of automorphisms $\mathcal{A}$ of a vector space V, such that Φ is compatible with the group law. The representation will be denoted by (Φ, V), and it is called* irreducible *if it has no proper group subrepresentation (Φ, W), where W is a subspace of V.*

Taking the Fourier transform of the vector fields Y_1 and Y_2 defined in (9.4), we obtain:

$$\mathcal{F}(Y_1 f) = iz_1\hat{f}, \quad \mathcal{F}(Y_2 f) = (z_2\partial_{z_1} - z_1\partial_{z_2})\hat{f}.$$

It is possible to write those vector fields also in terms of polar coordinates which are given by $(z_1, z_2) = (\Omega\cos(\varphi), \Omega\sin(\varphi))$ with $\Omega \in \mathbb{R}^+$ and $\varphi \in S^1$. In this case the fields become

$$\hat{Y}_1\hat{f} = i\Omega\cos(\varphi)\hat{f}, \quad \hat{Y}_2\hat{f} = \partial_\varphi\hat{f}.$$

The vector fields $\hat{Y}_1$ and $\hat{Y}_2$ do not contain any radial derivative and only depend on the angular direction in the Fourier space. Therefore they act independently on each

circle of an arbitrary radius Ω. Then it is possible to restrict the action of these vector fields to any circle with radius Ω on the Fourier space separately (see the explanations of Sugiura [153] for details). This is the reason why the vector fields Y_1 and Y_2 on the whole space (in the Fourier domain as well) are called reducible, while $\hat{Y}_1$ and $\hat{Y}_2$ which cannot be further reduced (once Ω is fixed) are called irreducible.

If we write the coherent state condition (9.5) on the Fourier domain in terms of $\hat{Y}_1$ and $\hat{Y}_2$,

$$\hat{Y}_1 \hat{f} = i\lambda \hat{Y}_2 \hat{f},$$

we find the coherent states

$$\hat{\Psi}^{\Omega}_{(q_1,q_2,\theta,\sigma)}(\varphi) = \hat{\Psi}_{(q_1,q_2,\theta,\sigma)}(\Omega\cos(\varphi), \Omega\sin(\varphi)),$$

where $\hat{\Psi}_{(q_1,q_2,\theta,\sigma)}$ is the Fourier transform of the Gabor filters, while $\hat{\Psi}^{\Omega}_{(q_1,q_2,\theta,\sigma)}$ is a function of the angular variable, which is defined on the circle of radius Ω.

In [4] and [5] Barbieri et. al. use the family of the coherent states

$$\hat{\Psi}^{\Omega}_{(q_1,q_2,\theta)},$$

obtained for a fixed value of σ, and for a single value of Ω.

In perfect analogy with equation (9.1) the Bargmann transform in these variables is expressed as the operator with kernel $\hat{\Psi}^{\Omega}_{(q_1,q_2,\theta)}$ as:

$$\begin{aligned} B^{\Omega}g(x,y,\theta) :=& \langle \hat{\Psi}^{\Omega}_{(q_1,q_2,\theta)},\ g\rangle_{L^2(S^1)} \\ =& \int_0^{2\pi} \hat{\Psi}^{\Omega}_{(q_1,q_2,\theta)}(\varphi) g(\varphi) d\varphi. \end{aligned}$$

In [4] and [5], this transform is applied to a white noise g defined on the annulus (on the Fourier domain). For every point (x, y) an orientation is selected by means of an integration analogous to the one expressed in (9.2):

$$\bar{\theta}^{\Omega}(x,y) = \frac{1}{2}\arg\Big(\int_0^{\pi} \Big\{B^{\Omega}g(x,y,\theta)\Big\} \mathrm{e}^{i\theta} d\theta\Big). \tag{9.6}$$

This integration gives an orientation preference at a single point (x, y) which depends on the fixed value of Ω and the orientation preference maps (with no scale parameters) are obtained by applying (9.6) at every point (x, y).

Although both our model and the model proposed in [4] and [5] make use of the idea of a Bargmann transform they differ on three points.

Firstly our method employs the coherent states corresponding to the reducible representations while the other technique uses the states restricted to the irreducible representations in the Fourier domain.

Secondly we start from a noise generated on the real domain and apply the Bargmann transform, while the other method introduces the noise in the Fourier domain on the

irreducible representations, and apply the Bargmann transform in the Fourier space. The choice made in the present study here is physiologically more plausible since the cortical maps can be formed up to a certain level in the early post natal period in the presence of a random basal activation (see [10] and [97]) before the exposure of the retina to any external stimulus. The present model has the potential to provide a reasoning and an explanation of how the formation of the cortical maps occurs at the neurophysiological level.

The third main difference is that the present model can also consider the scale selectivity while in the other model the scale is fixed. More generally it is possible to extend the present model in order to include other visual features by using generalized Gabor functions.

9.4 Experiments

We consider a stimulus $I(x, y)$ of 128×128 pixels with random values generated from a uniform distribution over $[-1, 1]$ at each pixel.

We obtain the total set of simple cell responses via the linear filtering of the test image I with a rotated and translated Gabor filter bank as described in (9.1) with different scale values σ. Then we represent the selected orientation $\bar{\theta}(x, y)$ and $\bar{\sigma}(x, y)$, via (9.2) and (9.3), at every point (x, y) on the 128×128 image plane.

Previously in the literature it was reported from the physiological experiments of Bosking [20] (see Figure 9.1) that the orientation preference map had certain characteristics (see the explanations of Bressloff and Cowan [23], and Petitot [130, p.87], [36, p.27]). To begin with, the orientation preferences on the map are distributed almost continuously across the cortex and the pinwheel architecture is crystalline-like. In other words there is a regular lattice of the pinwheels on the orientation preference map with a certain spatial periodicity. Furthermore the orientation map contains three types of points as described by Petitot [130, p.87], namely : a) Regular points around which the orientation iso-lines are parallel (the zones with the regular points are called *linear zones*), b) Singular points which are located at the center of the pinwheels (Those singularities might have positive or negative *chirality*. That is, when we turn around a pinwheel in the clockwise direction, the orientations turn in the clockwise direction - positive chirality - or in the counter clockwise direction - negative chirality. The pinwheels represent opposite chiralities when they are adjacent to each other), c) Saddle points at the center of regions where iso-orientation lines bifurcate (the case where two iso-orientation lines start from the same pinwheel and arrive at the opposite pinwheels).

We will see that in the present study, we are able to produce all the three kinds of points. In the first experiment we consider different fixed scales and apply (9.1) and (9.2) to obtain the orientation maps: Results are shown in Figure 9.4, where the orientation maps are visualized and the three kinds of points are highlighted.

Figure 9.5 shows the cross correlation between the simulated cortical maps where several peaks are shown to verify the crystalline-like periodic structure of the map. Notice that the periodicity of the peaks is dependent on the scale of the Gabor filters

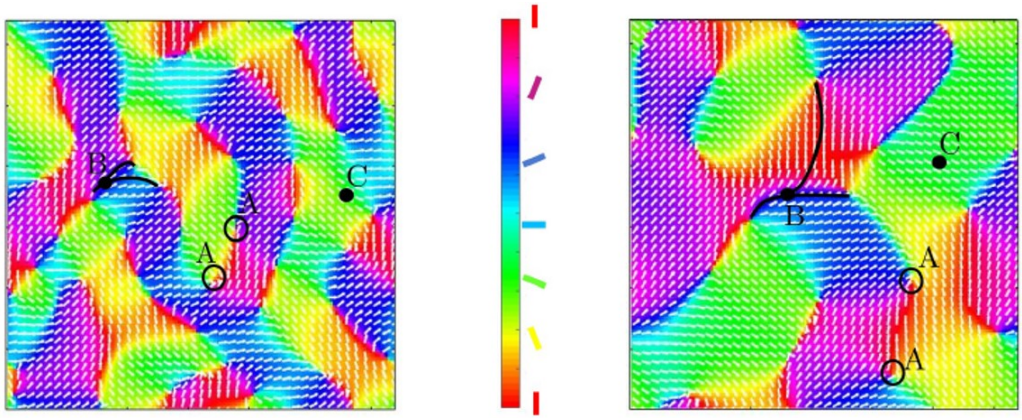

Figure 9.4: The orientation preference maps obtained through our model with two different scale values σ. Some examples of adjacent pinwheels with opposite chiralities (points A), saddle points (points B) and linear zones (points C) represented by a single color. The white lines represent the orientation correspondence at each point.

employed for the construction of the map.

Note that also the size of the pinwheel structure is strictly correlated to the scale of the Gabor filters, as shown in Figure 9.6.

As one passes through the V1-V2-V3 areas of the cortex the sizes of the simple cells increase and the lattice of the orientation map extends while the pinwheels are preserved, as visualized on the top of Figure 9.7 (see also the experimental results of Kennedy et. al. [106] and Levitt et. al. [114], which show the size differences between the simple cells in V1 and in V2 of baboons). Our simulations are able to reproduce the same type of orientation maps, which preserve the pinwheels through different cortex layers, by simply changing the scale of the Gabor filter bank as shown on the bottom of Figure 9.7.

In the next series of experiments we will compute the orientation maps by selecting at every point the preferred orientation and scale based on the three equations (9.1), (9.2) and (9.3). This case is the closer one to the physiological situation of a normal visual cortex, where cells with different orientations and sizes are present. In Figure 9.8 the relevant simulation result of the model is visualized, showing the orientation map rendering both the orientation selectivity and the scale selectivity.

In the final experiment, whose result is given in Figure 9.9, we used the same procedure as in the case of Figure 9.8 but using three different sets of scales which mimick the scale ranges of V1, V2, V3 and we obtained a result similar to Figure 9.7. This procedure is closer to the real receptive field composition of the primary visual cortex.

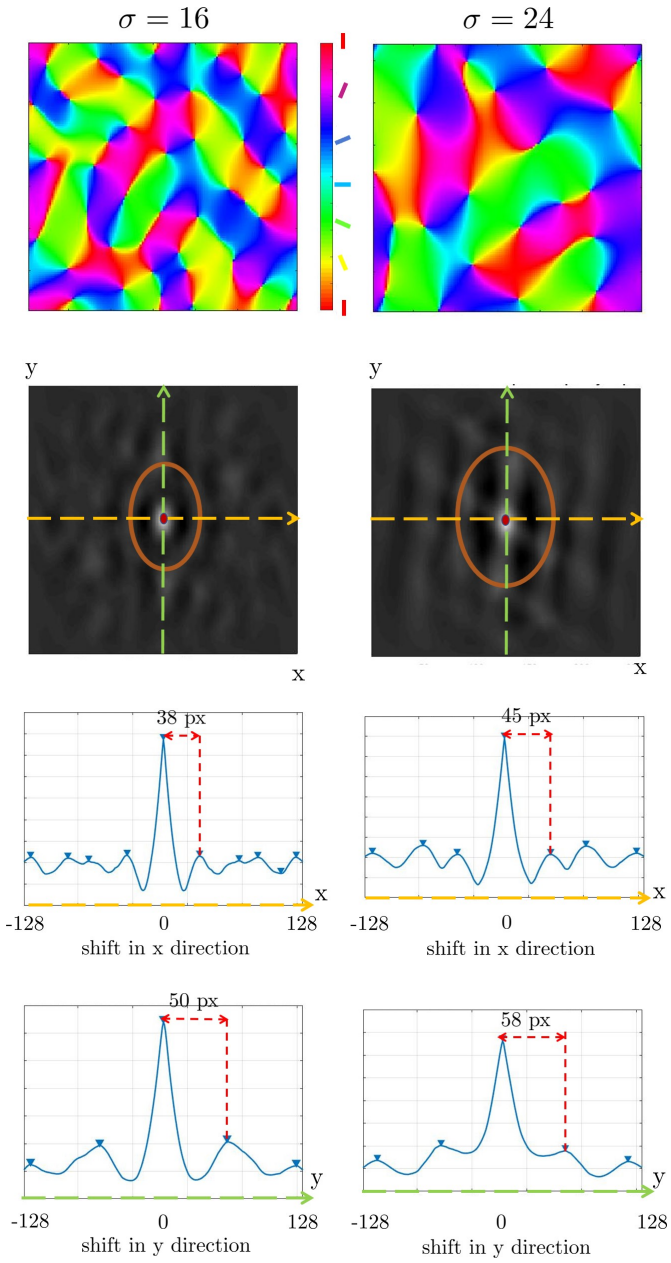

Figure 9.5: The results obtained by the Gabors with scale values $\sigma = 16$ (left column) and $\sigma = 24$ (right column). Top row: Orientation preference maps. Second row: Orientation preference map cross correlations. The average of the vertical and horizontal axes of ellipses (orange) representing the second peak values around the first peak corresponding to the exact match (due to no shift) indicates the spatially periodic configuration of the pinwheel grid structure of the orientation preference maps. Third row: Cross correlation values with respect to the shifts in x direction along the orange dashed arrow in the second row. Bottom: Cross correlation values with respect to the shifts in y direction along the green dashed arrow in the second row. Finally the spatial shift corresponding to the second peaks for $\sigma = 16$ is found as 44 pixels while for $\sigma = 24$ it is 52 pixels approximately.

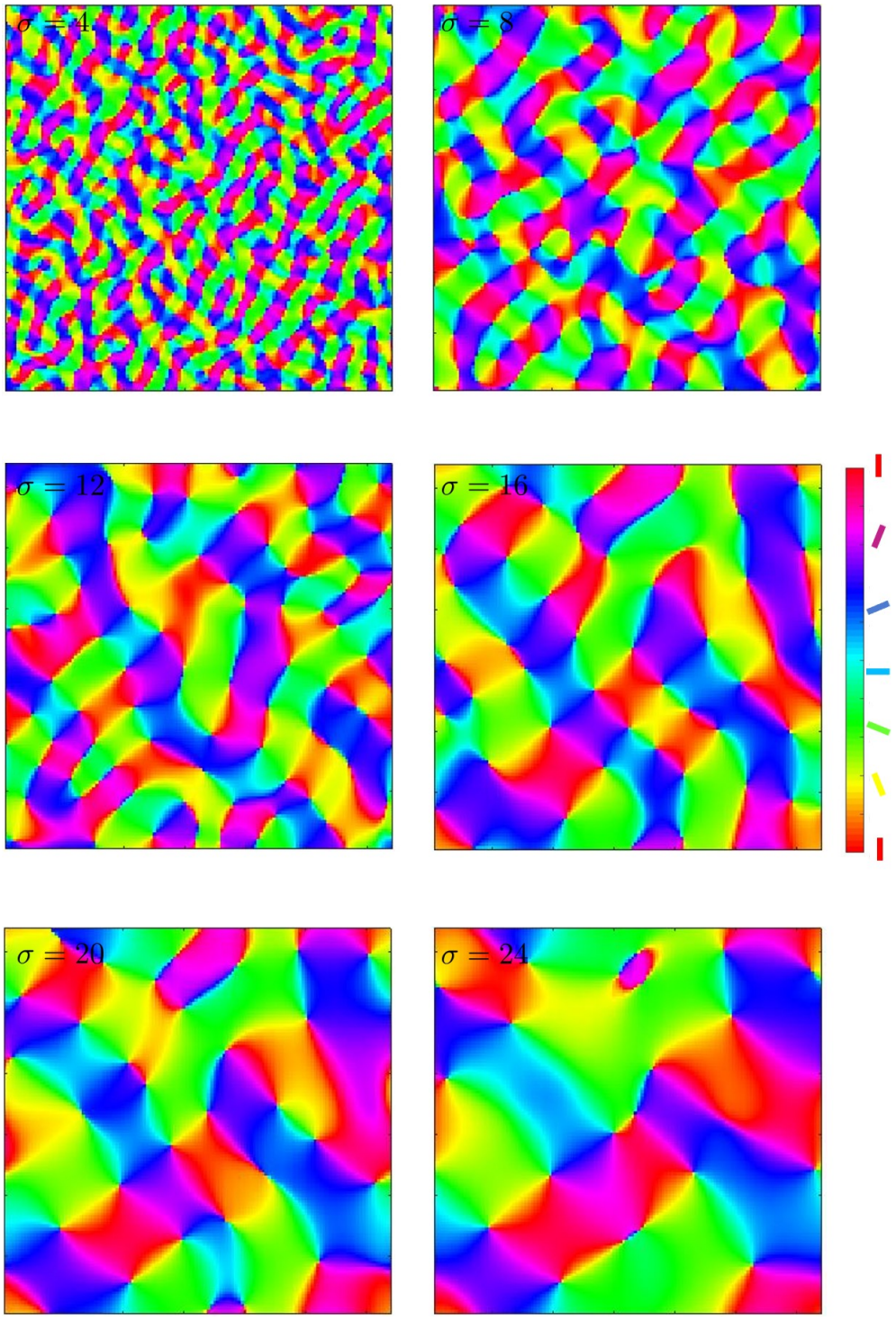

Figure 9.6: The orientation maps obtained by the Gabors of scales $\sigma = 4$ (top left), $\sigma = 8$ (top right), $\sigma = 12$ (middle left), $\sigma = 16$ (middle right), $\sigma = 20$ (bottom left), $\sigma = 24$ (bottom right) in pixels.

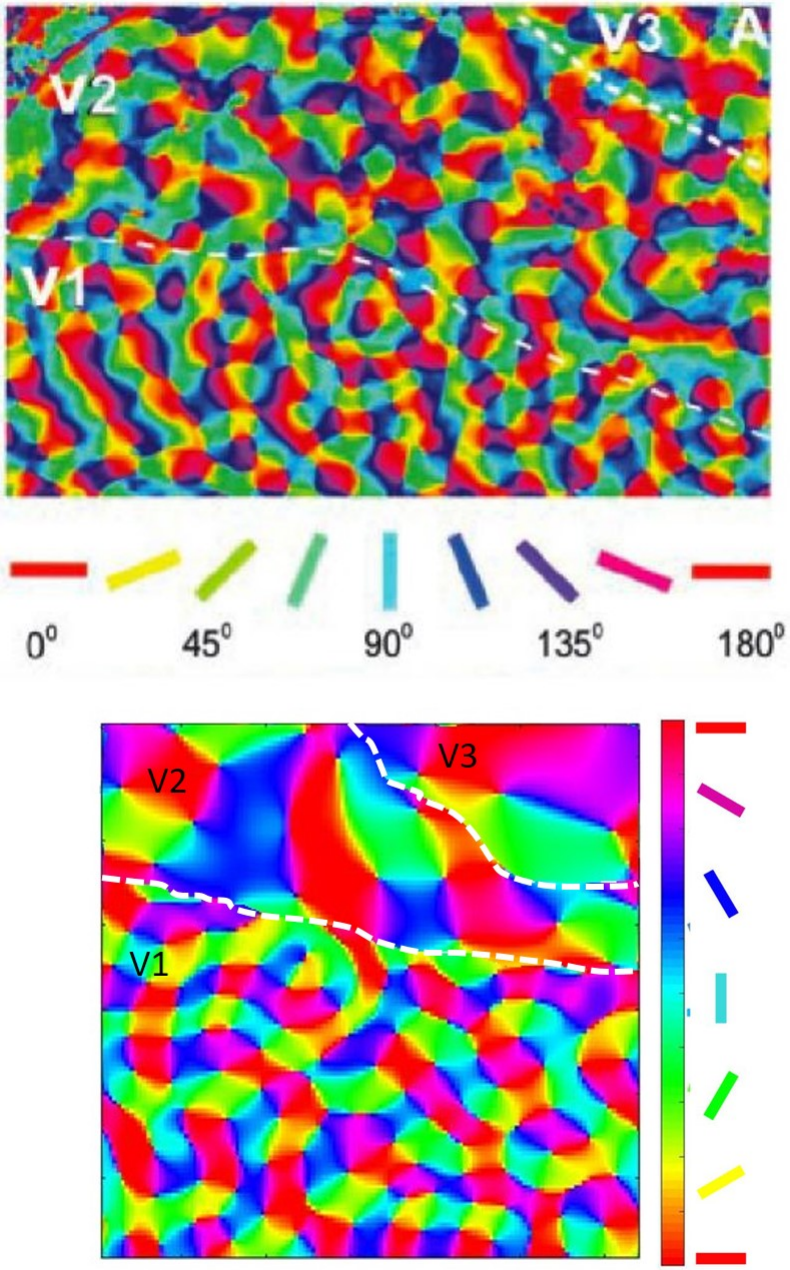

Figure 9.7: Top: The original neurophysiological results taken from [131, Figure 37]. Bottom: The simulation results obtained via our model.

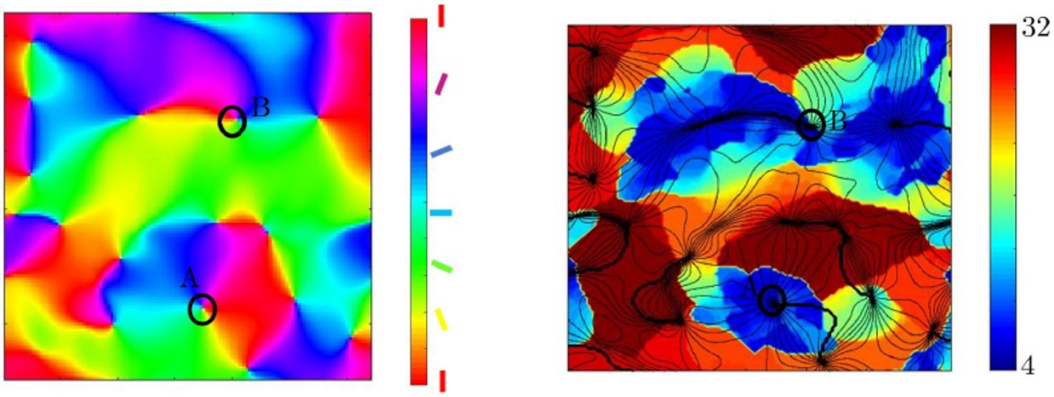

Figure 9.8: Left: The orientation preference map obtained through our model using the procedure based on (9.1), (9.2) and (9.3) with the scale set $\{4, 4.5, 5, \ldots 32\}$ used for the maximum scale selection. Right: The corresponding scale map where each color indicates a certain scale value found by (9.3) and the black curves represent the iso-orientation lines.

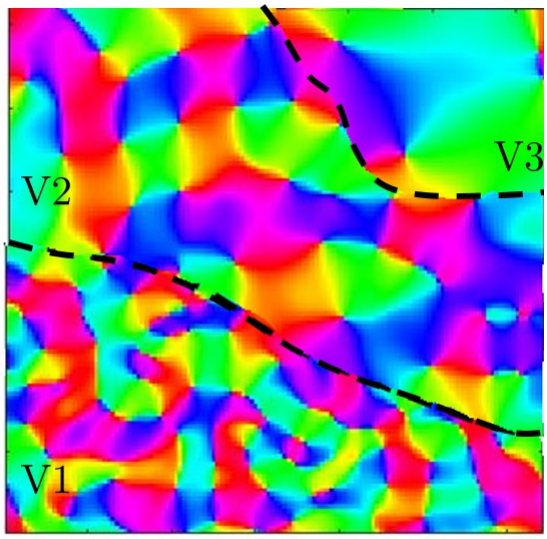

Figure 9.9: The multi-scale orientation preference maps obtained through our model using the procedure based on (9.1), (9.2), (9.3) and with scale sets $\{4, 4.5, 5, \ldots 8\}$ for V1, $\{4, 4.5, 5, \ldots 16\}$ for V2 and $\{4, 4.5, 5, \ldots 32\}$ for V3.

Chapter 10

Orientation-frequency maps through a Bargmann transform in the cortical space

Orientation preference maps have been a focused subject since the well known experiments of Hubel and Wiesel [86]. The characteristics of orientation preference maps of the simple cells in the visual cortex have been studied extensively. It is now agreed that orientation (OR) map is a spatially periodic map and OR preferences on the map vary smoothly. This continuity of the map is interrupted by certain singularities which are the *pinwheels* (see Section 2.4.3 for a description of pinwheels). On the other hand the existence and the organization characteristics of other functional maps are not very clear.

Selectivity to spatial frequency (SF) is realized as the level of the sensitivity of a simple cell to the details in a given visual stimulus at a fixed scale. Large frequency selectivity distinguishes the fine details in the stimulus while small frequency selectivity captures the coarse structures. Recently the functional organization of spatial frequency preferences and the interrelations between OR and SF preference maps of the simple cells in the visual cortex have been topics of interest in the neurophysiology community.

Considerable amount of studies suggests that SF map is organized in a continuous manner in several mammals such as cat [96], [151], [164], [156], [134], and monkey [127]. Pioneering studies [149], [96], [95] related to OR and SF preference maps propose a certain configuration based on neurohpysiological evidence. A common conclusion of those studies is that the organization of a SF map is constrained to OR map in such a way that those two maps together satisfy the uniform coverage hypothesis, which requires that all combinations of the visual properties are represented uniformly in the visual cortex (see Swindale et. al. [154] for more information about the hypothesis). More specifically Yu et. al. [173] and Nauhaus et. al. [127] reported an orthogonal composition of iso-OR and iso-SF lines (level sets showing the same preferred OR angles on the orientation map and the same preferred SF values on the spatial frequency map, respectively). Furthermore Shoham et. al. [149], Hübener et. al. [90], Issa et. al.

[96], [95] provided the results showing that pinwheel centers (PCs) were located at the extrema of SF maps. Those findings support the uniform coverage hypothesis.

However those observations are not obvious across a variety of species. Strong orthogonality of iso-lines was found in monkey (see Nauhaus et. al.[127]) while a weak tendency for such orthogonal relation between iso-lines was observed in ferret (see the results of Yu et. al. [173]). It is still a topic of discussion in cats. Moreover recent studies argue that those findings supporting the uniform coverage hypothesis might have been due to high-pass filtering procedures resulting in that the extreme SF values are over-represented at orientation PCs (see the explanations of Ribot et. al. [134], [135]).

In fact Ribot et. al. [135] take the advantage of recent imaging techniques and discuss the question of SF map representation by considering the doubts on the uniform coverage hypothesis at the level of OR and SF maps. They use high-resolution intrinsic optical imaging (see Kalatsky and Stryker [102] for more information about the method of recording data through this imaging technique) in cat visual cortex area 17 and area 18 (i.e., A17 and A18) in order to map the SF preference patterns near orientation map PCs. They find the results showing that PCs are located rather at the points around SF extrema, where SF gradients are noticeably sharp, than at exact SF extrema and the iso-orientation lines are non-orthogonal to iso-frequency lines (see the results presented by Ribot et. al. [134], [135]). They deduce from those observations that the uniform coverage might not be the true case and it might be rather that OR and SF preference maps together induce a different configuration than previously suggested orthogonal organization of OR and SF maps. They call this new configuration *pinwheel-dipole* architecture due to the fact that the iso-frequency regions around PCs resemble electric dipoles (see Figure 10.1 and Figure 10.3 for some examples of experimentally observed and idealized dipoles).

They first obtain the SF preference values of the simple cells at each point on the retinotopic plane by applying a curve fitting with a function of difference of Gaussians (DOG) on the SF response curves of the simple cells activated by grating stimuli having different spatial frequencies. Once they obtain the SF preference values they use the following procedure: They first show that the SF representation around majority of pinwheel locations includes a wide range of SF values with also semi-global minima and maxima found over a frequency interval. Then, in order to provide a more accurate characterization of SF representation, they check if a mathematically defined dipole model fits accurately with SF map around the detected pinwheel locations. Finally they show that the dipole model fits accurately to SF map near the majority of PCs. They deduce from those results that it might as well be the case of that instead of only extrema of SFs, a large range of SFs are represented around PCs, contradicting the uniform coverage hypothesis.

The purpose in our present study here is to reproduce the neurophysiological results proposing the new paradigm based on pinwheel-dipole configuration of OR and SF maps and compare them statistically to the real experimental results presented by Ribot et. al. [135]. In order to achieve it we use our extended model framework explained in Chapter 5 in combination with an analogous orientation-frequency selection procedure to the one

employed in the model of multi-scale orientation preference map construction explained in Chapter 9, which uses the integration over fiber and maximum scale selection mechanisms. We note two main differences in that analogy: Firstly, we use the extended framework based on intrinsic variables orientation and frequency (see Chapter 5) while the multi-scale model uses the framework of Sarti-Citti-Petitot [146] (see Section 4.4 for details), which employs the intrinsic variables orientation and scale. Secondly, the maximum selection mechanism finds the frequency value instead of the scale, corresponding to the simple cell giving the highest response among all cells responding to a stimulus at a certain point $q \in M$ on the retinal (or retinotopic) plane M. The representations of selected orientation and frequency values at every point on the retina give OR and SF preference maps, respectively.

Once we construct the OR map and the associated SF map we follow exactly the two step procedure explained by Ribot et. al. [135], which detects pinwheels in OR map and identifies the singularities (potentially dipoles) in the corresponding SF map around the detected pinwheels at the first step; selects the dipoles according to a mathematical dipole model among those detected singularities at the second step. This whole procedure provides some statistical data which confirms existence of colocalized pinwheel-dipole structures and supports the proposed pinwheel-dipole configuration in the real neurophysiological case of Ribot et.al. [135]. We compare our results produced by our model and obtain the relevant statistics which we compare to the results reported by Ribot et. al. in [134] and [135].

The particularity of our model is based on two points: Firstly it uses a natural procedure at the neural level since the cell responses are obtained via a filtering of a specific visual stimulus with Gabor functions representing the receptive profile of OR-SF selective simple cells without any pre-, post- or intermediate processing of the stimulus/response values of the cells. Secondly, the choice of the specific stimulus is a random noise. This choice is neurophysiologically motivated by the same reasoning as in the case of multi-scale orientation map model (see Section 9.1 for more information).

We refer to Chapter 5 for the details of the related geometrical framework to our model and here we start with Section 10.1, where we give the descriptions of pinwheels and dipoles. Then in Section 10.2 we summarize the procedure which Ribot et. al. [135] employs in order to obtain spatial frequency maps. In Section 10.3 we present our model which constructs orientation and spatial frequency maps. Finally in Section 10.4 and Section 10.5 we provide the simulation framework that we use and the statistical comparison of our simulation results to the neurophysiological results of Ribot et. al. [135].

We explicitly note that this study has been conducted in collaboration with Jérôme Ribot and Jonathan Touboul from Mathematical Neuroscience Team, Collège de France, Paris.

10.1 Pinwheel and dipole structures

Pinwheel and dipoles are identified by their several characteristics as explained in the literature (see the descriptions of Petitot [131] for pinwheels, Romagnoni et. al. [137] and Ribot et. al. [135] for dipoles), although their structural properties are still not completely known.

Recall that pinwheels (or pinwheel centers) are the singular points in the continuous orientation maps around which one finds the simple cells selective to all possible orientation angles (see the top row of Figure 10.1 for some pinwheels highlighted in an experimentally obtained OR map). They are the representations of the orientation hypercolumns on the 2-dimensional retinotopic plane (see also Section 2.4.3).

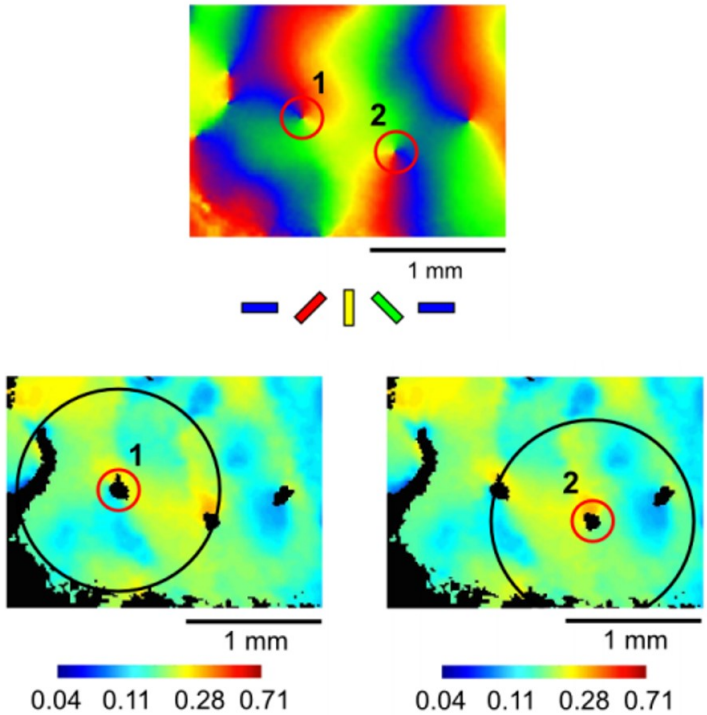

Figure 10.1: Figures taken from Ribot et. al. [135]. Top: Two pinwheels detected in an OR map. Bottom: Two dipoles corresponding to the pinwheel locations 1 and 2 and shown in the associated SF map. The black areas in the red circles represent unreliable data regions and they are discarded. The black circles represent the hypercolumns containing the regions with all possible SF values around dipoles.

Dipoles are the counter-parts of the pinwheels in SF maps (see the bottom row of Figure 10.1 for some dipoles observed in an experimentally obtained SF map). A dipole is a singularity in SF map and it is located in a circular region centered at a PC. Two important characteristics of a dipole are noted: Firstly, a dipole is located nearby the corresponding PC location in SF map and around this PC location sharp transition of SF

preferences are observed. Secondly, in a certain circular region around the dipole a wide range (including semi-global minima and maxima) of all possible SF values are found. As a result of those two properties we observe that iso-orientation and iso-frequency lines tend to intersect each other with non-orthogonal angles around those pinwheel-dipole locations (see Figure 10.2).

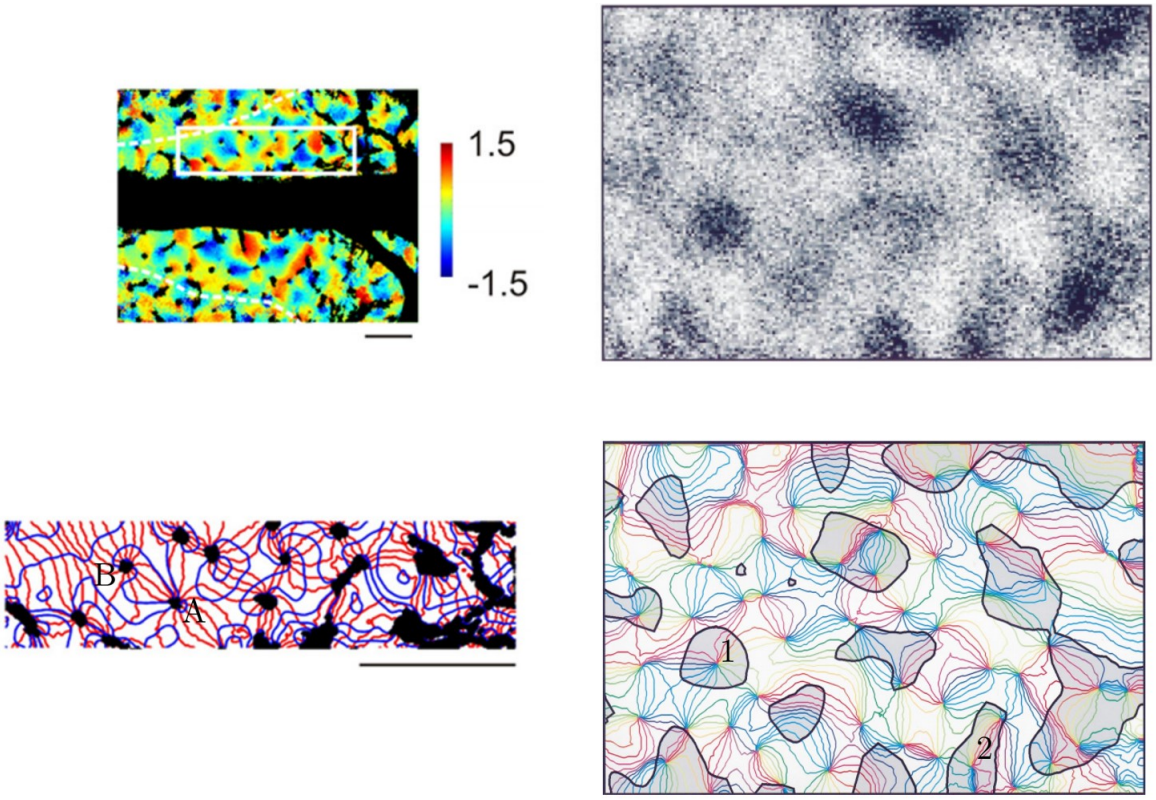

Figure 10.2: Figures adapted from Ribot et. al. [134] (left column) and Hübener et. al. [90] (right column). Examples of non-orthogonal and orthogonal configurations of iso-frequency and iso-orientation lines are shown. Left top: Spatial frequency map of a cat obtained by high resolution optical imaging. Left bottom: Iso-orientation lines (red) and iso-frequency lines (blue) in the region highlighted by white rectangle in the SF map. In the vicinity of singularities (e.g., points A and B) those iso-lines are not orthogonal. Right top: The SF map of a cat. Right bottom: Iso-orientation lines and SF domains obtained from the SF map. Here the low SF domains are highlighted (grey regions). Iso-orientation lines tend to intersect the borders of the iso-frequency domains with orthogonal angles (e.g., points 1 and 2).

In [136], Romagnoni et. al. provide the topological identification of pinwheel-dipole structure via the notions of *exhaustivity* and *parsimonity*. In order to describe those notions they first consider a small region $\mathcal{O}$, which is interpreted as an open disk on the retinotopic plane. Then they define the OR map as the continuous function $\bar{\theta} : \mathcal{O} \to S^1$.

Analogously they define the SF map $\bar{\omega}$ as a continuous function $\bar{\omega} : \mathcal{O} \to Q$ where $Q = [\omega_{\min}, \omega_{\max}]$ is an interval (with $0 < \omega_{\min} < \omega_{\max} < \infty$) representing all the possible SF values to which the simple cells are selective. Then they define *topological redundancy* as the maximum number of connected components of the iso-lines in the map. As an example one can consider the idealized pinwheel and dipole topologies given in Figure 10.3. In the example of the pinwheel topology we see that every iso-OR line connects the pinwheel center to the boundary (e.g., P_1 and P_2). On the other hand we see two types of iso-SF lines in the dipole topology: One of them has two components (e.g., D_1^1 and D_1^2) and each one of them connects the singularity point (possibly dipole) to the boundary. The other type (e.g., D_2) connects the singularity directly to itself. In those cases the redundancy in the pinwheel topology is 1 while in the dipole topology it is 2. They call $\bar{\theta}$ and $\bar{\omega}$ exhaustive if $S^1 \subset R(\bar{\theta})$ and $Q \subset R(\bar{\omega})$, respectively. They name a map which has the minimum redundancy possible as *parsimonious map*. In this case the OR map of the pinwheel topology given in Figure 10.3 is parsimonious since it has redundancy 1.

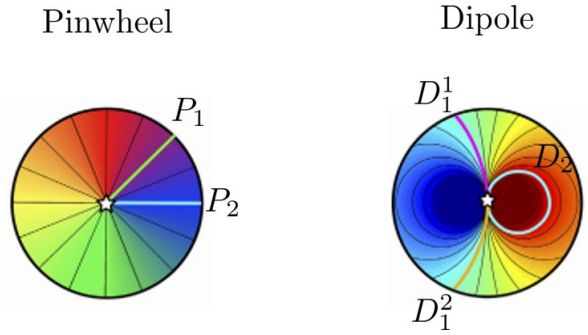

Figure 10.3: Adapted from [137]. Idealized pinwheel (left) and dipole (right) topologies highlighting different redundancies.

They finally show that those pinwheel and dipole topologies are the unique topologies which are exhaustive and posses the redundancy values 1 and 2, respectively. Their conclusion is that if OR and SF maps satisfy the aforementioned exhaustivity condition with the associated redundancy values, then one necessarily finds pinwheel-dipole structures around PCs. We refer to [137, Theorem 1] where Romagnoni et. al. formalize and prove this result.

10.2 Experimental orientation and frequency maps

In this section we explain the procedure which Ribot et. al. employ in [135] to obtain OR and SF maps by using the data collected from the cat visual cortex A17 and A18. Those maps will be the neurophysiological reference for our simulation results for a comparison.

In the first step the intrinsic signals of A17 and A18 in the presence of a visual stimuli displayed on a CRT (cathode ray tube) monitor are recorded with recent high-resolution

optical imaging techniques. The OR maps are obtained via computing the phase of the Fourier transform of the temporal signal at each point corresponding to A17 and A18, as explained by Kalatsky and Stryker [102]. In order to obtain SF maps Ribot et. al. [135] perform a curve fitting on the simple cell SF response curves. The empirical model which they use for the curve fitting is the difference of Gaussians given by:

$$\mathrm{DOG}(SF^i_{\mathrm{stim}}(q)) = A_1\, \mathrm{e}^{\frac{SF^2_{\mathrm{stim}}(q)}{2\sigma_1^2}} - A_2\, \mathrm{e}^{\frac{SF^2_{\mathrm{stim}}(q)}{2\sigma_2^2}},$$

where $SF^i_{\mathrm{stim}}(q)$ is the SF of the stimulus activating the point $q \in M$ on the retinotopic plane M, $A_1, A_2 \in \mathbb{R}^+$ are the magnitudes of the Gaussians and $\sigma_1, \sigma_2 \in \mathbb{R}^+$ are the scale values of the Gaussians. The whole interval of SF values is sampled suitably by SF samples SF^i_{stim} with $i \in \{1, 2, \ldots, N\}$ where N is the number of the samples.

Optimum parameter set $\{A_1, A_2, \sigma_1, \sigma_2\}$ is determined at each retinotopic position q separately as the parameters minimizing

$$\Big(\frac{\sum_i^N (S(SF^i_{\mathrm{stim}}) - \mathrm{DOG}(SF^i_{\mathrm{stim}}))^2}{\sum_i^N (S(SF^i_{\mathrm{stim}})^2 + \mathrm{DOG}(SF^i_{\mathrm{stim}})^2)}\Big), \tag{10.1}$$

where $S(SF^i_{\mathrm{stim}}(q)) \in \mathbb{R}$ denotes the intrinsic signal value of the stimulation (with frequency $SF^i_{\mathrm{stim}}(q)$) measured at the point q on the retinotopic plane.

They obtain the SF preference of the simple cells at q as the SF value corresponding to the peak of the DOG tuning curve with optimized parameters through (10.1). Finally they repeat the same procedure at every point q on the retinotopic plane M and represent the preferred SF values on M via a proper color map (see Figure 10.9 for examples of fitted functions of DOG and the raw response curves).

10.3 The model of orientation and frequency maps

In this section we will present our geometric model which constructs the OR and SF maps.

The receptive profiles of the extended model framework are provided by (5.2). In OR and SF map constructions we do not consider the phase behavior of the simple cells since there is no activity propagation in map construction. In this case the receptive profile with frequency $\omega \in \mathbb{R}^+$, centered at (q_1, q_2) on the retinotopic plane $M \simeq \mathbb{R}^2$ and rotated by $\theta \in S^1$ is given by (5.2).

The response of a simple cell at $q \in M$, sensitive to θ and with frequency ω given to a generic stimulus $I : M \to \mathbb{R}$ is obtained through the classical formula provided in (5.7).

The receptive profiles given by (5.2) are coherent states since they satisfy the coherent state condition given by (5.12). As in the case of the model constructing the multi-scale orientation maps (see Section 9.3.2) we can write the convolution (5.7) giving the

simple cell responses as the Bargmann transform for each frequency ω and every point $q = (q_1, q_2)$ on the retinal plane M:

$$O^I_{(\theta,\omega)}(q) = (B^{\mathrm{SE}(2)} I)(q, \theta, \omega) = \langle \Psi_{(q,\theta,\omega,\phi)}, I \rangle_{L^2(\mathbb{R}^2)},$$

where we fix phase $\phi = 0$.

Note that the coherent states correspond to the reducible representations of the Bargmann transform since the outputs $O^I_{(\theta,\omega)}$ are obtained for all possible frequency values to which the simple cells are selective. The representations corresponding to Bargmann transforms with several frequency values are not restricted to irreducible domain (i.e., annulus in the Fourier domain), similarly to the case of the coherent states with several scale values. We refer to Section 9.3.2 for more details.

We use the integration over fiber mechanism given by

$$\bar{\theta}(q_1, q_2) = \frac{1}{2} \arg \Big(\int_0^{\pi} \mathrm{Re} \Big\{ O^I_{(\theta,\omega)}(q_1, q_2) \Big\} \mathrm{e}^{i\theta} d\theta \Big), \tag{10.2}$$

in combination with the maximum selection for frequency

$$\bar{\omega}(q_1, q_2) = \underset{\omega \in \mathbb{R}^+}{\mathrm{argmax}} \Big(\mathrm{Re} \Big\{ O^I_{(\bar{\theta},\omega)}(q_1, q_2) \Big\} \Big), \tag{10.3}$$

in order to find the preferred orientation $\bar{\theta}(q)$ and spatial frequency $\bar{\omega}(q)$ of the simple cells at the point q, respectively. We assume that there is a unique maximum generically so different orders of the application of those two mechanisms give equivalent results.

In order to obtain OR and SF preferences of the simple cells we perform the three step procedure based on (5.7), (10.2) and (10.3) at every point q on the retinotopic plane M. Finally we represent $\bar{\theta}(q)$ and $\bar{\omega}(q)$ at every point q on the 2-dimensional retinotopic plane in terms of certain color maps (see Figure 10.4 for some examples of OR and SF maps obtained via the procedure with (5.7), (10.2) and (10.3)).

Finally we remark that although Gabor functions are different from DOG they extract the frequency information similarly. The Gabors directly finds the preferred SF by finding the SF value for which one of the Gabors in the set of Gabors corresponding to all possible preferred SF values gives the maximum response. In other words, SF values of stimulus are encoded directly by Gabors with different frequencies. In the case of DOG the parameters σ_1 and σ_2 play the analogous role of the frequency of Gabor functions. Those two parameters σ_1 and σ_2 are optimized in such a way that they provide the SF response curve whose peak coincides with the peak response of the simple cell SF response curve. An important point is that the use of DOG requires *a priori* the intrinsic signal measurements for the SF response curve fitting procedure which is not possible in the case of the model. Therefore we consider Gabor functions as the mathematical interpretation of simple cell receptive profiles and they provide directly the results starting from raw visual stimulus in a natural way.

10.4 Model simulations

In our simulation framework visual stimulus I is a 128×128 image which has a random value generated from a uniform distribution over the interval $[-1, 1]$ independently at each one of its pixels. We obtain the output $O_{(\bar{\theta},\bar{\omega})}$ by using (5.7) with 32 orientation samples $\theta \in \{0, \frac{\pi}{32}, \ldots, \frac{31\pi}{32}\}$ and logarithmically sampled 50 frequency samples in the interval $[\frac{2\pi}{100}, \frac{2\pi}{10}]$. Preferred orientation and frequency values at each point on the retinotopic plane are found via (10.2) and (10.3), respectively, as described in Section 10.3. Then OR and SF maps are represented in terms of certain color maps (see Figure 10.4 showing examples of OR and SF maps).

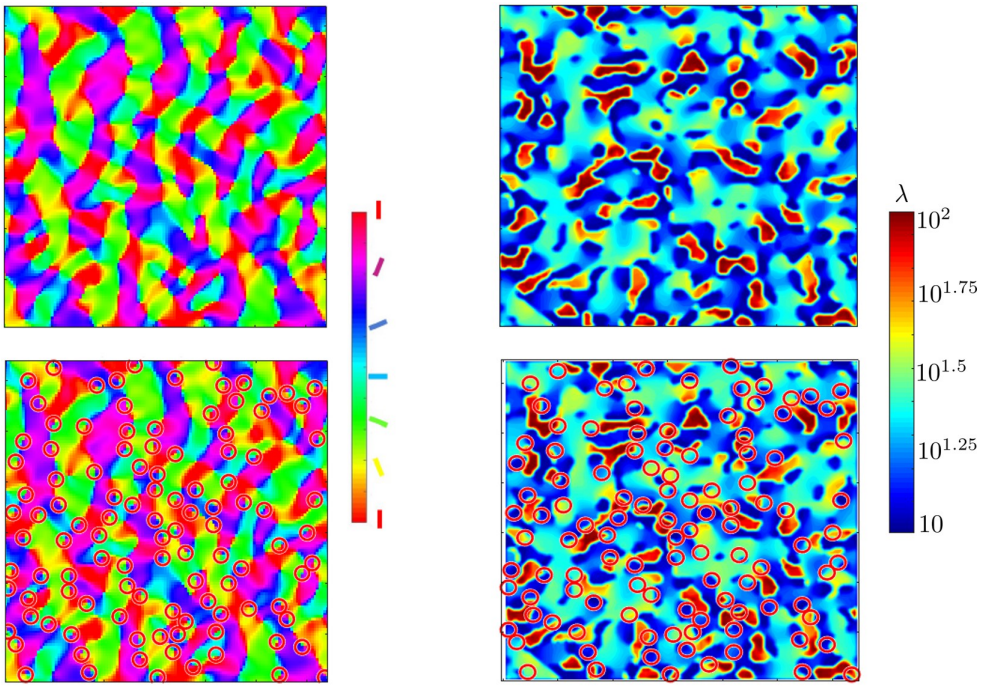

Figure 10.4: Orientation (left column) and frequency (right column) maps. Preferred values $\bar{\theta}$ and $\bar{\omega}$ are selected among all sampled outputs $O_{(\theta_i,\omega_j=\frac{2\pi}{\lambda_j})}(q)$ with $\theta_i = \frac{\pi}{N}(i-1)$, $\lambda_j = 10^{1+(j-1)\frac{1}{M}}$, $i \in \{1, 2, \ldots, N\}$, $j \in \{1, 2, \ldots, M\}$, $N = 128$ and $M = 100$ at every point $q \in M$ through (10.2), (10.3). Each color represents the orientation or frequency preference at the corresponding position on M. Top left: Orientation map obtained via Gabors with scale value of 8 pixels. Top right: Spatial frequency map corresponding to the orientation map. Bottom left: The same orientation map now with highlighted pinwheel centers. The red circles represent the regions of interests around the pinwheel centers. Bottom right: The same spatial frequency map with highlighted singularity (potentially dipole) locations.

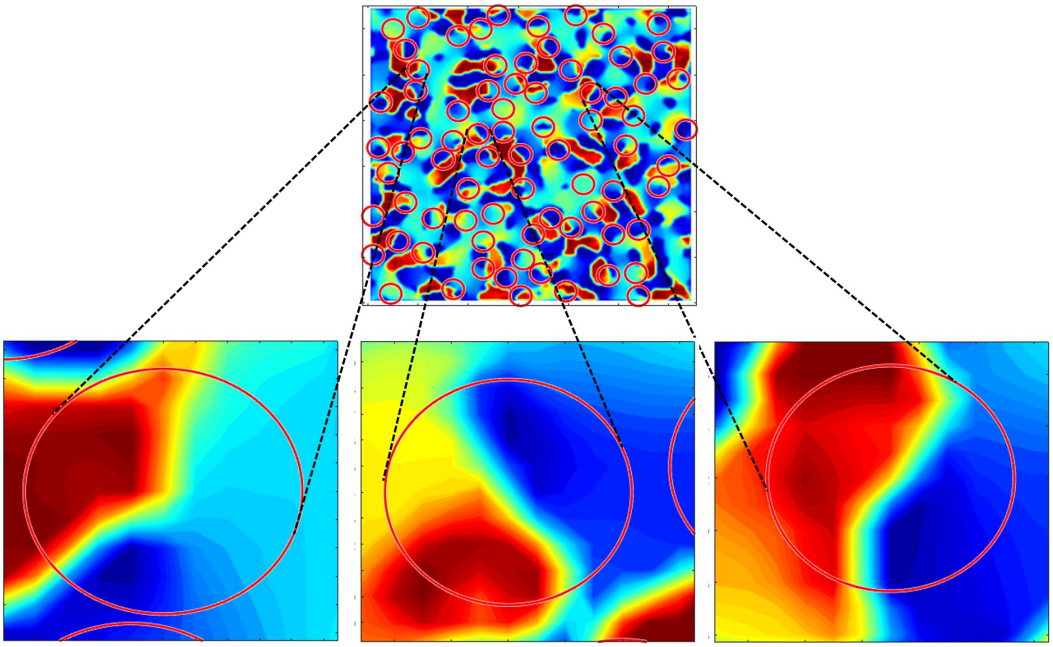

Figure 10.5: Examples of dipoles (bottom) highlighted from the same SF preference map as given in Figure 10.4.

In order to compute the OR and SF map periodicities we employ the same technique which is used by Ribot et. al. in [134] and [135]. We compute the 2D spatial autocorrelation of the SF map. The average distance between the first and second peak rings gives us the half spatial periodicity of the SF singularities. In Figure 10.6 one can see the procedure steps and the computation of the average periodicity of SF singularities in the case of simulations. See also Figure 10.7 where some figures related to the singularity period computations in the experimental framework of Ribot et. al. [134], [135] are presented.

The periodicity is quantitatively important since it determines up to which level SF singularities (and/or pinwheels) residing in the vicinity of each other can be accepted as valid candidates for the performed analysis since the singularities very close to each other could bring problems due to their mutual interactions.

It is reported in [135] and [137] that SF map singularities are colocated with PCs. Furthermore, the SF response pattern of the simple cells in the cat primary visual cortex shows a sharp selectivity near those SF singularities. It is predicted within those aforementioned studies that the visual cortex tends to optimize a balanced detection of different visual properties and this could lead to a new functional architecture of cortical maps.

Indeed such sharp selectivity around PCs (thus SF map singularities) are observed in our simulation results as well. We observe in Figure 10.8 that the SF selectivity switches rapidly from high (i.e., low wavelenght λ selectivity) to low (i.e., high wavelenght λ selectivity) SF selectivity along the dipole axis (orange dashed line) and around the

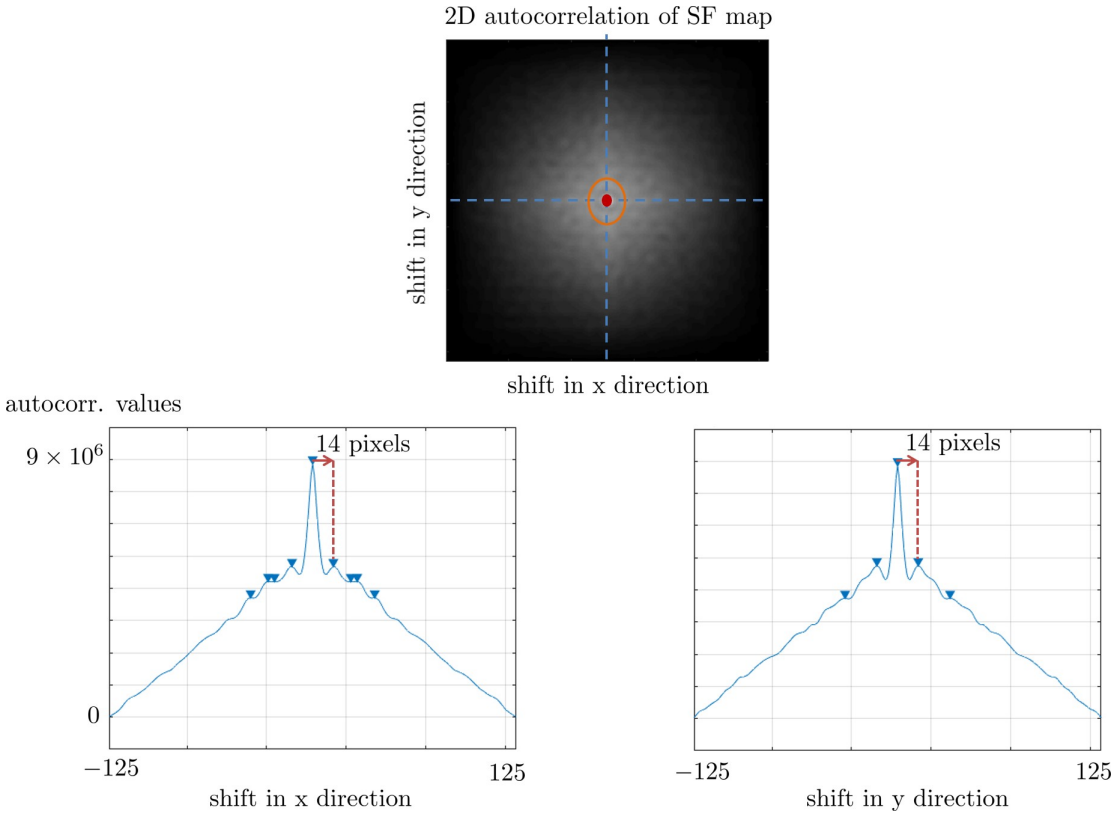

Figure 10.6: Top: 2D spatial autocorrelation result of the same SF map given in Figure 10.4. The central peak is higlighted by the red dot and the secondary peaks which accumulate to a ring around the central peak is by the orange circle. Blue dashed lines correspond to the x and y axes along which the autocorrelation results are shown in the bottom row plots. Bottom: The autocorrelation values with respect to x (left) and y (right) shifts. The blue markers highlight the local peak values. The spatial periods of OR and SF maps are 14 pixels. In order to avoid touching of region of interest circles to each other, we calculate the region of interest circle diameter (= 4 pixels) regarding the spatial period. See Figure 10.7 for comparison.

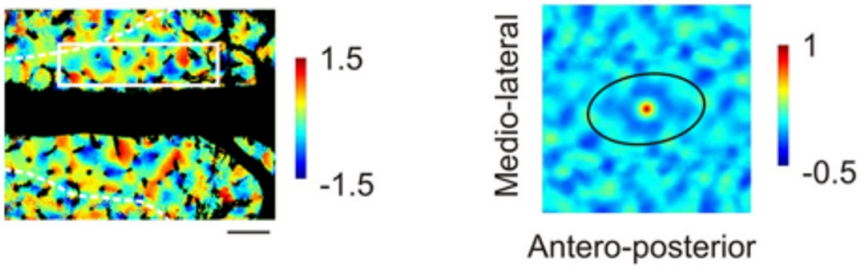

Figure 10.7: Figures taken from [134]. Left: Experimentally obtained map of local SF extrema expressed in octaves. Right: 2D spatial autocorrelation result of the SF map on the left. The secondary peaks, which represent characteristic periods in various directions, are linked by a black ellipse.

singularity point (px(15,105)). Compare those figures to the ones in Figure 10.9 which is directly taken from [135].

Moreover we also note in the same figures that the cells which are sensitive to high SF values suppress low SF stimulus (observe the negative peaks indicating that those cells with high SF selectivity suppress low SF values, providing a stronger high-pass filtering characteristic for high SF values) and vice versa for the cells sensitive to low SF values. In [22] a similar type of observation was reported by Bredfeldt and Ringach in the case of macaque, although there, it was observed that the cells sensitive only to *high* spatial frequencies were suppressing *low* spatial frequencies while in our simulation results analogous characteristics are observed for both types of cells around SF singularities.

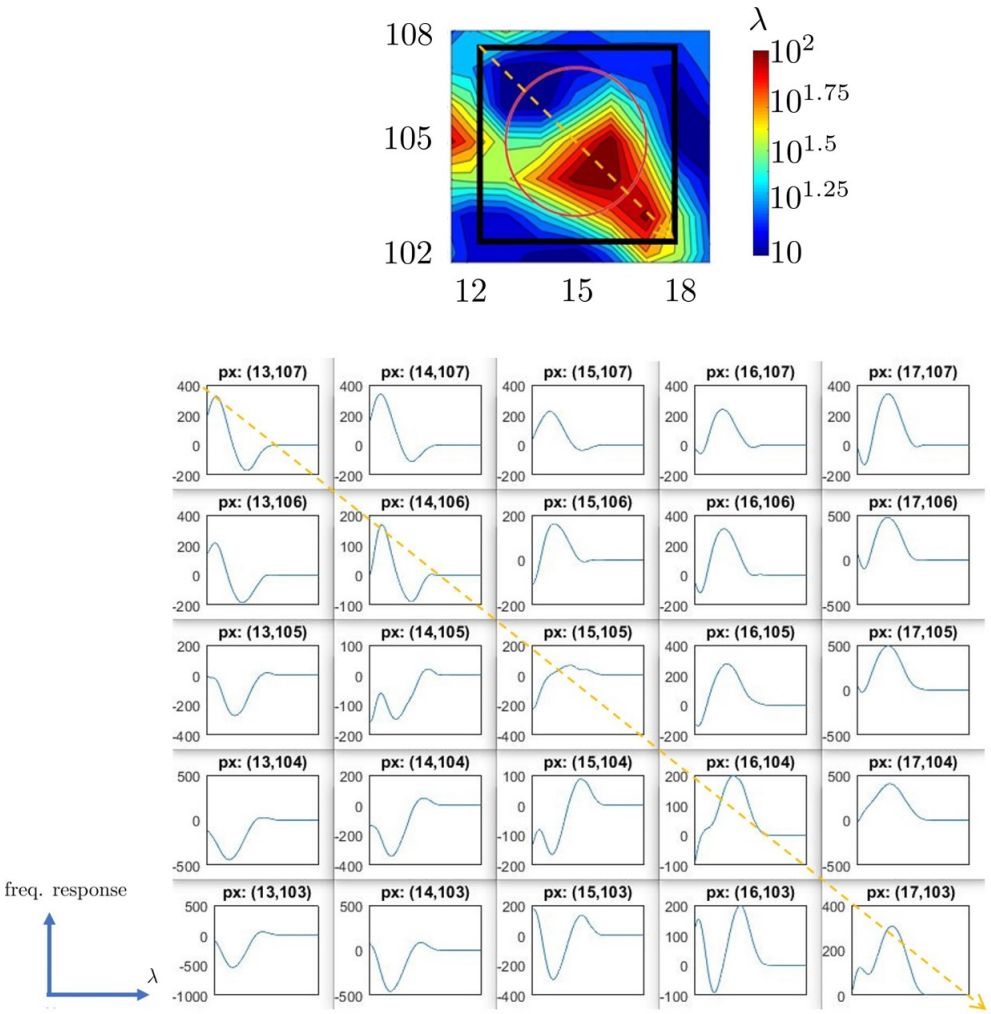

Figure 10.8: Frequency response curves of the model around a SF singularity (top). Black frame corresponds to the zone in which one finds the cell SF selectivity patterns given on the bottom for each pixel. Red circle is the region of interest. Orange dashed line represents the dipole axis along which a sharp frequency transition is observed. Bottom: Frequency selectivity pattern of each cell around the SF singularity. In each plot horizontal axis and vertical axis represent, wavelength λ ($\lambda = \frac{2\pi}{\omega}$ with ω denoting frequency) and the response that the cell gives to stimulus with different frequencies, respectively. The title shows the corresponding pixel indices (e.g., px(15,105) denotes the pixel coordinates (15,105)). The singularity corresponds to px(15,105) which is at the exact center of the black frame. Around the singularity there is the sharp frequency transition and the cells suppress the SF values which they are not selective to.

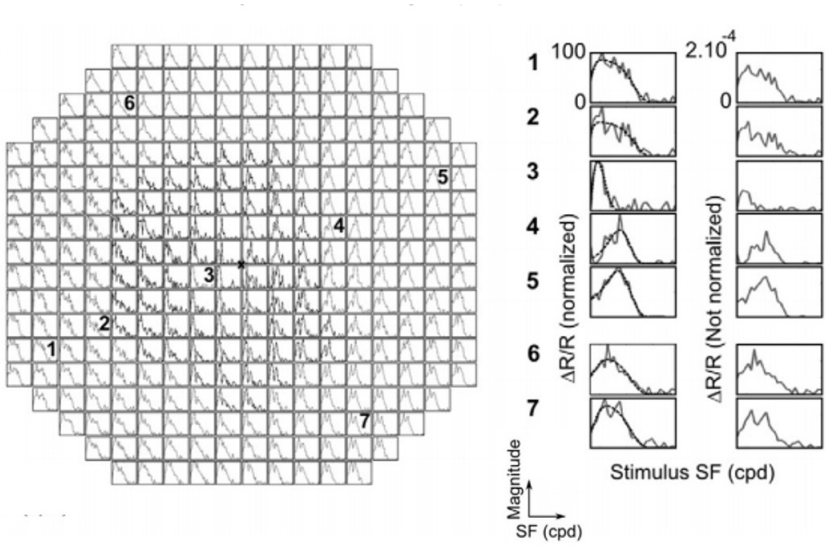

Figure 10.9: Figure taken from [135] for comparison to Figure 10.8. Left: Example of the tuning curves of the simple cells located around a PC (nearby pixel 3) and responding to stimuli with 30 different SF values. Right: Representative tuning curves (numbered from 1 to 7 in the figure on the left hand side) are enlarged in the left panel and they are fitted to the functions of difference of Gaussians (dashed line). Right panel shows the same curves without rescaling. Positions 1-5 correspond to the axis of the dipole. Positions 6 and 7 correspond to the simple cells with intermediate preferred SF values. See [135] for details.

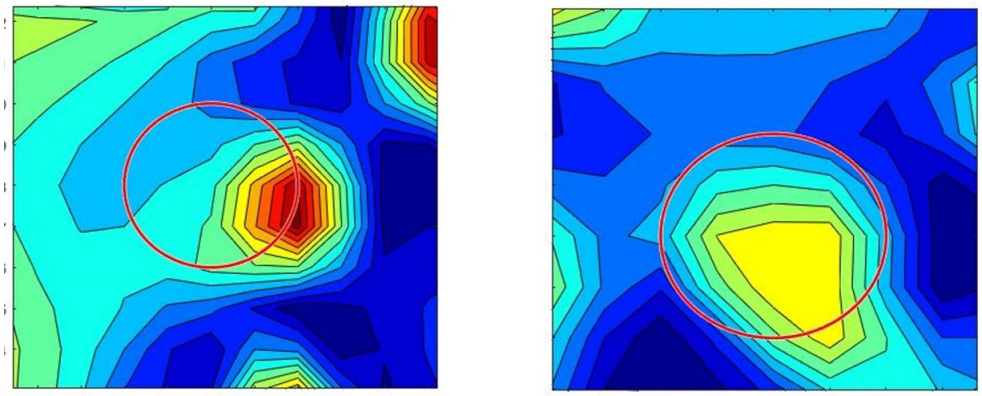

Figure 10.10: SF singularities (poles) which are not dipoles. They lack one of the extrema in their regions of interest. However they are not the type of poles which reside at the existing extremum. Therefore they do not fulfill uniform coverage requirements either.

10.5 Statistical comparison with neurophysiological data

The model results up to now support the conclusions of Ribot et. al. [135] qualitatively. In order to confirm a more precise matching of the model results with the neurophysiological observations, we perform a statistical comparison. In order to achieve it we employ the same statistical procedure which is explained by Ribot et. al. in [135].

The procedure is based on two steps. In the first step, they detect the PC locations and exclude pinwheels whose regions of interest coincide (region of interest is a circle centered at PC location, with a radius of 4 pixels in our case. The red circles show the corresponding regions of interest in Figures 10.4, 10.5 and 10.8. The region of interest diameter is calculated as 2/7 of SF map singularity periodicity, which is 14 pixels). Then they check if there are local maximum and minimum in the vicinity of each selected SF map singularity. The *vicinity* is defined as the circle centered at the PC location and with the diameter of SF map periodicity (14 pixels in our case). Finally they define the upper third and lower third SF values as maximum and minimum SF values. That is, if in the vicinity of PC locations there are both maximum and minimum SF values in the SF map, then it is accepted that the corresponding SF singularity passes the first step and is a valid candidate for the next step: dipolar model fitting.

In the second step they fit a mathematically defined dipolar model (see Section *Geometrical description of a pinwheel-dipole* in [135] for details) to the candidate SF singularities which passed the first step. For each fit they calculate the coefficient of fit R^2 which shows the goodness of fit. For this purpose they employ the built-in Matlab® function *regress*. Then they accept as dipole singularities only those which satisfy $R^2 > 0.8$.

We apply almost the same procedure in order to obtain the related statistics to our OR and SF maps, where the only difference is that we use different region of interest values since our framework is based on pixel units.

We perform our experiments with Gabor functions having a scale value of 8 pixels in order to obtain the outputs described by (5.7) where I is the 128×128 noise stimulus. The paramaters for sampling orientations θ_i and frequencies ω_j in their corresponding intervals are provided in Figure 10.4. We use the same sampling parameters. In the first step we observe that among 110 PCs (after the elimination of those in mutual interaction) 75.5% of PC locations contain a local maximum and a minimum in the vicinities of the PC locations on the associated SF map. So the first step of the test has the score = 75.5% in our case in close accordance with neurophysiological results reported in [135] as 89.6% and 76.2% for A17 and A18 of the cat visual cortex, respectively.

In the second step we perform the model fitting and we observe that %53 of the singularities which passed the first step score $R^2 > 0.8$ and %73 score $R^2 > 0.7$. In [135] the authors report the percentage of those satisfying $R^2 > 0.8$ as %66 of the candidates which passed the first step, for both A17 and A18. The simulation results seem to be consistent with the findings of Ribot et. al. [135] related to pinwheel-dipole architecture.

Furthermore we observe also some poles with only a maximum or a minimum SF value in their vicinities, where one of the SF extrema is missing. Furthermore those poles

are not of the type which was suggested for orthogonal architectures where the pole is located at the existing extremum. Differently from that, the existing extremum in the case of poles in our case is rather on one side of the pole. This type of pole singularities in SF maps were reported by Ribot et. al. [135] as well. One can see some examples of such non-dipole singularities (poles) obtained via our simulations in Figure 10.10 .

For the representations of the dipole model and the experimentally observed dipole structures we refer to [135, Figure 4] and [135, Figure 5], respectively.

Chapter 11

Conclusion

The aim of this thesis was to provide consistent geometrical models of the visual cortex with phenomenological and neurophysiological evidence, and to study geometric flows in relation to image processing within corresponding geometric settings to the models. Regarding this main goal, we provided novel results related to visual models, image processing, geometric flows and feature map construction.

We provided a generalized sub-Riemannian visual cortex model which considers position, orientation and frequency detection mechanisms of simple cells with their changing phase behavior. We explained the model framework by using Lie group theory and differential geometry. Furthermore we provided some applications which relied on the model framework, namely, an image enhancement algorithm employing sub-Riemannian diffusion or Laplace-Beltrami flow, and orientation and frequency map construction.

It was conjectured in [35] that the joint action of an iterative diffusion of a function and a maximum selection applied on the diffusion result was equivalent to the mean curvature flow. However a formal proof of the conjecture was missing in both Euclidean and sub-Riemannian setting. We proved the conjecture in the Euclidean setting.

Moreover although the existence of solutions to sub-Riemannian mean curvature flow in Carnot groups and general Hörmander structures [29], [48] were known, the uniqueness was shown only up to certain assumptions by Capogna-Citti in [29] and by Ferrari et. al. in [63]. Here we provided the uniqueness of the solution to sub-Riemannian mean curvature flow in the Heisenberg group without such assumptions.

Finally we showed two neurophysiologically inspired geometric models for feature map construction. The first one was based on the geometric framework of the visual cortex model with orientation and scale selectivity, which was proposed by Sarti, Citti and Petitot [146]. We showed that our model produces orientation maps at both single and multi-scale levels together with the corresponding scale maps. The second model was based on the extended sub-Riemannian framework with frequency and phase as mentioned above. We produced orientation and frequency maps by using this model and provided a statistical comparison of those maps with the recent neurophysiological results reported by Ribot et. al. [134], [135].

This thesis leads to several future research directions:

- Extension of the proof of the equivalence of the iterative diffusion followed by the maximum selection and mean curvature flow from Euclidean to sub-Riemannian setting,
- Image inpainting in the sub-Riemannian framework of the extended model with frequency and phase,
- Generalization of the proposed visual cortex model with also ocular dominance by using higher dimensional Lie groups.

Bibliography

[1] Altschuler, S. J., Grayson, M. A., et al. *Shortening space curves and flow through singularities*. Institute for Mathematics and its Applications (USA), 1991.

[2] Ambrosio, L. and Masnou, S. A direct variational approach to a problem arising in image reconstruction. *Interfaces and Free Boundaries*, 5(1):63–81, 2003.

[3] Barbieri, D., Citti, G., Cocci, G., and Sarti, A. A cortical-inspired geometry for contour perception and motion integration. *Journal of mathematical imaging and vision*, 49(3):511–529, 2014.

[4] Barbieri, D., Citti, G., Sanguinetti, G., and Sarti, A. Coherent states of the euclidean group and activation regions of primary visual cortex. *arXiv preprint arXiv:1111.0669*, 2011.

[5] Barbieri, D., Citti, G., Sanguinetti, G., and Sarti, A. An uncertainty principle underlying the functional architecture of v1. *Journal of Physiology-Paris*, 106(5):183–193, 2012.

[6] Bargmann, V. On a hilbert space of analytie functions and an associated integral transform. part ii. a family of related function spaces application to distribution theory. *Communications on pure and applied mathematics*, 20(1):1–101, 1967.

[7] Barles, G. and Georgelin, C. A simple proof of convergence for an approximation scheme for computing motions by mean curvature. *SIAM Journal on Numerical Analysis*, 32(2):484–500, 1995.

[8] Baspinar, E., Citti, G., and Sarti, A. A geometric model of multi-scale orientation preference maps via Gabor functions. *ArXiv e-prints*, Dec. 2017. DOI: 10.1007/s10851-018-0803-3. arXiv: 1712.04329 [q-bio.NC].

[9] Baspinar, E. and Citti, G. A diffusion driven curvature flow. *arXiv preprint arXiv:1603.01156*, 2016.

[10] Bednar, J. A. and Miikkulainen, R. Constructing visual function through prenatal and postnatal learning. *Neuroconstructivism: Perspectives and prospects*, 2:13–37, 2004.

[11] Bekkers, E., Duits, R., Berendschot, T., and Haar Romeny, B. ter. A multi-orientation analysis approach to retinal vessel tracking. *Journal of Mathematical Imaging and Vision*, 49(3):583–610, 2014.

[12] Blakemore, C. and Campbell, F. On the existence of neurones in the human visual system selectively sensitive to the orientation and size of retinal images. *The Journal of physiology*, 203(1):237, 1969.

[13] Bonfiglioli, A, Lanconelli, E, Uguzzoni, F, et al. Uniform gaussian estimates for the fundamental solutions for heat operators on carnot groups. *Advances in Differential equations*, 7(10):1153–1192, 2002.

[14] Bonfiglioli, A., Lanconelli, E., and Uguzzoni, F. *Stratified Lie groups and potential theory for their sub-Laplacians*. Springer Science & Business Media, 2007.

[15] Bonhoeffer, T., Grinvald, A., et al. Iso-orientation domains in cat visual cortex are arranged in pinwheel-like patterns. *Nature*, 353(6343):429–431, 1991.

[16] Bonhoeffer, T., Kim, D.-S., Malonek, D., Shoham, D., and Grinvald, A. Optical imaging of the layout of functional domains in area 17 and across the area 17/18 border in cat visual cortex. *European Journal of Neuroscience*, 7(9):1973–1988, 1995.

[17] Bony, J.-M. Principe du maximum, inégalité de harnack et unicité du probleme de cauchy pour les opérateurs elliptiques dégénérés. *Ann. Inst. Fourier (Grenoble)*, 19(1):277–304, 1969.

[18] Boscain, U., Chertovskih, R. A., Gauthier, J.-P., and Remizov, A. Hypoelliptic diffusion and human vision: a semidiscrete new twist. *SIAM Journal on Imaging Sciences*, 7(2):669–695, 2014.

[19] Boscain, U., Duplaix, J., Gauthier, J.-P., and Rossi, F. Anthropomorphic image reconstruction via hypoelliptic diffusion. *SIAM Journal on Control and Optimization*, 50(3):1309–1336, 2012.

[20] Bosking, W. H., Zhang, Y., Schofield, B., and Fitzpatrick, D. Orientation selectivity and the arrangement of horizontal connections in tree shrew striate cortex. *Journal of neuroscience*, 17(6):2112–2127, 1997.

[21] Brakke, K. The motion ofa surface by its mean curvature. *Mathematical Notes Series, Princeton University Press, Princeton, NJ*, 1978.

[22] Bredfeldt, C. E. and Ringach, D. Dynamics of spatial frequency tuning in macaque v1. *Journal of Neuroscience*, 22(5):1976–1984, 2002.

[23] Bressloff, P. C. and Cowan, J. D. A spherical model for orientation and spatial–frequency tuning in a cortical hypercolumn. *Philosophical Transactions of the Royal Society of London B: Biological Sciences*, 358(1438):1643–1667, 2003.

[24] Bressloff, P. C. and Cowan, J. D. The functional geometry of local and horizontal connections in a model of v1. *Journal of Physiology-Paris*, 97(2):221–236, 2003.

[25] Bressloff, P. C., Cowan, J. D., Golubitsky, M., Thomas, P. J., and Wiener, M. C. Geometric visual hallucinations, euclidean symmetry and the functional architecture of striate cortex. *Philosophical Transactions of the Royal Society B: Biological Sciences*, 356(1407):299–330, 2001.

[26] Brezis, H and Pazy, A. Convergence and approximation of semigroups of nonlinear operators in banach spaces. *Journal of Functional Analysis*, 9(1):63–74, 1972.

[27] Calin, O. and Chang, D.-C. Sub-riemannian geometry. *Cambridge University Press*, 24:134, 2009.

[28] Cang, J., Rentería, R. C., Kaneko, M., Liu, X., Copenhagen, D. R., and Stryker, M. P. Development of precise maps in visual cortex requires patterned spontaneous activity in the retina. *Neuron*, 48(5):797–809, 2005.

[29] Capogna, L. and Citti, G. Generalized mean curvature flow in carnot groups. *Communications in Partial Differential Equations*, 34(8):937–956, 2009.

[30] Capogna, L., Citti, G., and Magnani, C. S. G. Sub-riemannian heat kernels and mean curvature flow of graphs. *Journal of Functional Analysis*, 264(8):1899–1928, 2013.

[31] Capogna, L., Danielli, D., Pauls, S. D., and Tyson, J. *An introduction to the Heisenberg group and the sub-Riemannian isoperimetric problem*, volume 259. Springer Science & Business Media, 2007.

[32] Chen, Y. G., Giga, Y., Goto, S., et al. Uniqueness and existence of viscosity solutions of generalized mean curvature flow equations. *J. Differential Geom*, 33(3):749–786, 1991.

[33] Chow, W.-L. Über systeme von liearren partiellen differentialgleichungen erster ordnung. *Mathematische Annalen*, 117(1):98–105, 1940.

[34] Citti, G., Franceschiello, B., Sanguinetti, G., and Sarti, A. Sub-riemannian mean curvature flow for image processing. *SIAM Journal on Imaging Sciences*, 9(1):212–237, 2016.

[35] Citti, G. and Sarti, A. A cortical based model of perceptual completion in the roto-translation space. *Journal of Mathematical Imaging and Vision*, 24(3):307–326, 2006.

[36] Citti, G. and Sarti, A. *Neuromathematics of vision*, volume 32. Springer, 2014.

[37] Cocci, G., Barbieri, D., Citti, G., and Sarti, A. Cortical spatiotemporal dimensionality reduction for visual grouping. *Neural computation*, 2015.

[38] Courant, R., Friedrichs, K., and Lewy, H. Über die partiellen differenzengleichungen der mathematischen physik. *Mathematische annalen*, 100(1):32–74, 1928.

[39] Crandall, M. G., Ishii, H., and Lions, P.-L. Users guide to viscosity solutions of second order partial differential equations. *Bulletin of the American Mathematical Society*, 27(1):1–67, 1992.

[40] Crandall, M. G. and Liggett, T. M. Generation of semi-groups of nonlinear transformations on general banach spaces. *American Journal of Mathematics*:265–298, 1971.

[41] Creusen, E. J., Duits, R., and Haije, T. C. D. Numerical schemes for linear and non-linear enhancement of DW-MRI. In *Scale Space and Variational Methods in Computer Vision*, pages 14–25. Springer, 2012.

[42] Danielli, D., Garofalo, N., and Nhieu, D.-M. Sub-riemannian calculus on hypersurfaces in carnot groups. *Advances in Mathematics*, 215(1):292–378, 2007.

[43] Das, A. and Gilbert, C. D. Long-range horizontal connections and their role in cortical reorganization revealed by optical recording of cat primary visual cortex. *Nature*, 375(6534):780, 1995.

[44] Daugman, J. G. Uncertainty relation for resolution in space, spatial frequency, and orientation optimized by two-dimensional visual cortical filters. *JOSA A*, 2(7):1160–1169, 1985.

[45] DeAngelis, G. C., Ohzawa, I., and Freeman, R. D. Receptive-field dynamics in the central visual pathways. *Trends in neurosciences*, 18(10):451–458, 1995.

[46] DeAngelis, G. C., Ohzawa, I., and Freeman, R. Spatiotemporal organization of simple-cell receptive fields in the cat's striate cortex. i. general characteristics and postnatal development. *Journal of neurophysiology*, 69(4):1091–1117, 1993.

[47] Deckelnick, K. Error bounds for a difference scheme approximating viscosity solutions of mean curvature flow. *Interfaces and Free Boundaries*, 2(2):117–142, 2000.

[48] Dirr, N., Dragoni, F., and Renesse, M. von. Evolution by mean curvature flow in sub-riemannian geometries. *Communications on Pure and Applied Mathematics*, 9(2):307–326, 2010.

[49] Dobbins, A., Zucker, S. W., and Cynader, M. S. Endstopped neurons in the visual cortex as a substrate for calculating curvature. *Nature*, 329(6138):438, 1987.

[50] Duits, R. and Franken, E. Left-invariant parabolic evolutions on se (2) and contour enhancement via invertible orientation scores part i: linear left-invariant diffusion equations on se (2). *Quarterly of Applied Mathematics*, 68(2):255–292, 2010.

[51] Duits, R. and Franken, E. Left-invariant parabolic evolutions on se (2) and contour enhancement via invertible orientation scores. part ii: nonlinear left-invariant diffusions on invertible orientation scores. *Quart. Appl. Math*, 68(2):293–331, 2010.

[52] Duits, R. and Franken, E. Left-invariant diffusions on the space of positions and orientations and their application to crossing-preserving smoothing of hardi images. *International Journal of Computer Vision*, 92(3):231–264, 2011.

[53] Duits, R., Führ, H., Janssen, B., Bruurmijn, M., Florack, L., and Assen, H. van. Evolution equations on gabor transforms and their applications. *Applied and Computational Harmonic Analysis*, 35(3):483–526, 2013.

[54] Duits, R. and Van Almsick, M. The explicit solutions of linear left-invariant second order stochastic evolution equations on the 2d euclidean motion group. *Quarterly of Applied Mathematics*:27–67, 2008.

[55] Ecker, K. and Huisken, G. Mean curvature evolution of entire graphs. *Annals of Mathematics*, 130(3):453–471, 1989.

[56] Evans, L. C. Convergence of an algorithm for mean curvature motion. *Indiana University Mathematics Journal*, 42(2):533–557, 1993.

[57] Evans, L. C. and Spruck, J. Motion of level sets by mean curvature. ii. *Transactions of the american mathematical society*, 330(1):321–332, 1992.

[58] Evans, L. C. and Spruck, J. Motion of level sets by mean curvature iii. *The Journal of Geometric Analysis*, 2(2):121–150, 1992.

[59] Evans, L. C. and Spruck, J. Motion of level sets by mean curvature iv. *The Journal of Geometric Analysis*, 5(1):77–114, 1995.

[60] Evans, L. C., Spruck, J., et al. Motion of level sets by mean curvature i. *J. Diff. Geom*, 33(3):635–681, 1991.

[61] Favali, M., Abbasi-Sureshjani, S., Romeny, B. H., and Sarti, A. Analysis of vessel connectivities in retinal images by cortically inspired spectral clustering. *Journal of Mathematical Imaging and Vision*, 56(1):158–172, 2016.

[62] Favali, M., Citti, G., and Sarti, A. Local and global gestalt laws: a neurally based spectral approach. *Neural computation*, 2017.

[63] Ferrari, F., Liu, Q., and Manfredi, J. J. On the horizontal mean curvature flow for axisymmetric surfaces in the heisenberg group. *Communications in Contemporary Mathematics*, 16(03):1350027, 2014.

[64] Field, D. J., Hayes, A., and Hess, R. F. Contour integration by the human visual system: evidence for a local association fieldi. *Vision research*, 33(2):173–193, 1993.

[65] Field, D. and Tolhurst, D. The structure and symmetry of simple-cell receptive-field profiles in the cat's visual cortex. *Proceedings of the Royal Society of London B: Biological Sciences*, 228(1253):379–400, 1986.

[66] Fitzpatrick, D. The functional organization of local circuits in visual cortex: insights from the study of tree shrew striate cortex. *Cerebral Cortex*, 6(3):329–341, 1996.

[67] Folland, G. B. and Stein, E. M. Estimates for the ∂_b– complex and analysis on the heisenberg group. *Communications on Pure and Applied Mathematics*, 27(4):429–522, 1974. ISSN: 1097-0312. DOI: 10.1002/cpa.3160270403. URL: http://dx.doi.org/10.1002/cpa.3160270403.

[68] Folland, G. B. Subelliptic estimates and function spaces on nilpotent lie groups. *Arkiv för matematik*, 13(1):161–207, 1975.

[69] Folland, G. B. *Harmonic Analysis in Phase Space.(AM-122)*, volume 122. Princeton university press, 2016.

[70] Franceschiello, B., Sarti, A., and Citti, G. A neuromathematical model for geometrical optical illusions. *Journal of Mathematical Imaging and Vision*:1–15, 2017.

[71] Franchi, B., Serapioni, R., and Cassano, F. S. Regular hypersurfaces, intrinsic perimeter and implicit function theorem in carnot groups. *Communications in analysis and geometry*, 11(5):909–944, 2003.

[72] Franchi, B., Serapioni, R., and Cassano, F. S. Rectifiability and perimeter in the heisenberg group. *Mathematische Annalen*, 321(3):479–531, 2001.

[73] Franken, E. and Duits, R. Crossing-preserving coherence-enhancing diffusion on invertible orientation scores. *International Journal of Computer Vision*, 85(3):253, 2009.

[74] Franken, E. M. Enhancement of crossing elongated structures in images. *Eindhoven University of Technology. Eindhoven, The Netherlands*, 2008.

[75] Frobenius, G. Ueber das pfaffsche problem. *Journal für die reine und angewandte Mathematik*, 82:230–315, 1877.

[76] Gage, M et al. An isoperimetric inequality with applications to curve shortening. *Duke Math. J*, 50(4):1225–1229, 1983.

[77] Gage, M. and Hamilton, R. S. The heat equation shrinking convex plane curves. *Journal of Differential Geometry*, 23(1):69–96, 1986.

[78] Gage, M. E. Curve shortening makes convex curves circular. *Inventiones mathematicae*, 76(2):357–364, 1984.

[79] Gerhard, H. and Alexander, P. Geometric evolution equations for hypersurfaces. In *Calculus of variations and geometric evolution problems*, pages 45–84. Springer, 1999.

[80] Giga, Y. *Surface evolution equations*. Springer, 2006.

[81] Goto, Y., Ishii, K., and Ogawa, T. *Method of the Distance Function to the Bence-Merriman-Osher Algorithm for Motion of Mean Curvature*. Graduate School of Mathematics, Kyushu University, 2002.

[82] Grayson, M. A. The heat equation shrinks embedded plane curves to round points. *Journal of Differential geometry*, 26(2):285–314, 1987.

[83] Hoffman, W. C. Higher visual perception as prolongation of the basic lie transformation group. *Mathematical Biosciences*, 6:437–471, 1970.

[84] Hoffman, W. C. The visual cortex is a contact bundle. *Applied Mathematics and Computation*, 32(2-3):137–167, 1989.

[85] Hörmander, L. Hypoelliptic second order differential equations. *Acta Mathematica*, 119(1):147–171, 1967.

[86] Hubel, D. H. and Wiesel, T. Shape and arrangement of columns in cat's striate cortex. *The Journal of physiology*, 165(3):559–568, 1963.

[87] Hubel, D. H. and Wiesel, T. N. Receptive fields of single neurones in the cat's striate cortex. *The Journal of physiology*, 148(3):574–591, 1959.

[88] Hubel, D. H. and Wiesel, T. N. Receptive fields, binocular interaction and functional architecture in the cat's visual cortex. *The Journal of physiology*, 160(1):106–154, 1962.

[89] Hubel, D. H. and Wiesel, T. N. Receptive fields and functional architecture in two nonstriate visual areas (18 and 19) of the cat. *Journal of neurophysiology*, 28(2):229–289, 1965.

[90] Hübener, M., Shoham, D., Grinvald, A., and Bonhoeffer, T. Spatial relationships among three columnar systems in cat area 17. *Journal of Neuroscience*, 17(23):9270–9284, 1997.

[91] Huisken, G. Asymptotic-behavior for singularities of the mean-curvature flow. *Journal of Differential Geometry*, 31(1):285–299, 1990.

[92] Huisken, G. et al. *Flow by mean curvature of convex surfaces into spheres*. Australian National University, Centre for Mathematical Analysis, 1984.

[93] Ishii, H. A generalization of the bence, merriman and osher algorithm for motion by mean curvature. *Curvature flows and related topics (Levico, 1994)*, 5:111–127, 1995.

[94] Ishii, H., Pires, G. E., Souganidis, P. E., et al. Threshold dynamics type approximation schemes for propagating fronts. *Journal of the Mathematical Society of Japan*, 51(2):267–308, 1999.

[95] Issa, N. P., Rosenberg, A., and Husson, T. R. Models and measurements of functional maps in v1. *Journal of neurophysiology*, 99(6):2745–2754, 2008.

[96] Issa, N. P., Trepel, C., and Stryker, M. P. Spatial frequency maps in cat visual cortex. *The Journal of Neuroscience*, 20(22):8504–8514, 2000.

[97] Jegelka, S., Bednar, J. A., and Miikkulainen, R. Prenatal development of ocular dominance and orientation maps in a self-organizing model of v1. *Neurocomputing*, 69(10):1291–1296, 2006.

[98] Jerison, D. The poincar inequality for vector fields satisfying hrmanders condition. *Duke Math. J.*, 53(2):503–523, June 1986. DOI: 10.1215/S0012-7094-86-05329-9. URL: https://doi.org/10.1215/S0012-7094-86-05329-9.

[99] Jerison, D. S. and Sánchez-Calle, A. Estimates for the heat kernel for a sum of squares of vector fields. *Indiana University mathematics journal*, 35(4):835–854, 1986.

[100] Jones, J. P. and Palmer, L. A. An evaluation of the two-dimensional gabor filter model of simple receptive fields in cat striate cortex. *Journal of neurophysiology*, 58(6):1233–1258, 1987.

[101] Jost, J. and Jost, J. *Riemannian geometry and geometric analysis*, volume 42005. Springer, 2008.

[102] Kalatsky, V. A. and Stryker, M. P. New paradigm for optical imaging: temporally encoded maps of intrinsic signal. *Neuron*, 38(4):529–545, 2003.

[103] Kalisa, C. and Torresani, B. N-dimensional affine weyl-heisenberg wavelets. In *Annales de LInstut Henri Poincare, Physique theorique*, volume 59 of number 2, pages 201–236, 1993.

[104] Kanizsa, G. *Organization in vision: Essays on Gestalt perception*. Praeger Publishers, 1979.

[105] Kanizsa, G. *Grammatica del vedere: saggi su percezione e gestalt*. Il mulino, 1980.

[106] Kennedy, H, Martin, K., Orban, G., and Whitteridge, D. Receptive field properties of neurones in visual area 1 and visual area 2 in the baboon. *Neuroscience*, 14(2):405–415, 1985.

[107] Kimmel, R., Malladi, R., and Sochen, N. Images as embedded maps and minimal surfaces: movies, color, texture, and volumetric medical images. *International Journal of Computer Vision*, 39(2):111–129, 2000.

[108] Kimmel, R., Sochen, N. A., and Malladi, R. On the geometry of texture. Technical report, TECHNION-ISRAEL INST OF TECH HAIFA DEPT OF COMPUTER SCIENCE, 2000.

[109] Koenderink, J. J. The structure of images. *Biological cybernetics*, 50(5):363–370, 1984.

[110] Koenderink, J. J. and Doorn, A. J. van. Representation of local geometry in the visual system. *Biological cybernetics*, 55(6):367–375, 1987.

[111] Koffka, K. *Principles of Gestalt psychology*, volume 44. Routledge, 2013.

[112] Köhler, W. *Gestalt psychology: An introduction to new concepts in modern psychology*. WW Norton & Company, 1970.

[113] Leoni, F. Convergence of an approximation scheme for curvature-dependent motions of sets. *SIAM journal on numerical analysis*, 39(4):1115–1131, 2001.

[114] Levitt, J. B., Kiper, D. C., and Movshon, J. A. Receptive fields and functional architecture of macaque v2. *Journal of neurophysiology*, 71(6):2517–2542, 1994.

[115] Lindeberg, T. Feature detection with automatic scale selection. *International journal of computer vision*, 30(2):79–116, 1998.

[116] Lindeberg, T. A computational theory of visual receptive fields. *Biological cybernetics*, 107(6):589–635, 2013.

[117] Lindelöf, E. Sur lapplication de la méthode des approximations successives aux équations différentielles ordinaires du premier ordre. *Comptes rendus hebdomadaires des séances de lAcadémie des sciences*, 116:454–458, 1894.

[118] Lu, C., Cao, Y., and Mumford, D. Surface evolution under curvature flows. *Journal of Visual Communication and Image Representation*, 13(1):65–81, 2002.

[119] Maffei, L. and Fiorentini, A. Spatial frequency rows in the striate visual cortex. *Vision research*, 17(2):257–264, 1977.

[120] Marĉelja, S. Mathematical description of the responses of simple cortical cells. *JOSA*, 70(11):1297–1300, 1980.

[121] Masnou, S. and Morel, J.-M. Level lines based disocclusion. In *Image Processing, 1998. ICIP 98. Proceedings. 1998 International Conference on*, pages 259–263. IEEE, 1998.

[122] Merriman, B., Bence, J. K., and Osher, S. *Diffusion generated motion by mean curvature*. Department of Mathematics, University of California, Los Angeles, 1992.

[123] Montgomery, R. *A tour of subriemannian geometries, their geodesics and applications*, number 91. American Mathematical Soc., 2006.

[124] Movshon, J. A., Thompson, I. D., and Tolhurst, D. J. Spatial summation in the receptive fields of simple cells in the cat's striate cortex. *The Journal of physiology*, 283:53, 1978.

[125] Mumford, D. Elastica and computer vision. In *Algebraic geometry and its applications*, pages 491–506. Springer, 1994.

[126] Nagel, A., Stein, E. M., and Wainger, S. Balls and metrics defined by vector fields i: basic properties. *Acta Mathematica*, 155(1):103–147, 1985.

[127] Nauhaus, I., Nielsen, K. J., Disney, A. A., and Callaway, E. M. Orthogonal micro-organization of orientation and spatial frequency in primate primary visual cortex. *Nature neuroscience*, 15(12):1683–1690, 2012.

[128] Nitzberg, M., Mumford, D., and Shiota, T. *Filtering, segmentation and depth*. 1993.

[129] Osher, S. and Sethian, J. A. Fronts propagating with curvature-dependent speed: algorithms based on hamilton-jacobi formulations. *Journal of computational physics*, 79(1):12–49, 1988.

[130] Petitot, J. The neurogeometry of pinwheels as a sub-riemannian contact structure. *Journal of Physiology-Paris*, 97(2):265–309, 2003.

[131] Petitot, J. Neurogéométrie de la vision. *Modeles mathématiques et physiques des architectures fonctionelles. Paris: Éd. École Polytech*, 2008.

[132] Petitot, J. and Tondut, Y. Vers une neurogéométrie. fibrations corticales, structures de contact et contours subjectifs modaux. *Mathématiques informatique et sciences humaines*, (145):5–102, 1999.

[133] Plancherel, M. and Leffler, M. Contribution à l'étude de la représentation dune fonction arbitraire par des intégrales définies. *Rendiconti del Circolo Matematico di Palermo (1884-1940)*, 30(1):289–335, 1910.

[134] Ribot, J., Aushana, Y., Bui-Quoc, E., and Milleret, C. Organization and origin of spatial frequency maps in cat visual cortex. *Journal of Neuroscience*, 33(33):13326–13343, 2013.

[135] Ribot, J., Romagnoni, A., Milleret, C., Bennequin, D., and Touboul, J. Pinwheel-dipole configuration in cat early visual cortex. *NeuroImage*, 128:63–73, 2016.

[136] Romagnoni, A., Ribot, J., Bennequin, D., and Touboul, J. Parsimony, exhaustivity and balanced detection in neocortex: supporting information.

[137] Romagnoni, A., Ribot, J., Bennequin, D., and Touboul, J. Parsimony, exhaustivity and balanced detection in neocortex. *PLoS Comput Biol*, 11(11):e1004623, 2015.

[138] Rothschild, L. P. and Stein, E. M. Hypoelliptic differential operators and nilpotent groups. *Acta Mathematica*, 137(1):247–320, 1976.

[139] Sagiv, C., Sochen, N. A., and Zeevi, Y. Y. The uncertainty principle: group theoretic approach, possible minimizers and scale-space properties. *Journal of Mathematical Imaging and Vision*, 26(1-2):149–166, 2006.

[140] Sanguinetti, G., Citti, G., and Sarti, A. Image completion using a diffusion driven mean curvature flowin a sub-riemannian space. *VISAPP (2)*, 8:46–53, 2008.

[141] Sanguinetti, G., Citti, G., and Sarti, A. Implementation of a model for perceptual completion in r2× s1. In *International Conference on Computer Vision and Computer Graphics*, pages 188–201. Springer, 2008.

[142] Sanguinetti, G., Citti, G., and Sarti, A. A model of natural image edge co-occurrence in the rototranslation group. *Journal of vision*, 10(14):37–37, 2010.

[143] Sarti, A. and Citti, G. On the origin and nature of neurogeometry. *La Nuova Critica*, 2011.

[144] Sarti, A. and Citti, G. The constitution of visual perceptual units in the functional architecture of v1. *Journal of computational neuroscience*, 38(2):285–300, 2015.

[145] Sarti, A., Citti, G., and Manfredini, M. From neural oscillations to variational problems in the visual cortex. *Journal of Physiology-Paris*, 97(2):379–385, 2003.

[146] Sarti, A., Citti, G., and Petitot, J. The symplectic structure of the primary visual cortex. *Biological Cybernetics*, 98(1):33–48, 2008.

[147] Sarti, A., Citti, G., and Petitot, J. Functional geometry of the horizontal connectivity in the primary visual cortex. *Journal of Physiology-Paris*, 103(1):37–45, 2009.

[148] Schmidt, K. E., Goebel, R., Löwel, S., and Singer, W. The perceptual grouping criterion of colinearity is reflected by anisotropies of connections in the primary visual cortex. *European Journal of Neuroscience*, 9(5):1083–1089, 1997.

[149] Shoham, D., Hübener, M., Schulze, S., Grinvald, A., and Bonhoeffer, T. Spatio–temporal frequency domains and their relation to cytochrome oxidase staining in cat visual cortex. *Nature*, 385(6616):529–533, 1997.

[150] Silverman, M. S., TOOTELL, R., and DEVALOIS, R. Deoxyglucose and electrophysiological evidence for spatial-frequency columns in cat striate cortex. In *PERCEPTION*, volume 14 of number 1, A15–A15. PION LTD 207 BRONDESBURY PARK, LONDON, ENGLAND NW2 5JN, 1985.

[151] Sirovich, L. and Uglesich, R. The organization of orientation and spatial frequency in primary visual cortex. *Proceedings of the National Academy of Sciences of the United States of America*, 101(48):16941–16946, 2004.

[152] Stellwagen, D and Shatz, C. An instructive role for retinal waves in the development of retinogeniculate connectivity. *Neuron*, 33(3):357–367, 2002.

[153] Sugiura, M. *Unitary representations and harmonic analysis: an introduction*, volume 44. Elsevier, 1990.

[154] Swindale, N. V., Shoham, D., Grinvald, A., Bonhoeffer, T., and Hübener, M. Visual cortex maps are optimized for uniform coverage. *Nature neuroscience*, 3(8):822–826, 2000.

[155] Tanaka, S., Miyashita, M., and Ribot, J. Roles of visual experience and intrinsic mechanism in the activity-dependent self-organization of orientation maps: theory and experiment. *Neural Networks*, 17(8):1363–1375, 2004.

[156] Tani, T., Ribot, J., OHashi, K., and Tanaka, S. Parallel development of orientation maps and spatial frequency selectivity in cat visual cortex. *European Journal of Neuroscience*, 35(1):44–55, 2012.

[157] Thompson, I., Kossut, M, and Blakemore, C. Development of orientation columns in cat striate cortex revealed by 2-deoxyglucose autoradiography . *Nature*, 301(5902):712–715, 1983.

[158] Tolhurst, D. and Thompson, I. On the variety of spatial frequency selectivities shown by neurons in area 17 of the cat. *Proceedings of the Royal Society of London B: Biological Sciences*, 213(1191):183–199, 1981.

[159] Tolhurst, D. and Thompson, I. Organization of neurones preferring similar spatial frequencies in cat striate cortex. *Experimental Brain Research*, 48(2):217–227, 1982.

[160] Tootell, R. B., Switkes, E., Silverman, M. S., and Hamilton, S. L. Functional anatomy of macaque striate cortex. ii. retinotopic organization. *Journal of neuroscience*, 8(5):1531–1568, 1988.

[161] Tootell, R. B., Silverman, M. S., and De Valois, R. L. Spatial frequency columns in primary visual cortex. *Science*, 214(4522):813–815, 1981.

[162] Tsao, D. Y., Conway, B. R., and Livingstone, M. S. Receptive fields of disparity-tuned simple cells in macaque v1. *Neuron*, 38(1):103–114, 2003.

[163] Unser, M. Splines: a perfect fit for signal and image processing. *IEEE Signal Processing Magazine*, 16(6):22–38, 1999.

[164] Villeneuve, M., Vanni, M., and Casanova, C. Modular organization in area 21a of the cat revealed by optical imaging: comparison with the primary visual cortex. *Neuroscience*, 164(3):1320–1333, 2009.

[165] Vittone, D. *Submanifolds in Carnot groups*, volume 7. Edizioni della Normale, 2008.

[166] Vivier, L. et al. Convergence of an approximation scheme for computing motions with curvature dependent velocities. *Differential and Integral Equations*, 13(10-12):1263–1288, 2000.

[167] Wagemans, J., Elder, J. H., Kubovy, M., Palmer, S. E., Peterson, M. A., Singh, M., and Heydt, R. von der. A century of gestalt psychology in visual perception: i. perceptual grouping and figure–ground organization. *Psychological bulletin*, 138(6):1172, 2012.

[168] Watson, A. B. and Robson, J. G. Discrimination at threshold: labelled detectors in human vision. *Vision research*, 21(7):1115–1122, 1981.

[169] Wertheimer, M. Untersuchungen zur lehre von der gestalt. ii. *Psychologische forschung*, 4(1):301–350, 1923.

[170] Wertheimer, M. Laws of organization in perceptual forms. 1938.

[171] Young, R. A. The gaussian derivative model for spatial vision: i. retinal mechanisms. *Spatial vision*, 2(4):273–293, 1987.

[172] Young, R. A., Lesperance, R. M., and Meyer, W. W. The gaussian derivative model for spatial-temporal vision: i. cortical model. *Spatial vision*, 14(3):261–319, 2001.

[173] Yu, H., Farley, B. J., Jin, D. Z., and Sur, M. The coordinated mapping of visual space and response features in visual cortex. *Neuron*, 47(2):267–280, 2005.

[174] Zucker, S. Differential geometry from the frenet point of view: boundary detection, stereo, texture and color. In *Handbook of mathematical models in computer vision*, pages 357–373. Springer, 2006.

Acknowledgements

I would like to thank to Prof. Giovanna Citti and Prof. Alessandro Sarti in the first place, for their enthusiasm, deep curiosity in science and their endless patience with me. The things that I learned from them are priceless.

Besides, thanks to Jérôme Ribot and Jonathan Touboul for their collaboration and fruitful suggestions related to mathematical neuroscience.

I should mention many names from Bologna and Paris who made my days in those two beautiful cities incredibly joyful and who made this period of my life full with valuable memories. I would like to thank first of all to the whole dmUNIBO Ph.D. office. In particular I want to mention the names of Benedetta, Marta, Michele and Martin, since they never hesitated to share their close friendship and always kept the mutual respect. Their friendship is valuable for me.

Apart from those, I owe many thanks to Yasemin for her patience, support and share.

I would like to thank also to Tiphaine for everything.

My special thanks go to my mother Nevin, my father Huseyin, for their endless love, support and their extraordinary friendship; and to my brother, for being a very close friend to me, which is more important than being only a brother in my opinion.

Finally, I want to thank to all pirates and clowns with all my heart, for that they never let me down.